Dissertations, Theses, and Masters Projects   Theses, Dissertations, & Master Projects

2018

First Measurements of the Parity-Violating and Beam-Normal Single-Spin Asymmetries in Elastic Electron-Aluminum Scattering

Kurtis David Bartlett

College of William and Mary - Arts & Sciences, kurtisbartlett@gmail.com

Follow this and additional works at: https://scholarworks.wm.edu/etd

Part of the Nuclear Commons

First Measurements of the Parity-Violating and Beam-Normal Single-Spin
Asymmetries in Elastic Electron-Aluminum Scattering

Kurtis David Bartlett
Belmont, New Hampshire

Master of Science, College of William & Mary, 2014
Bachelor of Science, University of New Hampshire, 2012

A Dissertation presented to the Graduate Faculty
of The College of William & Mary in Candidacy for the
Degree of Doctor of Philosophy

Department of Physics

College of William & Mary
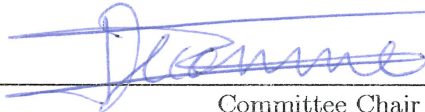August, 2018

APPROVAL PAGE

This Dissertation is submitted in partial fulfillment of
the requirements for the degree of

Doctor of Philosophy

_____
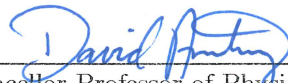
Kurtis David Bartlett

Approved by the Committee July 2018

_____

Committee Chair
Assistant Professor Wouter Deconinck, Physics
College of William & Mary

_____

Chancellor Professor of Physics David Armstrong, Physics
College of William & Mary

_____

Class of 2017 Professor of Physics Joshua Erlich, Physics
College of William & Mary

_____

Assistant Professor Justin Stevens, Physics
College of William & Mary

_____

Dr. Gregory R. Smith, Senior Staff Scientist
Thomas Jefferson National Accelerator Facility

ABSTRACT

The Q$_{weak}$ collaboration has made the first measurements of the elastic parity-violating and beam-normal single-spin asymmetries from t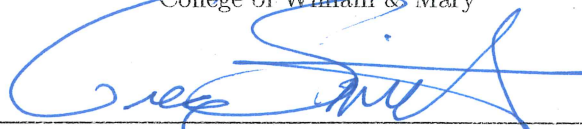he ^{27}Al nucleus. Both are the result of ancillary measurements conducted during the Q$_{weak}$ experiment at Jefferson Lab. The goal of the experimental was to determine the proton's weak charge, Q_W^p, via a measurement of the elastic parity-violating electron-proton scattering asymmetry. During the experiment, ancillary measurements were made with different beam configurations on a separate aluminum alloy target, in an effort to directly measure the aluminum background coming from the experiment's liquid hydrogen target cell.

This dissertation discusses three primary results: the parity-violating ^{27}Al asymmetry analysis used to correct for the aluminum target background in the final Q$_{weak}$ analysis, its extended analysis leading to the extraction of the pure elastic parity-violating ^{27}Al asymmetry, and the determination of the elastic beam-normal single-spin ^{27}Al asymmetry. The parity-violating result was also used to make a semi model-independent determination of ^{27}Al neutron distribution radius, an important test for models used to describe neutron-rich matter. The beam-normal single-spin asymmetry stands to possibly shed light on an observed disagreement between theory and a previous measurement performed on ^{208}Pb, as ^{27}Al is the next highest atomic mass nucleus to have this observable measured.

The elastic parity-violating ^{27}Al asymmetry was found to be 1.927 ± 0.173 ppm at $\langle Q^2 \rangle = 0.0236 \pm 0.0001 \, \text{GeV}^2$. This measured parity-violating asymmetry implies a ^{27}Al neutron distribution radius of 3.024 ± 0.104 fm. Calculating the difference between this radius and the ^{27}Al proton distribution radius yields the neutron skin, which was found to be 0.092 ± 0.104 fm. This skin value is consistent with zero, within its uncertainty, and it confirms the naive expectation for a light nucleus like ^{27}Al.

The beam-normal single-spin ^{27}Al asymmetry was found to be -16.322 ± 2.679 ppm at $\langle Q \rangle = 0.154 \, \text{GeV}$. This value agrees with the previous observed trend of beam-normal single-spin asymmetries measured from light nuclei, which motivates the need for future measurements of higher atomic mass nuclei.

TABLE OF CONTENTS

ACKNOWLEDGEMENTS

knowledge that covers many disciplines in science, it came of use numerous times during this experiment.

A special mention and thanks goes to Greg Smith a senior staff scientist at Jefferson Lab, a fellow Q_{weak} collaboration member, a committee member, and a good friend. Through out my time working on this project Greg has always been an amazing resource and by extension a wonderful third advisor. I must therefore thank him for the numerous long and enjoyable conversations, the helpful advise, the supportive advocacy, the useful comments and improvements on this work, and the occasional weekend sailing trip on the river.

Special thanks goes to my colleagues in the aluminum background sub-group: Katherine Mesick and Joshua Magee. I am glad I had the chance to not only be apart of, but also later helm this important working sub-group. This role/opportunity gave me the ability to continue the aluminum analysis and extract the important physics discussed in this dissertation. My hope is that I will continue to have the opportunity to call both of you my colleagues in future endeavors.

Additional thanks goes to the numerous student members of the Q_{weak} collaboration and the graduate student members of the William & Mary physics department. Mentioned in no particular order they are Juan Carlos Cornejo, Valerie Gray, Scott Barcus, M. Perry Nerem, Melissa Beebe, Victoria Owen, Doug Beringer, Keith Thrasher, Dan Salmon, Josh Hoskins, Jim Dowd, Aria Johansen, Anashe Bandari, Wade Duvall, Anna Lee, Rakitha Beminiwattha, Buddhini Waidyawansa, Marty McHugh, Don Jones, Manolis Kargiantoulakis, Adesh Subedi, Scott MacEwan, Nur, and the others who I do not directly mention by name.

I aslo extend my thanks to the remaining member of my committee, Justin Stevens and Josh Erlich, for accepting responsibility to review the work discussed in this document.

The results detailed in this dissertation would not have been possible without theory support from Charles Horowitz, Farrukh Fattoyev, and Zidu Lin at Indiana University. I must express my gratitude for the support they have provided on this work.

Thanks to the Tuckers, in particular Preston, Martha, Sam and Dexter, for providing a place where I could temporarily escape the pressures and stress associated with working on such a monumental project as that of a graduate degree. For showing me their lovely Virginia hospitality, I will feel permanently indebted. Of course I would have never had this opportunity without meeting Mallory Tucker. My time at William & Mary became all the more special once I met her; thanks Alice Perrin for facilitating our introduction. Since our first meeting over coffee to today, she has been the motivating factor that has given me the strength to complete this project. I must state my gratitude for the continual unwavering support she has given me during this journey, even during the difficult times. She will always hold a place in my heart.

Lastly, I would like to thank my family. Their guidance and support that gave me the opportunity to pursue a graduate degree in the first place, and it still guides and bolsters me to this day.

This dissertation is dedicated to my parents, Timothy and Cynthia, both of whom sacrificed to ensure their children had the opportunity to receive a quality education.

LIST OF TABLES

LIST OF FIGURES

LIST OF EQUATIONS

Chapter 1

Introduction

Humanity's quest to determine the most fundamental components of the known physical Universe has led to the study of fundamental physics. Particle and nuclear physics are examples of sub-fields from the broader fundamental physics field. These sub-fields have been explored since the start of the 20th century and primarily focus on the study of subatomic structure of matter in the Universe. The most championed scientific theory from this sub-field is the Standard Model. Developed initially in the 1960's and 1970's, it has been continually tested. However, a handful of observations cannot be explained within the construct of the Standard Model. As a result, we believe the theory is incomplete and thus requires further development.

One method for testing the Standard Model is to precisely measure physical observables that it predicts. The Q_{weak} experiment, conducted at the Thomas Jefferson National Accelerator Facility from 2010 to 2012, is an example of an experiment performing such a measurement. Q_{weak}, as the experiment is referred to, has made the first direct determination of the proton's weak charge via a precise measurement of the elastic parity-violating electron proton scattering asymmetry. A precise determination of proton's weak charge allows for a correspondingly precise determination of the weak mixing angle, a fundamental parameter of the Standard Model [1–3]. Any observed deviation from the Standard Model predicted value would indicate the presence of new physics. Such a presence would require an extension to the Standard Model.

Several ancillary physics measurements were made during the Q_{weak} experiment. Two of

these ancillary measurements are the focus of this dissertation: the first measurements of the parity-violating and beam-normal single-spin asymmetries in elastic electron aluminum scattering. These are measurements of asymmetries from a secondary target, that were used to determine the largest background correction to the proton's parity-violating asymmetry.

Both of these measurements have interesting physics implications. First, the parity-violating aluminum asymmetry measurement can be used to determine the neutron distribution radius of the aluminum nucleus. A precise determination of the neutron radius in this light nucleus would act as a test for models that describe neutron-rich matter, such as heavy nuclei and neutron stars. Secondly, the aluminum beam-normal single-spin asymmetry could provide insight into an observed disagreement between the measured and predicted lead asymmetry, as aluminum is the next heaviest mass nucleus to have this observable measured. If a disagreement is found between theory and experiment, then that might indicate the need for an improved theoretical prediction of how the beam-normal single-spin asymmetry evolves with atomic mass.

Chapter 2 provides an introduction to the fundamental theory supporting this experiment, while Chapter 3 describes the techniques used to make the measurements. Chapter 4 provides a description of the experimental apparatus. Chapter 5 gives a detailed description of the physics analysis for the determination of the parity-violating aluminum asymmetry. This chapter also discusses the analysis steps used to extract the aluminum neutron distribution radius from the parity-violating asymmetry. Chapter 6 gives a similar description to that of the previous chapter, but for the case of the aluminum beam-normal single-spin asymmetry measurement. My analysis contributions to the proton's parity-violating asymmetry analysis are discussed in Chapter 7. Finally, Chapter 8 concludes this work by stating the impact these results had on the Q_{weak} experiment and will have on future experiments.

This dissertation includes several appendices that contain images, plots, and mathematical derivations. Appendix A includes information and calculations regarding the aluminum auxiliary target. Appendix B and C contain analysis components that do not directly fit into the main body of the text.

In closing, the content put forth in this dissertation aims to be the definitive record of the analyses associated with the aluminum target measurements and their applications

within the Q_{weak} experiment.

Chapter 2

The Standard Model

We think that there are four fundamental forces in the Universe: gravity, strong, weak, and electromagnetic. The Standard Model uses a mathematical structure to describe the dynamics of the latter three forces. A description for gravity is absent from this theory. Historically, gravity has been described by a separate theoretical framework called General Relativity. Attempts have been made to combine gravity and the Standard Model, in what is often referred to as a Quantum Gravity, however none of these theories have been confirmed by experiment. In addition to the absence of gravity, the Standard Model fails to provide a theoretical description for dark matter and dark energy, both of which have been indirectly observed by way of astrophysical measurements.

This chapter will provide an introduction to the particle structure of the Standard Model, their interactions as governed by the electromagnetic and weak forces in the theory, and their physical properties. This introduction will also act as a foundation to support the work discussed later in this dissertation.

2.1 Overview

At its heart, the Standard Model (SM) is a quantum field theory. It combines our understanding of the strong, weak, and electromagnetic forces through the use of a $SU(3)_c \times SU(2)_L \times U(1)_Y$ gauge group structure. The subscripts are labels that denote what these groups represent. For example the strong force $SU(3)_c$, labeled "c" for color,

describes the color charge of the strong force which binds the fundamental particles known as quarks together. The particular quantum field theory that is used to describe the dynamics of strong force systems is known as Quantum Chromodynamics (QCD). The last two forces, which govern the physics of interest in this dissertation, are unified under the SM into what is known as the electroweak sector. The two labels "L" and "Y" describe the preferred left-handed, or chiral, nature of the weak force and the weak hypercharge quantum number, respectively.

Particles, represented by fields in the SM can be divided into two fundamental classes. The first class are known as bosons; these are the force carrying particles. They mediate, or more colloquially, transmit the force between the second class of particles, which are called fermions. The two classes can be differentiated based on a characteristic property known as spin. Bosons are integer spin while fermions are half-integer, or fractional, spin. The former are governed by Boson-Einstein statistics and the latter by Fermi-Dirac statistics.

Bosons are the physical representations of the gauge fields that are introduced to preserve gauge invariance, an important property of the SM. In particular the $SU(3)_c$ part, representing the strong force, is mediated by the gluons (g). The $SU(2)_L$ and $U(1)_Y$ parts of the unified electroweak sector lead to the W and B bosons before the Higgs mechanism causes this symmetry to break spontaneously. After this symmetry breaking, which is discussed in detail in Section 2.3.1, the W and B bosons transform into the experimentally observed $W^\pm$ and Z^0 weak force bosons along with the photon (γ) of the electromagnetic force.

Fermions can be divided up into further categories: types and generations. There are two major types, which are quarks and leptons. Each type has three generations that depend on a mass hierarchy. Out of the two major types, quarks can interact via all three forces in the SM. Leptons interact via both the electromagnetic and weak forces. Figure 2.1 provides a convenient way of displaying the fermions and bosons contained in the SM with their known attributes.

A selection of these fundamental particles, in particular the quarks, are observed to not exist on their own. This is due to the phenomena known as confinement. Usually they are observed as constituents in more complex objects such as composite particle systems
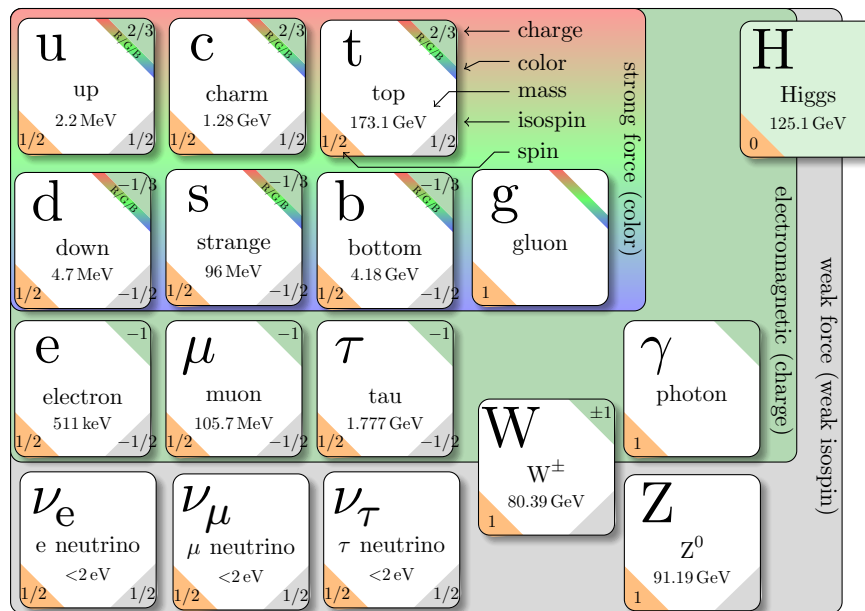
Figure 2.1: Diagram of the fundamental particles described by the SM. Reproduced from [4] with original from [5].

like hadrons. Hadrons can be divided into two sub-categories depending on their quark content: baryons or mesons. Baryons are tri-quark bound particles, the most famous of which are the proton and neutron. The proton is constructed from a combination of the up-up-down quarks and the neutron is constructed from a combination of the up-down-down quarks. These two particular examples are usually found as nucleons in the nucleus in an atom. Mesons are combinations of quark-antiquark pairs and are important for describing the nucleon-nucleon force that binds the nucleons of the nucleus together. More exotic, unstable, versions of these baryonic and mesonic systems exist when they contain the larger mass/higher generations of quarks. Together, particle and nuclear physics looks to study and understand the dynamics and characteristics of these fundamental and complex particle systems as they exist in Nature.

2.2   Symmetries of Nature

When studying these fundamental or complex particle systems, it is often useful to understand their symmetries. Symmetries are best described as an invariance of a given system under a set of transformations. These transformations can be either continuous or discrete. For

symmetries in general, Noether's Theorem states that if the action of a physical system is invariant under a continuous group of transformations then there exists a conserved quantity associated with that invariance [6]. This important concept leads to the idea of a conservation law. For example, invariance of Lagrangian densities or physical phenomena under continuous linear translations in time and space lead to the conserved quantities of energy and linear momentum.

2.2.1   Gauge Invariance

In quantum field theories, conserved quantities can be constructed to respect the symmetries observed in nature. For example, we expect the physics of a particle in a quantum system to be invariant under arbitrary global phase transformations. However, for the less restrictive case of local phase transformations, such a transformation does not leave the Lagrangian invariant. The invariance is preserved with the introduction of a new mathematical structure, which is known as a gauge field.

Consider the Dirac Lagrangian density* for a spin-$\frac{1}{2}$ field ψ with mass m,

$$\mathcal{L}_{Dirac} = \bar{\psi}(i\gamma^{\mu}\partial_{\mu} - m)\psi. \tag{2.1}$$

This Lagrangian is invariant under a global phase transformation acting on the field ψ given by

$$\psi \rightarrow \psi' = e^{-i\alpha}\psi, \tag{2.2}$$

where, in the case of the $U(1)$ group, α is an arbitrary constant that is independent of position. Such a global phase transformation can be interpreted as having no observable effect on the action of the system. When this global phase transformation is changed to a local phase transformation, the phase factor α now depends on position in spacetime,

$$\psi \rightarrow \psi' = e^{-i\alpha(t,\vec{x})}\psi. \tag{2.3}$$

Under such a local phase transformation the Lagrangian is no longer invariant.

---

*From this point forward, the use of Lagrangian is assumed to mean Lagrangian density.

A new term called a gauge field is introduced to preserve the invariance of the Lagangrian. This new gauge field, given the label $A_\mu(x)$ with coupling constant e, is used to modify the ordinary covariant derivative Eq. (2.1) into a gauge covariant derivative,

$$\partial_\mu \to \mathcal{D}_\mu \equiv \partial_\mu - ieA_\mu. \tag{2.4}$$

A_μ describes a new integer-spin particle field which behaves as a boson. The presence of the coupling constant e in the last term of the covariant derivative allows cancellation when including the interaction term in the full theory of Quantum Electrodynamics (QED). With this covariant derivative, the local phase transformation leaves the Lagrangian invariant when we simultaneously require the gauge field A_μ to transform as

$$A_\mu \to A'_\mu = A_\mu - \frac{1}{e}\partial_\mu\alpha. \tag{2.5}$$

This transformation is an enforcement of $U(1)$ gauge invariance.

This is an example of the mechanism that gives rise to the gauge fields in the SM. Similar gauge invariances can be imposed for higher-dimensional symmetry groups. An example of a $SU(2) \times U(1)$ group will be discussed later in this chapter in the context of the electroweak sector of the SM.

2.2.2   Parity

A parity ($\mathcal{P}$) transformation is an inversion of spatial coordinates. Mathematically it can be represented as a conversion from a right-handed to left-handed coordinate system. For a generic four-vector V_μ, a parity transformation is given by

$$V^\mu \xrightarrow{\mathcal{P}} V_\mu = V(t, \vec{x}) \xrightarrow{\mathcal{P}} V(t, -\vec{x}). \tag{2.6}$$

Since we are interested in fermion scattering, it is more important to identify how fermion field bilinears in the electroweak Lagrangian change under parity transformations. Various types of the fermion field bilinears such as scalars, pseudo-scalars, vectors, and axial-vectors, undergo parity transformations in different ways. Table 2.1 provides a summary of how

parity inversion transforms these quantities.

Table 2.1: Examples of how the fermion field bilinears transform during parity inversion.

Type	Action
Scalar	$\overline{\psi}1\psi \xrightarrow{\mathcal{P}} \overline{\psi}1\psi$
Pseudo-scalar	$\overline{\psi}\gamma^5\psi \xrightarrow{\mathcal{P}} -\overline{\psi}\gamma^5\psi$
Vector	$\overline{\psi}\gamma^\mu\psi \xrightarrow{\mathcal{P}} \overline{\psi}\gamma_\mu\psi$
Axial-vector	$\overline{\psi}\gamma^\mu\gamma^5\psi \xrightarrow{\mathcal{P}} -\overline{\psi}\gamma_\mu\gamma^5\psi$

A physical quantity relevant to this dissertation is the pseudo-scalar helicity. Helicity is the projection of the particle's spin along its direction of momentum. For massless particles, and for massive particles in the relativistic limit, the handedness of the particle is directly related to its helicity. The relationship between the helicity and handedness of a particle is given by the helicity operator,

$$h \equiv \hat{p} \cdot S = \frac{1}{2}\hat{p}_i \begin{pmatrix} \sigma^i & 0 \\ 0 & \sigma^i \end{pmatrix} = \begin{cases} \frac{1}{2} & \text{right-handed particle} \\ -\frac{1}{2} & \text{left-handed particle,} \end{cases} \tag{2.7}$$

where σ^i are the Pauli spin matrices.

Until 1957, parity symmetry was believed to be conserved by all of the fundamental interactions. An experiment conducted by C. S. Wu et $al.$ [7] studied the spatial asymmetry of β-decay emission from a polarized ^{60}Co source. They found that the weak interaction that governs β-decay violates parity symmetry, which confirmed an earlier hypothesis given by T. D. Lee and C. N. Yang [8]. This was the first experimental evidence that the weak interaction prefers a handedness. Subsequent experiments have confirmed this observation using complementary experimental techniques.

2.2.3 Isospin

An important approximate symmetry found in composite particle systems is nuclear isospin. Consider a nucleon in the nucleus of an atom as a particle with two potential states. The nucleon could either be in a proton or a neutron state. A new quantum number can be assigned to the nucleon depending on if it is in one of these states. This quantum number is

referred to as isopin (T) as it has an identical mathematical structure as spin-$\frac{1}{2}$ particles, which are governed by the properties of the $SU(2)$ group. This symmetry exists because the difference in the masses between the two particles is small and because the QCD interaction is flavour-independent. The mass of the proton (m_p) is $938.272\,081\,3 \pm 0.000\,005\,8$ MeV and the neutron (m_n) is $939.565\,413\,3 \pm 0.000\,005\,8$ MeV [9]. The underlying reason for this difference comes from the small mass difference of the constituent up and down quarks, electromagnetic effects, and the fact that they are weak isospin doublet partners.

A general state in isospace can be denoted using bra-ket notation $|T, T_3\rangle$, where T_3 is the 3rd component of isospin. The states of the nucleon in isospace are defined as:

$$\left|\tfrac{1}{2}, +\tfrac{1}{2}\right\rangle \equiv |p\rangle \ \ (\text{proton}), \tag{2.8}$$

$$\left|\tfrac{1}{2}, -\tfrac{1}{2}\right\rangle \equiv |n\rangle \ \ (\text{neutron}). \tag{2.9}$$

Using the general rules of the $SU(2)$ group, the nucleon isospin states can be combined to describe many-particle systems [10]. Consider a nuclear system with two nucleons, or an atomic mass (A) of two. The isospin of the nucleons in this coupled system can be arranged into an isotriplet or an isosinglet state. The isotriplet state takes the form

$$|1, 1\rangle \equiv |pp\rangle \,, \tag{2.10}$$

$$|1, 0\rangle \equiv \frac{1}{\sqrt{2}}(|pn\rangle + |np\rangle), \tag{2.11}$$

$$|1, -1\rangle \equiv |nn\rangle \,, \tag{2.12}$$

and the isosinglet the form

$$|0, 0\rangle \equiv \frac{1}{\sqrt{2}}(|pn\rangle - |np\rangle). \tag{2.13}$$

This type of coupling between isospin of nucleons and their associated states can be generalized to a nuclear system of arbitrary A.

Transformations in isospace are often classified by the difference between the initial and final isospin (ΔT) states. These transformations are labeled as either isoscalar $(\Delta T = 0)$ or isovector $(\Delta T = 1)$. Discrete nuclear transitions can cause these types of transformations

and are examples of a type of nuclear process of interest to the research described in this dissertation. Later sections will rely upon this terminology to describe the physics of these discrete nuclear processes.

2.3   Electroweak Sector of the Standard Model

In the late 1960s and early 1970s, Sheldon L. Glashow [11, 12], Steven Weinberg [13], and Abdus Salam [14, 15], introduced a $SU(2)_L \times U(1)_Y$ gauge theory that allowed the unification of the electromagnetic and the weak forces observed in nature. For this work they received the 1979 Nobel Prize in Physics [16]. Their theory employs the principle of gauge invariance, previously discussed in Section 2.2.1, to generate four massless fields as defined by the structure of the $SU(2)_L \times U(1)_Y$ group.

The weak force bosons are known to be massive. Thus a new mechanism called spontaneous symmetry breaking, also known as the Higgs mechanism, is required to break the symmetry of the $SU(2)_L \times U(1)_Y$ group and give the observed fields mass [17, 18]. This section will give an overview of how gauge invariance coupled with spontaneous symmetry breaking yields the experimentally-observed massive $W^{\pm}$, Z^0 and massless γ bosons of the SM. This overview follows a similar derivation outlined in a textbook by T. W. Donnelly *et al.* [10], with additional details taken from the seminal SM text written by P. Langacker [19].

Consider the electroweak Lagrangian $(\mathcal{L}_{EW})$

$$\mathcal{L}_{EW} = \mathcal{L}_{\phi} + \mathcal{L}_{gauge} + \mathcal{L}_f + \mathcal{L}_{Yuk}, \tag{2.14}$$

where the $\mathcal{L}_{\phi}$ describes the dynamics of the Higgs sector of the theory. The $\mathcal{L}_{gauge}$ and $\mathcal{L}_f$ describe the gauge field and kinetic fermion interactions, respectively. Finally, the $\mathcal{L}_{Yuk}$ piece describes the Higgs interaction that gives the fermions mass after spontaneous symmetry breaking.

In the single family version of this theory, a left-handed doublet representing the electron and electron-neutrino fermion fields is introduced to describe the left-handed chiral preference of the weak interaction in the $SU(2)_L$ part. A right-handed singlet is likewise introduced

for the electron, which doesn't include a right-handed neutrino as to match what is seen
in nature. These assignments are used because they have been confirmed by experimental
observation. As mentioned previously in Section 2.1, there are multiple flavours of fermions
in the SM and this theory can be generalized to account for the flavours not mentioned here.

$$\psi_L \equiv \begin{pmatrix} \psi_{\nu_e} \\ \psi_e \end{pmatrix}_L \quad \text{and} \quad \psi_R \equiv \psi_{eR} \tag{2.15}$$

As this theory depends on the handedness of the field, it is also convenient to define the
chiral projection operators

$$P_L = \frac{1}{2}(1 - \gamma_5) \quad \text{and} \quad P_R = \frac{1}{2}(1 + \gamma_5), \tag{2.16}$$

where γ_5 is a Dirac gamma matrix and P_L or P_R applied to the general fermion field (ψ)
selects the left and right handed components of that field. For the case of the electron, this
relation is given by

$$\psi_{eL} = P_L\psi_e \quad \text{and} \quad \psi_{eR} = P_R\psi_e. \tag{2.17}$$

To build the electroweak theory, the first step is to require local gauge invariance, as discussed
in Section 2.2.1. The derivative (∂_μ) in the kinetic terms of Eq. (2.14) is thus replaced by
the covariant derivative and two new gauge fields as

$$D_\mu = (\partial_\mu + \tfrac{ig}{2}\vec{\tau} \cdot \vec{W}_\mu + \tfrac{ig'}{2}Y B_\mu). \tag{2.18}$$

The $SU(2)_L$ piece of the theory introduces a triplet of vector fields ($\vec{W}_\mu$) with a coupling
constant, g. The $U(1)$ piece introduces a single vector field (B_μ) with coupling g'. $\vec{\tau}$
represents the Pauli matrices, which in this case are describing $SU(2)$ weak isospin (I).
Note that it is important to not confuse weak isospin with the isospin of a nucleon as was
introduced in Section 2.2.3. Y is known as the weak hypercharge. Both $\vec{\tau}$ and Y are known
as generators of the groups. The generators for this theory are related by the weak force

version of the well known Gell-Mann–Nishijima formula,

$$Q_{EM} = I_3 + \frac{Y}{2}, \tag{2.19}$$

where I_3 is the 3rd component of weak isospin.

At this point, the theory predicts that these new vector fields, $\vec{W}_\mu$ and B_μ, are massless. If a mass term is inserted into the Lagrangian by hand, which is a term quadratic in terms of the gauge vector fields, it would break the $SU(2) \times U(1)$ gauge invariance. In order to explain the massive gauge bosons represented by a combination of these fields, the $SU(2)_L \times U(1)_Y$ symmetry needs to therefore be broken while preserving the gauge invariance of the Lagrangian. This is accomplished by applying the Higgs mechanism, which spontaneously breaks the symmetry via the introduction of a new complex scalar field.

2.3.1 Spontaneous Symmetry Breaking

The Higgs mechanism [17, 18] as related to the property of spontaneous symmetry breaking in the electroweak model introduces a complex scalar weak isospin doublet field ϕ and its Hermitian adjoint $\phi^\dagger$, which have the form

$$\phi = \begin{pmatrix} \phi^+ \\ \phi^0 \end{pmatrix} \quad \text{and} \quad \phi^\dagger = \begin{pmatrix} \phi^- \\ \phi^{0\dagger} \end{pmatrix}. \tag{2.20}$$

The Higgs piece ($\mathcal{L}_\phi$) of Eq. (2.14) contains kinetic and potential energy terms that can be written as

$$\mathcal{L}_\phi = (D_\mu \phi)^\dagger D^\mu \phi - V(\phi^\dagger \phi). \tag{2.21}$$

D_μ is the covariant derivative defined in Eq. (2.18), which now acts on the complex scalar field ϕ. The potential term $V(\phi^\dagger \phi)$ has quadratic and quartic terms as given by

$$V(\phi^\dagger \phi) = \mu^2 \phi^\dagger \phi + \lambda (\phi^\dagger \phi)^2. \tag{2.22}$$

The potential takes on either a stable or unstable form depending on the sign of the coefficient μ^2. For the case when $\mu^2 > 0$ the potential is stable with minima occurring at $\phi^\dagger \phi = 0$.

When $\mu^2 < 0$, the potential becomes unstable at $\phi^\dagger \phi = 0$ and the minima instead occurs at $\phi^\dagger \phi = \frac{\mu^2}{\lambda}$. Figure 2.2 shows a simplified three dimensional representation of the potential for the two cases of μ^2. The actual potential depends on higher dimensional coordinate systems which are difficult to represent in a two dimensional projection.

<center>$\mu^2 > 0$ $\mu^2 < 0$</center>
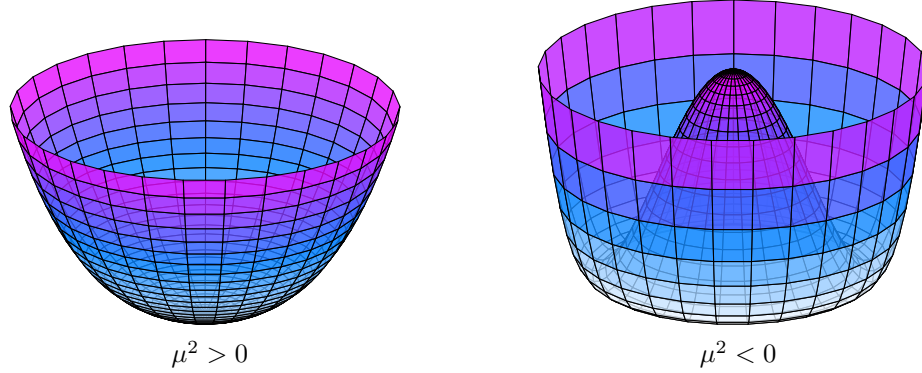
Figure 2.2: Diagram of a simplified three dimensional Higgs potential for stable ($\mu^2 > 0$) and unstable ($\mu^2 < 0$) cases. The potential is colloquially referred to as the *Mexican Hat Potential* as it resembles a sombrero. Reproduced from [20].

Spontaneous symmetry breaking occurs when the complex scalar (ϕ) develops a nonzero vacuum expectation value (VEV) of ν,

$$\langle \phi \rangle = \langle 0 | \phi | 0 \rangle = \frac{1}{\sqrt{2}} \begin{pmatrix} 0 \\ \nu \end{pmatrix} \quad \text{where} \quad \nu = \sqrt{\frac{\mu^2}{\lambda}}. \tag{2.23}$$

Then the fields are quantized around the vacuum, meaning $\phi = \langle \phi \rangle + \phi'$, where ϕ' are the fields with zero VEV. This quantization step is usually done in the unitary gauge allowing one to write the field ϕ as

$$\phi \rightarrow \phi' = \frac{1}{\sqrt{2}} \begin{pmatrix} 0 \\ \nu + H \end{pmatrix}, \tag{2.24}$$

where H is a scalar field representing the Higgs boson [19].

Working in the unitary gauge, the gauge field piece of the covariant derivative in Eq. (2.18)

acting on the nonzero vacuum state becomes

$$D_\mu\phi = \frac{i}{2\sqrt{2}}\begin{pmatrix} gW_\mu{}^3 + g'B_\mu & g(W_\mu{}^1 - iW_\mu{}^2) \\ g(W_\mu{}^1 + iW_\mu{}^2) & -gW_\mu{}^3 + g'B_\mu \end{pmatrix}\begin{pmatrix} 0 \\ \nu \end{pmatrix} \tag{2.25}$$

$$= \frac{i\nu}{2\sqrt{2}}\begin{pmatrix} g(W_\mu{}^1 - iW_\mu{}^2) \\ -gW_\mu{}^3 + g'B_\mu \end{pmatrix}. \tag{2.26}$$

Here terms proportional in H are neglected and $Y = \mathbb{1}_{2\times2}$.

Now focusing on the gauge field piece of the kinetic energy term of Eq. (2.21), it has the form

$$(D_\mu\phi)^\dagger D^\mu\phi = \frac{g^2\nu^2}{4}W_\mu{}^+W^{\mu-} + \frac{\nu^2}{8}(-gW_\mu{}^3 + g'B_\mu)(-gW^{\mu3} + g'B^\mu) \tag{2.27}$$

$$= \frac{g^2\nu^2}{4}W_\mu{}^+W^{\mu-} + \frac{\nu^2}{8}(g^2 + g'^2)Z_\mu Z^\mu + (0)A_\mu A^\mu, \tag{2.28}$$

where the following definitions for the observed gauge fields have been introduced:

$$W_\mu{}^\pm = \frac{1}{\sqrt{2}}(W_\mu{}^1 \mp iW_\mu{}^2), \quad Z_\mu = \frac{gW_\mu{}^3 - g'B_\mu}{\sqrt{g^2 + g'^2}}, \quad A_\mu = \frac{gW_\mu{}^3 + g'B_\mu}{\sqrt{g^2 + g'^2}}. \tag{2.29}$$

The $W_\mu{}^\pm$ field represents the boson in the weak charge-current interaction. The Z_μ and A_μ fields represent the bosons in the weak neutral and electromagnetic interactions, respectively. The coefficients of the terms quadratic in the fields yield the masses of these gauge bosons. In terms of the couplings g and g', the masses for the $W^\pm$, Z^0, and γ are:

$$m_W = \frac{\nu g}{2}, \quad m_Z = \frac{\nu}{2}\sqrt{g^2 + g'^2}, \quad \text{and } m_\gamma = 0. \tag{2.30}$$

The masses of these heavy bosons have been experimentally determined using high energy accelerators. The mass of the $W^\pm$ (m_W) is $80.385 \pm 0.015\,\text{GeV}$ and the mass of the Z^0 (m_Z) is $91.1876 \pm 0.0021\,\text{GeV}$ [9]. The VEV is fixed to a value of approximately $246\,\text{GeV}$ by the Fermi constant [9].

It can be seen in Eq. (2.29) that the observed Z_μ and A_μ fields are constructed from a

linear combination of the original $W_\mu{}^3$ and B_μ fields. This linear combination of fields can be represented by a matrix transformation. A convenient angle parameterization can be introduced to describe the amount of mixing that occurs in the electroweak theory using the coupling constants of the original fields,

$$\tan^2 \theta_W = \frac{g'^2}{g^2} \quad \text{or} \quad \sin^2 \theta_W = \frac{g'^2}{g^2 + g'^2} \quad \text{or} \quad \cos^2 \theta_W = \frac{g^2}{g^2 + g'^2} \qquad (2.31)$$

where θ_W is that mixing angle, which is also known as the Weinberg angle. Using these newly defined quantities, the linear combinations in the original gauge fields can be written as the following matrix transformation:

$$\begin{pmatrix} Z_\mu \\ A_\mu \end{pmatrix} = \begin{pmatrix} \cos \theta_W & -\sin \theta_W \\ \sin \theta_W & \cos \theta_W \end{pmatrix} \begin{pmatrix} W_\mu{}^3 \\ B_\mu \end{pmatrix}. \qquad (2.32)$$

It is important to note that the weak mixing angle parameter is scale-dependent as it is constructed from a combination of couplings which run with scale. Precision determinations of this mixing angle parameter at different energies act as a test of the scale dependence as predicted by the SM.

Up to this point, only the gauge bosons have been shown to have mass after spontaneous symmetry breaking. The fermions are also originally massless and the direct insertion of a mass term would also break the gauge invariance of the Lagrangian. The fermions thus acquire mass from the Higgs mechanism through the Yukawa interaction. The Yukawa interaction piece $(\mathcal{L}_{Yuk})$ from Eq. (2.14) for the case of the electron can be written as

$$\mathcal{L}_{Yuk} = \frac{g_e \nu}{2\sqrt{2}} (\bar{\psi}_{eL} \phi \psi_{eR} + \bar{\psi}_{eR} \phi^\dagger \psi_{eL}), \qquad (2.33)$$

where the mass of the electron (m_e) becomes $m_e = \frac{g_e \nu}{\sqrt{2}}$. Similar interaction terms arise for the rest of the fermions in the SM, which gives them mass. The exception to this are the neutrinos which remain massless as they don't have a right-handed state in this version of the theory. There are other Higgs field interactions in the SM that give the neutrinos with mass; these are discussed in Langacker's text [19].

2.3.2   Electroweak Neutral Current Interactions

In the electroweak theory, electrons can undergo a neutral current interaction via the exchange of either a massless photon γ or the massive Z^0 boson. The first is considered an electromagnetic interaction while the later is referred to as the neutral weak interaction. For the diagrammatic representation of these two boson interactions with fermions, see Fig. 2.3.

(a) γ vertex   (b) Z^0 vertex

Figure 2.3: Neutral electroweak vertex diagrams for the electromagnetic (a) and weak neutral-current (b) interactions.

Each of these types of interactions can be written in terms of the fermion gauge interaction and the fermion fields in the Lagrangian, expressed through vector fermion bilinears known as currents. The two currents for these neutral interactions are:

$$J_\mu^\gamma = Q_{EM}\bar{\psi}\gamma_\mu\psi, \tag{2.34}$$

$$J_\mu^{Z^0} = J_\mu^3 \cos\theta_W - J_\mu^Y \sin\theta_W. \tag{2.35}$$

$J_\mu^{Z^0}$ takes an analogous form to the Z_μ gauge field relation in Eq. (2.32). $W_\mu{}^3$ and B_μ in that relationship are replaced with their current forms, J_μ^3 and J_μ^Y as labeled by their group generators. These currents can be written in terms of the fermion fields.

$$J_\mu^Y = \frac{g'}{2}Y\bar{\psi}\gamma_\mu\psi \tag{2.36}$$

$$J_\mu^3 = -\frac{g}{2}\bar{\psi}_L\gamma_\mu\psi_L \tag{2.37}$$

Equation (2.35) can be expressed in expanded form in terms of the fermion fields and their weak couplings,

$$J_\mu^{Z^0} = \frac{g_z}{2}\left([2I_3 - 2Q_{EM}\sin^2\theta_W]\bar{\psi}_L\gamma_\mu\psi_L + [-2Q_{EM}\sin^2\theta_W]\bar{\psi}_R\gamma_\mu\psi_R\right), \tag{2.38}$$

where $g_Z = \frac{e}{\sin\theta_W \cos\theta_W}$ is the Z^0 coupling constant. This expression can be simplified by defining two new quantities known as the weak vector (g_V) and axial-vector (g_A) fermion couplings,

$$g_V \equiv I_3 - 2Q_{EM}\sin^2\theta_W \tag{2.39}$$

$$g_A \equiv I_3. \tag{2.40}$$

Table 2.2: Electromagnetic charge (Q_{EM}), 3rd component of weak isospin (I_3) quantum number along with the vector (g_V) and axial-vector (g_A) couplings of the fermions in the SM.

Type	Q_{EM}	I_3	$2g_V$	$2g_A$
e^-, μ^-, τ^-	-1	$-\frac{1}{2}$	$-1 + 4\sin^2\theta_W$	-1
ν_e, ν_μ, ν_τ	0	$\frac{1}{2}$	1	1
u, c, t	$\frac{2}{3}$	$\frac{1}{2}$	$1 - \frac{8}{3}\sin^2\theta_W$	1
d, s, b	$-\frac{1}{3}$	$-\frac{1}{2}$	$-1 + \frac{4}{3}\sin^2\theta_W$	-1

Table 2.2 contain values of weak vector and axial-vector couplings for the various families of fermions in the SM. These new definitions can be used, in conjunction with the chiral projection operators of Eq. (2.16), to rewrite Eq. (2.38) in the following compact form,

$$J_\mu^{Z^0} = \bar{\psi}\gamma_\mu(g_V - g_A\gamma^5)\psi. \tag{2.41}$$

This form of the Z^0 current allows the easy identification of the parity-violating nature of the combined vector and axial-vector pieces of the neutral weak interaction.

Also, both Eqs. (2.34) and (2.41) allow the identification of the vertex factors for the γ and Z^0 exchange diagrams shown in Fig. 2.3.

$$\gamma : -ieQ_{EM}\gamma_\mu \quad \text{and} \quad Z^0 : -i\frac{g_Z}{2}\gamma_\mu(g_V - g_A\gamma^5) \tag{2.42}$$

2.3.3 Nuclear Weak Charges

As this dissertation is interested in parity-violating (PV) electron-nucleus scattering at energies much lower than m_Z, it is useful to interpret the neutral weak interaction in terms of a low-energy effective theory formalism. Consider the neutral weak interaction when the

momentum transfer (q^2) of the interaction is $q^2 \ll m_Z$, an effective four-fermion interaction operator of the following form,

$$\mathcal{L}_{eff} = -\frac{G_F}{\sqrt{2}} J_\mu^{Z^0} J_{Z^0}^\mu \tag{2.43}$$

can be introduced as shown by Langacker [19]. Eq. (2.43) introduces the Fermi constant (G_F), which is related to the weak coupling g by the relation $G_F = \sqrt{2}(\frac{g^2}{8m_W^2})$.

This new neutral weak effective interaction can be expanded in terms of the current $J_\mu^{Z^0}$. By considering only the PV electron-quark interaction pieces of the new effective Lagrangian term, the following pieces survive

$$\mathcal{L}_{PV}^{Z^0} = \frac{G_F}{\sqrt{2}} \sum_{q=u,d} (C_{1q} \bar{\psi}_e \gamma_\mu \gamma^5 \psi_e \bar{\psi}_q \gamma^\mu \psi_q + C_{2q} \bar{\psi}_e \gamma_\mu \psi_e \bar{\psi}_q \gamma^\mu \gamma^5 \psi_q). \tag{2.44}$$

This expression introduces two new couplings, the vector-axial coupling (C_{1q}) and axial-vector coupling (C_{2q}). They are related to the weak vector and axial-vector charges by the following relations: $C_{1q} \equiv 2g_A^e g_V^q$ and $C_{2q} \equiv 2g_V^e g_A^q$. At lowest order in perturbation theory, or tree-level, these coupling for electron-quark scattering are

$$\begin{aligned} C_{1u} = -\tfrac{1}{2} + \tfrac{4}{3}\sin^2\theta_W, \quad & C_{2u} = -\tfrac{1}{2} + 2\sin^2\theta_W, \\ C_{1d} = \tfrac{1}{2} - \tfrac{2}{3}\sin^2\theta_W, \quad & C_{2d} = \tfrac{1}{2} - 2\sin^2\theta_W. \end{aligned} \tag{2.45}$$

Knowledge of these electron-quark couplings allows one to define a quantity known as the weak vector charge. The weak charge (Q_W) gives the strength of the neutral current quark-electron vector-axial interaction[†]. This concept of a weak charge is analogous to the charge (Q) of the electromagnetic force. For a nuclear system containing a number of protons Z and a number of neutrons N, the weak charge is defined as

$$Q_W \equiv -2[C_{1u}(2Z + N) + C_{1d}(Z + 2N)]. \tag{2.46}$$

In the case of the proton and neutron, Eq. (2.46) reduces down to the sum of the quark-

---

[†]The neutral current vector-axial interaction is taken to mean the quark's vector coupling to Z^0 and the electron's axial-vector coupling to Z^0.

electron vector-axial couplings of the constituent quarks in the nuclear system. The proton's

weak charge takes the form, based on its quark content, of

$$Q_W^p \equiv -2(2C_{1u} + C_{1d}) \tag{2.47}$$

and for the neutron

$$Q_W^n \equiv -2(C_{1u} + 2C_{1d}). \tag{2.48}$$

At tree-level and using a value of $\sin^2 \theta_W \approx 0.23$ [9], the weak charges of the proton and

neutron become $Q_W^p = 1 - 4\sin^2 \theta_W \approx 0.07$ and $Q_W^n = -1$. Thus in PV electron-nucleus

scattering the electron favors scattering from the neutrons of the nuclear system, as it

has a larger weak charge. Conversely, the suppressed weak charge of the proton acts as

a convenient observable to perform a precision measurement in a SM test, since non-SM

effects are not *a priori* expected to be suppressed in a similar fashion.

Chapter 3

Electron Scattering Techniques

The most important scientific tool in the nuclear or hadronic physicist's toolbox is particle scattering. Important structural information can be determined about the nucleus via the scattering of a particle probe from a nuclear or hadronic target. One option for a particle probe is the electron, the lightest electromagnetically charged lepton. Electrons are excellent probes for scattering experiments as they have a number of beneficial qualities. First, the electron is a fundamental particle; it has no known substructure. Electrons are easy to produce in the form of a controllable beam, which can be accelerated to relativistic energies. Depending on the energy of the beam, the electron can probe ever decreasing distance scales within the nucleus as given by the de-Broglie momentum-wavelength relation. Lastly, electron beams can be polarized, which allows for study of polarization-dependent structure observables in the nucleus.

Structure information is extracted from scattering experiments by interpreting measured cross sections. Cross sections are proportional to the probability for a given type of scattering interaction to occur and are typically reported as either a differential or total quantity. For a general introduction to the concept of a scattering cross section see the text by B. Povh *et al.* [21]. Typically, differential cross sections are reported with respect to a kinematic variable. For example, elastic scattering cross sections are often differentiated with solid angle ($d\Omega$). However, for inelastic scattering interactions, the cross section is often differentiated not only with respect to solid angle but also energy. The total cross section (σ) is the integrated form of the differential cross section over all angle and energy phase space. In the context of
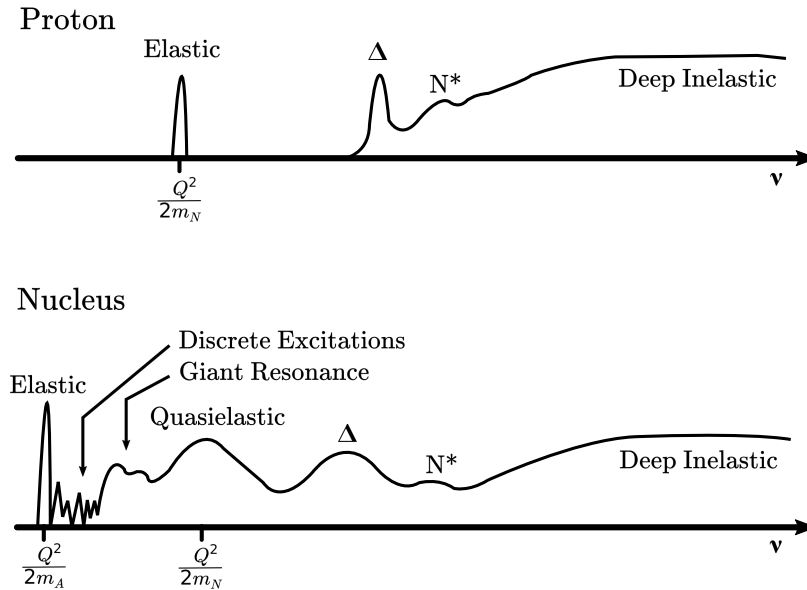
Figure 3.1: An engineered example of the electron scattering cross section spectrum from the proton (top) and a generic nucleus (bottom) versus energy transfer (ν). Recreated from textbook diagram [10], as an adaptation from the original version [22].

this dissertation, when a cross section is mentioned it refers to the differential form, which is denoted by symbol $d\sigma$. In specific cases, the cross section for either the elastic or inelastic form will be noted using the differential notation $\frac{d\sigma}{d\Omega}$ or $\frac{d^2\sigma}{d\Omega dE}$ respectively.

In electron-nucleus scattering, a number of different types of interactions can occur depending on the kinematics of the incident electron. For a given nuclear target and an electron beam at a fixed energy, a spectrum of scattered electrons is produced with a range of energies from just a few MeV to that of the primary beam and scattering angles over a full 4π. Measuring the cross section of these scattered electrons over this energy and angle spectrum allows the experimental determination of the internal structure of the target nucleus. An example of such a spectrum can be seen in Fig. 3.1 for the case of the proton and a generic nucleus.

Electron scattering can give structure information about the nucleus in its ground state via elastic scattering. As more energy is transferred to the nucleus, the interaction starts to become more inelastic. That transferred energy can be used to stimulate the nucleus to a higher excited state, which is often described in the context of the nuclear shell model
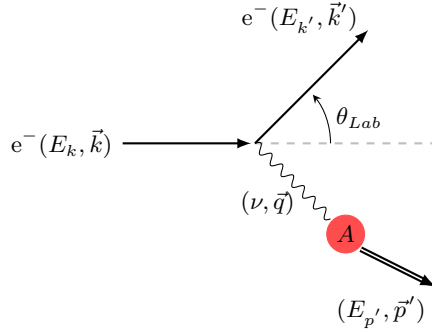
Figure 3.2: Inclusive electron scattering from an arbitrary nucleus with mass m_A, in the lab reference frame. Adapted from original illustration taken from the dissertation of V. M. Gray [24].

description of a discrete nucleon excitation. The energy could also be used to excite collective motion of the individual nucleons in the nucleus. An example of such collective excitation is the Giant Dipole Resonance. As the energy transfer approaches the nucleon's binding energy, approximately $8\,\mathrm{MeV}$, the nucleon can be ejected from the nucleus in what is known as a quasielastic reaction [21, 23]. The transferred energy may be so large that the scattered electron begins to probe the nucleon substructure of the nucleus, in what is known as deep inelastic scattering (DIS).

To give the reader a better understanding of scattering methods used to extract the physics described in this dissertation, this chapter will give a brief introduction to the theoretical framework of the physical observables measured in this experiment. To start off, this chapter introduces several kinematic quantities useful for describing the dynamics of electron-nucleus scattering, along with how those quantities are used to interpret the extended structure of the nucleus. It will also introduce the motivation for conducting the Q_{weak} experiment, along with giving a brief overview of previous parity-violating and beam-normal single-spin asymmetry measurements.

3.1 Scattering Kinematics

When discussing electron scattering, it is useful to define a collection of physical quantities that describe the kinematics of the interaction.

Consider the system where an incident electron with four-momentum $k_\mu = (E_k, \vec{k})$

scatters from a nucleus with four-momentum $p_\mu = (E_p, \vec{p})$, where E_k (E_p) is the energy and $\vec{k}$ ($\vec{p}$) is the three-momentum of the probe particle. After the interaction, the outgoing electron carries a four-momentum $k'_\mu = (E_{k'}, \vec{k}')$ and the recoiling nucleus $p'_\mu = (E_{p'}, \vec{p}')$. A diagram of this scattering system can be seen in Fig. 3.2. During the interaction, the four-momentum transferred between the electron and nucleus is given by $q_\mu = (\nu, \vec{q})$. Conservation of four-momentum allows the momentum transfer to be related to the momentum of the incoming and outgoing states by the following relation

$$q_\mu = k_\mu - k'_\mu = p_\mu - p'_\mu. \tag{3.1}$$

Theoretically, it is convenient to describe the momentum transfer of the reaction with the Lorentz invariant quantity $-q_\mu q^\mu$. Based on convention, this invariant quantity is defined as a positive definite quantity,

$$Q^2 \equiv -q_\mu q^\mu = \vec{q}^{\,2} - \nu^2 \geq 0, \tag{3.2}$$

where the energy transfer of the interaction is given by $\nu = E_k - E_{k'}$. For inclusive measurements where only the scattered electron is detected, the squared three-momentum transfer can be written in terms of the electron's momentum and lab scattering angle (θ_{Lab}) in the following way

$$\vec{q}^{\,2} = \vec{k}^2 + \vec{k}'^2 - 2|\vec{k}||\vec{k}'| \cos \theta_{Lab}. \tag{3.3}$$

Using the energy-momentum relation ($E^2 = \vec{k}^2 + m^2$), Eq. (3.2) can be reduced to the more convenient form of

$$Q^2 = 4|\vec{k}||\vec{k}'| \sin^2 \tfrac{\theta_{Lab}}{2} + 2(E_k E_{k'} - |\vec{k}||\vec{k}'| - m_e^2). \tag{3.4}$$

For experiments using high-energy relativistic electrons, when $E_k \gg m_e$ and $|\vec{k}'| \gg m_e$, the long wavelength limit can be applied to Eq. (3.4), where $|\vec{k}| \simeq E_k$ and $|\vec{k}'| \simeq E_{k'}$. Thus Eq. (3.4) reduces to

$$Q^2 \simeq 4 E_k E_{k'} \sin^2 \tfrac{\theta_{Lab}}{2}. \tag{3.5}$$

In the special case of elastic electron-nucleus scattering, the energy of the scattered

electron $E_{k'}$ can be related to the incident electron energy E_k by $E_{k'} = E_k f_{rec}^{-1}$, where the recoil factor (f_{rec}) is

$$f_{rec} = 1 + \frac{2E_k}{m_A} \sin^2 \frac{\theta_{Lab}}{2} \tag{3.6}$$

and m_A is the mass of the target nucleus. Equation (3.5) can be simplified to a dependence on just the two variables, E_k and θ_{Lab}, using this recoil energy relation, which takes the form of

$$Q^2 \simeq 4E_k^2 f_{rec}^{-1} \sin^2 \frac{\theta_{Lab}}{2} = \frac{4E_k^2 \sin^2 \frac{\theta_{Lab}}{2}}{1 + \frac{2E_k}{m_A} \sin^2 \frac{\theta_{Lab}}{2}}. \tag{3.7}$$

In later discussions about inelastic scattering processes, it is useful to introduce a kinematic variable that describes the amount of energy an excited final state has. This quantity is known as the invariant mass, given in units of energy, and is related to the momentum transfer by

$$W^2 = m_A^2 + 2m_A \nu - Q^2, \tag{3.8}$$

where m_A is the mass of the target in the initial state, ν the energy transfer in the reaction, and Q^2 the previously introduced momentum transfer from Eq. (3.5). When discussing quasi-elastic m_A in the invariant mass relation becomes the nucleon mass (m_N).

3.2 Electromagnetic and Weak Form Factors

In elastic electron-nucleus scattering, the electron can interact with the nucleus via the exchange of either a virtual photon or Z^0 boson. Figure 3.3 shows the lowest order Feynman diagrams that describe these possible electroweak interactions.

(a) γ Exchange   (b) Z^0 Exchange

Figure 3.3: Lowest order electroweak Feynman diagrams for electron-nucleus scattering, where either a photon (γ) or Z^0 is exchanged between the electron (e$^-$) and nucleus (A).

In the Born approximation, also known as the single boson exchange formalism, the

differential cross section for unpolarized electron-nucleus scattering can be written in terms

of the Mott cross section and a general Q^2 dependent function known as a form factor [10,

21], given by

$$\frac{d\sigma}{d\Omega} = \left(\frac{d\sigma}{d\Omega}\right)_{\text{Mott}} |F(q)|^2. \tag{3.9}$$

The Mott cross section describes the dynamics of an electron scattering from a point-like

target particle and has the following functional form in the lab frame

$$\left(\frac{d\sigma}{d\Omega}\right)_{\text{Mott}} = \frac{Z^2 \alpha^2 \hbar^2 c^2 \cos^2 \frac{\theta_{Lab}}{2}}{4 E_k^2 \sin^4 \frac{\theta_{Lab}}{2}}, \tag{3.10}$$

where Z is the atomic number of the nuclear target, α is the fine structure constant, c the

speed of light, and E_k along with θ_{Lab} are the kinematic variables introduced in the previous

section. When the target nucleus is not point-like, which is usually the case, it is known

to have an extended structure. This extended structure is generally described by the form

factor function $F(q)$ introduced in Eq. (3.9).

3.2.1 Electron-Nucleon Scattering

In the case of elastic electromagnetic electron-nucleon scattering, the form factor is broken

into longitudinal and transverse components that are characterized in the literature into

what is known as the electric and magnetic form factors, respectively. These form factors

carry the label of $G_E^{N,\gamma}(Q^2)$ and $G_M^{N,\gamma}(Q^2)$, and are referred to as the Sachs form factors.

Electromagnetic form factors are generally related to the QED current introduced in the

previous chapter, as given in Eq. (2.34). The formalism of this relation is described in detail

in Langacker's text [19], but is written for a general nucleon state as

$$\langle N| J_\gamma^\mu |N\rangle = \bar{u}\left[\gamma^\mu F_1^{N,\gamma}(Q^2) + \frac{i\sigma^{\mu\nu}}{2m_N}q_\nu F_2^{N,\gamma}(Q^2)\right]u, \tag{3.11}$$

where u are the fermion spinors, γ^μ are the gamma matrices, and $\sigma^{\mu\nu}$ their commutation

relation given by $\sigma^{\mu\nu} = \frac{i}{2}[\gamma^\mu, \gamma^\nu]$. Equation (3.11) uses the traditional Dirac ($F_1^{N,\gamma}(Q^2)$)

and Pauli ($F_2^{N,\gamma}(Q^2)$) notation for the form factors. These are related to the Sachs form

factors by [10, 25]

$$G_E^{N,\gamma}(Q^2) \equiv F_1^{N,\gamma}(Q^2) - \tau F_2^{N,\gamma}(Q^2) \tag{3.12}$$

$$G_M^{N,\gamma}(Q^2) \equiv F_1^{N,\gamma}(Q^2) + F_2^{N,\gamma}(Q^2), \tag{3.13}$$

where $\tau = \frac{Q^2}{4m_N^2}$ is a kinematic factor. These form factors are often given as isospin combinations, where the isoscalar ($\Delta T = 0$) and isovector ($\Delta T = 1$) combinations are defined as

$$\begin{aligned}
G_{E(M)}^{\Delta T=0}(Q^2) &= \frac{1}{2}[G_{E(M)}^p(Q^2) + G_{E(M)}^n(Q^2)], \\
G_{E(M)}^{\Delta T=1}(Q^2) &= \frac{1}{2}[G_{E(M)}^p(Q^2) - G_{E(M)}^n(Q^2)],
\end{aligned} \tag{3.14}$$

and similarly for $F_{1(2)}^{\Delta T=0}$ and $F_{1(2)}^{\Delta T=1}$.

Using the Sachs form factors the elastic electron-nucleon cross section can be written as

$$\frac{d\sigma}{d\Omega} = \left(\frac{d\sigma}{d\Omega}\right)_{\text{Mott}} \frac{E_{k'}}{E_k} \frac{[G_E^{N,\gamma}(Q^2)]^2 + \tau[G_M^{N,\gamma}(Q^2)]^2}{1+\tau} + 2\tau[G_M^{N,\gamma}(Q^2)]^2 \tan^2\frac{\theta_{Lab}}{2}, \tag{3.15}$$

This expression is known as the *Rosenbluth formula* [10, 26]. $G_E^{N,\gamma}$ and $G_M^{N,\gamma}$ contain the structural information about the nucleon's charge and magnetization distributions. As these form factors are defined in momentum space, their Fourier transformation to the zero energy transfer frame ($\nu = 0$), the so called Breit frame, gives the spatial charge and magnetization distributions of the nucleon [10]. In the limit $Q^2 \to 0$, the form factors yield the electric charge and magnetic moment of the nucleon. For the example of the proton: $G_E^{p,\gamma}(0) = Q_{EM}^p = 1$ and $G_M^{p,\gamma}(0) = \mu_p = 2.79\mu_N$ [9].

Theoretically, it is difficult to derive an expression for these form factors from first principles. A long series of cross section measurements have therefore been performed at a range of momentum transfers in an attempt to map the Q^2 dependence of these form factors. Experimentally, the form factors have been found to have a Q^2 dependence that generally follows the dipole function. This function, labeled G_D, can be written as [10]

$$G_D(Q^2) = \left(1 + \frac{Q^2}{0.71\,\text{GeV}^2}\right)^{-2} = (1 + 4.97\tau)^{-2}. \tag{3.16}$$

In the literature, the extracted form factors from nucleon cross section measurements are usually plotted as a ratio of the form factor over the dipole form, which shows any deviation from unity. The only exception to this dipole functional form is the neutron's electric form factor ($G_E^{n,\gamma}$), which has a proportional Q^2 dependence as the neutron does not have an electric charge. It is important to note that the neutron's form factors are typically determined from cross section measurements performed on light nuclei, such as deuterium or helium-3, as no pure neutron targets exists. The extraction of the neutron's form factors thus requires systematic corrections for the proton's contribution in those measurements. For a summary of the measurements performed to date, along with examples of the plots of world data, see articles [27, 28].

There are two interesting discrepancies associated with the proton's electric form factor that should be briefly mentioned, as they are deep sub-fields of research themselves. The first is known as the two-photon exchange (TPE) problem. Early cross section measurements at Q^2 greater than $1\,\mathrm{GeV}^2$ used the traditional Rosenbluth separation method, which disagreed with the more modern target polarization measurement techniques. This disagreement is partial resolved with the realization that higher-order, or multiple photon exchange, corrections were needed to fully understand the Q^2 dependence of $G_E^{p,\gamma}$. For those interested in this issue, more detail is given in the literature [27–29].

To use these extracted nucleon form factors, they are often parameterized with a fit. Historically, parameterizations by Galster *et al.* [30] have been used, however newer parameterizations are available, for example see the recent publication by Z. Ye *et al.* [31]. Parameterizing the low Q^2 dependence of $G_E^{p,\gamma}$ has led to the second discrepancy mentioned. This is related to the proton's charge radius problem. Since the Fourier transform of the nucleon form factors yields spatial distribution information, it can be shown that in the limit $Q^2 \to 0$ the radius of the charge distribution ($\langle r_N^2 \rangle^{\frac{1}{2}}$) can be written as

$$\langle r_N^2 \rangle = -6 \left. \frac{dG_E^N(Q^2)}{dQ^2} \right|_{Q^2=0}. \tag{3.17}$$

A derivation of Eq. (3.17) can be found in T. W. Donnelly's text [10]. Originally, there was disagreement between two methods for determining the proton's charge radius. The

first method uses electron-proton scattering data fits to $G_E^{p,\gamma}$ and Eq. (3.17). The second type of determination is made via atomic Lamb shift measurements performed on atomic and muonic hydrogen. Early analyses indicated that the electron-proton scattering method produced a charge radius that agreed with the atomic Lamb shift result, but disagreed with the muonic hydrogen Lamb shift result. Later alternative analysis of the electron-proton scattering results by D. W. Higinbotham *et al.* [32] have brought the charge radius into agreement with the muonic hydrogen result. It is fair to say that this is an active field of research, searching to find consensus on the correct value of the proton's charge radius. For present values of the charge radius and their corresponding references, see the PDG listing [9].

In addition to the electromagnetic electron-nucleon scattering form factors, there are also neutral-weak form factors. Just like their electromagnetic analogs, they describe the extended structure of the nucleon probed in neutral-weak Z^0 exchange. Following a similar procedure to that used to derive the electromagnetic form factors, the neutral-weak current can be related to the neutral-weak version of the Dirac ($F_1^{N,Z}(Q^2)$) and Pauli ($F_2^{N,Z}(Q^2)$) form factors by

$$\langle N | J_Z^\mu | N \rangle = \bar{u} \left[\gamma^\mu F_1^{N,Z}(Q^2) + \frac{i\sigma^{\mu\nu}}{2m_N} q_\nu F_2^{N,Z}(Q^2) + \gamma^\mu \gamma^5 G_A^{N,Z}(Q^2) \right] u. \qquad (3.18)$$

$G_A^{N,Z}$, the weak axial-vector form factor, is introduced to describe the axial-vector structure of the neutral-weak interaction. The neutral-weak version of the Dirac and Pauli form factors can be related to their Sachs version using analogous relations to those given in Eqs. (3.12) and (3.13).

Experimentally, the functional form of these form factors are not well known, mainly due to the difficulties of separating out the neutral-weak response from the dominant electromagnetic response in elastic electron-nucleon scattering. The reason for this will be discussed in more detail in the next section. The neutral weak form factors can be expressed solely in terms of the electromagnetic form factors by way of a decomposition involving the nucleon's constituent quark's form factors. This procedure is only possible because of the mixing between the electromagnetic and weak sectors of the SM. A detailed discussion of

this procedure can be found in reference [10, 33], but a brief summary is given here.

The decomposition of the electromagnetic and neutral weak form factors can be written as the following set of sums over quark flavour (f):

$$G_{E(M)}^{N,\gamma} = \sum_{f=u,d,s} Q_{EM}^f G_{E(M)}^f, \tag{3.19}$$

$$G_{E(M)}^{N,Z} = \sum_{f=u,d,s} g_V^f G_{E(M)}^f, \tag{3.20}$$

$$G_A^{N,Z} = \sum_{f=u,d,s} g_A^f G_A^f. \tag{3.21}$$

Q^f, g_V^f, and g_A^f are the electroweak charges and couplings introduced in Section 2.3.2. Only the three lightest quark flavours are considered in the decomposition, as the remaining heavier flavours only contribute to the uncertainty on the order of 10^{-2} relative to leading terms [33]. In expanded form, the form factors in the case of the proton ($N = p$) are written as

$$G_{E(M)}^{p,\gamma} = \tfrac{2}{3}G_{E(M)}^u - \tfrac{1}{3}G_{E(M)}^d - \tfrac{1}{3}G_{E(M)}^s, \tag{3.22}$$

$$G_{E(M)}^{p,Z} = (1 - \tfrac{8}{3}\sin^2\theta_W)G_{E(M)}^u + (-1 + \tfrac{4}{3}\sin^2\theta_W)(G_{E(M)}^d + G_{E(M)}^s), \tag{3.23}$$

$$G_A^{p,Z} = G_A^u - G_A^d - G_A^s. \tag{3.24}$$

A neutral weak form factor is then derived by imposing isospin symmetry (labels $p \rightleftharpoons n$ and $u \rightleftharpoons d$) along with taking the proper linear combination of constituent quark electromagnetic form factors to match those of the nucleons. This form factor expression can be written as

$$
\begin{aligned}
G_{E(M)}^{N,Z} &= (1 - 4\sin^2\theta_W)G_{E(M)}^{p,\gamma} - G_{E(M)}^{n,\gamma} - G_{E(M)}^{s,\gamma} \\
&= Q_W^p G_{E(M)}^{p,\gamma} + Q_W^n G_{E(M)}^{n,\gamma} + Q_W^s G_{E(M)}^{s,\gamma},
\end{aligned}
\tag{3.25}
$$

where it depends only on the electromagnetic form factors of the proton, neutron, and strange quark sea, their corresponding weak charges, and the electroweak mixing parameter $\sin^2\theta_W$.

The strange quark electromagnetic form factor is introduced in the decomposition to

account for any non-zero strangeness that might contribute to the ground state of the nucleons, namely any contribution that comes from the quark sea. In a similar fashion to the electromagnetic form factors of the nucleon, the strange quark electromagnetic form factors have certain behavior in the static limit, $Q^2 \rightarrow 0$. The electric strange form factor, $G_E^s(0) = 0$, as the nucleon has no net strangeness. However, due to fluctuations in the strange quark sea, the radius of the strange charge distribution ($\langle r_s^2 \rangle$) is possibly non-zero [10]. Using an analogous equation to Eq. (3.17) but applied to the strange quark electromagnetic form factor, the strange radius (r_s^2) can be related to a parameter called ρ_s, which quantifies the amount of strange quark sea contributions by the relation $\langle r_s^2 \rangle = -\frac{3\rho_s}{2m_N^2}$. The magnetic strange form factor in the static limit becomes, $G_M^s(0) = \mu_s$, where μ_s is the strange magnetic moment. When the Q^2 dependence of the strange form factors are needed, both ρ_s and μ_s are used as coefficients on a dipole parameterization [33]. This parameterization is given by

$$
\begin{aligned}
G_E^s(Q^2) &\equiv \rho_s \tau G_D^V(Q^2), \\
G_M^s(Q^2) &\equiv \mu_s G_D^V(Q^2), \\
G_D^V(Q^2) &= (1 + 4.97\tau)^{-2}.
\end{aligned}
\tag{3.26}
$$

Again, $\tau = \frac{Q^2}{4m_N^2}$ is a momentum-transfer dependent kinematic factor. A series of parity-violating electron scattering experiments have been conducted over the last two decades with the intent to determine the strange electromagnetic form factors over a range of momentum transfers. An excellent review of the experimental results along with current determinations of the strange quark electromagnetic form factors can be found in the literature [34]. In addition to experimental determination, the strange form factors have also recently been calculated to high precision using lattice QCD methods [35, 36].

The previously introduced axial form factor is also often parameterized with a dipole type Q^2 dependence. In the low-Q^2 region, $Q^2 \leq 1\,\text{GeV}$, the form factor is written as

$$
\begin{aligned}
G_A(Q^2) &= \hat{G}_A G_D^A(Q^2), \\
G_D^A(Q^2) &= \left(1 + \frac{Q^2}{M_A^2}\right)^{-2}.
\end{aligned}
\tag{3.27}
$$

The axial mass is $M_A^2 = 1.00 \pm 0.04 \, \text{GeV}^2$ and the coefficient $\hat{G}_A = -1.2701 \pm 0.0025$ are determined from a world fit of neutrino scattering data [37].

3.2.2   Electron-Nucleus Scattering

For the case of many-body nuclear systems, such as nuclei, the form factors are also represented by longitudinal and transverse components. Each type of component is typically represented by a multipole expansion based on the angular momentum (J) and parity (π) quantum numbers of initial and final nuclear states. The form factor decomposed into longitudinal and transverse components can be written as

$$F^2(q) = v_L F_L^2(q) + v_T F_T^2(q). \tag{3.28}$$

This expression introduces two electron kinematic factors v_L and v_T, which correspond to the longitudinal and transverse components. These kinematic factors are given by

$$
\begin{aligned}
v_L &= \frac{Q^2}{\vec{q}^2}, \\
v_T &= \frac{Q^2}{2\vec{q}^2} + \tan^2 \tfrac{\theta}{2},
\end{aligned}
\tag{3.29}
$$

where $\vec{q}^2$ is the three momentum transfer and θ is the polar electron scattering angle.

Generally, the longitudinal and transverse components are expressed by the following electromagnetic multipole expansion,

$$F_L^2(q) = \sum_{J \geq 0} F_{CJ}^2(q), \tag{3.30}$$

$$F_T^2(q) = \sum_{J \geq 1} [F_{EJ}^2(q) + F_{MJ}^2(q)], \tag{3.31}$$

where the components are broken down into further sub-components that carry the labels *Coulomb* (CJ), *Electric* (EJ), and *Magnetic* (MJ). Each sub-components is related to the expectation value of the corresponding electromagnetic multipole operator acting on the initial (final) angular momentum-parity state ($\left| J_{i(f)}^{\pi} \right\rangle$) of the nuclear system. These are

defined by the following set of relations

$$F_{CJ}(q) \equiv \frac{\sqrt{4\pi}}{\sqrt{2J_i+1}} \left\langle J_f^\pi \middle| \middle| \widehat{M}_J(q) \middle| \middle| J_i^\pi \right\rangle,$$

$$F_{EJ}(q) \equiv \frac{\sqrt{4\pi}}{\sqrt{2J_i+1}} \left\langle J_f^\pi \middle| \middle| \widehat{T}_J^{el}(q) \middle| \middle| J_i^\pi \right\rangle, \qquad (3.32)$$

$$F_{MJ}(q) \equiv \frac{\sqrt{4\pi}}{\sqrt{2J_i+1}} \left\langle J_f^\pi \middle| \middle| \widehat{T}_J^{mag}(q) \middle| \middle| J_i^\pi \right\rangle.$$

Further information regarding the electromagnetic multipole operators $\widehat{M}_J(q)$, $\widehat{T}_J^{el}(q)$, and $\widehat{T}_J^{mag}(q)$ can be found in T. W. Donnelly's text [10].

In the elastic electromagnetic scattering case, where the initial state of the nuclear system is equal to the final state, parity symmetry restricts the type of multipole components that are available in the expansion [10]. The longitudinal form factor under parity symmetry continues to be an expansion of CJ multipoles of angular momentum, as it is in the general case given in Eq. (3.30), but for $J \geq 0$ (for even J). However, the transverse form factor becomes restricted to only the transverse MJ multipole sub-components of $J \geq 1$ (for odd J), as the EJ components are prohibited. In addition to these parity symmetry restrictions, the multipole expansion also becomes truncated by a conservation of angular momentum restriction.

Consider the ^{27}Al nucleus, as it is of interest to this dissertation. Aluminum has a ground state angular momentum of $J_0^\pi = \frac{5}{2}^+$ [38]. In electromagnetic electron-aluminum scattering the maximum number of multipole terms allowed in the expansion is $2J_0 - 1$ for the longitudinal form factor and $2J_0$ for the transverse form factor. In list form, the allowed multipole terms for aluminum are: $C0$, $C2$, $C4$, $M1$, $M3$, and $M5$.

Historically, a harmonic oscillator form factor parameterization by T. Stovall et $al.$ [39] has been used to describe the multipole structure of the aluminum nucleus. More recently, C. J. Horowitz [40] has performed a relativistic mean field (RMF) model calculation to motivate the work which is discussed later in this dissertation. C. J. Horowitz's calculation assumes the extreme single-particle model, which is a proton hole in a filled $1d_{5/2}$ shell of a RMF. As the Q_{weak} experiment is interested in forward-angle scattering, C. J. Horowitz only considered Coulomb multipole contributions to the calculated form factor and neglected

transverse contributions. Transverse contributions are suppressed at forward angles by the combination of the v_T kinematic factor and the size of the transverse multipoles when compared with the Coulomb multipoles. To confirm that this assumption is valid at Q_{weak} kinematics, C. J. Horowitz compared his calculation with cross section measurements that were conducted in a kinematic range, in terms of Q^2, that overlaps that of Q_{weak}. Data used for this comparison were taken from G. C. Li *et al.* [41]. There are also electromagnetic back-angle ($\theta > 90°$) scattering data which are more sensitive to transverse form factor contributions. For those who are interested see [42, 43] for an extreme single-particle model calculation of the M1, M3, and M5 transverse multipole form factors of aluminum.

For elastic electromagnetic scattering C. J. Horowitz calculates the longitudinal form factor of aluminum to be a sum of the squares of the possible Coulomb multipoles scaled by the proton's electric form factor in an expression given by

$$F_L^2(q) = (G_E^{p,\gamma}(q))^2 \left[|F_{C0}(q)|^2 + |F_{C2}(q)|^2 + |F_{C4}(q)|^2 \right]. \tag{3.33}$$

The squares of the C0, C2, C4 multipoles are plotted versus q in Fig. 3.4. It is clear by that plot that the C0 multipole is the dominant contribution to the form factor followed by the C2 contribution. Thus C. J. Horowitz further simplifies his form factor calculation by dropping the C4 contribution, which is about the same order of magnitude as the transverse magnetic multipole contributions at 10^{-4}–10^{-5}, see Fig. 3.4.

Additional corrections are also needed to account for Coulomb distortions effects, also known as distorted wave (DW) effects. As the incoming electron scatters from the dense positively-charged volume of the nucleus, the electron feels an acceleration or deceleration, when it is either incoming or outgoing, from the Coulomb potential of the electromagnetic force. These types of effects are traditionally taken into account by numerically solving the Dirac equation using the plane-wave Born approximation (PWBA) and are included in C. J. Horowitz's calculation for the C0 multipole contribution [40].

C. J. Horowitz's best estimate for the elastic electromagnetic electron-aluminum scattering
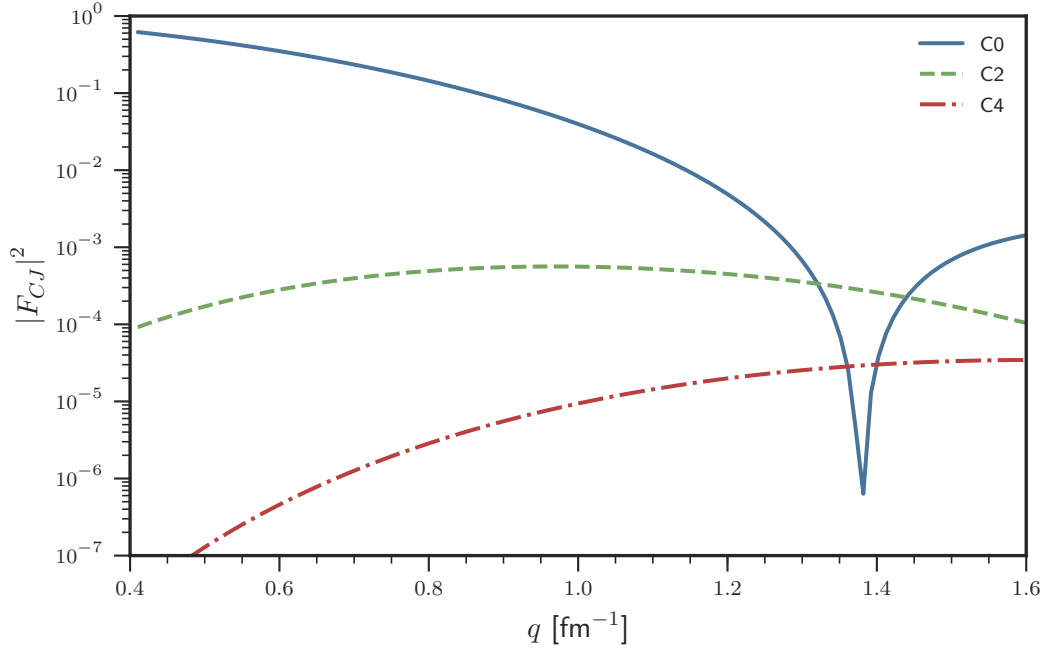
Figure 3.4: Squared Coulomb form factors for aluminum over a momentum transfer (q) range of interest for the Q_{weak} experiment. Calculated using a RMF model. Recreated, using data tables given by C. J. Horowitz [44], from his original calculation [40].

cross section at Q_{weak} kinematics is

$$\frac{d\sigma}{d\Omega} \approx \frac{d\sigma_{DW}}{d\Omega}(C0) + \left(\frac{d\sigma}{d\Omega}\right)_{\text{Mott}} \xi^2 |F_{C2}(q)|^2, \tag{3.34}$$

where $d\sigma_{DW}(C0)$ is the Coulomb distortion corrected cross section containing only the C0 multipole contribution, while ξ is a parameter used to bound the nuclear structure and Coulomb distortion effects on the C2 multipole contribution. The C2 contribution becomes particularly important around the diffractive minimum of the C0 contribution, as seen in Fig. 3.4. To bound the uncertainty in the calculation, C. J. Horowitz allows ξ to vary from 0.5–1.5 with the nominal value of $\xi = 1.0$. The differential cross section and uncertainty band from C. J. Horowitz's calculation can be seen in Fig. 3.5.

Just as with the electron-nucleon scattering case, electron-nucleus scattering also has neutral-weak form factors, denoted by the symbol $F_{CJ}^W(q)$. C. J. Horowitz calculates these terms by scaling the electromagnetic form factors with the respective weak charges of the nucleons in the aluminum nucleus. For their explicit forms, see his publication [40]. These
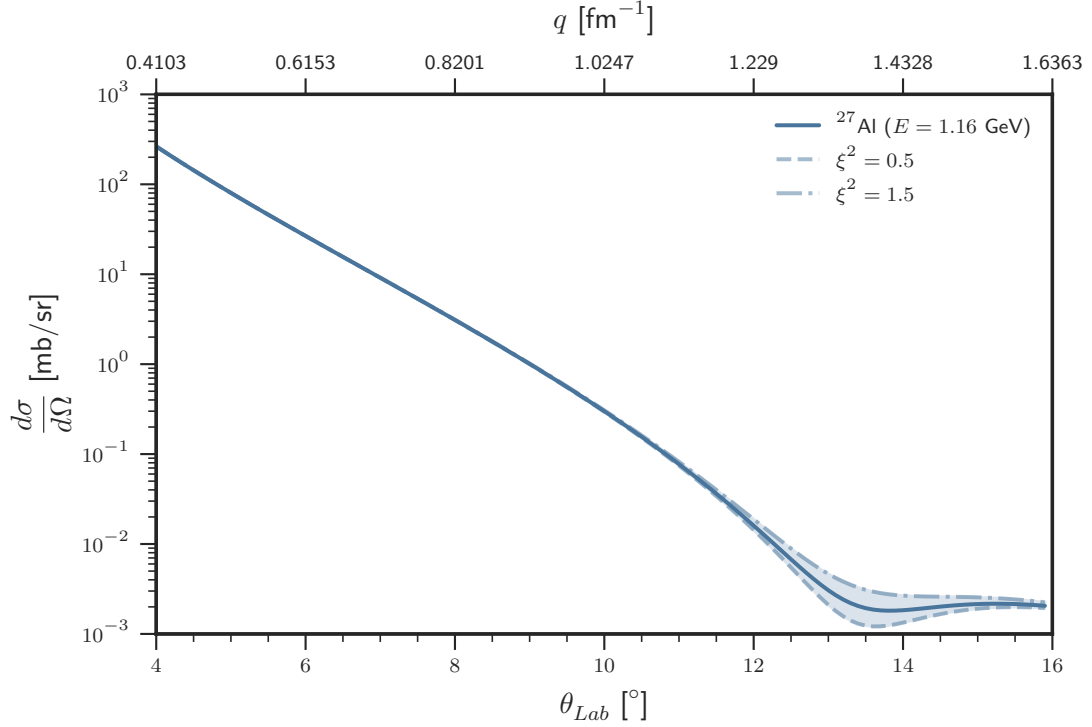
Figure 3.5: Forward-angle elastic electron-aluminum cross section calculated at $E =$ 1.16 GeV with a RMF model. Uncertainty given by ξ^2 parameter. Recreated, using data tables given by C. J. Horowitz [44], from his original calculation [40].

weak form factors will be used in the next section to calculate an electroweak observable known as a parity-violating asymmetry.

3.3   Parity-Violating Asymmetry

As previously mentioned in Section 3.2, when electrons scatter from a nucleus they either interact via the exchange of a photon or the neutral weak Z^0 boson. The dominant process is the electromagnetic photon exchange. The exchange of the neutral weak Z^0 is suppressed during this interaction due to its large mass. However the neutral weak interaction can be accessed by defining a measurable observable that utilizes the fact that the weak force violates parity symmetry.

A differential cross section is proportional to the square of the total amplitude from the scattering matrix [19]. Accounting for both the electromagnetic and neutral weak interactions in the single boson exchange formalism, the differential cross section can be

related to the scattering amplitude ($\mathcal{M}$) by

$$d\sigma_\pm \propto |\mathcal{M}_\gamma + \mathcal{M}_Z|^2 = |\mathcal{M}_\gamma|^2 \pm 2\,\mathrm{Re}(\mathcal{M}_\gamma^* \mathcal{M}_Z) + |\mathcal{M}_Z|^2. \tag{3.35}$$

The neutral weak amplitude ($\mathcal{M}_Z$) in the interference term, $2\,\mathrm{Re}(\mathcal{M}_\gamma^* \mathcal{M}_Z)$, undergoes a sign change during a parity transformation [10]. Thus the differential cross section becomes dependent on the parity state of the scattering system. The interference term can be isolated, and thus measured, by defining a physical observable called a parity-violating asymmetry.

Experimentally, a parity transformation in the laboratory is difficult so a helicity transformation, introduced in Section 2.2.2, of a polarized electron beam is used instead. This parity-violating asymmetry is a difference of helicity-dependent differential cross sections ($d\sigma_\pm$) and has the form of

$$A_{PV} = \frac{d\sigma_+ - d\sigma_-}{d\sigma_+ + d\sigma_-}. \tag{3.36}$$

By substituting in Eq. (3.35) into Eq. (3.36) and assuming $|\mathcal{M}_\gamma| \gg |\mathcal{M}_Z|$, A_{PV} reduces to

$$A_{PV} \approx \frac{\mathrm{Re}(\mathcal{M}_\gamma^* \mathcal{M}_Z)}{|\mathcal{M}_\gamma|^2}. \tag{3.37}$$

To gain an appreciation of how small this parity-violating asymmetry is, it is best to define a nominal asymmetry, absent of structure effects, in terms of the couplings associated with each scattering amplitude. The squared electromagnetic amplitude is proportional to $(\frac{4\pi\alpha}{Q^2})^2$. At low four-momentum transfers, as in this experiment, the interference term is proportional to $\frac{4\pi\alpha G_F}{\sqrt{2}Q^2}$. Thus ignoring factors of the SM couplings generally of $\mathcal{O}(1)$ the ratio in Eq. (3.37) is proportional to A_0, which is defined as

$$A_0(Q^2) \equiv -\frac{G_F Q^2}{4\pi\alpha\sqrt{2}}, \tag{3.38}$$

where G_F is the Fermi constant previously introduced and α is the fine-structure constant [37]. Evaluating A_0 at $Q^2 = 0.025\,\mathrm{GeV}^2$ yields values on the order of 10^{-6}. For ease of later notation these small asymmetry values are given in units that make use of the part-per notation. Asymmetries from this point forward in text will be given in units of part-per-

million (ppm $\equiv 10^{-6}$) or part-per-billion (ppb $\equiv 10^{-9}$).

3.3.1   On Nucleons

The parity-violating elastic electron-nucleon asymmetry can be written in the Born approximation, in the laboratory frame, using the previously defined Sachs form factors as given by [37]

$$A_{PV}^{eN} = A_0 \left[\frac{\epsilon G_E^{N,\gamma} G_E^{N,Z} + \tau G_M^{N,\gamma} G_M^{N,Z} - (1 - 4\sin^2\theta_W)\epsilon' G_M^{N,\gamma} G_A^{N,Z}}{\epsilon (G_E^{N,\gamma})^2 + \tau (G_M^{N,\gamma})^2} \right], \tag{3.39}$$

where the kinematic factors, included the previously defined τ, are given by

$$\tau = \frac{Q^2}{4m_N^2},$$

$$\epsilon = \frac{1}{1 + 2(1+\tau)\tan^2\frac{\theta}{2}}, \tag{3.40}$$

$$\epsilon' = \sqrt{\tau(1+\tau)(1-\epsilon^2)}.$$

In the case of the proton, these quantities have been included in a more general expression as given by [33, 45, 46]

$$A_{PV}^{ep} = A_0 \left[\frac{A_V^p + A_s^p + A_A^p}{\epsilon (G_E^{p,\gamma})^2 + \tau (G_M^{p,\gamma})^2} \right],$$

$$A_V^p = Q_W^p [\epsilon (G_E^{p,\gamma})^2 + \tau (G_M^{p,\gamma})^2] - [\epsilon G_E^{p,\gamma} G_E^{n,\gamma} + \tau G_M^{p,\gamma} G_M^{n,\gamma}],$$

$$A_s^p = -\epsilon G_E^{p,\gamma} G_E^{s,\gamma} - \tau G_M^{p,\gamma} G_M^{s,\gamma}, \tag{3.41}$$

$$A_A^p = -(1 - 4\sin^2\theta_W)\epsilon' G_M^{p,\gamma} G_A^{p,Z}.$$

In the forward angle limit, when $\theta \to 0$ and $Q^2 \to 0$, the kinematic variables given in Eq. (3.40) reduce to $\tau \to 0$, $\epsilon \to 1$, and $\epsilon' \to 0$. In this limit the hadronic structure previously described by the nucleon form factors can be described by a single term called $B(Q^2, \theta)$. Equation (3.41) in this forward angle limit becomes [46, 47]

$$A_{PV}^{ep} \xrightarrow{\theta \to 0} A_0 [Q_W^p + Q^2 B(Q^2, \theta)]. \tag{3.42}$$
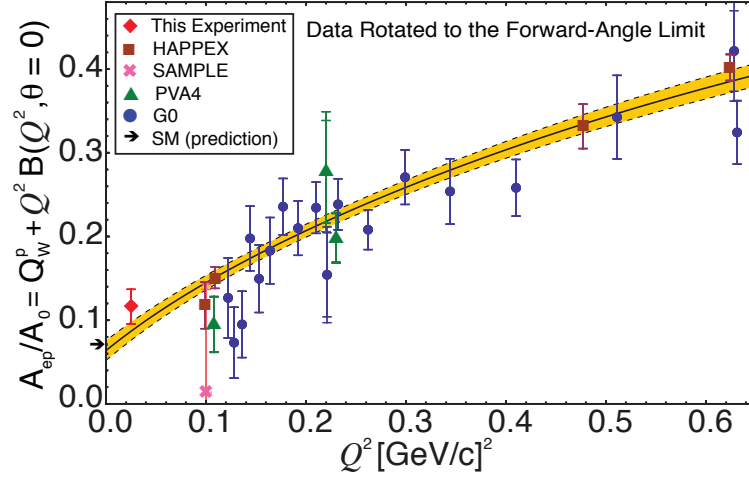
Figure 3.6: Univariate projection from a multivariate reduced asymmetry fit to the world's parity-violating electron scattering data. The low Q^2 diamond (red) is the reduced asymmetry measured by Q_{weak} during the commissioning period. The vertical axis intercept of the best fit line (black), with 1σ uncertainty band (yellow), is the proton's weak charge. The arrow (black) is the SM value of the weak charge. Figure taken from early Q_{weak} publication [49].

At Q_{weak} kinematics the hadronic structure term $Q^2 B(Q^2, \theta)$ contributes about $\sim 30\%$ to the total asymmetry and its uncertainty is dominated by the uncertainties in the strange radius and magnetic moment. For convenience, the A_0 term is divided out allowing a new quantity known as the reduced asymmetry to be defined. The reduced asymmetry takes the form of

$$\overline{A}_{PV}^{ep} \equiv \frac{A_{PV}^{ep}}{A_0} = Q_W^p + Q^2 B(Q^2, \theta). \tag{3.43}$$

In the case of the Q_{weak} experiment, the weak charge of the proton can be determined using Eq. (3.43) in a multivariate global fitting procedure first descried by R. D. Young et al. [48]. The multivariate fit is performed on the world's data set of parity-violating electron scattering asymmetries and is used to extrapolate to $Q^2 = 0$, where the intercept is the value of the weak charge of the proton. A univariate projection of this global fit can be seen in Fig. 3.6, which is from an analysis of the Q_{weak} commissioning data set [49]. Results of an updated global fit that includes the final high precision results of the Q_{weak} experiment will be given in Chapter 8.

3.3.2   On Nuclei

In the case of a nucleus, the parity-violating asymmetry in the Born approximation, assuming proton and neutron distributions are symmetric and the same, can be written as

$$A_{Born} = A_{PV}^{eA} = A_0 Q_W = A_0[ZQ_W^p + NQ_W^n], \tag{3.44}$$

where Z (N) are the number of protons (neutrons) in the nucleus and Q_W^p (Q_W^n) are the weak charges of the respective nucleons [40].

When a nucleus has different proton and neutron distributions, the structure differences can be included by taking the expression above and scaling it by the weighted sum of the products of the contributing electroweak multipoles. For the case of aluminum, which is slightly asymmetric (oblate spheroid, see reference [50]), the structure differences modify the parity-violating asymmetry expression as follows

$$A_{PV}^{eAl} = A_0 \frac{F_{C0}F_{C0}^W + F_{C2}F_{C2}^W + F_{C4}F_{C4}^W}{|F_{C0}|^2 + |F_{C2}|^2 + |F_{C4}|^2}. \tag{3.45}$$

Just as with the cross section calculation previously discussed, C. J. Horowitz also makes a few simplifications and modifications. He includes Coulomb distortions and neglects contributions from the electroweak C4 multipole, opting to use only the C0, C2, $C0_{\text{weak}}$, and $C2_{\text{weak}}$ with the ξ^2 parameter [40]. He calculates the asymmetry to be

$$A_{PV}^{eAl} \approx \frac{d\sigma_{DW}(C0)A_{DW}(C0) + d\sigma_{\text{Mott}}\xi^2 F_{C2}F_{C2}^W A_0}{d\sigma_{DW}(C0) + d\sigma_{\text{Mott}}\xi^2|F_{C2}|^2}, \tag{3.46}$$

where $d\sigma_{DW}(C0)$ is the C0 distorted-wave cross section introduced in Eq. (3.34), $A_{DW}(C0)$ is the distorted-wave asymmetry derived from Eq. (3.45) by dropping multipole terms other than C0, and $d\sigma_{\text{Mott}}$ is the Mott cross section from Eq. (3.10) along with other recently defined terms. Note that even though this calculation includes Coulomb distortion effect to first order it neglects effects from isospin mixing and the strange quark contributions. More information about isospin mixing can be found in reference [51], while the formalism of strange quark effects on parity-violating asymmetries is discussed in detail in reference [33].
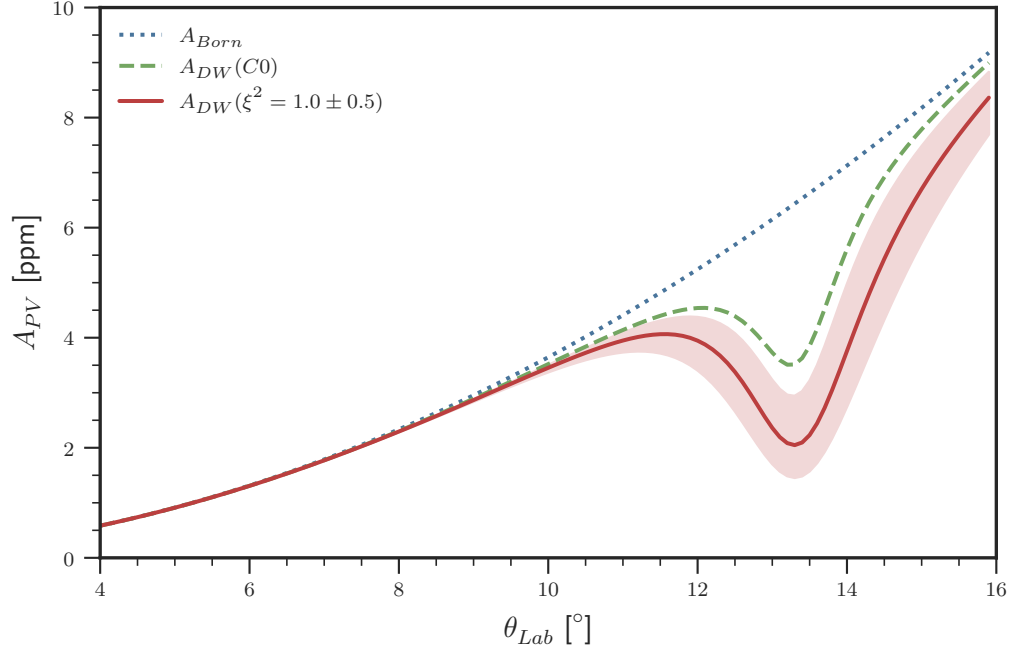
Figure 3.7: Forward-angle elastic parity-violating aluminum asymmetry calculated at $E = 1.16\,\text{GeV}$ with a RMF model. The blue curve is the Born approximation asymmetry given in Eq. (3.44). The green curve is the distorted-wave asymmetry considering only contributions from the C0 multipole. The red curve is C. J. Horowitz's best estimate for the asymmetry as given in Eq. (3.46). The red uncertainty band is determined by the ξ^2 parameter. Recreated, using data tables given by C. J. Horowitz [44], from his original calculation [40].

A plot of C. J. Horowitz's calculated aluminum asymmetry can be seen in Fig. 3.7.

3.3.3   Neutron Distribution Radius and Skin

A parity-violating asymmetry is an effective measurement of the total neutral-weak form factor (F^W) as given by

$$A_{PV} \approx A_0 \frac{F^W}{F^{EM}}, \tag{3.47}$$

if the electromagnetic form factor (F^{EM}) is known, which is typically the case for many nuclei. In a similar fashion to the formalism introduced in Section 3.2, the Fourier transform of this weak form factor yields the weak density (ρ_W) of the nucleus. This density can be related to the individual nucleon densities (ρ_N) by the relation [40]

$$\rho_W(\vec{r}) \approx Q_W^p \rho_p(\vec{r}) + Q_W^n \rho_n(\vec{r}), \tag{3.48}$$

where Q_W^N are the respective nucleon weak charges. Since the weak charge of the neutron is much larger than that of the proton, the weak density is predominantly a measure of the neutron density, or distribution, in the nucleus.

C. J. Horowitz *et al.* [52], introduced the idea that a single forward-angle parity-violating asymmetry measurement could use this effect to extract the radius of the neutron distribution radius (R_n), assuming minor form-factor model-dependencies. They show the squares of radii of these distribution are defined by the following set of relations

$$R_W^2 \equiv \frac{1}{Q_W^A} \int d^3\vec{r}\, r^2 \rho_W(\vec{r}),$$
$$R_p^2 \equiv \int d^3\vec{r}\, r^2 \rho_p(\vec{r}), \qquad\qquad (3.49)$$
$$R_n^2 \equiv \int d^3\vec{r}\, r^2 \rho_n(\vec{r}).$$

R_W and R_N are the weak and nucleon distribution radii and Q_W^A is the weak charge of the nucleus with mass A.

As electromagnetic scattering yields information about the charge radius (R_{ch}) of the nucleus and by extension its proton distribution radius (R_p), parity-violating electron scattering yields information about both the neutron and proton distributions, as the neutral-weak interactions couples to both. Thus the weak radius can be related to both the proton and neutron distribution radii. However, corrections are needed for the point proton and neutron rms radii, the strange radius, and the charge radius of the nucleus. C. J. Horowitz *et al.* [53] have calculated this relationship for spin-zero nuclei and they find a relation between R_n, R_W, and R_{ch} given by

$$R_n^2 = \frac{Q_W^A}{NQ_W^n} R_W^2 + \frac{ZQ_W^p}{NQ_W^n} R_{ch}^2 - \langle r_p^2 \rangle - \frac{Z}{N}\langle r_n^2 \rangle + \frac{Z+N}{NQ_W^n}\langle r_s^2 \rangle, \qquad (3.50)$$

where R_{ch} is the charge radius of the nucleus taken from experiment (see Eq. (3.17)), $\langle r_p^2 \rangle$ is the proton's charge radius, $\langle r_n^2 \rangle$ is the neutron's charge radius, and $\langle r_p^2 \rangle$ is the strange radius. Additionally, the proton distribution radius (R_p) can be related to the experimentally measured charge radius (R_{ch}) with the inclusion of several corrections. A. Ong *et al.* [54]

have calculated this relation for spherically symmetric nuclei, which is given by

$$R_p^2 = R_{ch}^2 - \langle r_p^2 \rangle - \frac{N}{Z} \langle r_n^2 \rangle - \frac{3}{4m_N^2} - \langle r_{so}^2 \rangle, \qquad (3.51)$$

where $\langle r_p^2 \rangle$ is the proton's charge radius, $\langle r_n^2 \rangle$ is the neutron's charge radius, m_N is the mass of the nucleon, and $\langle r_{so}^2 \rangle$ is the spin-orbit coupling term.

Traditionally, a phenomenological model such as the Woods-Saxon function is used to describe the functional form of these densities. The Woods-Saxon function, also known as a two-parameter Fermi function, has the form of

$$\rho(r) = \frac{\rho_0}{1 + \exp\left(\frac{r-R}{a}\right)}, \qquad (3.52)$$

where ρ_0 is the normalization factor, R is the radius of the density function, and a, the nuclear diffuseness, is related to the (10–90 % height) skin thickness (t) by the relation $t = 4\ln(3)a$ [10]. The density normalization factor ρ_0 is determined by the following normalization relations: $\int d^3\vec{r}\,\rho_p(\vec{r}) = Z$ and $\int d^3\vec{r}\,\rho_n(\vec{r}) = N$. The Woods-Saxon function is not the only model that can be used, other more complicated functions, such as the Helm model or RMF models, can also be used to describe these densities. An example of a more involved analysis using the Helm and various RMF models has been applied to the PREX [208]Pb measurement [53].

An example of the Woods-Saxon function plotted for the nucleon densities in aluminum is given in Fig. 3.8, where the nucleon radii are taken from C. J. Horowitz's aluminum calculation [40]. The functions are normalized using the previously mentioned normalization conditions. They also both assume a typical nuclear diffuseness value of 0.54 fm [10, 52]. It is easy to identify that the functions are slightly different, due to the normalization. Aluminum is a slightly asymmetric nucleus with one additional neutron compared to the total number of protons. However, it is easy to imagine the case when a nucleus is even more neutron rich. For example, [208]Pb would have an even larger difference. This difference is often called the neutron skin value of the nucleus. The neutron skin is simply defined as the difference
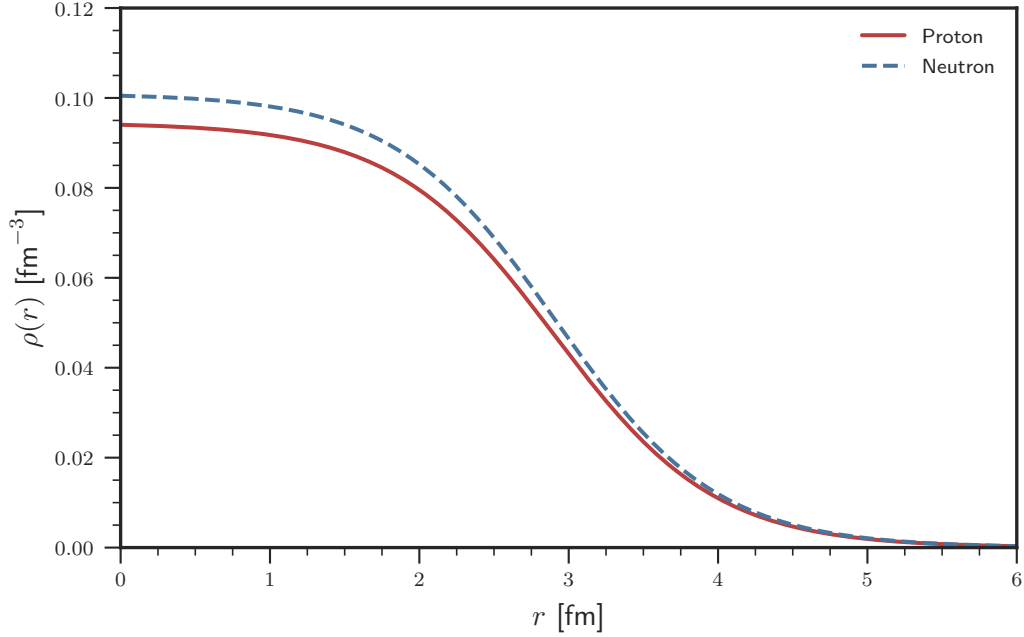
Figure 3.8: Woods-Saxon model of the nucleon densities in ^{27}Al.

between the neutron and proton distribution radii, as given by

$$\Delta R \equiv R_n - R_p. \tag{3.53}$$

For neutron-rich nuclei, like ^{208}Pb, the radius of the neutron distribution determines the density dependence of the symmetry energy and pressure in the equation of state of neutron-rich matter [40, 52]. Knowledge of this density dependence is particularly important for nuclear structure models used to study neutron-rich systems, such as neutron stars [55]. In the case of lighter nuclei, where $N \approx Z$, neutron distribution radii are independent of this density dependence in the symmetry energy [40]. However, measurements of the neutron distribution radii from these light nuclei act as additional constrains on these nuclear structure models [40].

3.3.4   Electroweak Radiative Corrections

The theoretical formalism thus far has only been described in the Born approximation, or single boson exchange, which is a simplification of the natural world. The one exception
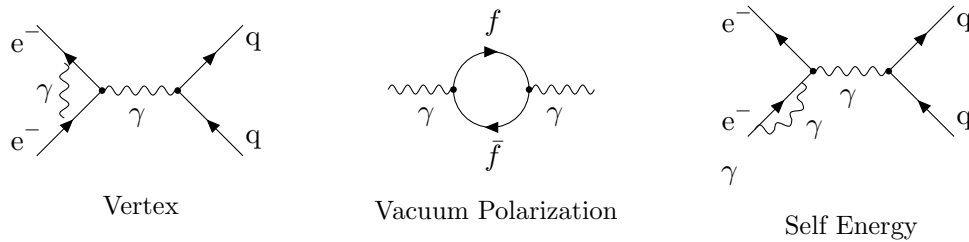
Figure 3.9: Examples of higher-order electromagnetic multi-boson exchange diagrams.

to this assumption was the previously mentioned Coulomb corrections included in C. J. Horowitz's aluminum calculation. All interactions involve higher-order multiple boson exchange diagrams, including electroweak interactions. When measured electroweak observables are compared with theoretical SM calculations, these higher order effects have to be accounted for by applying, what are known as, radiative corrections.

There are two categories of radiative corrections: electromagnetic (EM) and electroweak (EW). EM radiative corrections are modifications for effects arising from both real and virtual photon exchange, either in or out of the field of the nucleus. These in or out of field modifications are generally referred to as internal or external corrections. Internal corrections come from higher-order diagrams involving momentum loops of virtual photons and fermions. Examples of these diagrams, such as the self energy, vertex, and vacuum polarization types, can be seen in Fig. 3.9. External corrections usually account for the emission of real photons as a charged probe enters the field of the nucleus, in what is known as bremsstrahlung, or braking radiation. Both of these types of corrections effect not only the kinematics of the interaction, but also the cross section and asymmetry. EM internal and external corrections for electron-nucleon scattering have been calculated before by L. W. Mo and T. S. Tsai [56]. For the more general case of radiative corrections applied to electron-nucleus scattering, see reference [57]. The other type, EW radiative corrections, are similar to the EM except they consider diagrams that include exchanges of the weak $W^{\pm}$ and Z^0 bosons. Examples of these types of diagrams are given in Fig. 3.10. EW radiative corrections are particularly important when extracting $\sin^2 \theta_W$ from a measured electroweak observable, such as the proton's weak charge.

Taking into account these higher-order diagrams actually causes the couplings associated
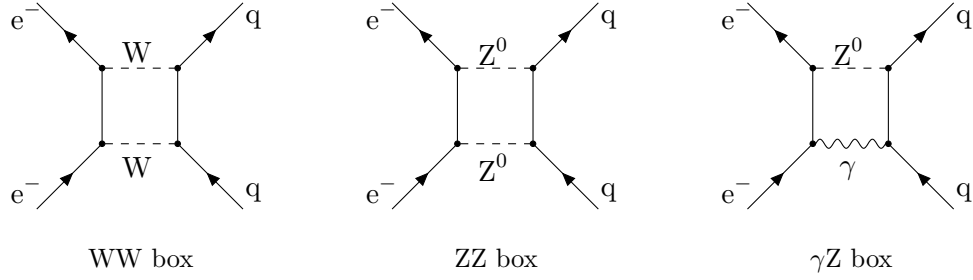
Figure 3.10: Examples of higher-order electroweak multi-boson exchange diagrams.

with these interactions to become dependent on an energy-scale. For example, the EM coupling α, which is the fine structure constant as $Q^2 \to 0$, becomes energy-scale dependent from vacuum polarization diagram contributions. These diagrams lead to divergent momentum integrals, which are corrected for with the use of renormalization techniques from quantum field theory, see reference [19, 58]. The interpretation of this effect is that virtual electron-positron pair loops hide, or screen, the true charge. At large distances only the screened charge can be seen, but as the energy increases and the distance decreases the interaction starts to see the true charge. This energy-scale dependence of α is known generally as a running of a coupling. In the case of EW interactions, the weak coupling, parameterized by $\sin^2 \theta_W$, is also energy-scale dependent. Various calculations of this running have been performed previously [59–61]. An example of the energy-scale dependence, given in the modified minimal subtraction ($\overline{MS}$) renormalization scheme, can be seen in Fig. 3.11.

Q$_{\text{weak}}$'s determination of the proton's weak charge is related to $\sin^2 \theta_W$ by a selection of radiative corrections written in the form of [47]

$$4\sin^2 \theta_W(0) = 1 - \frac{Q_W^p - \square_{WW} - \square_{ZZ} - \square_{\gamma Z}(0)}{\rho + \Delta_e} + \Delta'_e \qquad (3.54)$$

where ρ is the renormalization term of the ratio of the low energy neutral-current and charge-current interactions, Δ_e is the electron vertex correction involving the Z^0, Δ'_e is the electron anapole moment contribution, $\square_{WW}$ and $\square_{ZZ}$ are the WW and ZZ box contributions, and $\square_{\gamma Z}(0)$ is the γZ-box diagram. The pure weak box diagrams are easily calculated using perturbation theory. However, the γZ-box diagram can be problematic to calculate, due to the mass difference between the massless photon (γ) and the heavy Z^0. This energy
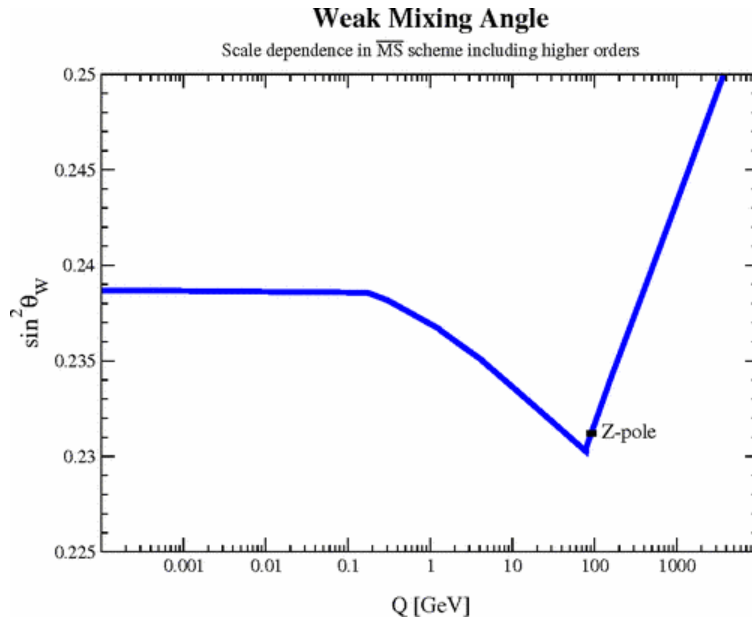
Figure 3.11: Running of the weak mixing angle with momentum transfer (Q). Figure taken from reference [59].

dependent correction has been the subject of much interest. Q_{weak} has made an ancillary asymmetry measurement in a kinematics region important for this correction and is the subject of the future dissertation by J. Dowd [62].

3.4   Motivation for the Q_{weak} experiment

Prior to the Q_{weak} experiment, the only parity-violating asymmetry data available for a weak charge extraction was above $Q^2 = 0.1 \, \text{GeV}^2$. Performing a world fit to this data, as outlined in Section 3.3.1, would yield large uncertainties as the reduced asymmetry fit was extrapolated to $Q^2 = 0.0$. The Q_{weak} experiment proposed to make a low Q^2 measurement of the elastic electron-proton asymmetry which would act as a fulcrum in an updated world fit, providing a dramatically improved constraint on the extrapolation uncertainty. In this low Q^2 the asymmetry's dependence on the hadronic contribution is small, thus the Q_{weak} measurement is said to be the first "direct" measurement of the proton's weak charge.

In addition to providing a determination of the proton's weak charge, and the corresponding quark couplings, the Q_{weak} measurement also provides a precision determination of the weak mixing angle. Such a determination acts as a Standard Model test, which
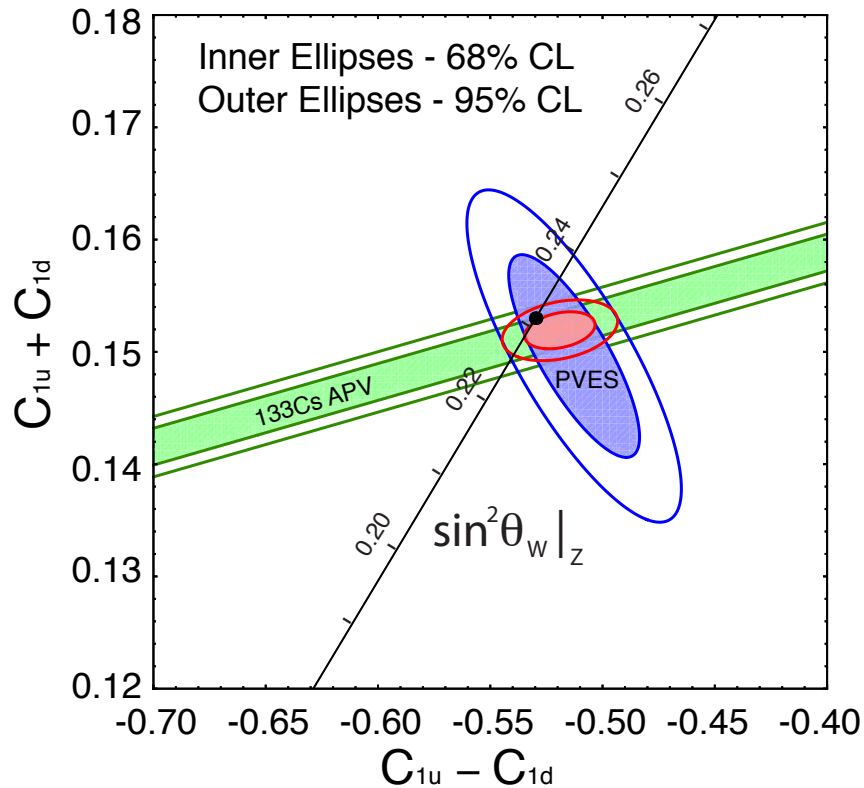
Figure 3.12: The isoscalar versus the isovector combinations of the quark couplings extracted from the Q_{weak} Run 0 data and the cesium atomic parity-violating result. Figure taken from early Q_{weak} publication [49].

can be compared to other previous precision measurements that make weak mixing angle determinations. These precision measurements also have the ability to set mass limits on new particles outside of the SM. This section will discuss these previous results and several candidate theories of physics beyond the SM that the Q_{weak} result would impact.

3.4.1 Previous Results

As introduced in Section 2.3.3, a determination of the proton's weak charge allows for the extraction of the quark couplings, given precise data from a complementary experiment more sensitive to the neutron. An example of such an experiment would be the low energy atomic parity-violating measurement in cesium result [63, 64]. However, other experiments have been able to put constraints on these couplings in the past [48]. Figure 3.12 is an example of such a constraint plot that uses only the most precise determinations from the atomic parity-violating result in cesium and the Run 0 data from the Q_{weak} experiment.
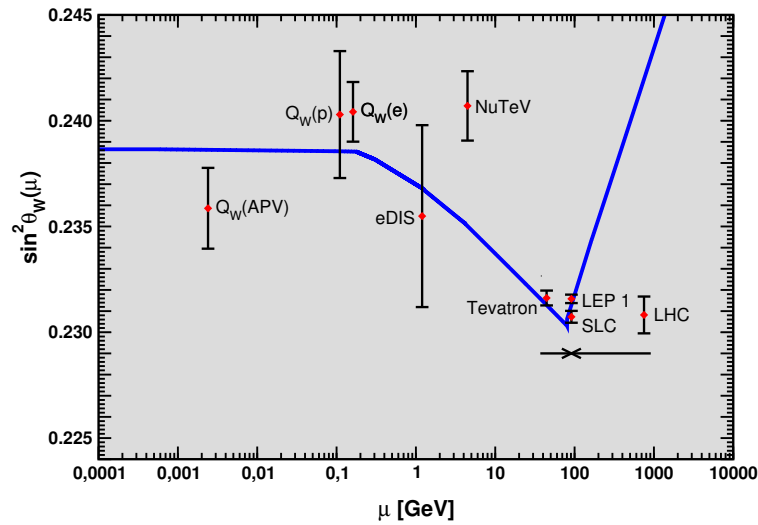
Figure 3.13: Running of the weak mixing angle compared with several experimental determinations. The early Q_{weak} result is given by $Q_W(p)$ point [49]. Figure taken from the 2016 PDG [9].

A slew of experiments with sensitivities to the weak mixing angle have also been conducted before Q_{weak}. At the lowest energy there are atomic parity-violation experiments that measure the parity-violating effects that occur in the inner most electron orbitals of certain heavy nuclei. These type of experiments have been conducted on thallium [65, 66], lead [67], bismuth [68], and with the most precision, on cesium [63, 64, 69]. Towards the medium energy range, numerous parity-violating electron scattering experiments have been conducted over the years, all of with different goals. These objectives range from measuring quark couplings to the nucleon's strange quark content, along with testing for the signature of new physics beyond the SM. An excellent review of medium energy parity-violating electron scattering experiments, from past, present, and future, that have made or will make weak mixing angle determinations can be found in reference [70]. At higher energy, around the masses of the weak bosons, measurements have been made by collider experiments at a variety of facilities. These results include measurements from the Tevatron, LEP, SLC, and the LHC, see the electroweak model review in the PDG [9] for implications of these measurements. Figure 3.13 shows the running of the weak mixing angle in the $\overline{MS}$ renormalization scheme with a selection of the most precise determinations of $\sin^2 \theta_W$ as extracted from these measurements [9].

3.4.2   Physics Beyond the Standard Model

There are a number of candidate theories which describe physics beyond the SM (BSM). The Q$_{\text{weak}}$ experiment has the ability to provide mass limits on particles predicted from a particular class of these BSM theories. For example, the Q$_{\text{weak}}$ experiment has the ability to provide limits to certain supersymmetric theories [71], theories with new Z$'$ bosons [72, 73], and theories involving leptoquarks [74]. Discussion regarding the details of these examples theories is considered outside the scope of this document.

Generally, new parity-violating lepton-quark physics can enter the SM Lagrangian with the introduction of a new contact interaction given by [48]

$$\mathcal{L}_{NP} = \frac{g^2}{4\Lambda^2} \bar{e}\gamma_\mu\gamma_5 e \sum_q h_V^q \bar{q}\gamma_\mu q, \tag{3.55}$$

where g is the coupling strength, Λ is the mass reach of the new physics, and h_V^q parameterizes the isospin dependence with relations $h_V^u = \cos\theta_h$ (up quark) and $h_V^d = \sin\theta_h$ (down quark). Q$_{\text{weak}}$'s sensitivity to this new contact interaction is given by the relation [46]

$$\frac{\Lambda_\pm}{g} = v\sqrt{\frac{4\sqrt{5}}{|Q_W^p \pm 1.96\delta Q_W^p - Q_W^p(SM)|}}, \tag{3.56}$$

where $v^2 = \sqrt{2}/(2G_F)$, Q_W^p is the measured weak charge of the proton with uncertainty δQ_W^p, and $Q_W^p(SM)$ is the SM predicted weak charge of the proton. Depending on the candidate theory, a particular coupling g can be chosen, which allows the determination of an upper mass limit. Any mass phase space below this limit is excluded. Typically these mass limits enter the TeV range.

3.5   Beam-Normal Single-Spin Asymmetries

An alternative observable typically measured as a background by parity-violating electron scattering experiments is a beam-normal single-spin asymmetry (BNSSA). These are parity-conserving and time-reversal invariant quantities that arise when transversely polarized electrons scatter from a nuclear target. They are caused by the interference between the

one-photon and two-photon exchange amplitudes, when considering interactions beyond the Born approximation. Written in terms of the differential cross sections and scattering amplitudes, the BNSSA has the form of

$$B_n = \frac{d\sigma^\uparrow - d\sigma^\downarrow}{d\sigma^\uparrow + d\sigma^\downarrow} = \frac{2\,\mathrm{Im}\,\mathcal{M}_{\gamma\gamma}^* \mathcal{M}_\gamma}{|\mathcal{M}_\gamma|^2}, \tag{3.57}$$

where $d\sigma^\uparrow$ $(d\sigma^\downarrow)$ are the differential cross sections for electrons with spin parallel (anti-parallel) to the normal vector $\hat{n} = \frac{k \times k'}{|k \times k'|}$ set by the scattering plane, and $\mathcal{M}_\gamma$ and $\mathcal{M}_{\gamma\gamma}$ are the one-photon and two-photon exchange amplitudes [75].

The imaginary part of the two-photon exchange amplitude is related to the leptonic $(L_{\mu\nu})$ and hadronic $(W_{\mu\nu})$ tensors with [76]

$$\mathrm{Im}\,\mathcal{M}_{\gamma\gamma} = \frac{e^4}{(2\pi)^3} \int \frac{d^3\vec{k}_1}{2E_1} \frac{L_{\mu\nu} W^{\mu\nu}}{Q_1^2 Q_2^2}, \tag{3.58}$$

where $W_{\mu\nu}$ is a function of the invariant mass of the intermediate nuclear state and the incoming (outgoing) virtual photon momentum transfer $Q_{1(2)}^2$, see Fig. 3.14. The calculation of this amplitude is usually performed by making various assumptions of the possible intermediate states that can occur during the interaction. Previous calculations of this observable has been performed for the proton [75, 77–81] and for a few spin-0 nuclei [76, 82]. No such calculation has yet been performed for ^{27}Al. However, at forward-angles the BNSSAs from nuclei were found, at first order, to scale with momentum transfer by [76]

$$B_n \approx \hat{B}_n \frac{A}{Z} \sqrt{Q^2}, \tag{3.59}$$

where A is the atomic mass of the nucleus, Z is its proton number, and $\hat{B}_n$ is a proportionality constant of approximately $-30\,\mathrm{ppm}\,\mathrm{GeV}^{-1}$ at $E_{beam} = 1\,\mathrm{GeV}$ [76].

Experimentally, these asymmetries are measured as an azimuthally varying quantity. As transversely polarized electrons scatter from an unpolarized target, a detector placed in the scattering plane measures a BNSSA given by

$$B_n(\phi_e) = B_n \vec{S} \cdot \hat{n} = B_n |\vec{S}| \sin(\phi_e - \phi_s), \tag{3.60}$$

Figure 3.14: Two-photon exchange diagrams that contribute to the BNSSA. Hashed blobs connected by double line represent all of the possible intermediate states of the nucleus. The intermediate electron carries momentum k_1, where the four-momentum for the virtual photons are q_1 and q_2, respectively.
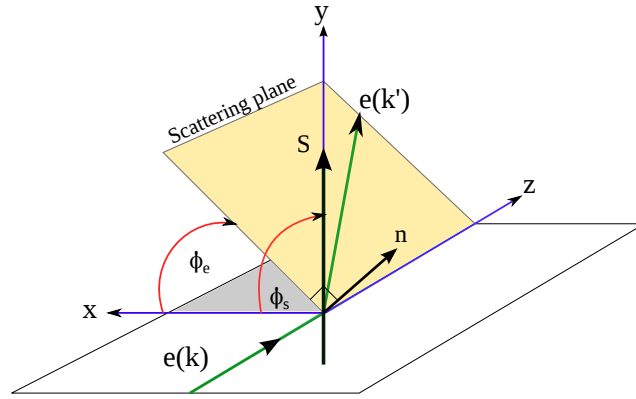
Figure 3.15: Diagram showing the scattering kinematics associated with azimuthal spin dependence of beam-normal single-spin asymmetries. Figure taken from dissertation of B. Waidyawansa [83].

where $\vec{S}$ is the spin of the electron in the transverse direction, $\hat{n}$ is the unit vector perpendicular to the scattering plane, ϕ_e is the azimuthal angle of the scatted electron, and ϕ_S is the azimuthal angle of the spin direction. Fig. 3.15 shows the diagrammatic relationship between these quantities. For example, an incoming electron with a transverse spin in the vertical direction would yield a maximally non-zero asymmetry in detectors 180° out of phase with the spin direction, which corresponds to detectors in the horizontal plane.

3.5.1 Previous Results

Previous parity-violating electron-scattering experiments have measured these BNSSA from a small range of nuclei. The HAPPEX and PREX experiments made measurements of these asymmetries on ^{1}H, ^{4}He, ^{12}C, and ^{208}Pb nuclei at forward angles [84]. The G0 experiment performed additional measurements on ^{1}H, except at higher momentum transfer [85].
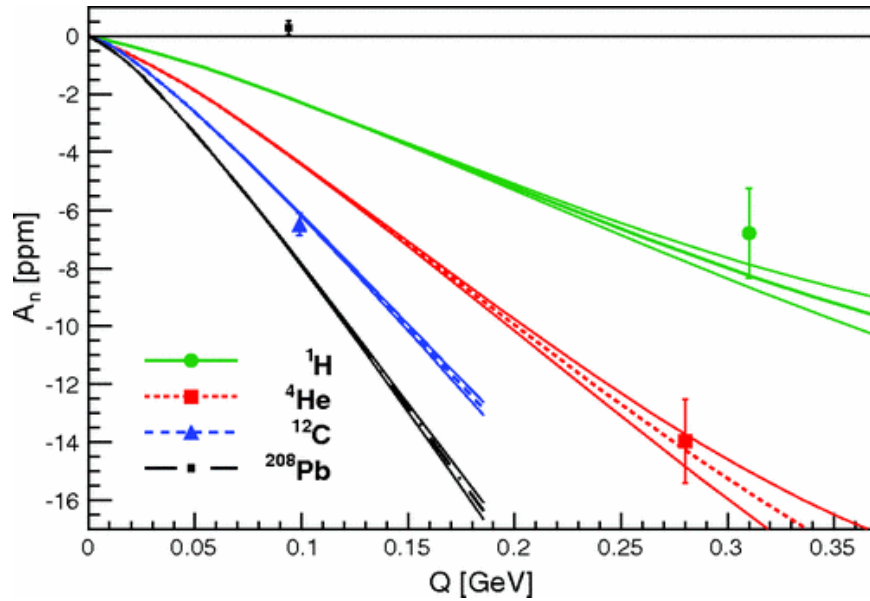
Figure 3.16: BNSSA measurements from the HAPPEX and PREX experiments compared with theoretical calculation [76]. Figure taken from original publication [84]. The original publication uses A_n to denote a BNSSA, which differs from the B_n notation used in this document.

SAMPLE has also measured the ^{1}H BNSSA, but at backward angles [86]. More recently, the A4 collaboration measured backward-angle asymmetries for ^{1}H and ^{2}H nuclei [87].

The Q_{weak} collaboration has made measurements of the BNSSA on ^{1}H, ^{12}C, and ^{27}Al. The lightest of these nuclei stand to confirm previous measurement performed at forward-angles. The asymmetry from ^{27}Al has never before been measured. Preliminary analyses of the ^{1}H and ^{12}C asymmetries have been conducted by D. B. P. Waidyawansa [83] and M. J. McHugh III [88], respectively. Chapter 6 discusses the analysis of the ^{27}Al BNSSA.

One of the most interesting results from these previous measurements was the observed disagreement PREX's ^{208}Pb measurement had with theory [84], see Fig. 3.16. This disagreement is believed to be caused by the lack of Coulomb distortions in previous theoretical calculations [76]. Since ^{12}C is the next highest atomic mass nucleus to have this observable measured, Q_{weak}'s measurement of the ^{27}Al BNSSA has the potential to support this explanation for the disagreement. However, the upcoming CREX experiment [89] hopes to make a measurement of this observable on ^{48}Ca, which would have an even greater potential of supporting the hypothesis that Coulomb distortion effects are required in these types of calculations.

Chapter 4

The Q_{weak} Experimental Apparatus

The custom-built Q_{weak} experimental apparatus was constructed and installed in the experimental Hall C at Thomas Jefferson National Accelerator Facility (Jefferson Lab), located in Newport News, Virginia. It makes use of the Jefferson Lab accelerator to scatter polarized electrons from fixed targets. A schematic drawing of the apparatus as assembled in Hall C can be seen in Fig. 4.1. The apparatus was designed with three goals, as outlined in the proposals for the experiment [1–3]. These were to achieve a high luminosity to minimize the uncertainty from counting statistics, have a large solid-angle acceptance for elastic scattering events, and use an apparatus designed with geometric symmetries that would cancel helicity-correlated systematic backgrounds.

Installation of the apparatus started in late 2010 and ran into February 2011, which marked the start of an early data commissioning period called Run 0. A photograph of the apparatus during the installation phase can be seen in Fig. 4.2. This initial commissioning period was used to test and evaluate the functionality of the apparatus and detector subsystems. A small amount of initial physics data were recorded during that period. The analysis of that commissioning period physics data has been published [49]. The commissioning period was followed by two separate data taking periods referred to as Run 1 and Run 2. Run 1 started in late February 2011 and continued until May 2011. Run 2
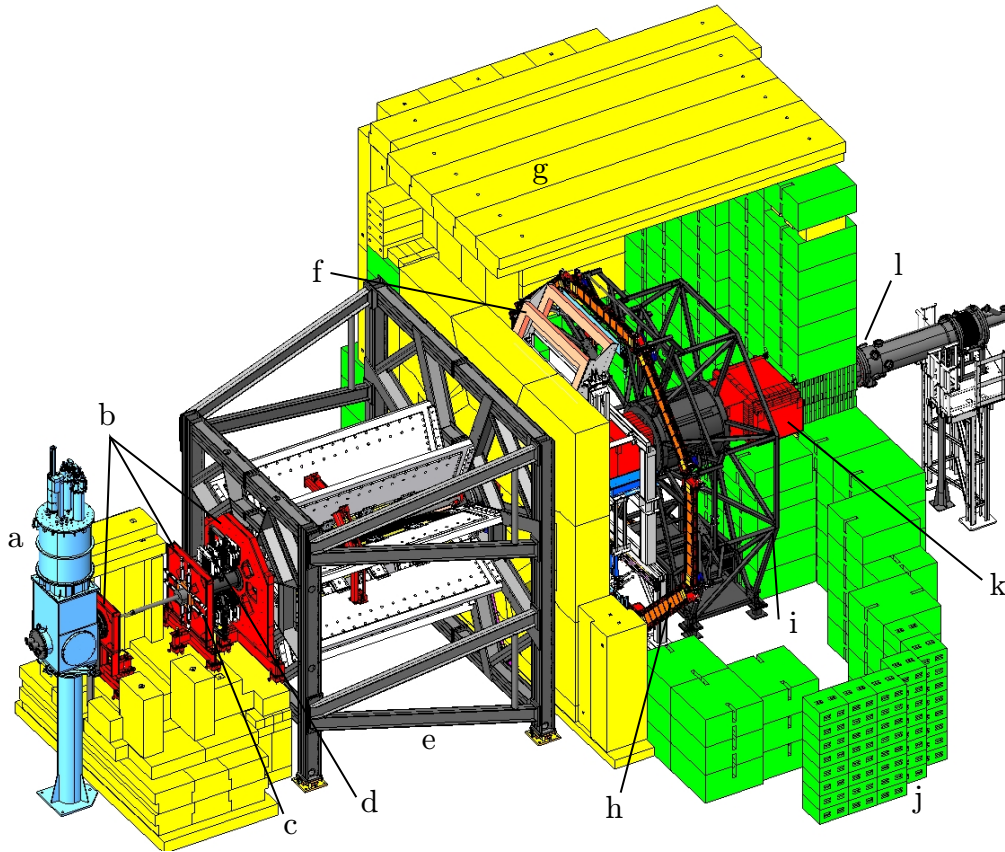
Figure 4.1: Isometric schematic drawing (CAD) of the Q$_{\text{weak}}$ experimental apparatus. The incident electron beam enters from the left of the image. The major subsystems are the: a) target (*cyan*), b) lead collimators (*red*), c) upstream luminosity monitors (*white*), d) horizontal drift chambers (*white*), e) eight-fold symmetric toroidal magnetic spectrometer, f) vertical drift chambers (*pink*), g) concrete shielding (*yellow*), h) main detectors (*black/orange*), i) support structure (*dark gray*), j) iron shielding (*green*), k) lead beamline shielding (*red*), and l) downstream luminosity monitors (*not visible*). Adapted from original figure taken from the Q$_{\text{weak}}$ instrumentation publication [90].

started six months later, in November 2011 and continued until May 2012. The six month accelerator shut-down period, separating the two runs, was used to improve elements of the apparatus in an attempt to minimize the helicity-correlated systematic corrections. The hard work put into these improvements during the down period allowed for increased efficiency in the data taking during Run 2, which led to an improved statistical uncertainty compared with Run 1.

The primary purpose of the apparatus was to perform a measurement of the parity-violating elastic electron-proton asymmetry. To perform this measurement an aluminum cell
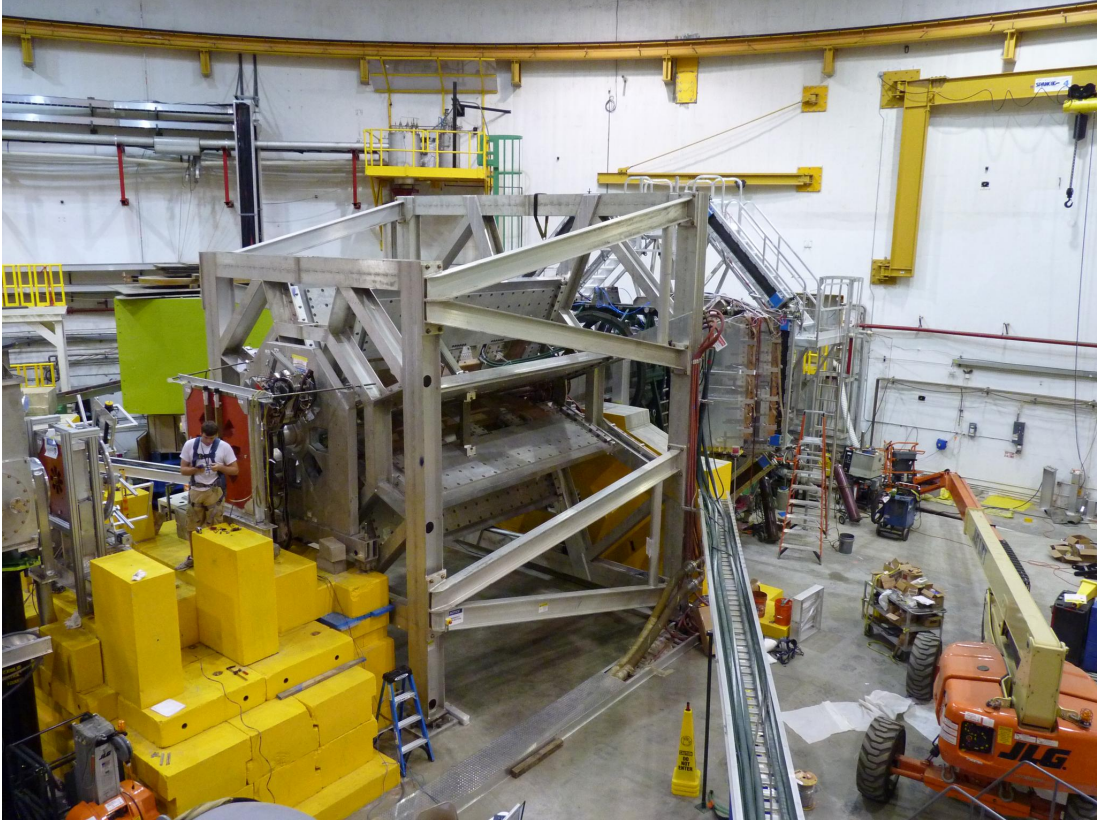
Figure 4.2: Photograph of the Q$_{\text{weak}}$ apparatus during its installation into Hall C at Jefferson Lab, prior to the installation of the shielding. Note the human figure located on top of the yellow shielding blocks in font of QTOR as a reference to the size of the apparatus.

filled with liquid hydrogen was used as the primary target. Most of the beam time available during Run 1 and Run 2 was dedicated to measuring the asymmetry from this target. Table 4.1 gives a summary of typical apparatus parameters used to make this asymmetry measurement.

Table 4.1: Typical experimental parameters for hydrogen target running.

Parameter	Run 1	Run 2
E$_{\text{Beam}}$ [GeV]	1.16	1.16
P$_{\text{Beam}}$ [%]	89	89
Target Length [cm]	34.4	34.4
I$_{\text{Beam}}$ [µA]	160	180
Luminosity [cm^{-2} s^{-1}]	1.5×10^{39}	1.7×10^{39}

Additionally, a selection of auxiliary targets were also used to measure background asymmetries during dedicated periods of systematic study. A majority of this time was dedicated

to measuring the aluminum background asymmetry for the weak charge measurement, using a separate aluminum alloy target. The purpose of this measurement is discussed later in this text. Table 4.2 gives typical apparatus parameters associated with measuring the asymmetry on this separate target.

Table 4.2: Typical experimental parameters for aluminum target running.

Parameter	Run 1	Run 2
E_{Beam}[GeV]	1.16	1.16
P_{Beam} [%]	89	89
Target Length [mm]	3.58	3.68
I_{Beam} [μA]	25	60
Luminosity $[\mathrm{cm}^{-2}\,\mathrm{s}^{-1}]$	3.2×10^{36}	7.8×10^{36}

The purpose of this chapter is to give an overview of the physical hardware required to conduct the experiment. Occasionally, details are provided on elements of the apparatus which are of direct interest to the analyses discussed in this dissertation. A more detailed overview of all of the hardware and instrumentation can be found in the collaboration's instrumentation publication [90]. Further information about each hardware subsystem can be found in a corresponding Ph.D dissertation authored by many of the early generation Q_{weak} students. For each of these subsystems, citations are given to these respective dissertations.

4.1 Apparatus Overview

The Q_{weak} experiment started in the injector of Continuous Electron Beam Accelerator Facility (CEBAF) at Jefferson Lab. There, an electron beam was generated and initially accelerated with the desired current at maximum polarization. The resulting beam was then further accelerated to approximately 1.16 GeV with a single pass through the double linear accelerator (linac) system of CEBAF. Once at that energy, the beam was directed to the experimental hall. Upon reaching Hall C, the beam passed through two independent polarimeters used to monitor the polarization of the beam during the experiment. Downstream of the polarimeters, beam diagnostic equipment recorded important beam current and position information for later use in analysis. Finally, the electron beam entered the target scattering chamber, where it was incident on a 34.4 cm long liquid hydrogen target

cell or a thick solid target in an array of auxiliary targets. The thick target in combination with the high current beam allowed the experiment to meet the first design goal of reaching a high luminosity.

Electrons that scattered off the target then passed through the thin downstream vacuum window of the target scattering chamber. A series of high-density collimators confined and shaped the scattered electron profile before they entered the magnetic field of the toroidal spectrometer (Q$_{\mathrm{weak}}$ toroid, QTOR). The field of the toroid magnet momentum selected elastically-scattered electrons and focused them onto the main detector array. Beam that did not interact in the target passed through the apparatus to a shielded beam dump at the opposite end of the experimental hall.

The main detector array consisted of eight synthetic quartz Cherenkov detectors positioned in an azimuthally-symmetric pattern about the beam axis. The symmetry of the detector array was important as it suppressed the negative effects of any helicity-correlated XY-plane beam motion and any residual transverse polarization in the electron beam. Both needed to be minimized as they had the potential to lead to large systematic corrections in analysis. The symmetry and large solid angle coverage of the detector array satisfied the last two apparatus design goals of the experiment.

The experiment also employed a range of auxiliary detector systems. During low beam current running, wire chambers were used to reconstruct paths of scattered electrons as they passed through the apparatus on an event-by-event basis. The primary purpose of these detectors was the precision determination of kinematic observables such as the momentum transfer. Special radiation-hard detectors called luminosity monitors (lumis) were placed close the beamline and used to monitor backgrounds. A spare detector just like the main detectors was also used to monitor electron flux in the super-elastic region behind the main detector array. Further details about these auxiliary detectors can be found in reference [90].

An overview of the components used in the experiment, on the level of the entire accelerator and experimental hall, can be seen in Fig. 4.3.
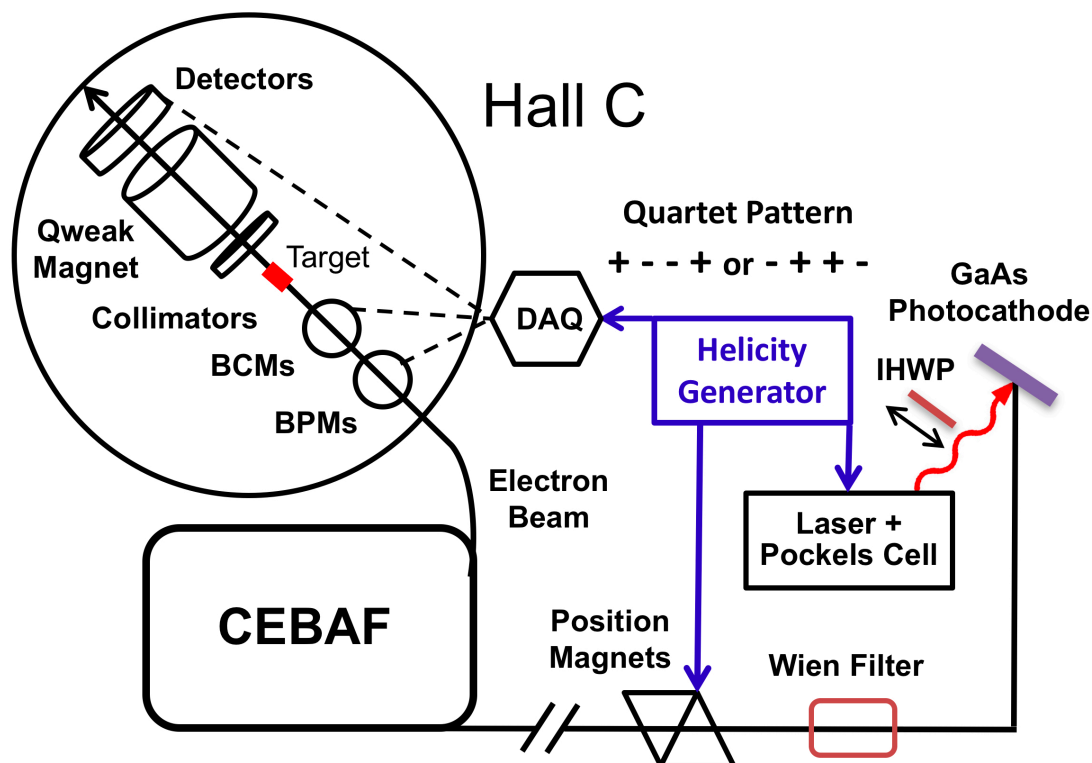
Figure 4.3: Overview of the apparatus elements needed to conduct the Q$_{\text{weak}}$ experiment. See text for details on how the polarized electron beam was generated, delivered, monitored, and used in the experiment.

4.2 Beam Generation and Acceleration

Generation of the polarized electron beam took place in the injector service building of CEBAF. A high-power laser of a particular wavelength was used to excite electrons from a semiconductor photocathode material using circularly polarized light. The wavelength of laser light was specifically chosen to match that of the band gap energy associated with the photocathode material. During this interaction the helicity state of the photon is transferred to the freed electron, which allowed control of the produced electron's polarization state. The polarized electrons were then electromagnetically bunched together into packets and accelerated, before they entered the linac portion of CEBAF.

To make use of the parity-violating effect of interest to this experiment, the helicity of the electron beam was modulated between parallel and anti-parallel (right-handed or left-handed)

states. This started with the generation of an electrical helicity signal. A custom made VME board, located in an electrically isolated VME power crate in the injector, generated an electronic signal at a frequency of 960.015 Hz. Four helicity signals were combined to create a helicity pattern called a quartet. The quartets took the form of either: $(+--+)$ or $(-++-)$. The helicity of the first period in the quartet was chosen using a pseudo-random algorithm, which avoided helicity-correlated contamination of the signal recorded by the experiment.

The circularly-polarized light used in the electron source originates from a laser emitting linearly-polarized light, which was incident on a special birefringent optical element called a Pockels cell. As the linearly-polarized light enters the Pockels cell, its birefrigent property causes the light to take on a circular polarization with a given handedness, effectively acting as a quarter-wave plate. The Pockels cell is useful as its birefrigence can be changed through the use of an applied high-voltage electric field. Depending on the polarity of the applied electric field, the handedness of the emitted circularly polarized light changes. The generated helicity signal was used to modulate the polarity of the 2.5 kV electric field applied across the cell through the use of a high-voltage switch. This 960.015 Hz Pockels cell modulation technique was the primary helicity reversal method used in the experiment. Figure 4.4 shows a simple diagram of the polarization state of the laser light as it passed through the various optical elements in the injector, before it reached the photocathode. One of these optical elements, known as an insertable half-wave plate (IHWP), was used in addition to the Pockels cell to flip the direction of polarization of the passing laser light. The IHWP acted as a secondary helicity reversal method, which was actuated on longer time scales than that of the Pockels cell, typically every 4–8 h. An additional optical element called a rotatable half-wave plate (RHWP) was placed just after the Pockels cell in an effort to maximize the amount of circular polarization the laser light had, before it exited the Pockels cell and interacted with the photocathode.

The semiconductor photocathode material used to produce the polarized electrons is a strained-superlattice gallium arsenide (GaAs) wafer. This material, historically used in the CEBAF injector, was selected based on its band gap energy and its ability to produce polarized electrons with high average polarizations of about 90 % [90]. Constant illumination
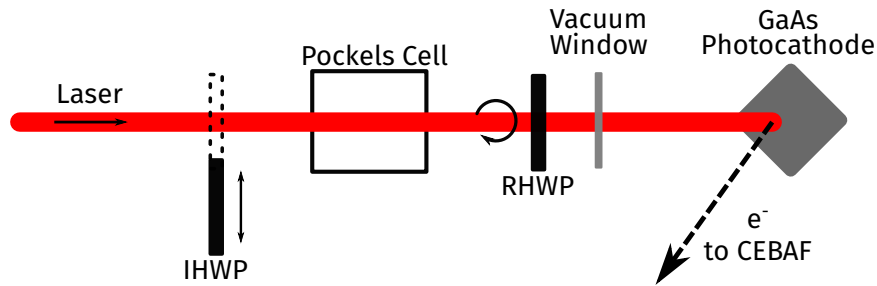
Figure 4.4: A simple diagram showing the polarization state of the laser light used to produce polarized electrons from the photocathode material. The solid black arrows generally indicate the polarization state of the light, either linear or circular.

of the photocathode material in a single location by the incident laser beam causes a reduction in the material's ability to produce polarized electrons. The observed reduction is attributed to spatial electron deficiencies that occur over time. To counteract this effect, the position of the incident laser beam on the surface of photocathode material was changed approximately every 2–4 weeks, via a lens, in a process referred to as a spot change. Over time, the ability of the photocathode material to provide polarized electrons degrades to such a point that a reactivation of the material is required. This technique revitalizes the electron content of material, making further polarized electron production possible with the same photocathode sample. The reactivation technique was applied once in Run 1 and once in Run 2.

Once polarized electrons were emitted from the surface of the wafer, an electric field would initially accelerate them into in a series of mechanical and magnetic elements, which shaped and bunched the electrons. This manipulation and acceleration allowed the electrons to be synced and subsequently injected into the linacs of CEBAF. Before the beam entered the linacs of CEBAF, it passed through a system of two magnetic Wien spin-flippers, one vertical and one horizontal. These are systems of magnets that are used to precess the spin of the passing electrons in a particular direction, which effectively changes the helicity of the beam. These Wien filters were an additional reversal method used to modulate the helicity of the beam. The settings of the Wien magnets were typically changed once a month.

After leaving the Wien magnets, the electrons entered the first linac of CEBAF where they were accelerated again via a series of multiple superconducting cavities, which used radio-frequency pulses to accelerate the electron bunches. The electron beam leaving the

first linac passed through a recirculating arc of magnets before it entered the other linac
where it was again accelerated. The exiting beam, known as 1-pass beam, had approximately
1.16 GeV of energy before it was delivered to Hall C. In general, depending on the beam
energy requirements of a given experiment, CEBAF has an additional recirculating arc after
the second linac that can be used to recirculate the beam again in a racetrack configuration.
The beam can be recirculated a total of five times before it has to be delivered to one of
the experimental halls. The experiment exclusively made use of 1-pass beam, except for
a short period when CEBAF delivered 2-pass beam at the 1.16 GeV energy. During this
limited running of 2-pass beam, the spin of the electrons precessed by 180° (labeled by "g-2
flip"), which acted as yet another form of helicity reversal. This period of 2-pass operation
occurred in Run 2 during Wien periods 6–7. Table 4.3 provides a summary of the various
helicity reversal time intervals used to label data in the experiment.

Table 4.3: Summary of the various data collection time intervals and quantities associated
with slow helicity reversals.

Type	Time Interval	Helicity Control
Runlet	6–8 min	–
Run	1 h	–
Slug	8 h	IHWP
Wien	1 mo	Wien magnets

A source of systematic uncertainty originated from the injector optical elements, previ-
ously mentioned. Various beam properties such as position, angle, and energy can become
correlated with helicity reversals, into what are known as helicity-correlated background
asymmetries (HCBA). These quantities cause false asymmetries in the experiment, thus a
large amount of effort was invested into minimizing these effects in the injector [91, 92]. In
addition, a series of beam position and current monitors were placed along the beamline in
the injector and in Hall C, in an effort to measure the effects of these helicity-correlated
parameters. The next section discusses the functionality of these monitors.

4.3   Beam Diagnostics

A series of beam diagnostic devices were used throughout the experiment to monitor electron beam characteristics. In particular, the quantities monitored were beam position, angle, current, and energy. Output from these devices was recorded in the experiment's data stream for later use in analysis. This section gives a brief overview of the diagnostic devices used to monitor these observables during the experiment, along with a short introduction of how they are used in analysis. A more detailed overview of each of these subsystems can be found reference [90].

4.3.1   Position Monitors

Beam position monitors (BPMs) are noninvasive monitoring devices constructed from two pairs of antennas that are positioned perpendicular to the beam, inside the beam pipe, at various positions along the beamline. The antennae are tuned to pick up the radio-frequency signal of the passing electron bunches coming from CEBAF. As the beam drifted along an axis in the XY-plane, the signal strength recorded by the closest antenna correspondingly increased while the other decreased, allowing a position determination. Both pairs working together allowed the simultaneous determination of beam positions and angles along both axes in the XY-plane.

A total of 23 BPMs were used in Hall C to monitor the position of the beam over the course of the experiment. Some of these monitors were later used in analysis to correct for HCBA associated with natural beam motion originating from the injector. Beam positions and angles reported in later chapters of this dissertation come from least square fits to the signals recorded by the last five BPMs located just upstream of the target. These quantities are then used to remove any false asymmetries associated with natural beam motion by a linear regression technique. This was the primary method for removing these effects in the ancillary aluminum data sets.

The weak charge measurement analysis made use of an additional technique to remove HCBA. A technique known as beam modulation, or dithering, was used periodically to purposely induce motion in the position of the beam with a known signal, larger than that of

natural motion. Intentional beam modulation allows the decoupling of measured asymmetries sensitivities to certain beam positions and angles better than the linear regression method. A beam modulation system was constructed using a series of magnet coils placed upstream of the target along the beamline. Details associated with the beam modulation system apparatus and the corresponding analysis used to determine beam motion corrections can be found in the dissertation of D. Jones [91].

4.3.2   Current Monitors

Two types of devices were used to measure the beam current during the experiment. The first, called a beam current monitor (BCM), was a noninvasive device that employed radio-frequency resonant cavities to monitor the charge of the beam. Six BCMs were used during the experiment, at varying positions along the beamline. These were labeled BCM: 1, 2, 5, 6, 7, and 8. These BCMs were absolutely calibrated between 1–180 μA using a second type of current monitoring device, known as an Unser monitor. The Unser, a Bergoz Parametric Current Transformer [93], has a stable linear gain that can be used to calibrate the BCMs during periods when the beam current is simultaneously ramped and modulated between on and off. Further details about the BCM calibrations can be found in K. E. Myers' dissertation [94]. It is important to note that during analysis the measured asymmetry used the current value recorded from a particular BCM monitor as a normalization factor.

4.3.3   Energy Measurements

Two types of beam energy measurements were conducted; each made use of the beamline arc entering Hall C. Absolute measurements were performed with position sensitive multi-wire scanners inserted into the beam, at different intervals along the arc. These scanners performed an invasive measurement of the beam angle. Knowledge of the angle of the beam coupled with the magnetic field strength of the magnets steering the beam through the arc allowed a beam momentum determination, which in turn yields the energy of the beam. A continuous relative measurement was made using a particular BPM (BPM3C12) to monitor for any drifts in beam energy that were occurring during the experiment. With the same functionality as a normal BPM, BPM3C12 was used in conjunction with the normal target

BPMs to determine the momentum of the beam in a similar manner to that of the invasive scanner technique.

4.4 Beam Polarimetry

The polarization of the beam was monitored by two polarimeters, located in the beamline corridor entering Hall C. These polarimeters operate using two separate techniques. The first polarimeter employed Compton scattering, in a noninvasive approach for determining the polarization. The second polarimeter used Møller scattering to measure the polarization in an invasive manner during dedicated measurement periods. A system of two polarimeters was desired, as they were used in conjunction to reduce the final uncertainty on the beam polarization correction during analysis.

The Compton polarimeter was comprised of four principal components: a beam chicane*, a high-power polarized laser acting as a photon source, a photon detector, and an electron detector. As the electron beam entered Hall C, a series of magnets bent the beam away from its normal path into a 11.1 m long chicane. When electrons passed through the chicane, the beam of the high-power laser would sporadically scatter polarized photons from the passing electrons. This interaction is a pure QED scattering process to lowest-order and is known as Compton scattering. Scattered electrons and photons are detected with separate purpose-built detectors. The polarization of the beam was determined by making helicity-dependent cross section asymmetry measurements with these detectors. These measurements had the added benefit of being noninvasive, as the majority of unscattered electrons continued down the beamline into Hall C for use in the experiment. Further details about the Compton polarimeter apparatus can be found in reference [90]. Information about the beam polarization analyses for the photon detector can be found in the dissertation of J. C. Cornejo [95] and for the electron detector in reference [96]. Further information about the electron detector can also be found in the dissertation of A. Narayan [97].

The Møller polarimeter, similarly to the Compoton polarimeter, determined the polarization of the beam by measuring the helicity-dependent cross section asymmetry of

---

*A term indicating a deviation to a path that later rejoins. An example would be a railway siding.

polarized electron-electron scattering. This interaction is another well known QED process called Møller scattering. A superconducting solenoid magnet was used to polarize a thin pure iron foil target, which was then inserted into the path of the beam. Polarized beam electrons would then Møller scatter from the polarized orbital electrons of the iron foil. The scattering profile of the Møller electrons was then directed and shaped using a series of quadrupole magnets and collimators. Møller electron pairs were then detected in coincidence by a pair of symmetric electron detectors. Since the polarized foil breaks the path of the beam, this measurement was invasive and it was performed periodically at an interval of 2–3 times per week in Run 1 and Run 2. During these measurements the electron beam current was reduced to approximately $2\,\mu A$ to prevent damage and reduce depolarization effects from beam heating to the thin iron foil. The Møller polarimeter was located directly downstream of the Compton polarimeter, which allowed cross-calibration between the two polarimetry techniques. Further details about the Møller polarimeter apparatus can be found in reference [90]. Details of the beam polarization analysis for the polarimeter can be found in J. A. Magee's dissertation [98].

The beam polarization uncertainty goal for the experiment was below $1\,\%$ (relative) [1]. Both of the polarimeters individually met this goal for the final result [46]. In addition, a direct comparison was conducted at low beam current to insure both polarimeters systematically agreed, which they were shown to do within their respective uncertainties [99]. Polarization values and their uncertainties are given in later sections for each of the physics analyses discussed in this dissertation.

4.5 Targets

To keep with the design goal of achieving a high luminosity, the collaboration used a high-powered liquid hydrogen (LH_2) target for the weak charge measurement. The target was designed to circulate approximately $58\,L$ of pressurized liquid hydrogen at $20\,K$ in a closed loop through a conical aluminum target cell. The $34.4\,cm$ long cell was capped on either end by thin caps, also known as windows, which were constructed from a high-strength aluminum alloy (Al 7075-T651). The upstream window was $22.2\,mm$ in diameter and $0.097\,mm$ thick.

Downstream, the target cell was capped with a 0.64 mm thick curved window. In the center of that window, a spot was machined to a thickness of 0.125 mm so non-interacting beam could pass on to the dump with minimal interaction.

The incident beam would traverse the length of the target cell, passing through the upstream window, the LH_2, and then the downstream target window, depositing approximately 2.1 kW of power from ionization and other radiative effects. A sophisticated cooling system was used to continuously circulate the LH_2 through the cell in an effort to keep the liquid at a constant temperature and density. An overview of individual target components and their performance is given in reference [90]. Target details discussed beyond the overview can be found in A. Subedi's dissertation [100].

4.5.1 ^{27}Al Alloy Targets

Beam passing through the LH_2 target would infrequently scatter from the thin aluminum windows into the acceptance of the main detectors. In order to study the background from these aluminum windows, an array of auxiliary targets was constructed from the same material as the windows. These were used routinely throughout the experiment to investigate this background during dedicated periods of systematic study.

These auxiliary targets were mounted into a frame suspended under the LH_2 target cell. The frame, or target ladder, had 24 locations for different types of targets.

Each target location in the ladder allowed for the mounting of a 2.5 cm square sample of material of varying thicknesses. Six of the target mounting locations were placed in the same plane (Z-position) as the downstream target window. Another 12 were placed in plane with the upstream target window. The remaining positions were dedicated to optics targets used at lower beam current to center the beam and aid in vertex reconstruction studies. Figure 4.5 shows the relative locations and numbering scheme used to describe this array of targets. Locations of the optics targets are not included in that diagram.

A range of targets was included in the ladder. Most were constructed from the Al 7075-T651 material used for the windows, but with varying thickness. Their intended purpose was to benchmark radiative corrections. Additional targets, such as pure aluminum, carbon, and beryllium were included as well. However, most were never used to make asymmetry
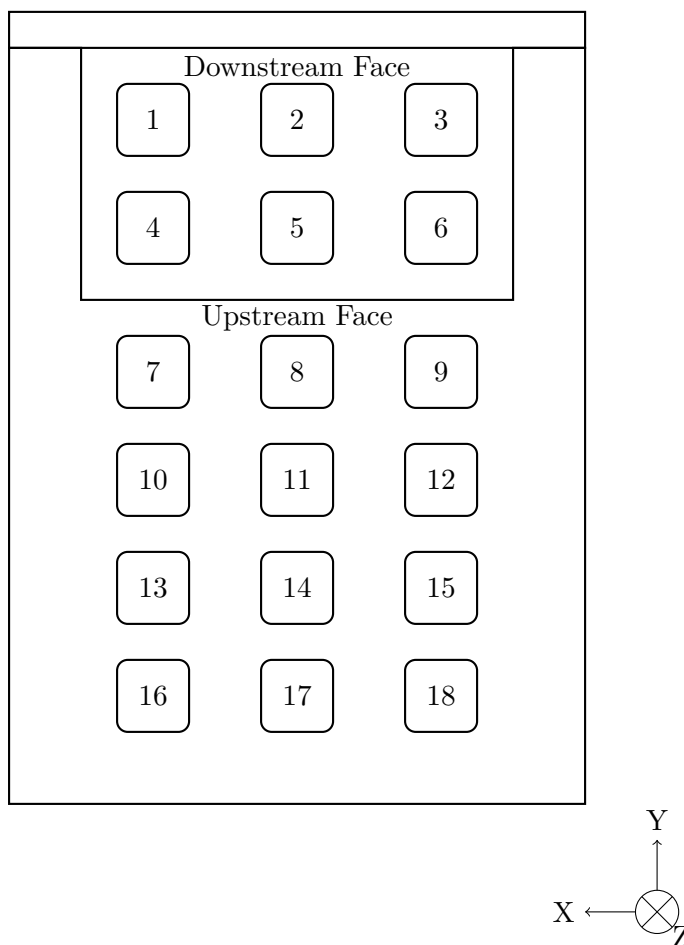
Figure 4.5: Diagram of target positions on the target ladder from the perspective of the incident electron beam. The numbering scheme of the target positions are included. Positions 1–6 are located on the downstream face of the target ladder. The rest, positions 7–18, reside on the upstream face.

measurements. Important properties, dimensions, and location information for all of the targets can found tabulated in Table 4.4 for the upstream locations and Table 4.5 for the downstream locations. These properties were surveyed during a post experiment investigation by members of the target subgroup. Further information describing the techniques used to quantify these physical properties can be found in the ELOG [101].

It is important to note that the calculated radiation lengths tabulated in Tables 4.4 and 4.5 differ from the values documented in the ELOG [101]. That initial analysis made the assumption that the radiation thickness for a given aluminum alloy target was that of pure aluminum. These radiation lengths have been calculated using the proper aluminum-alloy radiation length in Appendix A.1. This discrepancy is likely the cause of the disagreement

seen between data and simulation in early aluminum target radiative correction studies [94, 102].

Discussions in this dissertation exclusively focus on measurements made with the 3.68 mm thick aluminum alloy target from Run 2, which is highlighted in Table 4.5. This particular target was chosen as it had a radiation length similar to that of the filled LH$_2$ target cell.

Alloy Composition

Since the material selected for the target windows was a high-strength alloy, any asymmetry measurements conducted with targets made from this material suffer from alloy element scattering backgrounds. Knowing the amount of alloying elements present in this material allows the determination of these backgrounds in later asymmetry analyses.

The upstream windows and auxiliary targets were machined from the same lot of Al 7075-T651 material for both Run 1 and Run 2. Knowledge of the elemental composition of these upstream targets comes from an assay issued by the manufacturer at the time of purchase. The composition values from that assay are tabulated in Table 4.6. Uncertainties on the values in that table were not included in the assay and are thus not given. Further composition details about the upstream material, including the original assay, can be found in the ELOG [103].

Downstream auxiliary targets and the target window were also machined from same type of Al 7075-T651 material, except the material was from a separate manufactured lot for both Run 1 and Run 2. Their compositions slightly differ from those of the upstream targets. Table 4.7 contains assayed composition values for either lot used in Run 1 and Run 2. The Run 1 compositions were taken from a material assay sheet issued at the time of the material's purchase. Again, uncertainties were not included in that assay and are thus not given in the table. Further details regarding the Run 1 values can be found in the ELOG [103]. Run 2 compositions were determined from external testing performed by Applied Technical Services (ATS) in Georgia, using a sample of a spare solid target installed in position 6 of the downstream target ladder during Run 2. The actual target used for the aluminum asymmetry measurements could not be tested, as it was still activated at the time when these tests were conducted by ATS. Uncertainties on the Run 2 values are given as

the standard deviations reported by the assay from ATS. For further details on the Run 2 values, see reference [104].

Composition values from these alloy materials are taken into account during analysis through the modification of material definitions in simulation and by scaling the luminosity calculations used in the determination of rates and yields extracted from simulation.

Oxygen Contamination

Aluminum is naturally a reactive metal; exposed to ambient atmosphere it develops a layer of surface oxidation [105]. A thick layer of oxidation could stand to be a possible source of scattering background that would require additional corrections during analysis. The manufacturing of these solid ^{27}Al alloy targets regularly took place in a normal ambient atmosphere, where natural layers of oxidation were assumed to have formed.

Reviewing the surface science literature, Al 7075-T651 is known to develop an oxidation layer that ranges from 2–30 nm in normal atmosphere [105, 106]. Taking the extreme edge of that range and multiplying it by a factor of two to account for both sides of the target, a 60 nm thick oxidation layer compared with the 3.68 mm thickness of the Run 2 aluminum target can be considered negligible. Background corrections for this oxidation layer are thus not considered during analysis.

4.5.2   Target Material Improvements for Future Experiments

Future parity-violating experiments that require liquid cryogenic targets, such as MOLLER [107] and P2 [108], might want to consider alternative aluminum alloy materials for the target cell entry and exit windows. There are a selection of specialized aluminum-lithium alloys that have been developed for the aerospace industry which could provide similar if not improved material characteristics, while reducing the composition of the higher-Z elements present in the alloy. By selecting an alternative aluminum material prior to execution of the experiment, the analysis corrections required for the alloying elements could be minimized, making ancillary aluminum asymmetry measurements more feasible for those experiments.

Table 4.8 provides a brief selection of commercially available aluminum-lithium alloys, broken down by elemental composition and tensile strength values as compared with the

Al 7075-T651 alloy used in Q_{weak}. Tensile strength is not the only material property that should be used for comparison. As these materials are used to cap a cryogenic pressure vessel, further investigation of their performance at cryogenic temperatures would be needed before a particular alternative candidate material could be chosen for future experiments.

Aluminum-lithium alloys appear at first glance to be attractive alternative target window materials, as they have a dramatic reduction in the amount of Zinc, a dominant high-Z alloying element present in Al 7075-T651. Their next largest contributing high-Z element is copper, which is comparable to that of the 7075-T651 alloy at approximately the 2 % level. The trade-off comes at the expense of the introduction of Zirconium, another high-Z element but only at the sub 1 % level. A number of Zirconium isotopes have had their charge radii measured with elastic electron scattering, at an approximate momentum transfer range of 0.4–$2.80 \, \mathrm{fm}^{-1}$ [111, 112]. Their cross section should be fairly easy to determine over the kinematic range of interest for future experiments, with either theoretical calculation or a Fourier-Bessel coefficient form factor expansion.

4.6   Experimental Acceptance

The profile of electrons scattered from the target was shaped and momentum selected by a combination of collimators and the magnetic field from QTOR. This combination of collimators and a magnetic spectrometer restricts the polar scattering angle, θ, of these scattered electrons to be between $5.8° \leq \theta \leq 11.6°$, while suppressing backgrounds from other non-elastic scattering processes. This magnetic selection technique was used in conjunction with shielding to block direct line-of-sight neutral particles from making their way into the main detector array. Figure 4.6 shows the scattered electron flux passing through the elements of the apparatus. This section discusses each of these components and how they define the profile of electrons seen by the main detector array.

4.6.1   Collimators

Three 11–15 cm thick collimators located downstream of the target, at intervals of 74 cm, 2.72 m, and 3.82 m, divided the scattered electron flux into eight sectors via azimuthally
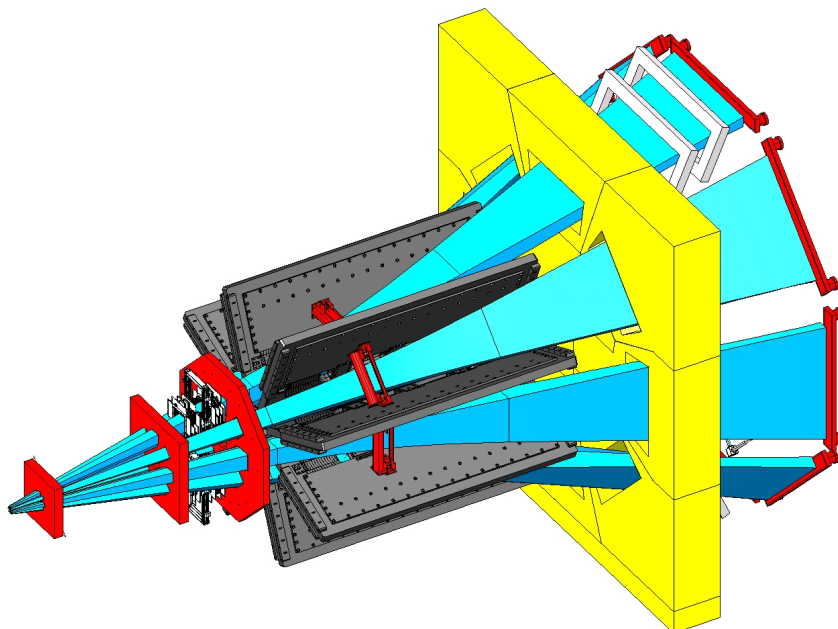
Figure 4.6: CAD drawing of the scattered electron flux profile (cyan) passing through the acceptance defining elements of the apparatus. Figure taken from Q$_{\text{weak}}$ instrumentation publication [90].

symmetric apertures. In order for the collimators to block and shape the flux, they were constructed from a 95.5 % lead to 4.5 % antimony mixture, which allowed the stopping of charged particles and neutral gamma rays outside of the apertures. The edges of the apertures in the second collimator define the profile of the scattered electron flux seen by QTOR. The first and third collimators primarily cleaned up backgrounds produced in the target and other secondary sources.

4.6.2 Spectrometer

A toroidal magnetic field produced from a spectrometer momentum selected elastically scattered electrons and focused them onto the plane of the main detector array. The field was produced by eight symmetric resistive copper coils operating at 150 V and a nominal current range of 8900–9100 A, in a racetrack configuration, supported in an aluminum superstructure. The center of the spectrometer was located approximately 6.5 m downstream of the target. Extra care was taken to ensure the materials used to construct the spectrometer were free of any ferromagnetic properties, which prevented scattering backgrounds from magnetized materials. The profile of the elastically selected electrons was approximately

$2\,\text{m} \times 10\,\text{cm}$ after leaving the field of the spectrometer.

Current scan studies were performed with QTOR for later use in benchmarking simulations. Additionally, reducing the current to $6700\,\text{A}$ allowed direct measurement of the inelastic $N \to \Delta$ asymmetry, which was useful for determining inelastic background corrections and other ancillary physics results.

4.6.3   Simulation

The experimental acceptance was studied using a custom Monte Carlo radiation tracking simulation software package called QwGeant4, which was constructed with the Geant4 C++ libraries [113–115]. The simulation incorporated all of the major apparatus elements used in the experiment, in their as-built locations. QwGeant4 is kept under SVN revision control on the Q$_{\text{weak}}$ web server [116]. This geometry coupled with the radiation tracking capabilities of the Geant4 libraries allowed the study of various systematic effects on the acceptance and detector rates.

As the acceptance of the apparatus was designed and optimized to perform the weak charge measurement, its performance for the aluminum ancillary measurements was not studied until the experiment was completed. Results from that analysis showed a large energy acceptance of approximately $150\,\text{MeV}$ [117]. Figure 4.7 shows the energy acceptance from this study for the downstream aluminum target as determined in QwGeant4. This large energy acceptance directly impacts the background analysis for those aluminum measurements.

4.7   Integrating Detectors

Eight Cherenkov detectors formed the main detector array used to measure asymmetries in the experiment. Positioned approximately $344\,\text{cm}$ radially from the beam axis and $575\,\text{cm}$ downstream from the center of QTOR, the main detectors were placed in an azimuthally symmetric pattern about that axis with the help of a superstructure. The array covered approximately $49\,\%$ of a 2π rotation in the azimuthal angle ϕ. A given detector in the array matches the position of a side of an octagon, thus the general sector surrounding any one detector in the main array is referred to as an octant.
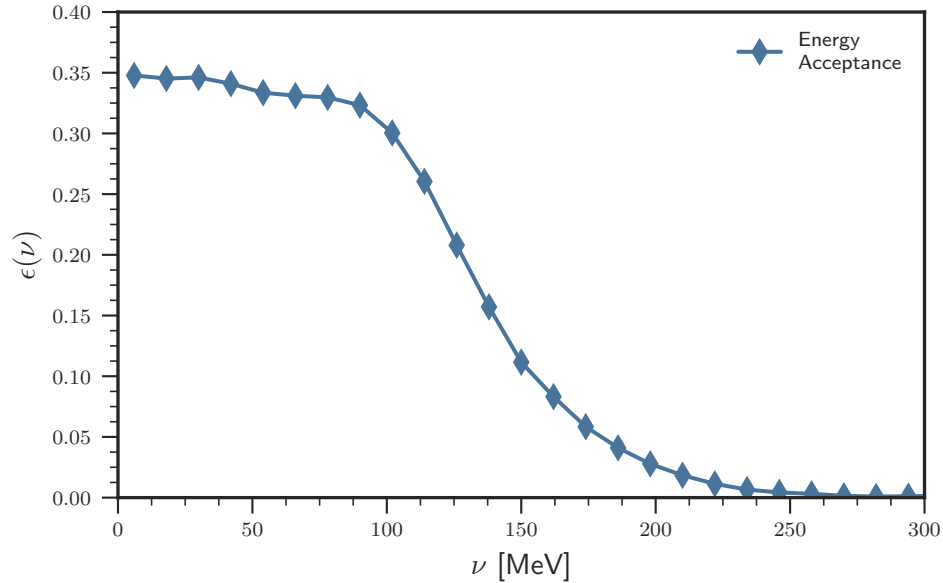
Figure 4.7: Energy (ν) acceptance for the aluminum target as determined by QwGeant4. Each point indicates the fraction fo accepted events in a given energy bin. The overall energy acceptance ($\epsilon(\nu)$) is the normalization weighted average of the distribution. Figure taken from the ELOG [117].

Each detector in the array was constructed from two pieces of Spectrosil 2000 synthetic quartz radiators, glued on end to form a single bar with an active area of $200\,\text{cm} \times 18\,\text{cm} \times 1.25\,\text{cm}$. On either end of the bar, additional pieces of $18\,\text{cm} \times 18\,\text{cm} \times 1.25\,\text{cm}$ light-guide were glued, forming a bar of $236\,\text{cm}$ in total length. Attached to the surface of the downstream faces of each light-guide were $130\,\text{mm}$ diameter photomultipler tubes (PMTs), used to read out the Cherenkov light. Each detector was enclosed in a light-tight covering held in an aluminum frame, which was then attached to the superstructure supporting the full array. Figure 4.8 gives the relative detector positions and PMT locations in the Q$_{\text{weak}}$ coordinate system.

Incoming electrons shower through the active area of the detector, generating cones of Cherenkov light. This light in the UV spectrum, propagates along the length of the bar to the PMTs via total internal reflection. Once there, the PMTs convert the Cherenkov light into an electrical current that is then captured and recorded with the experiment's data acquisition system. The main detectors had the ability to operate in two modes: current (integrating) mode and tracking (event) mode. Asymmetry measurements made use of current mode, where the PMT signal was integrated over each helicity reversal window. Tracking mode,
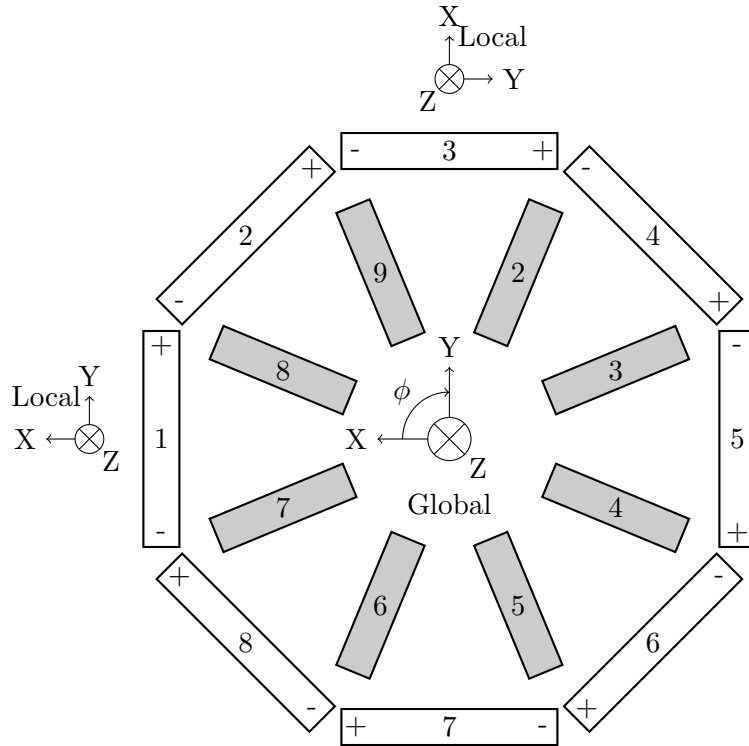
Figure 4.8: Main detector positions and labels in the Q$_{\text{weak}}$ coordinate system from the downstream beam perspective. The Q$_{\text{weak}}$ global coordinate system is referenced in the center, while local main detector coordinate systems are given for MD1 and MD3 as examples. PMT locations for an individual MD are given by the labels "+" and "-". The interior shaded gray rectangles, and corresponding number labels, represent the approximate locations of the coils in QTOR.

which is discussed in the next section, allowed the PMTs to measure individual pulses event-by-event during periods of systematic study.

During the hardware commissioning period, the main detectors were found to be sensitive to high levels of soft gamma-ray backgrounds present in the environment of Hall C. To reduce these backgrounds, 2 cm thick lead tiles, known are preradiators, were installed in the front of each main detector. Unknowingly at the time, the introduction of these preradiators caused a new type of false asymmetry in the experiment. This issue was only identified late in the analysis of the weak charge measurement. Later analysis chapters discuss how this new background is generated along with the methods used to determine a correction.

Further details regarding the construction, operation, and performance of the main detectors can be found in reference [90]. Additional information about the early development and construction of these detectors can be found in the dissertation of P. Wang [118].

4.8 Kinematics Determination

In both running periods, small segments of time were dedicated to operating the experiment in an alternative mode, referred to as event mode. During event mode the beam current was reduced by approximately six orders of magnitude, to 50–100 pA, which reduced the rate of detected scattered electrons in the main detectors. A set of auxiliary detectors called tracking chambers were inserted into the scattered electron profile. These tracking chambers allow the reconstruction of the geometric path the scattered electrons took through the apparatus. Information extracted from this reconstruction process is used to determine important kinematic parameters of the scattered electrons. Additionally, the reduced beam current running of event mode allowed the study of various systematic backgrounds.

The tracking system employed two sets of gas-filled wire chambers. One set, called the horizontal drift chambers (HDCs), were located between collimators two and three, upstream of QTOR. The second set, called the vertical drift chambers (VDCs), were placed just upstream of the main detector array. During event mode, positioning systems allowed the sets of wire chambers to be inserted into the scattered electron profile. Scattered electrons passing through both set of chambers could have their path reconstructed with custom offline analysis software. Knowledge of this path allowed the determination of the electron's lab scattering angle θ, and by extension its momentum transfer Q^2, see Section 3.1.

A more in-depth overview is given in Q$_{\text{weak}}$ instrumentation publication [90]. Further details regarding tracking software, analysis, and associated systematic studies on momentum transfer can found in the dissertations of S. Yang [119], J. Pan [120], and V. M. Gray [24].

4.9 Data Acquisition and Asymmetry Analysis

Data acquisition (DAQ) started at the output of the detector PMTs and beam monitors. Custom made front-end electronics integrated, digitized, and read out these signals for a given helicity-reversal window in each quartet. These collected signals were used to form asymmetries in the recorded data stream. Raw data, collected at a rate of about $4.5\,\mathrm{MB\,s^{-1}}$, was handled by the in-house JLab DAQ system known as CEBAF Online Data Acquisition (CODA). These data were saved for later offline analysis, in addition to being backed-up

to a data silo for preservation. Approximately 150 TB of raw data was recorded over the course of the experiment.

Custom offline analysis software was written to handle and reduce this data into manageable chunks, through the use of asymmetry time-averaging. Runlet-averaged asymmetries were stored in an SQL database for ease of later analysis. This database included values for detector signal yields, asymmetries, asymmetry differences, helicity state information, data quality tags, and target information. Detailed information about the DAQ subsystems and asymmetry formation procedures can be found in R. S. Beminiwattha's dissertation [121].

Table 4.4: The upstream targets physical properties.

Type	Run	Position	Thickness [mm]	Mass [g]	Area [cm^2]	Areal Density (ρ_A) [g cm^{-2}]	Radiation Thickness [% X$_0$]
C	1	12	3.171 60 ± 0.001 04	4.523 40 ± 0.000 15	6.445 10 ± 0.001 03	0.701 80 ± 0.000 17	1.6437
C	2	12	0.997 30 ± 0.002 27	1.060 60 ± 0.000 12	6.276 80 ± 0.000 45	0.169 20 ± 0.000 14	0.3963
Al Alloy (spare)	2	16	3.595 40 ± 0.019 82	6.274 00 ± 0.000 52	6.183 20 ± 0.000 97	1.014 70 ± 0.000 18	4.5201
Al Alloy (spare)	2	17	1.803 30 ± 0.011 98	3.136 90 ± 0.000 42	6.218 10 ± 0.000 77	0.504 50 ± 0.000 18	2.2473
Al	1 & 2	10	1.014 90 ± 0.000 45	1.731 80 ± 0.000 13	6.144 50 ± 0.000 45	0.280 30 ± 0.000 12	1.1674
Al Alloy	1 & 2	13	0.881 20 ± 0.000 55	1.524 30 ± 0.000 09	6.211 00 ± 0.000 32	0.245 40 ± 0.000 08	1.0932
Al Alloy	1 & 2	14	3.603 00 ± 0.001 02	6.294 00 ± 0.000 10	6.192 90 ± 0.000 32	1.016 10 ± 0.000 06	4.5263
Al Alloy	1 & 2	15	1.798 70 ± 0.000 70	3.135 90 ± 0.000 09	6.234 80 ± 0.000 32	0.503 00 ± 0.000 07	2.2407

Table 4.5: The downstream targets physical properties. The row highlighted in grey notes the target used to measured the aluminum asymmetry reported in this dissertation.

Type	Run	Position	Thickness [mm]	Mass [g]	Area [cm^2]	Areal Density (ρ_A) [g cm^{-2}]	Radiation Thickness [% X$_0$]
Al Alloy	1	1	1.77250 ± 0.00435	3.09570 ± 0.00013	6.33810 ± 0.00077	0.48840 ± 0.00013	2.1755
Al Alloy	1	2	7.11880 ± 0.00169	12.41730 ± 0.00010	6.17350 ± 0.00039	2.01130 ± 0.00006	8.9591
Al Alloy	1	3	3.58780 ± 0.00109	6.25180 ± 0.00007	6.18450 ± 0.00032	1.01120 ± 0.00006	4.5043
C	1	4	0.99730 ± 0.00227	1.06060 ± 0.00012	6.27680 ± 0.00045	0.16920 ± 0.00014	0.3963
Be	1	6	6.10540 ± 0.00337	7.05700 ± 0.00030	6.22130 ± 0.00052	1.13660 ± 0.00010	1.7435
Al Alloy	2	1	1.86370 ± 0.00082	3.24940 ± 0.00010	6.22320 ± 0.00052	0.52210 ± 0.00009	2.3298
Al Alloy	2	2	7.19800 ± 0.00143	12.56690 ± 0.00009	6.22060 ± 0.00045	2.02020 ± 0.00007	9.0150
Al Alloy	2	3	3.68280 ± 0.00083	6.42140 ± 0.00010	6.22060 ± 0.00052	1.03220 ± 0.00009	4.6061
C	2	4	3.18760 ± 0.00182	4.53120 ± 0.00012	6.44580 ± 0.00065	0.70300 ± 0.00011	1.6465
Al Alloy	2	6	3.66780 ± 0.00568	6.42320 ± 0.00021	6.22450 ± 0.00077	1.03190 ± 0.00012	4.6048

Table 4.6: Elemental composition, in units of % by weight [wt%], of the Al 7075-T651 material used for the hydrogen target cell entrance window and upstream targets.

Element	Run 1 & 2 [wt%]
Al	89.72
Zn	5.70
Mg	2.50
Cu	1.70
Cr	0.19
Fe	0.12
Si	0.06
Mn	0.01
Ti	0.04
Others(each, $\leq$)	0.05
Others(total, $\leq$)	0.15
Total	100.04

Table 4.7: Elemental composition, in units of % by weight [wt%], of the Al 7075-T651 material used for the hydrogen target cell exit window and downstream targets.

Element	Run 1 [wt%]	Run 2 [wt%]
Al	89.53	89.189 ± 0.047
Zn	5.90	5.868 ± 0.020
Mg	2.60	2.628 ± 0.075
Cu	1.50	1.813 ± 0.016
Cr	0.19	0.185 ± 0.003
Fe	0.14	0.114 ± 0.002
Si	0.08	0.094 ± 0.001
Mn	0.04	0.045 ± 0.001
Ti	0.02	0.030 ± 0.002
Others(each, $\leq$)	0.05	0.05
Others(total, $\leq$)	0.15	0.15
Total	100.00	99.966 ± 0.092

Table 4.8: Brief selection of possible alternative aluminum alloy target materials. Chemical composition specifications, given in units of % by weight [wt%], taken from an Aluminum Association technical report [109]. Typical tensile strengths taken from the material properties tabulated on the MatWeb database [110].

Alloy	7075-T651	2090	2091	8090
	Chemical Composition [wt%]			
Li	–	1.9–2.6	1.7–2.3	2.2–2.7
Mg	2.1–2.9	0.25	1.1–1.9	0.6–1.3
Si	0.4	0.1	0.2	0.2
Ti	0.2	0.15	0.1	0.1
Cr	0.18–0.28	0.05	0.1	0.1
Mn	0.3	0.05	0.1	0.1
Fe	0.5	0.12	0.3	0.3
Cu	1.2–2.0	2.4–3.0	1.8–2.5	1.0–1.6
Zn	5.1–6.1	0.1	0.25	0.25
Zr	–	0.08–0.15	0.04–0.16	0.04–0.16
Other ($\leq$)	0.05	0.05	0.05	0.05
Al	Rem.	Rem.	Rem.	Rem.
	Tensile Strength (Typical) [MPa]			
Ultimate	572	550	430	510
Yield	503	520	330	450

Chapter 5

Elastic Parity-Violating ^{27}Al Asymmetry Analysis

The Q_{weak} collaboration has made the first measurement of the elastic parity-violating ^{27}Al asymmetry. Originally required as a background correction measurement for the main weak charge analysis, this measurement can directly determine the neutron distribution radius of the ^{27}Al nucleus. Such a determination acts as a test of theoretical models used to describe neutron-rich matter, from heavy nuclei to neutron stars [40]. The measured asymmetry includes effects from large inelastic scattering backgrounds, because the apparatus used to conduct the measurement was not optimized for this purpose. A determination of the neutron distribution radius from this measurement relies upon the ability to apply corrections for these backgrounds with sufficient precision.

The analysis discussed in this chapter details the extraction of the pure elastic parity-violating electron-^{27}Al asymmetry from the measured asymmetry. Corrections for known systematic measurement-based effects and inelastic scattering backgrounds are discussed. Once the corrections are applied, the extracted parity-violating asymmetry with its uncertainties is compared to theoretical predictions. This resulting asymmetry is then used to determine the neutron distribution radius with a many-models correlation method, first introduced by the Lead Radius Experiment (PREX) [122].

5.1   Data Selection and Quality Checks

Throughout the Q_{weak} experiment, several periods of lower beam current operation were dedicated to asymmetry measurements on auxiliary aluminum alloy targets. Most of this time was spent measuring the parity-violating asymmetry from a solid $\approx 4\,\%\,X_0$ ^{27}Al alloy target[*] located in the downstream position. This target and the others available during the experiment were discussed in Section 4.5.

Asymmetry data on the ^{27}Al target was taken in Run 0, Run 1, and Run 2. The bulk of this data was recorded during Run 2. Presented here is an analysis of the parity-violating elastic electron-^{27}Al asymmetry using the data from Run 2 in Wien periods 6–9, see Section 4.2. No aluminum data was taken during Wien 7.

A small amount of additional data was recorded using this target during Wien 10. However the decision by the aluminum background subgroup, working on the aluminum correction for the weak charge measurement, was to drop this data set for reasons discussed below. Including this additional Wien 10 data would only yield a minor improvement to the overall statistical uncertainty associated with the measurement, when compared with the total systematic uncertainty.

The short segments of aluminum data that were collected during Run 0 and Run 1 had similar statistical uncertainties to that of Wien 10 in Run 2. Thus it was determined that their inclusion into the final data set was not worth the overall effort that would be needed to determine the separate systematic uncertainties associated with operating the experiment during these earlier runs compared with Run 2. Any future investigation of this analysis outside of this dissertation might consider including these additional data, if improvements can be made to the systematic uncertainties.

The decision to drop Wien 10 was made based on strange behavior found in the fit probabilities for individual main detector physics and null asymmetries. No improvement was found after applying many of the measurement-related systematic corrections, thus the decision to drop the Wien 10 data was made by the aluminum background subgroup. It is considered bad practice to discard data simply based on poor fit probabilities, but

---

[*]From this point forward, any reference to data taken with the ^{27}Al target is referencing this target, unless otherwise specified.

lack of definitive reasons as to why they occurred forced the decision to drop the data. An independent analysis of the entire Run 2 data set including this problematic Wien 10 has been completed and is discussed at length in the dissertation by J. A. Magee [98]. For those who are interested, that reference gives a more detailed explanation of the strange behavior associated with Wien 10. The raw asymmetry extracted from his analysis and the one detailed in this document only differ by 17 ppb, which is well within the statistical uncertainty associated with either value.

Two independent data quality checks were performed on the Run 2 data set by other members of the aluminum background subgroup. These checks used a two-tiered system of software and direct analysis cuts to label corrupted data for later exclusion. The software cuts were directly built into the Q_{weak} analyzer software package used to construct asymmetry observables during the offline data analysis. These software cuts primarily removed periods of unstable beam from beam current trips. Details regarding the implementation of these software data quality cuts can be found in the dissertation by R. S. Beminiwattha [121].

Additional cuts were placed on periods of hardware failure associated with the QTOR power supply and the charge feedback system, which is responsible for minimizing the measured charge asymmetry during the experiment. In particular, failures of the charge feedback system would typically result in measured charge asymmetries on the scale of a 1000 ppm. Any aluminum data taken during these hardware failure periods was excluded from the final data set.

A minimum quartet requirement was enforced for each of the runlets in the final data set. For the analyzer to properly perform regression corrections for the helicity-correlated beam motion, a minimum of 5000 quartets (≈ 21 s) were required for each runlet. Runlets with fewer quartets are excluded from the final data set.

The last tier of data quality checks used direct analysis methods applied to measured asymmetries to identify periods of corrupted data for exclusion. These checks employed a labeling systems of "good," "suspect," and "bad" tags that were applied to runlet-level aluminum data. The primary observable used to assign these data quality tags was the measured beam charge asymmetry. In particular, two properties associated with the measured beam charge asymmetry were monitored and used to assign these tags.

The first were periods of discontinuities in the charge asymmetry that would occur during state changes of the insertable half-wave plate (IHWP), located in the injector. Occasionally, the quartet-level measured charge asymmetry would jump during this state change, thus runlets measured during these jumps would be given the label of "bad" and subsequently removed from the final data set. Examples of acceptable, borderline, and bad IHWP transition runlets can be see in the dissertation by J. A. Magee [98] and Q_{weak} electronic log book (ELOG) entry [123].

The second property used to classify data was the width of the measured quartet-level charge asymmetry distribution. During Run 2, the measured quartet level charge asymmetry was approximately Gaussian distributed, with a width (σ) of 1.14 ppm [123]. Runlets with charge asymmetry less that 5σ would be marked as "good", $5 - 10\sigma$ as "suspect", and greater than or equal to 10σ as "bad." The details of which corresponding runlets were marked as either "suspect" or "bad" are documented in the following ELOG entries [123, 124].

In Wien 8, there were two periods of odd behavior, as seen in the distribution widths associated with the beam-energy difference and BCMDD 78 (see Section 5.3.1 for a description of this observable) observables. Upon further investigation it is believed that these artifacts come from tests of the new C100 SRF cavities and poor beam transmission through CEBAF. As widths of both of these observables were not unreasonably large, the runs from these periods were marked as "suspect." Further details about this observed behavior is documented in the ELOG [123].

The final Run 2 aluminum data set considered in this analysis comes from analysis pass 5b, using only runs with the "good" data quality label and cuts discussed above. A total of 1494 runlets, 131 runs, or 29 slugs pass these data quality cuts. The runs, and their associated properties, included in this final data set are tabulated in Table B.1.

5.2 Raw Asymmetry and Statistical Uncertainty

A raw asymmetry (A_{raw}) and statistical uncertainty are extracted from the Q_{weak} analysis database using the data quality cuts discussed above. Details on how these raw asymmetries

are formed in the Q$_{\text{weak}}$ analyzer software have already been discussed in Section 4.9. The raw asymmetries populating the database are runlet-based averages of quartet-level asymmetries. This analysis opted to use error-weighted slug-averaged asymmetries, which allowed the study of systematic effects over the long slug-level time scales. The particular observable reported in this analysis are the "mdallpmtavg" asymmetries, which are the weighted average of all eight main detectors, 16 PMTs.

Systematic effects were investigated by splitting the data into positive and negative helicity states, depending on the state on the IHWP and the Wien filter. These positive and negative states are subsequently averaged over the entire data set. A NULL hypothesis test was conducted by forming an unweighted average of these positive and negative averaged asymmetries, as defined by

$$A_{\text{NULL}} = \frac{A_{\text{POS}} + A_{\text{NEG}}}{2}. \tag{5.1}$$

A non-zero result would be an indication that there was an improper cancellation of false asymmetries in the data. The actual physics asymmetry was constructed from taking the error-weighted average of the positive and negative asymmetries, once a sign-correction is made for the various helicity state controls. These averages can be investigated over different time intervals, such as the run, slug, or wien level. The aluminum data set had consistent averages regardless of the choice of time interval [98, 125].

The slug-averaged raw asymmetries for the aluminum data set are plotted by the various types of averages in Fig. 5.1. The data is color coded, based on the state of the IHWP and Wien filter setting of either left (L) or right (R). The averages for the positive, negative, NULL, and physics asymmetries, indicated by the gray lines, are tabulated in Table 5.1.

Table 5.1: Unregressed aluminum asymmetry slug-based time averaging statistics. The labels NEG and POS refer to the slug average of the negative and positive state asymmetries. The NULL and PHYS labels refer to the respective unweighted-average and sign-corrected weighted-average of the NEG and POS asymmetries.

Quantity	Asymmetry [ppm]	χ^2/DOF	χ^2 Probability
NEG	-1.407 ± 0.093	1.26	0.225
POS	1.480 ± 0.099	1.62	0.073
NULL	0.036 ± 0.068	–	–
PHYS	1.441 ± 0.068	1.39	0.082
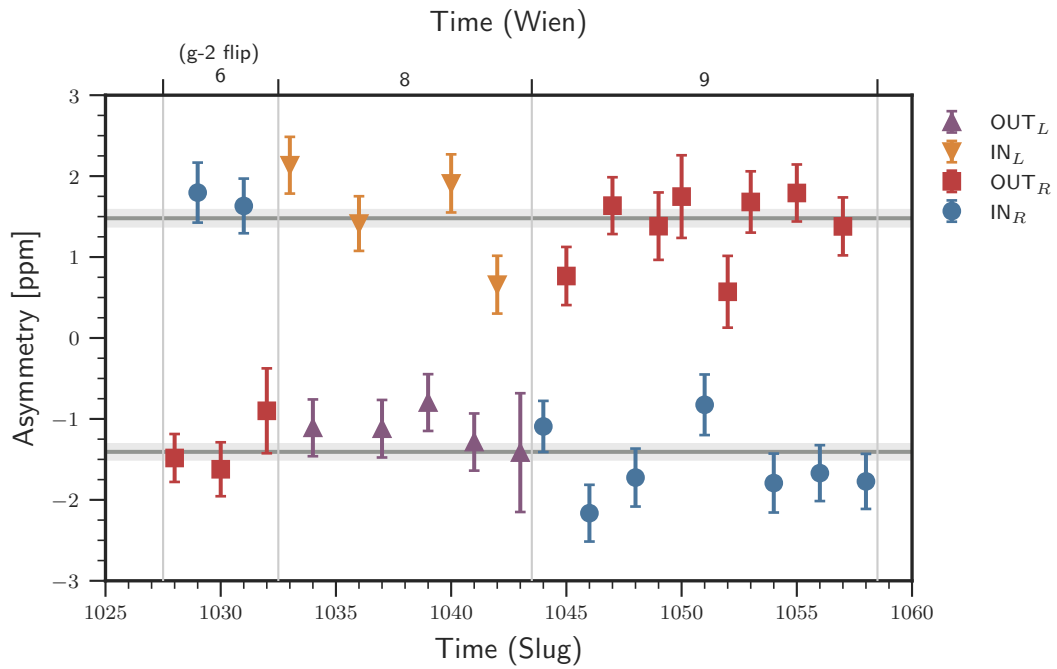
(a) IHWP plot
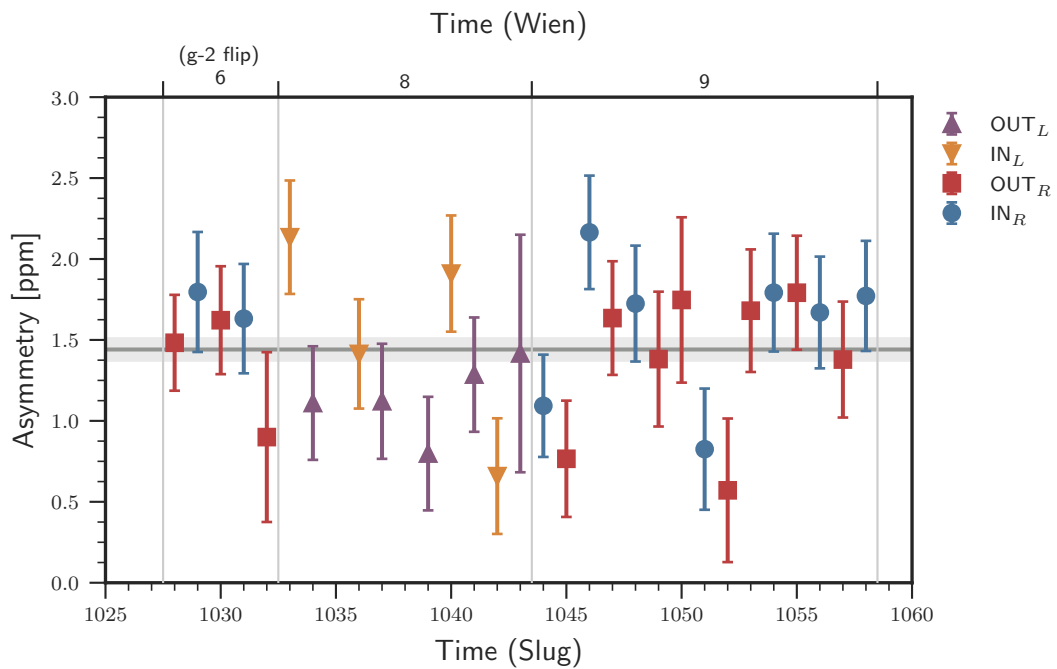
(b) Sign-corrected plot

Figure 5.1: Unregressed "raw" asymmetry slug plots for the Run 2 aluminum data set.

The validity of the positive, negative and physics averages are determined using a χ^2 per degree of freedom (DOF) and χ^2 probability metric. The NULL hypothesis is checked by

looking at its deviation from zero. For this data set, the χ^2 and probabilities were reasonable for the amount of spread seen in the slug averages. The NULL is consistent with zero within the statistical uncertainty. The raw asymmetry and statistical uncertainty for the aluminum data are taken as the PHYS entry in Table 5.1. This is a 4.7 % precision measurement of the raw aluminum asymmetry.

5.3   Measured Asymmetry Determination

With the final aluminum data set selected and a corresponding raw asymmetry A_{raw} determined, extraction of the physics asymmetry begins by correcting for several measurement based systematics, primarily corrections for false asymmetries introduced into the raw asymmetry by imperfections associated with both the polarized electron beam and the Q$_{weak}$ apparatus. Each of these corrections has a corresponding uncertainty that contributes to the total uncertainty associated with the final extracted asymmetry.

Known corrections are applied for the following quantities: the uncertainty associated with the BCM normalization (A_{BCM}), false asymmetries arising from helicity-correlated beam motion (A_{reg}), an isotropic false asymmetry from the beam halo interacting with beamline components (A_{BB}), any detector non-linearities (A_L), transverse asymmetries (A_T), and a polarization-dependent rescattering bias originating from the lead preradiators on the main detectors (A_{bias}). These corrections are applied to the raw asymmetry (A_{raw}) to get the measured asymmetry (A_{msr}) using

$$A_{msr} = A_{raw} + A_{BCM} + A_{reg} + A_{BB} + A_L + A_T + A_{bias}. \qquad (5.2)$$

In this section, each of these corrections and their corresponding uncertainties are discussed in the context of the aluminum analysis.

5.3.1   BCM Uncertainty

During Run 2, BCMs 1, 2, 5, 6, 7, 8 were available for beam current monitoring during the aluminum data taking. BCM 8 was chosen to be the reference charge monitor, which was

used in the experiment to normalize the recorded main detector signals (yields). As other BCM monitors were available, the question of whether BCM 8, a different monitor, or a combination of monitors should be used to normalize the measured main detector signal can be answered by looking at the BCM double difference observables associated with the various combination of BCMs. The BCM double difference between two monitors is given by

$$DD_{ij} = \frac{Q_i^+ - Q_i^-}{Q_i^+ + Q_i^-} - \frac{Q_j^+ - Q_j^-}{Q_j^+ + Q_j^-} = A_{Q,i} - A_{Q,j}, \qquad (5.3)$$

where $Q_{i(j)}^{+(-)}$ denotes the charge measured by BCM i or j for positive $(+)$ or negative $(-)$ beam helicity and A_Q is the charge asymmetry. Monitors in perfect agreement would yield a double difference of zero. Any disagreement found between these current monitors needs to be accounted for in terms of an additional uncertainty to A_{msr}. A guide of how this uncertainty was determined for the weak charge measurement is discussed in a technical report [126].

In the aluminum data quality checks, the BCM double difference for monitors 7 and 8 was investigated over Wiens 6, 8, and 9. The average of this BCM double difference asymmetry over the three Wiens is consistent with zero at the 12σ level [123]. A preliminary investigation was completed, by looking into the agreement of the other BCM monitors available in Run 2 for the aluminum data set, but no quantitative conclusions were drawn at that time. Further investigation is required to see if those double differences are consistent with zero over the aluminum data set.

At this time, the Run 2 BCM uncertainty from the weak charge asymmetry analysis is adopted, as a conservative effort to include this additional systematic uncertainty [46]. This uncertainty was determined to be

$$A_{BCM} = 0.0 \pm 2.1 \text{ ppb.} \qquad (5.4)$$

This correction is believed to be conservative because the aluminum data set was intertwined with the weak charge measurement throughout Run 2. Any future effort outside of this analysis should be dedicated to investigating this uncertainty specifically for the aluminum

analysis. Critics should note that the aluminum data taking was performed at a lower beam current. The behavior of the BCMs could be different compared with behavior used to determine this uncertainty. I anticipate that any future investigation will show that a full BCM renormalization is not warranted for the aluminum data set and that the additional uncertainty is smaller that the 2.1 ppb assumed here.

5.3.2   Helicity-Correlated Beam Corrections

Helicity-correlated beam motion, as introduced in Section 4.2, has the potential to lead to large false asymmetries measured by the main detectors in the aluminum data set; thus a correction is needed for this systematic effect.

A correction can be made to the raw asymmetry by measuring the helicity-correlated difference in beam parameters, such as position and angle, and the correlation between the raw main detector asymmetries and those beam parameters. These include: positions X and Y, angles X' and Y', and energy E. Mathematically, this correction is expressed as

$$A_{reg} = -\sum_i \frac{\partial A_{raw}}{\partial \chi_i} \Delta \chi_i, \tag{5.5}$$

where $\frac{\partial A}{\partial \chi}$ is the detector correlation for a given beam parameter χ_i and $\Delta \chi$ is the helicity-correlated difference in beam parameter χ_i. The correlation, also know as a sensitivity, can be determined with two linear regression methods: natural motion and beam modulation.

The first method uses the beam related monitoring devices to determine correlations between the measured main detector asymmetries and beam positions and angles that arise from natural beam motion. The second method uses magnetic coils to modulate the position and angle of the beam with a known signal, allowing a precise determination of the correlation between the measured asymmetry and the beam parameters. Since the size of the raw asymmetry in the aluminum data is an order of magnitude larger than that of the weak charge measurement and the correction is expected to be of the same size as the weak charge analysis, the linear regression method was chosen to determine this systematic correction, which is the easier of the two methods in terms of analysis effort.

The linear regression correction is performed in the Q$_{\text{weak}}$ analyzer using a particular set

of beam monitor variables. This analysis opts for the "on" regression set, as the monitors it uses are closest to the target and are fairly well behaved over the length of the aluminum data set. The behavior of these helicity-correlated differences and sensitivities has been previously investigated [127]. Plots of these quantities from this study are included in Appendix B.2.

The particular set of target beam monitors used to determine the detector sensitivities and helicity-correlated differences in this analysis is tabulated in Table 5.2. Monitor definitions for the rest of the available regression sets can be found in the ELOG [128].

Table 5.2: Analysis variable definitions for the various beam parameters used in the "on" regression set.

Beam Parameter	Monitor Variable
X	diff_qwk_targetX
Y	diff_qwk_targetY
X' (slope)	diff_qwk_targetXSlope
Y' (slope)	diff_qwk_targetYSlope
E	diff_qwk_energy

The regression correction is applied to the quartet asymmetries, then averaged and saved to the database at the runlet-level. Asymmetries take from the database are subsequently averaged at the slug time scale in this analysis. The effects of these corrections on the slug-averaged asymmetries can be seen in Fig. B.1. Following the same analysis steps as applied to the extraction of the raw asymmetry, the positive, negative, NULL, and physics asymmetries are determined for these regression corrected asymmetries. The χ^2 and probabilities for these regression corrected quantities are comparable to those determined in the raw asymmetry extraction. Additional details about this correction for the aluminum data set are documented in an ELOG on the subject [125]. The net correction A_{reg} is determined by taking the difference of the physics asymmetries listed in Table 5.3 and Table 5.1, which is 0.4 ppb.

Two uncertainties are believed to contribute to the overall uncertainty on A_{reg}. The first comes from the choice of regression set compared with the other available options. Using the steps described above, the regressed asymmetry was extracted for each of the available regression sets. A comparison was made between the size of the correction from a given set and the "on" set. These differences were typically on the order of less than 1 ppb and

Table 5.3: Regressed aluminum asymmetry slug-based time averaging statistics, using regression set "on". The labels NEG and POS refer to the slug average of the negative and positive state asymmetries. The NULL and PHYS labels refer to the respective unweighted-average and sign-corrected weighted-average of the NEG and POS asymmetries.

Quantity	Asymmetry [ppm]	χ^2/DOF	χ^2 Probability
NEG	-1.417 ± 0.093	1.27	0.218
POS	1.469 ± 0.099	1.63	0.070
NULL	0.026 ± 0.068	–	–
PHYS	1.441 ± 0.068	1.40	0.079

are tabulated in Table 5.4. The largest difference was seen between set 8 and set "on" at -0.987 ppb. Rounding to the nearest part-per billion, the uncertainty due to the regression set selection is 1.0 ppb.

The second uncertainty comes from the choice of time interval for which the regression correction is applied to the data. By default, the correction is applied to the runlet asymmetries. However, using the slug averaged differences and sensitivities, the regression correction can be applied at the slug time scale. Comparing the extracted physics asymmetry from either choice of time interval only yields an asymmetry difference of 1.0 ppb. A total uncertainty on A_{reg} was calculated by taking the quadrature sum of both of these 1.0 ppb uncertainties, yielding a value of 1.4 ppb. Further information regarding the determination of these uncertainties can be found in the ELOG [127].

Table 5.4: Regression scheme dependence on regression monitor set with respect to "on" set.

Regression Set	Correction [ppb]	Difference w/ "on" [ppb]
on	0.410	–
on 5+1	0.106	-0.304
set 3	0.106	-0.304
set 4	0.454	0.044
set 7	-0.266	-0.676
set 8	-0.577	-0.987
set 10	0.474	0.064
set 11	0.410	0.000
set 13	0.508	0.098

In summary the regression correction for the entire Run 2 aluminum data set was

determined to be

$$A_{reg} = 0.4 \pm 1.4 \text{ ppb.} \tag{5.6}$$

5.3.3   Beamline Background

A false asymmetry arises from the secondary scattering of electrons from beamline compo-
nents, such as the tungsten beam collimator. This background is believed to be constituted
by isotropically distributed low-energy neutral particles carrying large asymmetries. The
source of these secondary electrons is thought to come from the diffuse extended transverse
distribution of the beam (so called "halo"), as it passes through the various beamline
components downstream of the target, on its way to the dump.

Much of the work performed on investigating this background for the weak charge mea-
surement was the subject of the dissertation by E. Kargiantoulakis [92]. I briefly summarize
that work. The beamline background was found to only weakly contaminate the measured
main detector asymmetries. However, other detectors, such as the upstream luminosity
monitors (US lumis), were found to predominantly measure this beamline background
asymmetry. Thus a formalism was developed to determine a correction for this background
asymmetry by using the correlation between the measured main detector asymmetry and
the US lumi asymmetry, already referenced above. In this section I discuss the application
of this beamline background formalism for the Run 2 aluminum data set.

Slug-averaged regressed US lumi asymmetries were extracted from the entire Run 2
data set and were typically an order of magnitude larger than the measured main detector
asymmetries. A correlation slope was extracted by comparing these US lumi asymmetries
with the slug-averaged regresssed main detector asymmetries discussed in Section 5.3.2.
Figure 5.2 shows the correlation plot of these asymmetries. A linear fit was applied to these
data, using a non-linear least squares method. The correlation (C_{MD}^{USLumi}) or the slope of
this best fit line was determined to be [129]

$$C_{MD}^{USLumi} = \frac{A_{MD}}{A_{USLumi}} = 6.6 \pm 5.9 \text{ ppb/ppm.} \tag{5.7}$$

A beamline background correction was applied to the slug-averaged regressed main
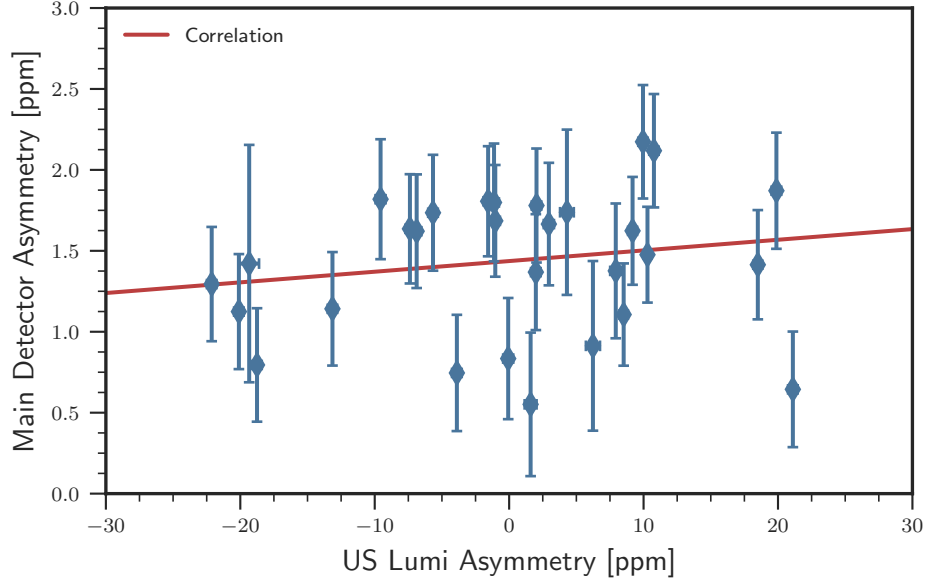
Figure 5.2: Sign-corrected slug averaged main detector asymmetry to upstream lumi asymmetry correlation for the Run 2 aluminum data set.

detector asymmetries on a slug-by-slug basis, using

$$A_{BB} = -C_{MD}^{USLumi} A_{USLumi},\qquad(5.8)$$

where C_{MD}^{USLumi} is the correlation slope extracted over the entire Run 2 aluminum data set and A_{USLumi} is the slug-averaged regressed US lumi asymmetry. These corrections were typically on the order of 50 ppb, however the corrections for Wien 8 were closer to 100 ppb. Figure 5.3 shows each of the corrections for the entire Run 2 data set.

After applying the beamline background correction, the positive, negative, NULL and physics asymmetries were extracted, see Table 5.5 for a tabulation of these values and Fig. B.12 for plots. The NULL asymmetry improved by an order of magnitude after including this correction and the physics asymmetry only shifts by -4.7 ppb, much less than the statistical uncertainty. This demonstrates that the formalism used to determine this correction is valid for the aluminum data set.

The final overall beamline background correction is just the shift in the physics asymmetries between the regressed and beamline background plus regressed data. The uncertainty is taken to be that of the central value of the extracted correlation slope, which is slightly
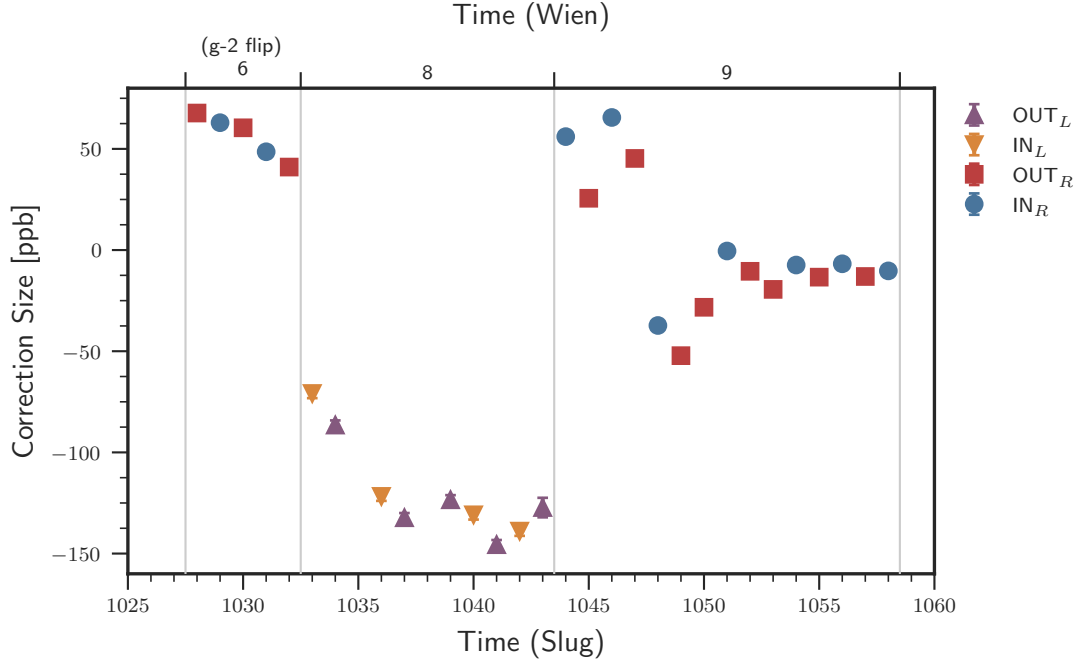
Figure 5.3: Beamline background corrections to slug-averaged regressed main detector asymmetries. Figure recreated from data tabulated in the ELOG [125].

inflated to account for any systematic uncertainty beyond the statistical uncertainty already present in the correlation slope. The final beamline background correction for the Run 2 aluminum data set was

$$A_{BB} = -4.7 \pm 6.6 \text{ ppb.} \tag{5.9}$$

Originally, the beamline background was treated as a physics background correction to the measured asymmetry using the formalism discussed in Section 5.4. However, when

Table 5.5: Combined beamline background and regressed aluminum asymmetry slug-based time averaging statistics, using regression set "on". The labels NEG and POS refer to the slug average of the negative and positive state asymmetries. The NULL and PHYS labels refer to the respective unweighted-average and sign-corrected weighted-average of the NEG and POS asymmetries.

Quantity	Asymmetry [ppm]	χ^2/DOF	χ^2 Probability
NEG	-1.435 ± 0.093	1.11	0.339
POS	1.439 ± 0.099	1.71	0.051
NULL	0.002 ± 0.068	–	–
PHYS	1.437 ± 0.068	1.35	0.101

the main detector US lumi correlation technique was developed, the collaboration decided that it would be applied as a false asymmetry correction before the background physics corrections [92]. However, the amount of signal fraction from this beamline background asymmetry still needed to be included in this analysis. A value for this beamline background fraction was determined for the aluminum data set from blocked-octant running, as discussed below.

During the experiment, time was dedicated to a type of systematic study called blocked-octant running. Tungsten shutters with the same profile of the acceptance defining apertures in collimator 2, were placed in front (upstream face) of the openings of octant 1 and 5 in collimator 2. The shutters would block the scattered electron profile seen by main detectors 1 and 5, which allowed the measurement of detector rates and yields originating from this beamline background. These measured yields were used to determine a background fraction for this process, as detailed in an ELOG [130]. The background fraction from the aluminum data was determined to be

$$f_{BB} = 0.69 \pm 0.06 \ \%.$$ (5.10)

5.3.4   Non-linearity

A correction was needed to account for the non-linear signal response contaminating the main detector recorded raw asymmetry. The source of this non-linearity comes from two sources: the main detector photomultipier tubes and the BCMs that monitor the charge asymmetry used to normalize the raw asymmetry.

This correction was determined after the experiment was completed, by using a combination of equipment bench tests and data analysis. Details of this work can be found in the dissertation by W. Duvall [131]. The non-linearity factor (f_L) for the Run 2 aluminum data set is given as $0.1 \pm 0.5\,\%$. This factor is then used to scale A_{raw} to give the non-linearity correction A_L and its uncertainty as

$$A_L \equiv -f_L A_{raw},$$
$$\delta A_L \equiv \delta f_L |A_{raw}|.$$ (5.11)

The A_L correction for the entire Run 2 aluminum data set calculated using this f_L value, and the "PHYS" value from Table 5.1 as A_{raw}, was

$$A_L = -0.001 \pm 0.007 \text{ ppm.} \tag{5.12}$$

5.3.5   Transverse Leakage

As discussed in Chapter 4, one of the design goals of the Q_{weak} apparatus was to minimize systematic effects that would arise from geometric asymmetries. Leakage of beam-normal single-spin asymmetries, also known as transverse asymmetries, are an example of such a geometric systematic effect that has to be accounted for in this analysis. The transverse asymmetries affecting A_{raw} originate from residual transverse beam polarization combined with imperfections in the azimuthal symmetry of the main detector array. A transverse polarization causes an azimuthal variation in the main detector asymmetries. A correction (A_T) for this effect is constructed with the knowledge of two quantities: the amount of residual transverse beam polarization (P_T) and the symmetry breaking factor of the apparatus (f_S). This factor quantifies how asymmetric the azimuthal symmetry is in the Q_{weak} apparatus [83]. It can be determined with two separate methods. One option, which was not explored in this analysis but is mentioned here for completeness, would be to study the azimuthal variation of the asymmetry as determined in a well benchmarked Monte Carlo simulation, using the as-built geometry. The other is to study the variation using measured asymmetries from periods of dedicated transverse polarized beam. The latter method was used for this analysis, due to the precedent set by the weak charge analysis.

Chapter 6 covers the physics analysis associated with these periods of transverse running in greater detail. However, the amplitude of this variation and the constant offset from the transverse data have to be known here as they are used to determine this leakage correction. To summarize the techniques used in that future chapter, the azimuthal variation and constant offset are extracted from fits to transverse data taken with transversely polarized beam during Run 2 for two separate polarization directions: vertical or horizontal. The asymmetry measured in the main detectors are fitted with a generalized sinusoidal function that has three free parameters: the amplitude, the phase, and a constant offset. Values for

the amplitude are used to help determine the residual transverse beam polarization and the constant offset is taken to be a measure of the symmetry breaking factor of the apparatus. Table 5.6 contains values for these amplitudes and constant offsets determined from the fits in Chapter 6.

Table 5.6: Amplitudes and constant offsets extracted from sinusoidal fits to transverse asymmetries versus main detector from the pure transverse aluminum data set. Uncertainties provided are statistical only.

Polarization Direction	Amplitude [ppm]	Constant [ppm]
Vertical	-8.619 ± 0.727	0.203 ± 0.514
Horizontal	-8.486 ± 0.499	-0.106 ± 0.353

The amount of residual transverse beam polarization is determined by looking at the azimuthal variation of regressed main detector asymmetries for the entire Run 2 aluminum data set. To avoid any confusion, it is important to note that there are data measured with longitudinally polarized beam. The expectation is that the measured asymmetry (from the purely longitudinal beam) versus azimuthal position (main detector location) is constant. Fitting the parity-violating measured asymmetry versus main detector places limits on the amount of residual transverse polarization that might have contaminated the beam during aluminum data taking.

To extract the residual polarization values, a generalized function constructed from both sine and cosine components is fitted to the Run 2 parity-violating aluminum data set. The generalized function has the form of

$$A = B_T \big[P_T^V \cos \phi + P_T^H \sin \phi \big] + C, \tag{5.13}$$

where B_T is the size of the aluminum beam-normal single-spin asymmetry, ϕ is the azimuthal angle in the Q$_{\text{weak}}$ global coordinate system, C is a constant offset representing the parity-violating asymmetry, and P_T^V (P_T^H) is the vertical (horizontal) component of the residual transverse polarization.

A non-linear least squares fit was performed on the Wien-averaged main detector asymmetries for Wiens 6, 8, and 9 using Eq. (5.13). P_T^V, P_T^H, and C were treated as
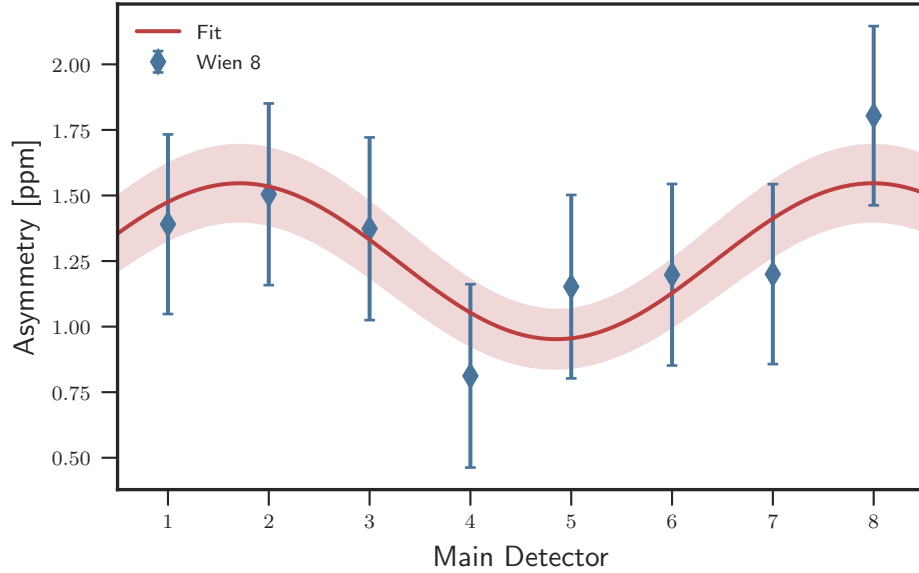
Figure 5.4: Residual transverse polarization extraction using a sinusoidal fit to main detector regressed asymmetries in Wien 8. Uncertainties on blue data points are statistical only. A 1σ uncertainty associated with the fit is given by the red band.

free parameters with the fit being optimized using a χ^2 minimization routine. A value of $B_T = -8.5 \pm 0.4$ ppm was used in the fit to set the size of the beam-normal single-spin asymmetry, which is the error-weighted average of the vertical and horizontal amplitudes from the fits performed on the fully transverse data sets given in Table 5.6. Figure 5.4 gives an example of one of these fits for Wien 8, the plots for Wiens 6 and 9 can be seen in Appendix B.4.

Extracted values for P_T^V and P_T^H from the fits over all three Wiens are then averaged to obtain final values which are used to calculate the transverse leakage correction. These extracted values were determined to be $P_T^V = -0.48 \pm 0.95\,\%$ and $P_T^H = 2.32 \pm 0.85\,\%$.

As the analysis breaks the residual transverse polarization and symmetry factors into vertical and horizontal components, they can be combined to form the final transverse leakage correction using

$$A_T = f_S^V P_T^V + f_S^H P_T^H. \tag{5.14}$$

Using this expression a transverse leakage correction for the entire Run 2 aluminum data set

is determined to be

$$A_T = -3.4 \pm 8.8 \text{ ppb.} \tag{5.15}$$

Further details about this analysis can be found in the ELOG [132].

5.3.6 Rescattering Bias

Late in the weak charge measurement analysis, an additional false asymmetry was discovered when investigating the asymmetries seen by the individual photomultipler tubes (PMTs) attached to the main detectors. Based on the symmetry of these detectors, it was expected that the difference of these PMT asymmetries would be zero. This asymmetry difference, called the PMT double difference (A_{DD}), is defined as

$$A_{DD} \equiv A_+ - A_-, \tag{5.16}$$

where A_+ and A_- are the measured asymmetries from the positive and negative PMTs at each end of a given main detector, see Fig. 4.8. For the weak charge measurement these differences were typically measured to be 300 ppb for the eight main detectors [46], indicating the presence of a false asymmetry that required a correction. This correction is known as the rescattering bias (A_{bias}).

The source of this systematic effect was determined to be transverse asymmetries acquired by the scattered electrons as they passed through the lead preradiators attached to the front of each main detector, thus the name of rescattering bias. As scattered electrons leave the target and pass through the magnetic field of the spectrometer, they acquire some amount of transverse polarization from spin precession. Once these scattered electrons shower through the lead preradiators, prior to detection in the quartz of the main detectors, their transverse polarization causes them to develop a non-zero analyzing power from low-energy Mott scattering, which causes a difference in the asymmetries measured by either PMT. A correction for this effect in terms of the previously defined quantities is given as

$$A_{bias} \equiv \frac{A_+ - A_-}{2}. \tag{5.17}$$

Significant effort went into trying to understand this effect by two independent collaboration subgroups. Much of their work on this topic is discussed in detail in a technical report on the subject [133] and in an ELOG [134]. One subgroup was able to determine an A_{bias} correction by modeling the transport of these transversely polarized electrons through the preradiators with a detailed Geant4 simulation [113–115]. This simulation study investigated the effects from the parameterizations of the Cherenkov-light yield in the quartz, the flux distribution of electrons passing through the main detector, and optical effects associated with the light collection by the PMTs.

Using the machinery developed for determining a correction for the weak charge measurement, a similar analysis was performed to determine a rescattering bias correction for the Run 2 aluminum data set. To gain an appreciation for the size of this effect in the aluminum data set, it is important to first look at the PMT double difference. A preliminary determination of the Run 2 aluminum PMT double difference was performed and documented in an ELOG [135]. However, that analysis opted for an alternative definition of PMT double difference than that given in Eq. (5.16). A more recent calculation has been completed using the slug-averaged asymmetry from the pass5b database and the definition given in Eq. (5.16). Fig. 5.5 shows these calculated PMT double differences versus main detector number, as extracted from this updated analysis. Note that the uncertainties on the points in that figure are incorrect, as the true uncertainty on the PMT double difference has to be calculated at the quartet level, thus any main-detector averaged PMT double difference is only valid to 10 %. The author leaves the proper calculation of these uncertainties as a future task that should be revisited. With that caveat in mind, the main detector averaged PMT double difference is determined to be 374 ± 106 ppb. This double difference is consistent within its quoted uncertainty with the one determined from the weak charge data set.

Based on the suggestion of the subgroup working on this simulation-based analysis, an effective model was used to calculate the rescattering bias correction for the aluminum data set. Specifically, effective model "6" was chosen to determine the correction [136]. Details about this particular model choice are discussed in the technical report [133]. However, a few important points regarding the determined correction are mentioned here as they impact the interpretation for the aluminum analysis. First, the correction determined from this
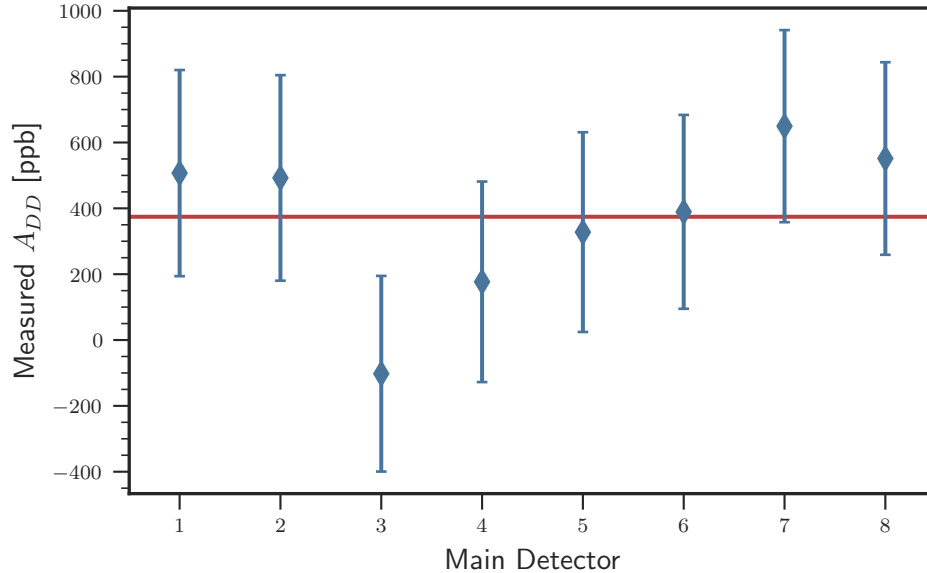
Figure 5.5: Measured PMT double difference asymmetry calculated with the slug-averaged PMT asymmetries for the aluminum data set. The error-weighted average is given by the red line.

model does not account for any analyzing power dependencies across the face of the quartz bar (in the local x direction), it only considers these along the bar (in the local y direction). These local x variations are believed to have a small effect on the correction. Symmetrized aluminum electron flux distributions determined from tracking analysis were used as the model's flux input for each of the main detectors and well as the best optical models for a given detector.

An A_{bias} correction of 4.2 ± 0.6 ppb is determined from this effective model by taking the error-weighted average of the individual A_{bias} values determined for each main detector. These values are plotted in Fig. 5.6. The uncertainty on that value is from simulation statistics only and is not a true total uncertainty associated with this correction.

The effective model can also be used to calculate a PMT double difference, which can then be compared to the measured value in an effort to check its validity. The model gives a PMT double difference value of 290.5 ± 1.2 ppb, which is extracted from an error-weighted average of the double differences calculated for the eight main detectors. See Fig. 5.7 for a plot containing these values. Comparing to the measured value, the effective model double difference disagrees by 83.9 ppb, but is still within the uncertainty of the measured double
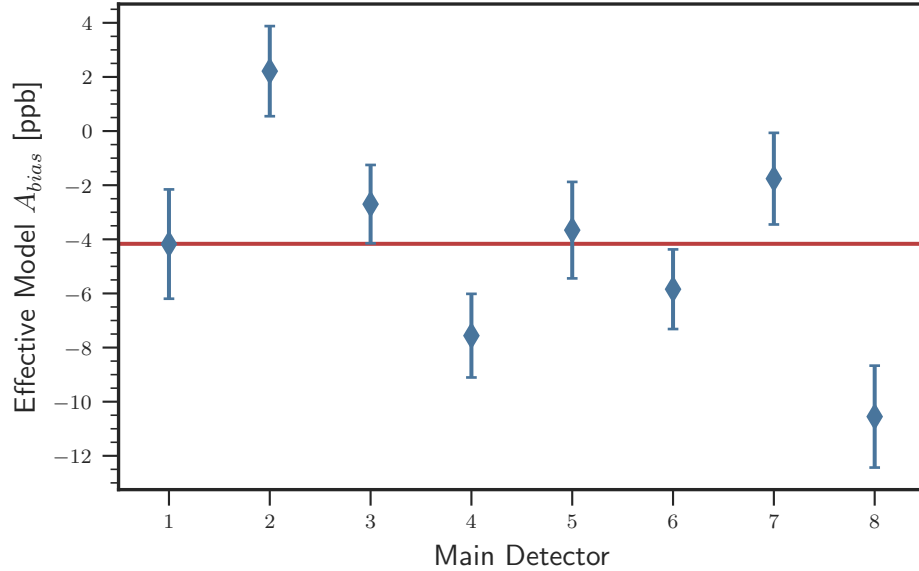
Figure 5.6: Main detector rescattering bias corrections for the aluminum data set, as predicted by effective model "6" with conditions mentioned in text. The average correction is given by red line. Figure recreated with data taken from the ELOG [136].

difference 374.4 ± 106.4 ppb. The effect of this discrepancy can be included in the predicted A_{bias} correction by scaling that value by the ratio of the measured to effective model double differences. Performing this scaling changes the central value of A_{bias} to 5.4 ppb, which agrees well with an earlier prediction from the other subgroup working on this correction. They chose to use a simple phenomenological approach that did not employ the sophisticated simulation work. Results from that earlier study are documented in the ELOG [134].

Uncertainty in A_{bias} comes from many of the inputs used in the effective model. However, it was determined that the largest of these uncertainties comes from the optical modeling of the as-built main detectors. Further details about the uncertainties that go into the simulation-based analysis are discussed in reference [133]. Based on recommendations by the subgroup, focused on this analysis, the final uncertainty on the A_{bias} correction for the weak charge measurement is adopted here for the aluminum correction. Thus for the entire Run 2 aluminum data set a rescattering bias correction is determined to be

$$A_{bias} = 5.4 \pm 3.0 \text{ ppb.} \tag{5.18}$$
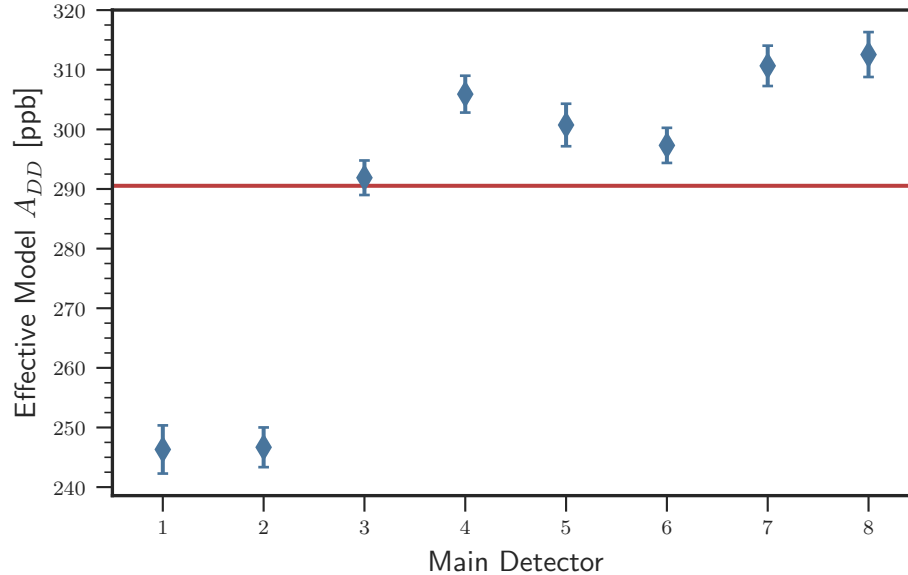
Figure 5.7: Main detector PMT double differences determined from effective model "6" for the aluminum analysis. Average double difference given by red line. Figured recreated with data taken from the ELOG [136].

5.3.7 Beam Polarization

The polarization of the beam needs to be taken into account as a correction to A_{msr}. This is applied as a scaling factor to A_{msr} before including corrections for background physics processes.

Beam polarization was monitored by the combination of both the Møller and Compton polarimeters during the Run 2 aluminum data set. An overview of their function has already been discussed in Section 4.4. Beam polarization values determined during Run 2 were extracted by the polarimetry subgroup. Based on their suggestions, polarization corrections were applied on the slug time scale using values from their analysis [137]. The polarization corrections of interest for the slugs in the Run 2 aluminum data set are tabulated in Table 5.7.

These values are applied to the slug-averaged beamline background plus regression-corrected main-detector asymmetries for the given slug ranges. Average positive, negative, NULL, and physics asymmetries were extracted with this correction included. Values of these averages are tabulated in Table 5.8 and plots are given in Fig. B.15.

Table 5.7: Beam polarization values for a given slug range.

Slug Range	Polarization [%]
1028–1032	88.602
1033–1043	88.688
1044–1047	89.520
1048–1052	89.741
1053–1058	87.714

Table 5.8: Combined polarization, beamline background, and regressed aluminum asymmetry slug based time averaging statistics, using regression set "on". The labels NEG and POS refer to the slug average of the negative and positive state asymmetries. The NULL and PHYS labels refer to the respective unweighted-average and sign-corrected weighted-average of the NEG and POS asymmetries.

Quantity	Asymmetry [ppm]	χ^2/DOF	χ^2 Probability
NEG	-1.616 ± 0.105	1.13	0.321
POS	1.620 ± 0.112	1.74	0.046
NULL	0.002 ± 0.076	–	–
PHYS	1.618 ± 0.076	1.38	0.089

An effective polarization correction is determined by taking the ratio of the beamline background corrected physics asymmetry in Table 5.5 with the polarization-corrected physics asymmetry in Table 5.8, which yields a value of 0.8880. The uncertainty on this effective polarization is determined by using the relative uncertainty recommended by the polarimetry subgroup. They give a relative value of 0.62% for the Run 2 polarization; details of their analysis used to determine this value can be found in the ELOG [137].

Using the effective polarization and the recommended relative uncertainty, a final polarization correction for the Run 2 aluminum data set is

$$P = 88.80 \pm 0.55 \ \%. \tag{5.19}$$

5.4   Background Corrections

The large energy bite of the Q_{weak} apparatus allows the acceptance of a non-negligible amount of scattered electrons that originate from non-elastic physics processes in the target. The asymmetries carried by these electrons have the potential to be on the order of or even

larger than that of the elastic parity-violating ^{27}Al asymmetry. Thus a successful extraction of the elastic parity-violating ^{27}Al asymmetry requires precision corrections for all known physics backgrounds that dilute the measured asymmetry. The difficulty of this analysis lies in the ability to determine these corrections.

Each background correction requires two components: the detector yield fraction (f_i) and the background asymmetry (A_i). The detector yield fraction, also referred to as a background fraction, is calculated from the product of the rate and the photoelectric response of the Q_{weak} detector system, weighted with the cross section carried by the detected scattered electrons. This yield (Y_i) as it is known, is determined in QwGeant4, Q_{weak}'s Geant4 Monte Carlo simulation [116], using either theoretical or empirical fits to data for each known scattering process. Separate simulations are used to determine the main-detector averaged yields per physics scattering process, where yields are extracted from the simulation using the methods discussed in a technical report [138]. The background fraction for a given process is defined as

$$f_i = \frac{Y_i}{\sum_i Y_i},$$ (5.20)

where i denotes a particular scattering process and the $\sum_i Y_i$ is the total yield of all processes included in the simulation. The asymmetries carried by the detected electrons are also calculated using theoretical models or are taken as extrapolations from previous measurements. The sum of the products of these two pieces, over all background processes, gives the total asymmetry correction to the polarization-corrected measured asymmetry.

To understand the challenges of this analysis one has to realize the number of possible scattering processes the incident electron beam can undergo during an interaction with the ^{27}Al nucleus. This understanding is best developed by quantifying the problem in terms of energy. The average nucleus requires approximately 8 MeV, the binding energy per nucleon, to have a nucleon removed from the nuclear potential [23]. Any incident electron that deposits that amount of energy or greater, by definition, inelastically scatters and can alter the asymmetry measured in the detector. A non-negligible fraction of these incident electrons deposit 8 MeV or more of energy in the target, given the incoming electron beam carries an energy of approximately 1.16 GeV, coupled with the 150 MeV energy acceptance

of the apparatus.

These inelastic scattering processes can be split into two general categories. The first are processes that excite the ^{27}Al nucleus without destructive deformation, while the second are processes that destructively deform the ^{27}Al nucleus via the removal of a nucleon. The first group can be further broken down into two sub-categories: discrete and collective excitations. Both of these typically occur in the 0–20 MeV energy range.

For the case of discrete excitations, it is best to view the nucleus within the context of the nuclear shell model. The shell model describes the nucleus as a collection of energy levels, where the individual nucleons occupy these levels according to their quantum numbers. This is analogous to the atomic shell model where electrons orbiting the nucleus occupy varying energy levels. Energy introduced from an external source can cause a nucleon (or, in the case of the atomic model, an electron) to jump to a higher level in a discrete step. After some fixed lifetime, the nucleon de-excites back to the ground state of the nucleus by releasing radiation, typically via the emission of a gamma-ray.

Collective excitations describe the motion of multiple nucleons inside of the bound nucleus. The most important of these excitations is the Giant Dipole resonance (GDR), which is best described as the neutron distribution moving out of phase with the proton distribution. Other, higher-mode giant collective excitations are also possible, though the probability of their excitation is less than that of the GDR. Additionally, rotational and vibrational degrees of freedom can be involved in these collective excitations, see reference [139].

Examples of destructive excitations include quasi-elastic and inelastic scattering. Quasi-elastic scattering is described by the electron interacting with the nucleus with enough energy so that a nucleon is ejected in the final state. Inelastic scattering in this context is similar, however the liberated nucleon is also excited, with the most probable nucleon excitation being the $\Delta(1232)$. Additionally, the term inelastic scattering can also be used to describe the deep inelastic piece of the scattering energy spectrum, where the electron has enough energy to probe the structure of the individual nucleons. Deep inelastic effects are not considered in this analysis, as the kinematics of this experiment make these reactions unlikely.

Apart from known background physics processes associated with the ^{27}Al, additional

corrections are needed for the following: elastic scattering from non-^{27}Al elements in the target alloy material, neutral particles transported through the apparatus, and charged pions. Only elastic scattering contributions are considered for the alloy elements in this analysis, as those are the dominant yield fractions at these forward-angle kinematics. Both the neutral particle and charged pion contributions were determined in simulation for this analysis.

To summarize, this section discusses the known corrections for background physics processes needed to extract the pure elastic parity-violating electron-^{27}Al asymmetry. These include corrections for the discrete excited states of the ^{27}Al nucleus, collective motion from the GDR, quasi-elastic scattering, inelastic scattering involving an excitation of the Δ (often labeled $N \rightarrow \Delta$), neutral particle backgrounds, charged pions, and elastic scattering from non-^{27}Al elements in the target alloy material.

5.4.1 Quasi-elastic Scattering

The background fraction determination for the quasi-elastic scattering process was performed in QwGeant4 using a cross section generator built from an empirical fit to world data. The cross section for inelastic electron-nucleon scattering in the one photon approximation is given by

$$\frac{d\sigma}{d\Omega dE'} = \frac{\alpha^2 \cos^2 \frac{\theta}{2}}{4E^2 \sin^4 \frac{\theta}{2}} [W_2(W^2, Q^2) + 2W_1(W^2, Q^2) \tan^2 \frac{\theta}{2}], \tag{5.21}$$

where α is the fine structure constant, θ is the lab polar scattering angle, and the structure of the interaction is described by the functions $W_1(W^2, Q^2)$ and $W_2(W^2, Q^2)$ [10]. These structure functions are dependent on the invariant mass W^2 and the momentum transfer Q^2 of the reaction.

Functional forms for these structure functions are determined by empirical fits to world data from inclusive electron-nucleus scattering experiments [140], which is known as the Bosted-Mamyan generator. In particular, these fits return separate values for the quasi-elastic and inelastic $N \rightarrow \Delta$ regions of the inelastic scattering spectrum, which correspond to different invariant mass and momentum transfer regions for a given scattering angle θ. Performing calculations with only the quasi-elastic piece of this fit allowed the determination

of acceptance averaged yields in simulation and correspondingly allowed the determination of the quasi-elastic background fraction. The original structure function fitting code can be found at the P. Bosted's website [141].

At the time when this empirical fit was performed, limited inelastic inclusive electron-^{27}Al data were available in the same kinematic region as Q_{weak}. The authors of the empirical fit specifically expressed caution about its validity at lower Q^2 [140]. However, more recently comparison were performed between this fit and newly released low Q^2 inelastic electron-^{27}Al scattering data that was made available in a conference proceedings [142]. The results from this study are documented in the ELOG [143]. That comparison confirmed the conclusions drawn by the authors of the fit; the fit performs well in the $N \to \Delta$ section of the inelastic spectrum but generally disagrees in the quasi-elastic region at the 5–10 % level. Using the results from that comparison, a 10 % (relative) uncertainty was applied to yields extracted from the simulations using the quasi-elastic piece of this empirical fit.

No previous parity-violating quasi-elastic asymmetry measurements have been conducted with an aluminum target at forward-angle kinematics. Alternative methods for determining this background asymmetry were required. Working in collaboration with C. J. Horowitz and Z. Lin at Indiana University, a model-derived estimate of the quasi-elastic background asymmetry (A_{quasi}) was determined at Q_{weak} kinematics.

They employed a relativistic Fermi gas (RFG) model from a previous calculation that was performed on ^{12}C at backward angles [144]. According to C. J. Horowitz, the model does a decent job at predicting the quasi-elastic asymmetry, but a poor job at predicting the cross section [145]. With that limitation in mind, an acceptance averaged quasi-elastic asymmetry from that model was calculated to be $A_{quasi} = -0.338$ ppm [145, 146].

The estimate from the RFG model agrees well with the free nucleon quasi-elastic asymmetry estimate, which is calculated as the cross section weighted average of the respective elastic parity-violating asymmetries from the number of nucleons in the ^{27}Al nucleus [146]. However, both the RFG model and free nucleon asymmetry calculations fail to completely account for nuclear medium effects, such as final state interactions (FSI) and meson-exchange currents (MEC). The authors of a similar and separate calculation performed on a series of spin-0 nuclei, claim FSI effects only contribute at 1 % level to the

parity-violating quasi-elastic asymmetry at forward scattering angles [147]. C. J. Horowitz believes FSI effects on the cross section predicted by the RFG model could be on the order of 15–20 % [145]. Based on his insight, a conservative 50 % (relative) uncertainty was placed on the RFG model asymmetry estimate in an effort to account for these nuclear medium effects, which gives $\delta A_{quasi} = 0.169$ ppm.

In summary, an empirical fit to world cross section data is used in QwGeant4 to determine detector yields that are then used to calculate a quasi-elastic background fraction and the acceptance-averaged quasi-elastic background asymmetry was then determined from a RFG model. These contributions for the aluminum analysis are determined to be

$$f_{quasi} = 12.77 \pm 1.22 \text{ \%}, \tag{5.22}$$

$$A_{quasi} = -0.338 \pm 0.169 \text{ ppm}. \tag{5.23}$$

5.4.2 Inelastic Scattering

The background fraction piece of the inelastic $N \to \Delta$ process was calculated using the same method as discussed in Section 5.4.1 for the quasi-elastic background. Instead of the using the quasi-elastic piece of the empirical fit to world data, the inelastic $N \to \Delta$ piece was used to calculate acceptance-averaged yields and the $N \to \Delta$ background fraction.

The uncertainty on these yields was determined during the same low Q^2 fit-to-data comparison discussed for the quasi-elastic background section. At the invariant mass (W) of the $\Delta(1232)$, the comparison showed agreement at the 5 % level [143]. However, in the higher invariant mass region, the disagreement increased to about 10 %. A conservative uncertainty of 10 % was placed on simulation extracted $N \to \Delta$ yields in order to match this disagreement seen in the inelastic region and the uncertainty placed on the quasi-elastic background.

During Wien 7 of Run 2, a period of data taking was dedicated to measuring the asymmetry at the $N \to \Delta$ peak, which is accessed by reducing the current of QTOR from 8900 A to 6700 A. At this lower current, the spectrum of inelastic scattered electrons was focused on the main detector array, allowing a measurement of this $N \to \Delta$ asymmetry.

Four runs taken during that time used the ^{27}Al target in an effort to measure this inelastic asymmetry from the ^{27}Al nucleus. These were runs 14 337, 14 338, 14 364, and 14 365. Since only this limited amount of data is available, any extracted asymmetry is statistically limited. However, these data can be used to determine the inelastic background asymmetry diluting the elastic ^{27}Al measurement, with a few assumptions.
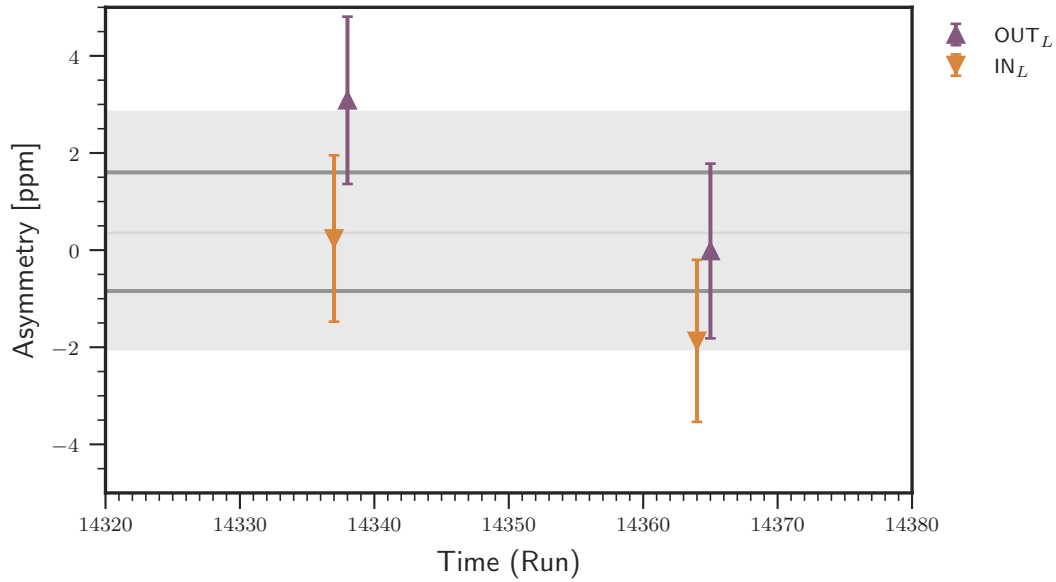
(a) IHWP plot
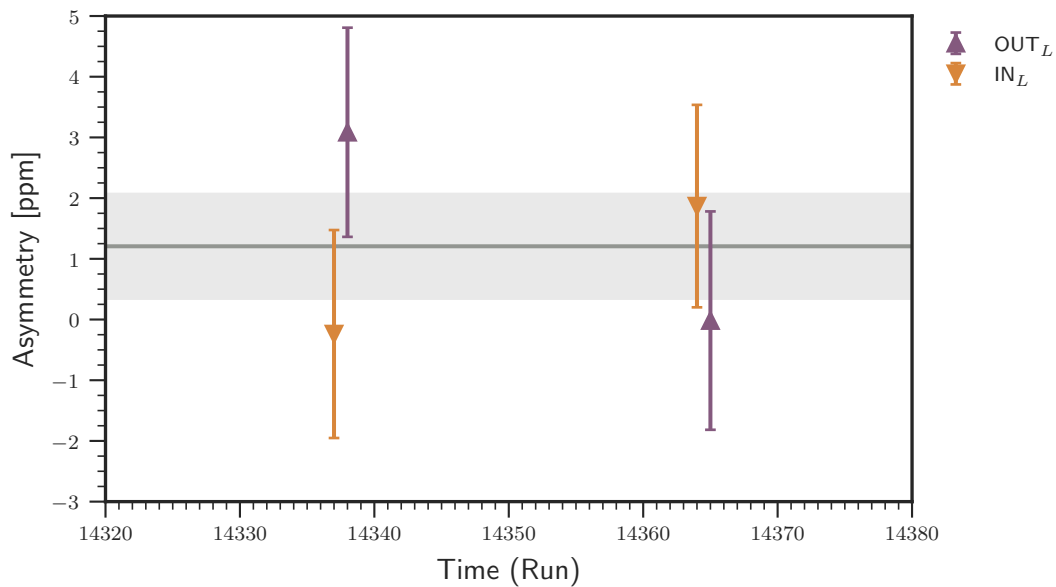
(b) Sign-corrected plot

Figure 5.8: Regressed asymmetry plots for the ^{27}Al $N \rightarrow \Delta$ data set.

A run-averaged asymmetry was extracted from these four runs, using the same analysis technique as that used on elastic aluminum data set [148]. Results from that analysis are shown in Fig. 5.8. The averaged regressed asymmetries for the various combinations of IHWP are given in Table 5.9.

Table 5.9: $N \to \Delta$ regressed aluminum asymmetry run-based time averaging statistics, using regression set "on". The labels IN and OUT refer to the IHWP state asymmetries. The NULL and PHYS labels refer to the respective unweighted-average and sign-corrected weighted-average of the IN and OUT asymmetries.

Quantity	Asymmetry [ppm]	χ^2/DOF	χ^2 Probability
IN	-0.843 ± 1.195	0.78	0.378
OUT	1.600 ± 1.244	1.55	0.213
NULL	0.379 ± 0.862	–	–
PHYS	1.206 ± 0.862	0.84	0.472

A final $N \to \Delta$ asymmetry at 6700 A would require additional efforts to determine its various systematic uncertainties. However, this result can be used to determine an inelastic background correction asymmetry (A_{inel}) with a few minor corrections. First is a beam-polarization correction, which was determined to be $P = 88.60 \pm 0.55\,\%$ during that period of inelastic running [137]. Applying this correction shifts the averaged regressed asymmetry to $1.362 \pm 0.973\,\mathrm{ppm}$.

Assuming the $N \to \Delta$ asymmetry evolves with Q^2 to first order, A_{inel} can be determined by applying a Q^2 scaling factor in the following way

$$A_{inel} = \frac{Q^2_{8900}}{Q^2_{6700}} A_{inel}^{6700},\tag{5.24}$$

where Q^2_{8900} and Q^2_{6700} are the momentum transfers at 8900 A and 6700 A, and A_{inel}^{6700} is the polarization corrected $N \to \Delta$ asymmetry extracted from data at 6700 A.

Momentum transfers used to calculate this scaling factor were determined in QwGeant4 with the Bosted-Mamyan inelastic generator for both of the QTOR current settings. The main detector averaged Q^2 from these simulations was determined to be $0.0238\,\mathrm{GeV}^2$ for 6700 A and $0.0281\,\mathrm{GeV}^2$ for 8900 A. Simulation uncertainties associated with these values are below $0.2\,\%$ (relative). Taking the ratio of these momentum transfers yields a scaling

factor of 1.1815. Applying this scaling factor to the measured asymmetry yields an inelastic background asymmetry of $A_{inel} = 1.609 \pm 1.149$ ppm, where the uncertainty is dominated by the statistics of the measured asymmetry [148]. This is a 71 % precision determination of the inelastic background asymmetry.

Future effort should be dedicated to reducing the uncertainty associated with this background asymmetry, as it is the largest in the aluminum analysis. Since a majority of the other background corrections employ theoretically-derived values, a theoretical calculation of this asymmetry could be used in a future analysis. Reviewing the literature, a previous calculation of the $N \rightarrow \Delta$ asymmetry was performed for the ^{12}C nucleus, at kinematic regions outside of the Q$_{weak}$ experiment, with a relativistic Fermi gas model [149]. In a similar fashion to the model used to determine the quasi-elastic background asymmetry, this Fermi gas model does not include nuclear medium effects, such as FSI and MEC. Any future calculation performed with such a model could be compared with the measured and scaled asymmetries in an effort to confirm the scaling assumptions used in this analysis. Additional, this comparison might allow a dramatic reduction in the size of the uncertainty on the background asymmetry.

To summarize, the same empirical fit used to determine the quasi-elastic background fraction has been applied here for the inelastic background and a kinematically scaled measurement of the $N \rightarrow \Delta$ ^{27}Al asymmetry has been used to calculate a background asymmetry. A correction for the inelastic $N \rightarrow \Delta$ background† has been made with

$$f_{inel} = 7.39 \pm 0.74 \text{ \%}, \tag{5.25}$$

$$A_{inel} = 1.609 \pm 1.149 \text{ ppm}. \tag{5.26}$$

†Late in the analysis of this background contribution, the realization was made that additional corrections are needed for the radiative elastic tail and quasi-elastic contributions before the inelastic asymmetry can be Q scaled to the elastic peak. To perform this extra analysis step, background fractions from those pieces have to be determined in simulation. Once the corrections are included, the central value and uncertainty of this inelastic background correction will change, directly effecting the final result of this analysis. This task is left as a future improvement.

5.4.3   Discrete Nuclear Excited States

Focusing first on the determination of the background signal fraction, a model is needed for the cross sections from the spectrum of possible ^{27}Al discrete excitations. These cross sections are used in the formation of a event generator in QwGeant4. Aluminum is a fairly ubiquitous material that has been studied many times before in electron scattering experiments. In particular two previous experiments have looked at the electroexcitation of these discrete states in the ^{27}Al nucleus in a comparable kinematic region as that of the Q_{weak} experiment. The first of these experiments was conducted at the Kelvin Laboratory, Glasgow, UK in the mid 1970s [150]. The second, more recent, experiment was conducted at MIT Bates Laboratory, Middleton, MA in the late 1980s [151, 152]. Both experiments used an electron beam in a fixed target setting to excite the nucleons of the ^{27}Al nucleus to these higher energy states. The main result of both these endeavours are determinations of the electromagnetic form factors from cross section measurements of these discrete excited state scattering. These extracted form factors happen to be in a momentum transfer range that matches well with Q_{weak}'s kinematic acceptance. Thus a simple Gaussian function fitted to these data was used to model the momentum transfer evolution of these form factors in a first Born approximation calculation of their cross sections.

Referenced in the later MIT Bates publication [152] is a supplemental document containing a tabulation of all the measured cross sections and their corresponding extracted form factors from each of the discrete excited states measured by the MIT Bates experiment. These tabulated data can be found in the American Institute of Physics, Physics Auxiliary Publication Service archives [153]. The data from the Glasgow experiment is tabulated in Table 2 of that publication [150].

Combing the extracted form factors from both sources, there are data on 37 of the most strongly populated discrete excited states, ranging in energy from 0.844 MeV to 8.820 MeV. Subsequent measurements using other nuclear diagnostic methods have shown ^{27}Al to have many more excited states [38]. However, as background corrections are only needed for scattering from the most probable states, only data from the MIT Bates and Glasgow electroexcitation experiments are considered in the determination of cross sections for this
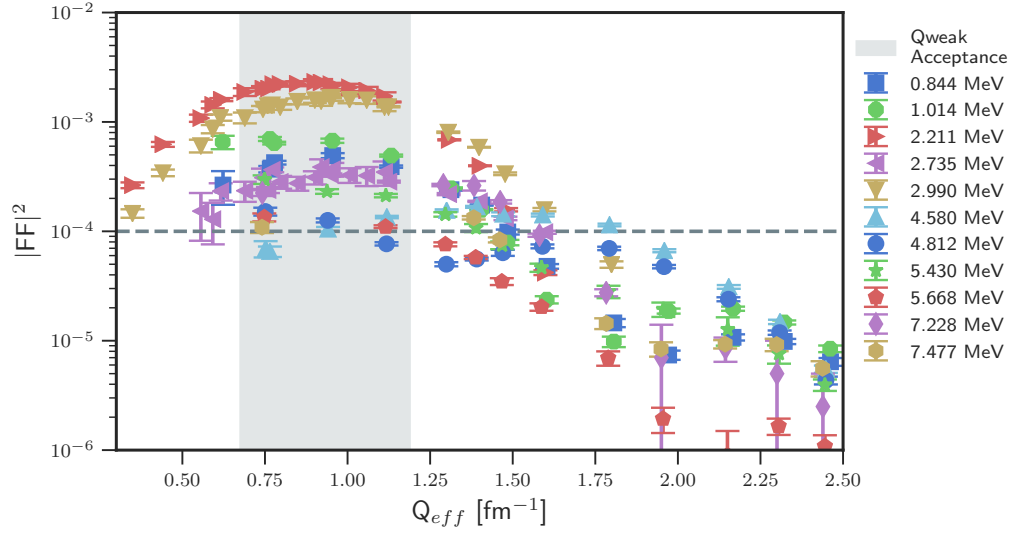
Figure 5.9: Extracted form factors for the 11 most probable discrete excited states from the MIT Bates experiment [153]. Q_{weak}'s momentum transfer acceptance is given in the grey shaded region. The dashed line is the 10^{-4} cutoff imposed on the data set.

analysis.

Making 37 individual background corrections for all measured discrete excited states is not necessary. Depending on the size of the form factor, the inclusion of additional states starts to yield diminishing returns in terms of the size of their background correction contribution. Thus to simplify the analysis, a cut-off of 10^{-4} was placed on the magnitude of the measured form factor data, which matches the assumption made in the elastic scattering cross section calculation by Horowitz in Section 3.2.2. Any excited states with extracted form factors larger than 10^{-4} within the Q_{weak} momentum transfer acceptance were considered, while the rest were excluded. This cut reduced the number of discrete states from 37 to 11. The energy levels of these remaining states are: 0.844 MeV, 1.014 MeV, 2.211 MeV, 2.735 MeV, 2.990 MeV‡, 4.580 MeV, 4.812 MeV, 5.430 MeV, 5.668 MeV, 7.228 MeV, and 7.477 MeV. Figure 5.9 shows a comparison of these 11 considered states with the Q_{weak} momentum transfer acceptance.

---

‡This state is an unresolved doublet of the 2.981 MeV and 3.004 MeV excited states. The energy resolution of the MIT Bates experiment prevented their separation and are thus treated as a single state [152].

The form factors were modeled with a simple Gaussian function written as

$$F(Q, c, \mu, \sigma) = ce^{-\frac{(Q-\mu)^2}{2\sigma^2}}, \tag{5.27}$$

where c is a multiplicative constant, μ the mean of the Gaussian distribution, and σ is the standard deviation (width) of that distribution. A non-linear least squares method, called scipy.optimize.curve_fit from the Python SciPy [154] package, was used to perform the fitting for each of the selected excited states. The best fit values were determined with a χ^2 minimization routine included in that Python package. Only data between $0.3\,\mathrm{fm}^{-1}$ and $1.8\,\mathrm{fm}^{-1}$ for each of the excited states are considered in a given fit. This reduced fit range allowed for better modeling of the form factor over the momentum transfer range of interest to this analysis. It also avoided the requirement for more sophisticated modeling that would be needed to account for the diffractive minimum present in most of the selected excited states at higher momentum transfer.

An example of this modeled data, for the largest contributing excited state, can be seen in Fig. 5.10. In that figure, the $2.211\,\mathrm{MeV}$ state data from both the MIT Bates and Glasgow experiments are plotted along with the Gaussian fit function over the range previously mentioned. The Q_{weak} momentum transfer range of interest is indicated by the grey shaded region. Visual comparisons of data to fits for the other 10 considered excited states can be seen in Appendix B.6. Parameters extracted from the 11 fits are tabulated in Table 5.10.

The fitting routine also returns a covariance matrix that can be used to calculate the uncertainty in the fit using the general propagation of uncertainty formula [155]. This calculation yields a function that can be used to determine the uncertainty for a given value of momentum transfer. Figure 5.11 provides an example of this uncertainty function for the $2.211\,\mathrm{MeV}$ state. The data used in those fits only included statistical uncertainties and thus many of the fits had poor χ^2 values and probabilities. In a conservative effort to account for these poor fit metrics, a scaling factor of $(\chi^2/DOF)^{\frac{1}{2}}$ was applied to the fit uncertainties [9]. The last column in Table 5.10 gives the scaled uncertainties at the average momentum transfer $(Q = 0.778\,\mathrm{fm}^{-1})$ for each of the considered excited states. Further details about these fits and their uncertainties can be found in the ELOG [156].
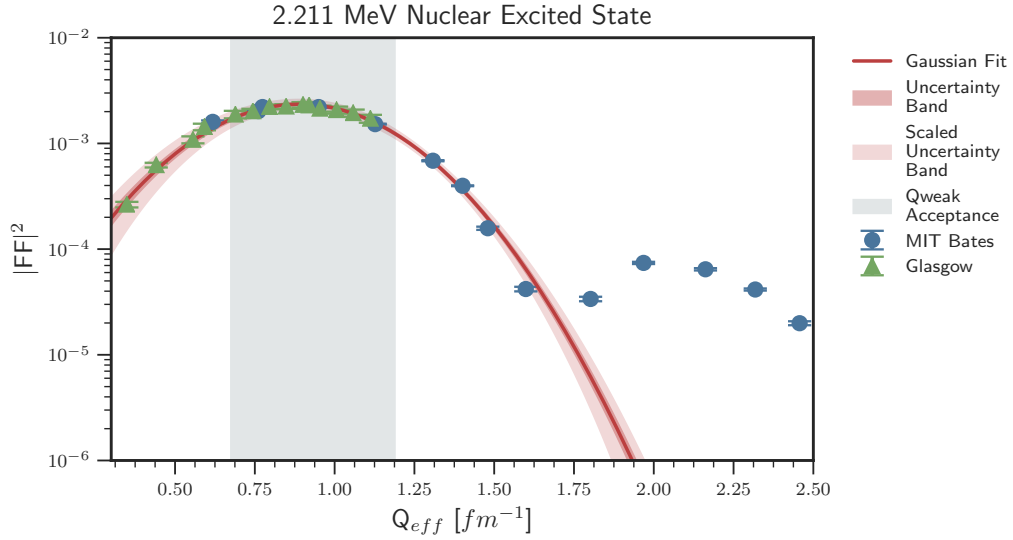
Figure 5.10: Gaussian function fitted to ^{27}Al's 2.211 MeV excited state form factor data.

Parity-violating asymmetries associated with these excited states are unknown, so estimates are used in this analysis. Following the advise of C. J. Horowitz, from his publication motivating this analysis [40], asymmetries for the discrete excited states are expected to be on the order of the elastic ^{27}Al asymmetry. However, C. J. Horowitz specifically mentions two important points regarding the asymmetry for these states. The first is that at forward angles, he expects these asymmetries to be dominated by Coulomb multipole terms. Secondly, the sign of the asymmetry depends on whether the excited state transition is isoscalar $(+A_{PV})$ or isovector $(-A_{PV})$.

In this analysis, the magnitudes of the excited state asymmetries are calculated in QwGeant4 with Eq. (3.44), which sets the scale of the asymmetry at approximately that of the calculated elastic asymmetry from Horowitz's model, or approximately 2 ppm. The variations between these asymmetries are due to the differences in the excited states' acceptance-averaged momentum transfers used in these calculations. The isospin of these excited states are also not well known, as indicated by the Table of Isotopes [38]. Traditionally, the isospins of these transitions are identified by performing a comparison between the energies and spin-parity states of the discrete excitation spectra of fellow nuclear isobars [139]. Examples for a comparison to ^{27}Al would be either ^{27}Mg or ^{27}Si nuclei; such a comparison has already been performed with these nuclei. Isospins for the states in ^{27}Al were assigned based

Table 5.10: Extracted Gaussian fit parameters for the 11 considered excited states. Uncertainties given in the last column are relative and include the scaling factor.

Energy Level [MeV]	c	μ [fm^{-1}]	σ [fm^{-1}]	Uncertainty (scaled) [%]
0.844	0.000 478	0.9600	0.3072	15.89
1.014	0.000 719	0.9049	0.2815	24.60
2.211	0.002 351	0.8895	0.2647	11.49
2.735	0.000 318	0.9615	0.4139	8.15
2.990	0.001 665	0.9577	0.2999	6.31
4.580	0.000 159	1.3896	0.4825	12.15
4.812	0.000 230	0.2536	0.5944	26.85
5.430	0.000 269	0.7793	0.4466	18.42
5.668	0.000 137	0.8912	0.3636	18.31
7.228	0.000 356	1.0592	0.3218	35.92
7.477	0.000 210	1.0785	0.2994	75.08

on the recommended upper limits of gamma-ray emission studied with nuclear spectroscopy techniques [157, 158]. All excited states considered in this analysis are believed to be predominately isoscalar transitions ($\Delta T = 0$) from the ^{27}Al ground state and are thus assigned a positive asymmetry [159].

Uncertainty in the sign of that asymmetry primarily comes from isospin mixing effects that occur during these excitations. Horowitz warns that transitions of mixed isospin would have an asymmetry somewhere in-between the positive and negative bounds set by Eq. (3.44). This warning was also echoed by the author who performed the original isobar comparison [157, 158]. Effects of isospin mixing on asymmetries measured in ^{12}C have been explored previously [51]. The formalism developed in that publication to determine the size of these effects has not been applied in this analysis, but could be investigated in the future for completeness. Combining the results from the nuclear isobar comparison with the belief that the excited states are dominated by Coulomb multipoles at these kinematics, conservative uncertainties of 50 % (relative) are applied to simulation-extracted excited state asymmetries.

Calculated background fractions and acceptance-averaged asymmetries for each of the 11 states considered are tabulated in Table 5.11 with their uncertainties.
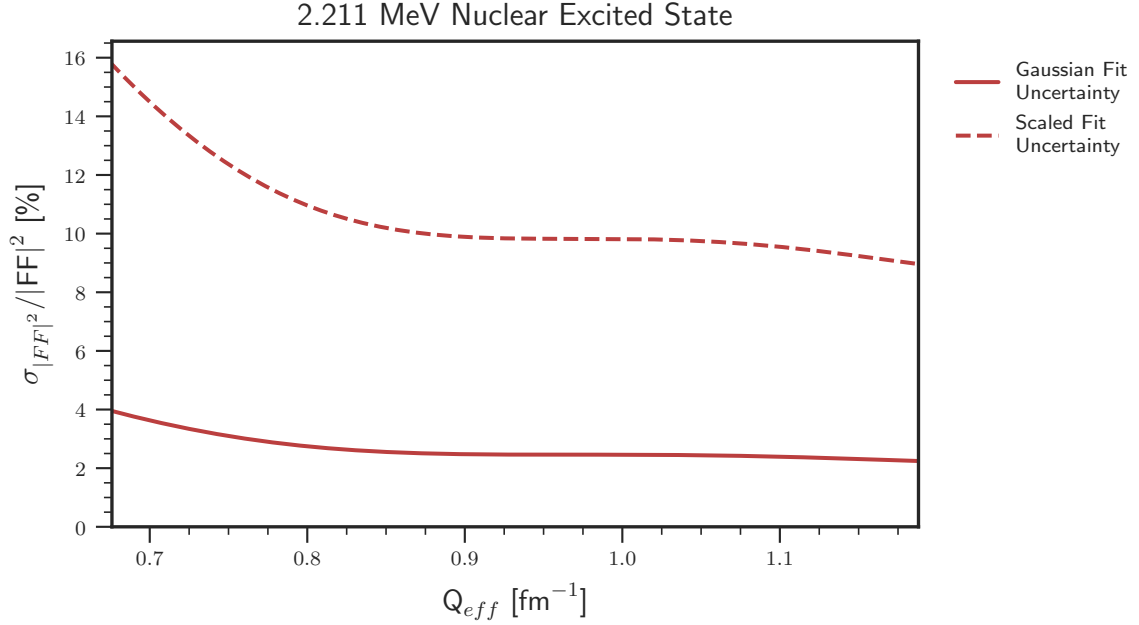
Figure 5.11: Calculated fit uncertainty (relative) for 2.211 MeV excited state. Uncertainty assigned to simulation extracted yields taken from average Q value of the scaled uncertainty curve.

5.4.4   Giant Dipole Resonance

The background fraction piece of the correction for the Giant Dipole Resonance (GDR) was taken from a Goldhaber-Teller model calculation of the cross section [160], where the proton distribution is assumed to oscillate out of phase with the neutron distribution. In addition, the model also assumes the nucleons are spherically distributed inside of the nucleus, which is not the case for the ^{27}Al nucleus. That calculation gives the GDR cross section as a multiplicative factor on the elastic cross section, written as

$$\left(\frac{d\sigma}{d\Omega}\right)^{L+T}_{GDR} \bigg/ \left(\frac{d\sigma}{d\Omega}\right)_{el} = \left(\frac{N^2\hbar^2\Delta^2}{2\mu A^2 \hbar\omega}\right) + \left(\frac{N^2\hbar\omega}{2\mu A^2 c^2}\frac{(1+\sin^2\frac{\theta}{2})}{\cos^2\frac{\theta}{2}}\right), \tag{5.28}$$

where the first term in the sum is the longitudinal polarization component and the second is the transverse polarization component of the mediating photon, N is the number of neutrons, A is the atomic mass, $\mu = (NZ/A)M$ is the reduced mass of the system, Δ is the 3-momentum of the mediating photon, and $\hbar\omega$ is the energy of the GDR excitation. From that expression it is easy to see that the longitudinal term dominates at forward angles.

Table 5.11: Simulation extracted background fractions and asymmetries for the discrete excited states in the aluminum target material.

Energy Level [MeV]	Background Fraction (f_i) [%]	Asymmetry (A_i) [ppm]
0.844	0.27 ± 0.04	2.619 ± 1.310
1.014	0.41 ± 0.10	2.563 ± 1.282
2.211	1.35 ± 0.16	2.543 ± 1.271
2.735	0.19 ± 0.02	2.590 ± 1.295
2.990	0.93 ± 0.07	2.617 ± 1.308
4.580	0.06 ± 0.01	2.783 ± 1.392
4.812	0.09 ± 0.02	2.379 ± 1.189
5.430	0.17 ± 0.03	2.490 ± 1.249
5.668	0.08 ± 0.02	2.542 ± 1.271
7.228	0.18 ± 0.06	2.706 ± 1.353
7.477	0.10 ± 0.07	2.753 ± 1.377

The implementation of this cross section into QwGeant4 relies upon a value for the GDR excitation energy, which was taken to be 20.8 MeV as measured from a total photoabsorption experiment performed on ^{27}Al [161, 162]. It is important to note that Eq. (5.28) is not integrated over the entire GDR energy spectrum. The finite energy width of the GDR excitation is not taken into account in that expression. To account for this effect, a factor of 9 MeV representing the width [161] of the GDR excitation energy spectrum was used to scale the calculated cross section in QwGeant4 [163].

The parity-violating asymmetry for the GDR is not known at all. Again, following the advice noted in C. J. Horowitz's aluminum publication [40], the magnitude of the GDR asymmetry is calculated with Eq. (3.44). However, this excitation is known to be an isovector transition ($\Delta T = 1$), thus the calculated asymmetry is assumed to be negative [40].

Information about cross section uncertainties come directly from the Goldhaber-Teller model publication [160], where the authors discussed an observed disagreement between the model and their data at the 50 % level. Even though the model was compared with data taken at backward angles, the magnitude of their disagreement was adopted as a conservative uncertainty on the yields extracted from simulation for this correction. Uncertainty on the asymmetry was applied in a similar approach. Knowing that the GDR is primarily an isovector transition, uncertainty from isospin mixing is probably minimal here, but could be checked with more sophisticated models in the future. Also the GDR is a non-destructive

collective excitation, the spherically symmetric asymmetry assumption probably is not that far off from reality. However, a conservative uncertainty of 50 % (relative) is also applied to the asymmetry.

Extracted from simulation, the background fraction and asymmetry for this GDR process are determined to be

$$f_{GDR} = 0.578 \pm 0.29 \text{ \%},\tag{5.29}$$

$$A_{GDR} = -2.217 \pm 1.108 \text{ ppm}.\tag{5.30}$$

5.4.5 ^{27}Al Alloy Elements

As discussed in Section 4.5.1 the material used for the aluminum target was an alloy containing high-Z elements in concentrations as high as almost 6.0 wt% (% by weight). The presence of these alloy elements leads to backgrounds that require correction before the pure elastic aluminum asymmetry can be extracted.

Working again in collaboration with C. J. Horowitz and Z. Lin, elastic cross sections and parity-violating asymmetries were calculated for six of the most common naturally occurring isotopes of the elements found in the aluminum target material [164, 165]. These calculations were performed at forward-angles for a beam energy of $E = 1.16$ GeV with a relativistic mean field model, similar to the one used by C. J. Horowitz for his calculation of ^{27}Al [40]. In particular, these calculations included Coulomb distortions (distorted-wave) but assumed spherically symmetric proton and neutron densities, thus only the C0 multipole terms were included [164]. High-order multipole terms were not considered in these calculations. Cross section and asymmetry curves from these calculations are plotted in Fig. 5.12 and Fig. 5.13, respectively.

Tabulated output from these calculations was used to construct custom cross section and asymmetry generators in QwGeant4 (labeled generators 2750–2755). An interpolation routine was used to select cross section and asymmetry values within the bounds of the tabulated data tables based on a randomly selected scattering angle θ for each thrown Monte Carlo event, which are then propagated through the Q$_{\text{weak}}$ apparatus with the radiation transport routines built into Geant4.
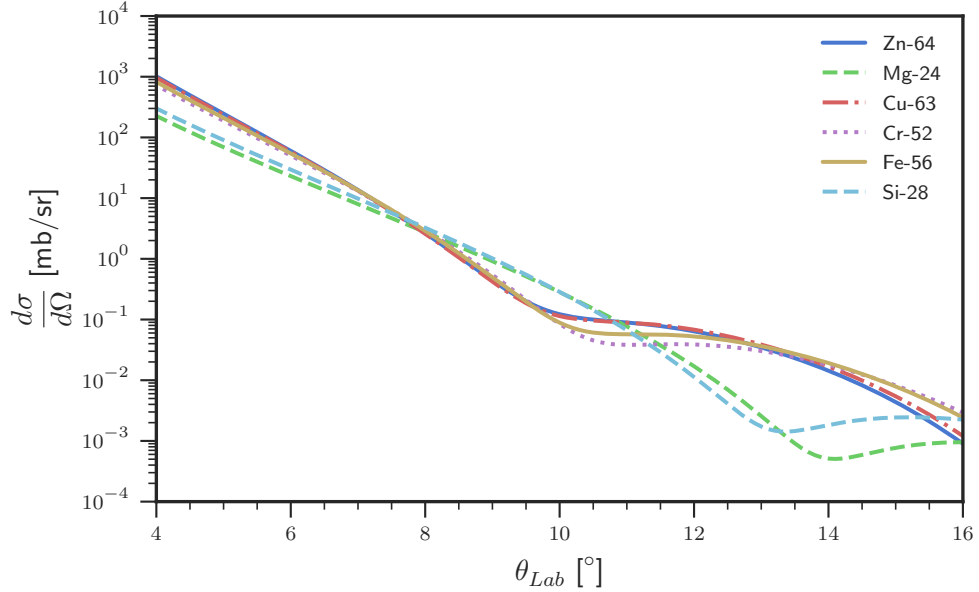
Figure 5.12: Forward-angle distorted-wave elastic electron cross sections calculated for the six largest composition by weight alloy elements in the aluminum target. Calculation performed at $E = 1.16\,\text{GeV}$ with RMF model. Curves generated from data tables given by C. J. Horowitz [164, 165].

Calculations of cross sections and asymmetries for the smallest contributions of manganese and titanium in the alloy were not considered by Horowitz. Separate methods were used to determine cross sections and asymmetries for these contributions. Using legacy code, cross sections for the manganese and titanium contribution were calculated with different form factor parameterizations [166]. Fourier-Bessel coefficients from earlier electron scattering cross section measurement made on titanium, tabulated in the Atomic Data and Nuclear Data tables [111], were used in an inverse Fourier transform parameterization of its form factor. Scaling the form factor by the Mott cross section, given in Eq. (3.10), gave an estimate of titanium's cross section over the Q_{weak} acceptance in QwGeant4 simulations. Similarly, a cross section estimate for manganese was calculated with a simple Uniform Gaussian form factor model [111]. Estimates of their asymmetries are given by the symmetric Born asymmetry in Eq. (3.44).

In QwGeant4, concentrations of the alloy elements are taken into account in two places. The first is in the material definition of the aluminum target and the second is in the calculation of the luminosity. The most important of these two is the latter, as the luminosity
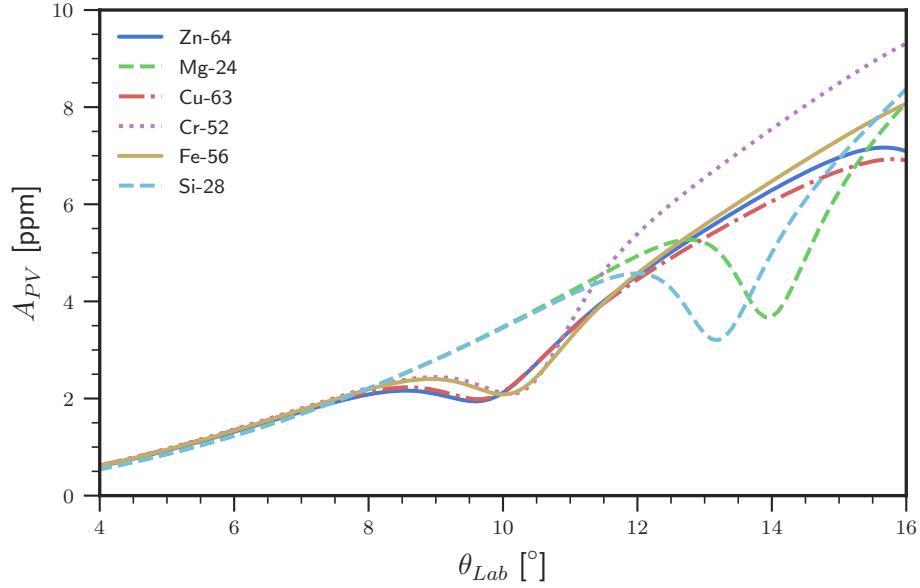
Figure 5.13: Forward-angle distorted-wave elastic electron parity-violating asymmetries for the six largest composition by weight alloy elements in the aluminum target. Calculation performed at $E = 1.16\,\mathrm{GeV}$ with RMF model. Curves generated from data tables given by C. J. Horowitz [164, 165].

(L) is used in the calculation of the rates and yields extracted from the simulation [138]. Concentrations (C_i) for a given alloy element, from Table 4.7, are used to scale L in the following way

$$L_i = C_i \frac{\rho_A N_A N_B}{M_A} = C_i L_{\text{Al-alloy}}, \tag{5.31}$$

where ρ_A is the areal density of the aluminum alloy target, N_A is Avogadro's number, N_B is the flux of particles in the beam, and M_A is the average mass of the target nucleus.

Combining the cross section and asymmetry generators with the implemented concentration information, QwGeant4 simulations allowed determination of the acceptance averaged detector yields and asymmetries measured from each of these elements in the aluminum target. Knowledge of these yields, in combination with the rest of the scattering backgrounds, allowed the determination of their background fractions.

Uncertainties in the acceptance-averaged yields and asymmetries extracted from simulation are believed to be dominated by model uncertainties. Simulation-extracted yields from C. J. Horowitz's zinc, magnesium, copper, chromium, iron, and silicon calculations were given a conservative 10 % (relative) uncertainty. Asymmetries from those calculations

were given 50 % (relative) uncertainty, because they assumed spherically symmetric nucleon densities for nuclei that are known to have a more complex structure. In addition, most of the high-Z alloy elements have a diffractive minimum occurring in the middle of the Q_{weak} acceptance, where high-order multipole contributions are important to get the correct value of the asymmetry. For manganese and titanium cross section and asymmetry models, conservative relative uncertainties of 50 % were applied to both yields and asymmetries. Uncertainty contributions from simulation statistics and assayed alloy compositions are considered negligible compared to the applied model uncertainties, thus they are not included in the quoted uncertainties. To further reduce the uncertainty on these alloy element contributions, additional effort would have to be put into an investigation to see how well C. J. Horowitz's models agree with historical cross section measurements.

Calculated background fractions and acceptance averaged asymmetries, extracted from simulation, are tabulated in Table 5.12 with their model uncertainties.

Table 5.12: Simulation extracted background fractions and asymmetries for the alloy elements present in the aluminum target material.

Element	Background Fraction (f_i) [%]	Asymmetry (A_i) [ppm]
Zn	2.375 ± 0.249	1.815 ± 0.908
Mg	2.088 ± 0.219	2.013 ± 1.006
Cu	0.683 ± 0.073	1.857 ± 0.929
Cr	0.100 ± 0.011	1.920 ± 0.960
Si	0.080 ± 0.009	1.984 ± 0.992
Fe	0.054 ± 0.006	1.883 ± 0.941
Mn	0.018 ± 0.009	2.343 ± 1.172
Ti	0.014 ± 0.007	2.148 ± 1.074

5.4.6 Neutral Particles

Neutral particles, such as gamma-rays, neutrons, and neutral pions produced in secondary reactions in the apparatus occasionally enter the acceptance of the experiment. They are believed to originate from beamline elements and edges of the collimators. Data recorded during event-mode running allowed the determination of a background fraction from these neutral events. In addition, simulations with QwGeant4 allowed for an estimate of the size of asymmetry these neutral particles carried. Details about this analysis are discussed at

length in a technical report [167].

During that investigation, a background correction and asymmetry estimate was determined specifically for the aluminum data set. Taking the values from that analysis, the corrections for the neutral background in the aluminum data set are

$$f_{neutral} = 0.00 \pm 0.45 \text{ \%}, \tag{5.32}$$

$$A_{neutral} = 1.7 \pm 0.2 \text{ ppm}. \tag{5.33}$$

It is important to note that the neutrals analysis attempts to avoid double counting the beamline background asymmetry correction already applied in this analysis by imposing a sum rule between the fraction of total neutral events, the fraction from beamline background, and the fraction noted here. During the neutrals investigation, this assumed sum rule was shown not to hold for the aluminum data. Details about this sum rule violation are discussed in the neutrals background technical report [167]. However, to ensure the numbers extracted from this analysis were not inconsistent with similar analyses conducted for other data sets, conservative uncertainties were applied to the neutrals background fraction for the aluminum data set.

5.4.7   Pions

With a beam energy of 1.16 GeV and an energy acceptance of approximately 150 MeV, the possibility of a substantial pion background is highly unlikely due to the pion threshold. However, to ensure this background was not an issue for the aluminum data set, yield simulations were performed with a pion generator in QwGeant4. That generator was based on the Wiser pion cross section fitting code [116, 168, 169], written to produce cross sections from pion production data taken on light nuclear targets at the Stanford Linear Accelerator, at much higher beam energies. That code allowed cross section calculations from both the nucleons in the nucleus, thus an estimate for ^{27}Al was made using a nucleon scaling argument, which neglected nuclear medium effects. The background fraction from this rough estimate was determined to be $f_{pion} = 0.06\,\%$, which is negligible compared to the rest of

the backgrounds, even with a large conservative uncertainty. Based on this estimate, a pion correction was not included in this analysis.

5.5 Multiplicative Radiative and Acceptance Corrections

After correcting the measured asymmetry for background physics processes, the extraction of the final asymmetry required a multiplicative correction called R_{tot}. R_{tot} is constructed from the product of four separate corrections written in the form

$$R_{tot} = R_{acc} R_{det} R_{rc} R_{Q^2},\tag{5.34}$$

where R_{acc} is a finite asymmetry acceptance correction, R_{det} is a correction for position dependence in detector light collection, R_{rc} is a correction for electromagnetic radiative effects, and R_{Q^2} is a momentum transfer uncertainty correction. This section discusses how each of these terms was determined for the aluminum data set.

5.5.1 Acceptance Correction

The background-corrected measured asymmetry represents an asymmetry average taken over a range of momentum transfers in the acceptance of the apparatus. Simulation was used to correct this averaged asymmetry to an asymmetry quoted at an averaged momentum transfer, using

$$R_{acc} \equiv \frac{A(\langle Q^2 \rangle)}{\langle A(Q^2) \rangle},\tag{5.35}$$

where $A(\langle Q^2 \rangle)$ is the theoretical asymmetry reported at the average momentum transfer of the experiment and $\langle A(Q^2) \rangle$ is the simulation determined acceptance-averaged asymmetry over the range of momentum transfers in the acceptance.

In QwGeant4, a custom cross section and asymmetry generator (generator 2700) based on C. J. Horowitz's theoretical calculation of elastic aluminum scattering introduced in Sections 3.2.2 and 3.3.2, was used to calculate $\langle A(Q^2) \rangle$. A main detector averaged value of $\langle A(Q^2) \rangle$ was determined to be 2.0812 ± 0.0006 ppm, where the quoted uncertainty was from simulation statistics only.

$A(\langle Q^2 \rangle)$ was calculated from a Q^2 interpolation of the theoretical elastic aluminum asymmetry, introduced in Eq. (3.46), from data tables given by C. J. Horowitz [44, 165]. Using a simulation acceptance and detector averaged $\langle Q^2 \rangle$ of $0.2357 \pm 0.0010\,\mathrm{GeV}^2$ [170] as input into the interpolation, $A(\langle Q^2 \rangle)$ was determined to be 2.0728 ppm. The uncertainty on $\langle Q^2 \rangle$ was not propagated to $A(\langle Q^2 \rangle)$ in an attempt to avoid double counting momentum transfer uncertainties accounted for in other corrections.

Taking the ratio of $A(\langle Q^2 \rangle)$ to $\langle A(Q^2) \rangle$ yields R_{acc}, which was calculated to be 0.9960. Uncertainty in that value comes primarily from the model uncertainty in C. J. Horowitz's theoretical asymmetry calculation, but also from simulation statistics. Model uncertainty in C. J. Horowitz's calculation is explored with the ξ parameter discussed in Section 3.3.2. The model uncertainty for this analysis was determined by taking the percent difference of theoretical asymmetries calculated with the nominal $\xi = 1.0$ and the extreme bound of $\xi = 1.5$, at the average Q^2. This calculation yielded a relative model uncertainty of $0.38\,\%$. Applying and propagating these model uncertainties in the calculation of R_{acc}, yields a final uncertainty on R_{acc} of 0.0054. In summary, R_{acc} for the aluminum data set was determined to be

$$R_{acc} = 0.9960 \pm 0.0054. \tag{5.36}$$

5.5.2 Light-Weighting Correction

The magnitude of light output seen by either PMT on each of the Cherenkov detectors was found to be dependent on the position of the radiating electrons passing through the quartz. This position effect was additionally compounded by the presence of QTOR's magnetic field, which caused a correlation between the momentum transfer of the detected electrons and their detection location. During event mode, this correlation was investigated with the wire chambers and main detectors. A correction to the asymmetry, which depends on Q^2, was determined from these studies.

For the aluminum data set this correction, known as the light-weighting correction, was determined from an analysis performed on tracking data recorded from the aluminum target. Corrections for each main detector were calculated by taking the ratio of the average Q^2 values extracted from tracking-reconstructed momentum transfer distributions to the average
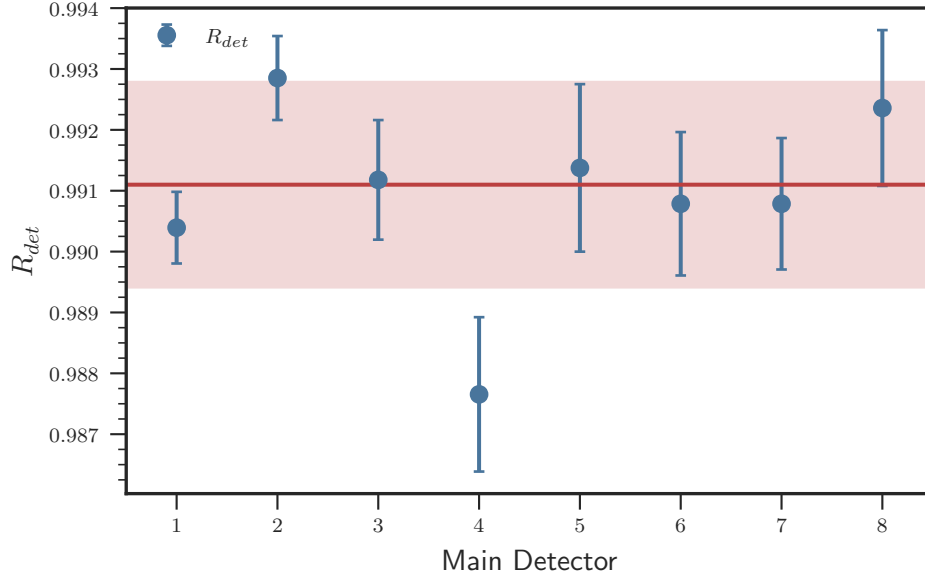
Figure 5.14: Unscaled light-weighting corrections for each of the main detectors. The red line gives the error-weighted average using the uncertainties on the points. The red uncertainty band gives total systematic uncertainty applied to the average.

Q^2 values weighted with the position-dependent PMT light responses (light-weighting). Since these are ratios of Q^2 values and the correction is for an asymmetry, the ratio was scaled by the slope of the asymmetry with respect to Q^2. The slope was determined to be 0.9706, see Section 5.5.4 for details about how this slope was calculated. Corrections for each of the main detectors without the slope scaling factor are plotted in Fig. 5.14.

The main detector average correction including the scaling factor was determined to be 0.9913, see reference [171, 172]. A relative uncertainty on this value of 0.17% was adopted from the similar analysis performed for the weak charge measurement. It includes contributions from PMT gain-matching, event selection cuts, tracking reconstruction bias due to wire chamber inefficiencies, and run-to-run noise variations [173]. R_{det} for the aluminum data set was thus determined to be

$$R_{det} = 0.9913 \pm 0.0017. \tag{5.37}$$

5.5.3   Radiative Correction

Electromagnetic radiative corrections are applied to the asymmetry as a multiplicative factor called R_{rc}. This correction accounts for depolarization effects of internal and external bremsstrahlung, and ionization that occurs in the target, as the electrons interact. Effects of radiative corrections on electromagnetic cross sections are well known and a formalism to correct for these effects have been developed by L. W. Mo and Y. S. Tsai [56, 57]. However, their effects on parity-violating asymmetry measurements are not as well known. Previous work on the subject has been done for large acceptance experiments such as the SAMPLE experiment [174] and the G0 experiment [175].

This analysis presently only includes a partial implementation of these types of corrections. In particular, the elastic cross section generator, including the alloy elements, and the discrete excited state generator included corrections for internal radiative effects using the formalism by L. W. Mo and Y. S. Tsai [56, 57, 176]. The rest of the generators are missing these internal corrections and should be included in future work. External radiative effects are assumed to be accounted for by radiation transport routines included in Geant4. Studies into these external effects in simulation seem to indicate that they are small [177].

As presently implemented, radiative effects only shift the momentum-transfer and asymmetry since they are weighted by cross section during their extraction from the simulation. The ratio of the weighted asymmetries with and without these radiative effect allows for the determination of R_{rc}. A series of simulations with the elastic generator were used to determine this preliminary correction, by turning on and off these effects. Details of this analysis are documented in the ELOG [177]. A preliminary R_{rc} correction was determined to be [177]

$$R_{rc} = 0.998 \pm 0.005, \tag{5.38}$$

where the uncertainty on that value was taken from the weak charge analysis [46].

This correction is considered only partially complete because of how well our simulation is believed to match measurement. Section 5.6 discusses this disagreement further. To briefly summarize, a tuning parameter called ΔE used in the L. W. Mo and Y. S. Tsai formalism needs to be properly determined for the experiment's acceptance. L. W. Mo and Y. S.

Tsai provide guidelines on how this tuning parameter should be chosen for traditional cross section measurements in their publication [56]. However, any effect from this disagreement has already been folded into this analysis by way of an inflated uncertainty, which is applied to the elastic yields used to calculate the background fractions, see Section 5.6.

5.5.4 Q^2 Uncertainty Correction

Traditionally, parity-violating asymmetry measurements have reported their momentum transfer uncertainty as an additional uncertainty on the asymmetry. This analysis elects to follow the same convention with the application of the R_{Q^2} correction for the aluminum data set.

Studies into the momentum transfer Q^2 and its uncertainty for the aluminum data set were conducted both with tracking data and Monte Carlo simulation. Following the precedent set by the weak charge measurement, the central Q^2 value for the aluminum data set was extracted from high-statistics QwGeant4 simulations. From those simulations, the main detector and acceptance averaged Q^2 was determined to be $\langle Q^2 \rangle = 0.023\,57\,\text{GeV}^2$ [170].

Uncertainty on that central value comes from a range of systematic effects which include: simulation statistics, beam properties, target properties, collimator geometry, QTOR properties, and main detector locations. Table 5.13 gives a list of these major sources of uncertainty, their relative effect on the central value, and additional references where more information about a given contribution can be found. The total combined uncertainty on Q^2 was determined to be $0.44\,\%$ (relative) [178]. Applying this relative uncertainty to $\langle Q^2 \rangle$, yields

$$\langle Q^2 \rangle = 0.02357 \pm 0.00010 \text{ GeV}^2. \tag{5.39}$$

To fold this relative uncertainty on Q^2 into an uncertainty on the aluminum asymmetry, the slope of the Q^2 dependence on the asymmetry was needed. C. J. Horowitz's theoretical aluminum asymmetry calculation, given in Eq. (3.46), was used to calculate the partial derivative of the aluminum asymmetry with respect to Q^2 [189]. Performing this calculation

Table 5.13: Major sources of relative uncertainty on momentum transfer Q^2 for the aluminum data set. An overview of the uncertainty analysis is given in the text. For further details about individual uncertainties see the ELOG [178] or the references given in the last column.

Source	Uncertainty [%]	Running Total [%]	Reference
Simulation Statistics	0.06	0.06	[179]
Raster Size	0.05	0.08	[180]
Beam Position	0.14	0.16	[178]
Target Thickness	0.00	0.16	[181]
Magnetic Field Strength	0.083	0.18	[182, 183]
Beam Energy	0.19	0.26	[178]
Target Z-Location	0.14	0.30	[184]
Magnetic Field Map	0.20	0.36	[185]
Main Detector Locations	0.072	0.37	[186]
Collimator Locations	0.24	0.44	[187, 188]
Collimator Imperfections	0.068	0.44	[188]
Total (quadrature sum)	–	0.44	[178]

yielded a slope term in the form of

$$\text{Slope } = \frac{\partial A}{\partial Q^2} \frac{Q^2}{A} = \frac{\partial A}{A} \bigg/ \frac{\partial Q^2}{Q^2} \, , \tag{5.40}$$

where $\frac{Q^2}{A}$ is a normalization factor used to allow the slope term to scale relative uncertainties. Figure 5.15 shows the result of this calculation. This normalized slope term was calculated to be 0.9706 at the average Q^2 for the aluminum data set.

The uncertainty on Q^2 is thus applied to the asymmetry by the correction R_{Q^2}, which has a central value of 1 by definition. Scaling the relative Q^2 uncertainty by the normalized slope yields the uncertainty on the R_{Q^2} correction of

$$R_{Q^2} = 1.0000 \pm 0.0043. \tag{5.41}$$

5.6   Simulation Benchmarking

Much of this analysis relies upon QwGeant4 simulations to determine the relative contributions of background scattering processes entering the acceptance. The results from these simulations are only valid if they agree with data. One method used to benchmark the
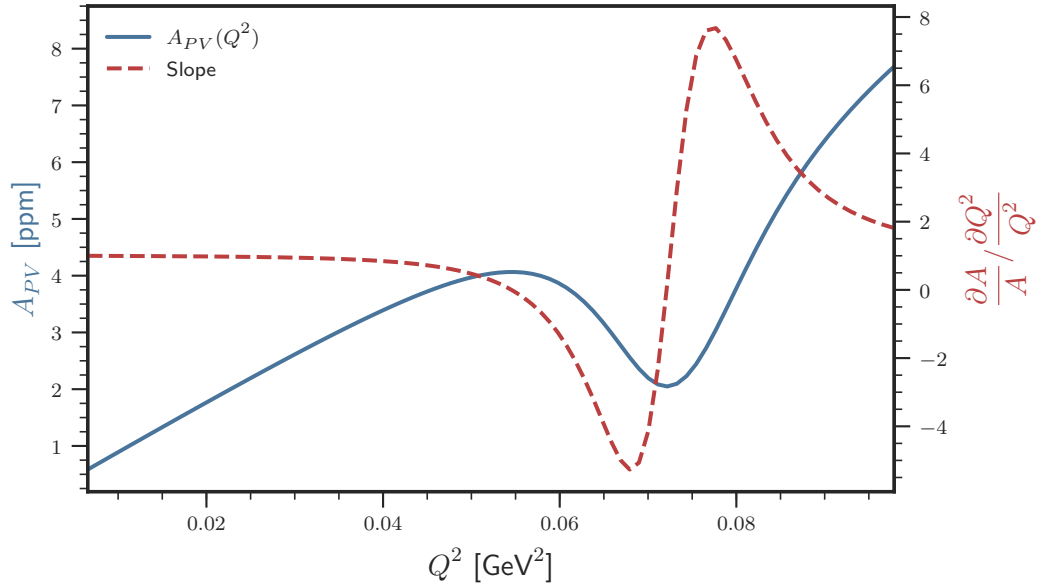
Figure 5.15: Normalized slope of C. J. Horowitz's theoretical aluminum asymmetry calculation and its dependence on momentum transfer Q^2. The solid blue curve gives the aluminum asymmetry quantified by the left vertical axis and the dashed red curve is the normalized calculated slope quantified by the right vertical axis.

simulation was a comparison between simulation-predicted rates and event-mode recorded rates from the ^{27}Al target.

During Run 1, a series of main detector rate measurements were performed at a range of QTOR current settings, in what is known as a QTOR scan. These rates were directly compared to total rates extracted from simulation for all of the known scattering processes that occur in ^{27}Al [190]. That analysis showed that the total rate from simulation disagreed with data by 4.87 % at the elastic peak current of 8921 A. The agreement worsened as the current decreased. Figure 5.16 shows an absolute comparison between simulation and data rates. It also shows the normalized residuals for each point in the rate scan. Simulation values used in that analysis were from the most recent versions of the event generators. Previous comparisons saw agreement at the 21 % level [94] and then the 10 % [98] once additional processes were included.

The cause of this disagreement is believed to be a result of not fully implementing radiative corrections. The first indication came from looking at the disagreement at lower QTOR currents. As the current decreases the profile of elastically scattered electrons moves
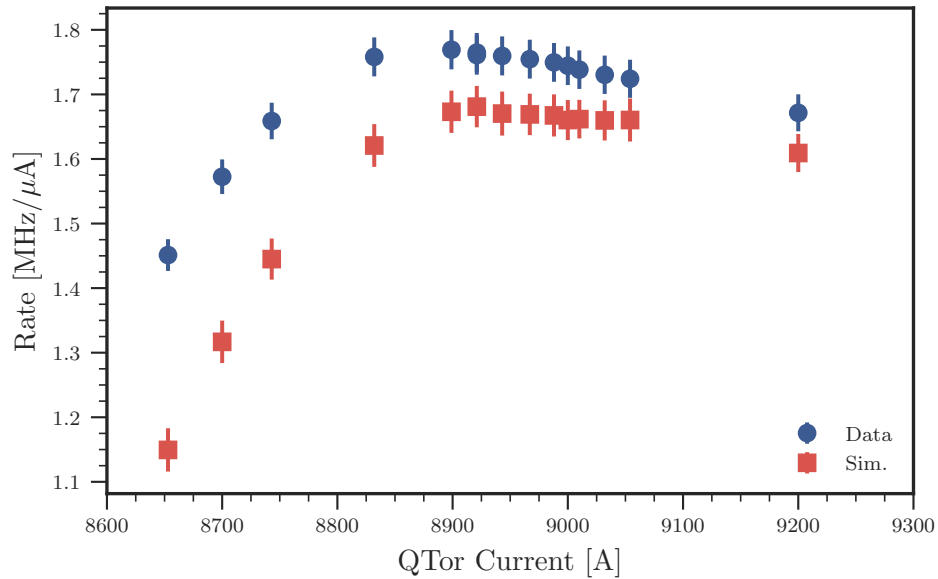
(a) Absolute Rate Comparison
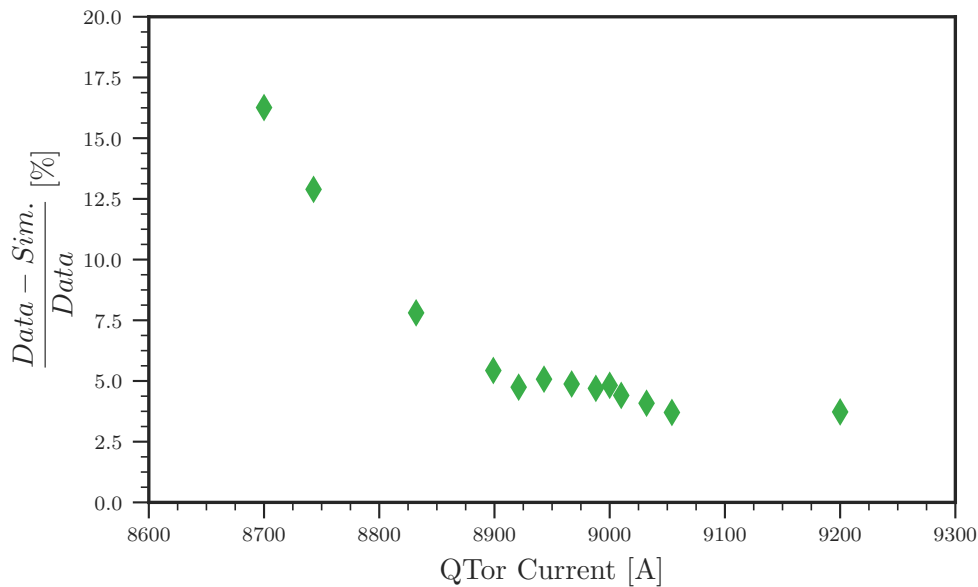
(b) Normalized Residuals

Figure 5.16: Comparison between total rates determined from simulation and Run 1 data recorded from the ^{27}Al target.

off of the focal plane of the detector array, allowing only events from the elastic radiative tail to enter into the acceptance. This assumption was eventually confirmed by a second investigation performed with the simulation, where the radiative correction parameter ΔE from the L. W. Mo and Y. S. Tsai formalism was varied over a range of values [191]. Initially,

a guess of 20 MeV was chosen for ΔE based on the minimal guidance given in L. W. Mo and Y. S. Tsai publications [56, 57]. However, that investigation proved that the discrepancy could all be explained by simply increasing the ΔE parameter to approximately 50 MeV.

Correcting this disagreement would require updated simulation values that make use of a different ΔE. However, for this analysis this disagreement was taken into account by folding the 4.8 % difference into the uncertainty placed on the elastic yield extracted from simulation. This quantity was used to calculate all of the background fractions for the non-elastic scattering processes with Eq. (5.20).

5.7 ^{27}Al Asymmetry Extraction

Starting with A_{raw}, a pure elastic parity-violating asymmetry was determined by applying the previously discussed corrections in the following manner. First measurement-based systematic corrections, discussed in Section 5.3, were applied to A_{raw} with Eq. (5.2). The resulting corrected asymmetry, A_{msr} was then corrected for the amount of beam polarization, background asymmetries, and the multiplicative factor R_{tot} with

$$A_{PV} = R_{tot} \frac{\frac{A_{msr}}{P} - \sum_i^N f_i A_i}{1 - \sum_i^M f_i}. \tag{5.42}$$

The sum over i to N for the background corrections $(f_i A_i)$ include terms for all of the background processes discussed in Section 5.4. These specifically include terms for quasi-elastic scattering, inelastic $(N \to \Delta)$ scattering, scattering from the 11 selected discrete excited states, 8 elastic alloy-element scattering contributions, and neutral particles entering the acceptance. The background fraction sum over i to M in the denominator include terms for all of the aforementioned background processes, but differs slightly from the background correction sum by including the beamline background fraction as discussed in Section 5.3.3. Table 5.14 provides a tabulated summary of these corrections for ease of reference.

The pure elastic parity-violating asymmetry A_{PV} was extracted from A_{raw} using Eq. (5.42) via a Monte Carlo method. Each correction input used in the calculation was sampled from a normal (Gaussian) distribution with a mean and width given by the

value and uncertainty for that correction. A_{PV} was calculated 10^6 times, with each calculated value stored into a histogram. At the end of sampling, the final A_{PV} value is taken as the mean of the distribution stored in that histogram, where the combined uncertainty is taken as the width of that distribution. The benefit of this method is that the uncertainties on the inputs are correctly propagated to the total calculated width.

During this calculation the inputs from systematic effects are assumed to be uncorrelated. Additionally, the statistical uncertainty is not included as an uncertainty on A_{raw} in Eq. (5.2) and by extension Eq. (5.42), as the measured statistical uncertainty is considered separate from the systematic uncertainties associated with each of the considered inputs. The final statistical uncertainty on A_{PV} was calculated using the relative statistical uncertainty from A_{raw}, with

$$\delta A_{PV} \text{ (statistical)} = \frac{\delta A_{raw}}{A_{raw}} A_{PV}. \tag{5.43}$$

Individual contributions to the final systematic uncertainty from each correction were determined by turning off all of the widths of the normally distributed inputs except for the correction of interest, allowing the calculation of A_{PV} with an uncertainty from just a single correction. The uncertainty contributions extracted with this method neglect the effects from intrinsic correlations that are included in the full randomized calculation of Eq. (5.42). To include these correlations, the opposite approach would have to be taken, where all the inputs except for the correction of interest would have to be randomized within their uncertainties. The uncertainty contribution would then be extracted by taking the quadrature difference between the resulting A_{PV} and the full calculation with randomized inputs. The difference between including or not including these correlations is small and thus the simpler method has been employed here.

5.7.1   Final Elastic Parity-Violating ^{27}Al Asymmetry

The pure elastic parity-violating electron-^{27}Al scattering asymmetry was determined to be

$$A_{PV} = 1.927 \pm 0.091 \text{ (statistical)} \pm 0.148 \text{ (systematic) ppm} \tag{5.44}$$

$$= 1.927 \pm 0.173 \text{ (total) ppm} \tag{5.45}$$
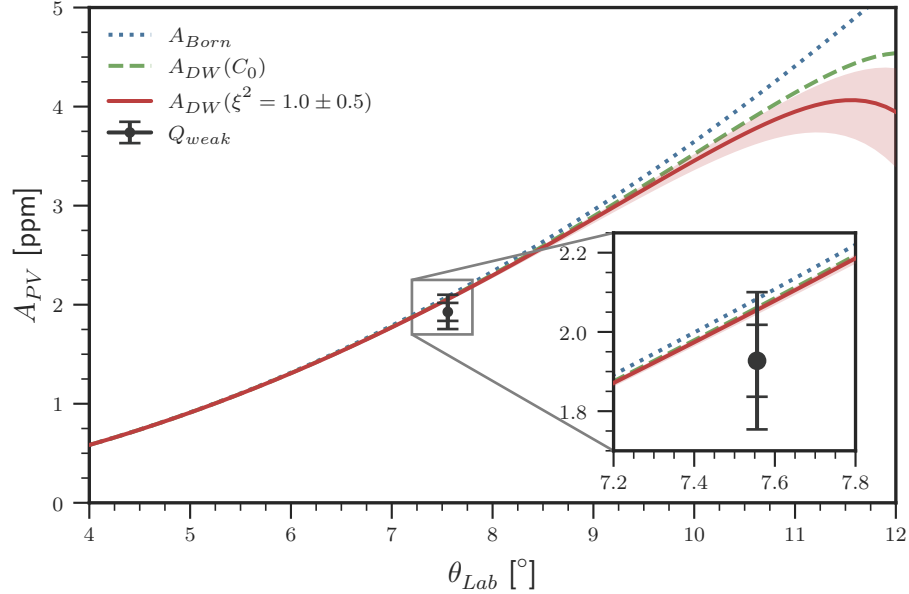
Figure 5.17: Comparison between the measured pure parity-violating elastic electron-^{27}Al asymmetry and a RMF asymmetry calculation by C. J. Horowitz [40]. The inset box provides a zoomed view of the measured point's agreement with theory. The inner uncertainty bar on the point represents the statistical uncertainty and the outer represent the total uncertainty. Curves reproduced from data tables given by C. J. Horowitz [40, 44].

at $Q^2 = 0.023\,57 \pm 0.000\,10\,\text{GeV}^2$. This is a $9\,\%$ precision determination of the asymmetry. The result is dominated by the systematic uncertainty for the reasons that are discussed in the next section. A comparison between the extracted asymmetry and C. J. Horowitz's calculated elastic RMF asymmetry calculation, Eq. (3.46), can be see in Fig. 5.17. The point is placed at the acceptance average scattering angle $\langle\theta\rangle = 7.5558 \pm 0.0023°$ as determined from simulation [170].

The measured asymmetry agrees within its total uncertainty with the theory calculation. The theory calculation predicts an asymmetry value of $2.055\,\text{ppm}$ at the acceptance-averaged scattering angle. To quantify the agreement between the central value and theory, the measured asymmetry only differs at the 0.74σ level.

5.7.2 Uncertainty Contribution Summary

As indicated in Eq. (5.44), the result is dominated by the systematic uncertainty. The primary systematic contribution causing this is the uncertainty on the inelastic background

asymmetry. Uncertainty contributions for the rest of the systematic corrections are below the final statistical uncertainty, as seen in Fig. 5.18.

Any future efforts should be invested primarily in reducing the uncertainty in the inelastic background asymmetry. Section 5.4.2 briefly discussed a possible avenue for a reduction in that correction's uncertainty, however it would require additional theoretical help. If this uncertainty could be reduced below that of the statistical, then the decision of not including additional data from Wien 10 or Run 1 could be reevaluated. Any improvements gained in either of these two uncertainties would ultimately result in a reduction in the total uncertainty, which would improve the neutron distribution radius determination.

5.8 Extraction of the ^{27}Al Neutron Distribution Radius

The neutron distribution radius (R_n) for ^{27}Al was determined using a many-model correlation technique first employed for the PREX analysis [122]. However, other approaches for extracting this radius can also be taken, see Section 3.3.3 and reference [53].

Working with C. J. Horowitz, F. Fattoyev, and Z. Lin at Indiana University, a selection of 11 RMF models were used to calculate theoretical parity-violating asymmetries from their assumed neutron distribution radii. The models selected were: FSUGold [192], FSUGarnet [193], FSUGold2 [194], IUFSU [195], NL3 [196, 197], RMF(022, 028, 032) [193] and TAMUC-FSU(a, b, c) [198]. This particular collection of models was selected because they were tuned to reproduce several nuclear structure observables, such as nucleon binding energies, measured charge radii, and strengths of the isoscalar and isovector giant resonances in selected nuclei [199]. Additionally, these models also predict masses for neutron stars that agree with astrophysical observations of pulsars [55].

A non-linear least squares method from the Python Scipy package [154] was used to fit the model's predicted asymmetries versus their R_n values, at the average momentum transfer of the data set. This fit resulted in a correlation between R_n and A_{PV} in the form of

$$R_n = (-0.6007 \pm 0.0002\,\mathrm{fm\,ppm}^{-1})A_{PV} + (4.1817 \pm 0.0011\,\mathrm{fm}). \qquad (5.46)$$

Using the central value of the final asymmetry given in Eq. (5.44), this model correlation implies $R_n = 3.024\,\text{fm}$. The uncertainty on that value is determined by taking slope of the fit to translate the uncertainty on A_{PV}. Performing this calculation and including the small uncertainty originating for the fitting routine, a final neutron distribution radius was determined to be

$$R_n = 3.024 \pm 0.104 \text{ (experimental)} \pm 0.003 \text{ (fit) fm} \tag{5.47}$$

$$= 3.024 \pm 0.104 \text{ (total) fm.} \tag{5.48}$$

A comparison of this implied R_n and the collection of RMF models is plotted in Fig. 5.19.

From Fig. 5.19 it is evident that the measured parity-violating asymmetry lies outside of the range of asymmetry values predicted by the collection of RMF models. Instead of being an interpolation method as seen in the PREX analysis [122] example, the application of this technique for this analysis is more of an extrapolation, which leads to questions of about its validity for this case.

There are a handful of possible explanations that could resolve the disagreement between the measured asymmetry and those predicted by the collection of RMF models. For example the asymmetries extracted from these RMF models are sensitive to the choice of kinematic parameters and charge radii, which are used as inputs in their calculation [199]. A known systematic effect associated with the technique comes from the choice of ^{27}Al charge radius used in these calculations. The RMF models assumed a value of $R_{ch} = 3.035 \pm 0.002\,\text{fm}$, taken from an unpublished Fourier-Bessel charge radius extraction, tabulated in the Atomic Data and Nuclear Data Tables [111]. Interestingly, this values differs from the $R_{ch} = 3.013\,\text{fm}$ used initially by C. J. Horowitz for calculating the parity-violating asymmetry [40]. The early agreement seen between the measured asymmetry and C. J. Horowitz's theory calculation seem to indicate a preference for the smaller ^{27}Al charge radius.

The charge radius of ^{27}Al has been previously measured four times, using two separate experimental techniques. Three of these measured results used electromagnetic electron scattering techniques [111, 200, 201], as discussed in Section 3.2. The most recent determination was made by G. Fricke *et al.* [202] using muonic atom $2p \rightarrow 1s$ transition energy

measurements. The most precise measurements, which are the latest electron scattering and muonic ^{27}Al results, disagree outside of their respective uncertainties by about 9σ, see Fig. 5.20. However, they do agree with the older electron scattering results that have much larger uncertainties. Based on this disagreement it is difficult to say which charge radius value is correct. These measurements can be averaged and assigned an inflated uncertainty to account for this disagreement. Following the procedures laid out in the PDG [9], an average charge radius value was found to be $R_{ch} = 3.043 \pm 0.007$ fm. This is larger than the value used by C. J. Horowitz in his calculation for R_n.

Taking the analysis one step further, the neutron skin of ^{27}Al can be calculated using the formalism introduced in Section 3.3.3. A proton distribution radius for ^{27}Al was calculated using a similar expression to that of Eq. (3.51), which was found to be $R_p = 2.932 \pm 0.007$ fm [199]. The uncertainty on that value is taken as the inflated uncertainty from the averaged charge radius result previously mentioned. The difference between the neutron and proton distribution radii yields the neutron skin thickness, which is calculated to be

$$\Delta R = R_n - R_p = 0.092 \pm 0.104 \text{ (total) fm.} \tag{5.49}$$

This result is consistent with zero as one would naively expect for ^{27}Al, where $N \approx Z$.
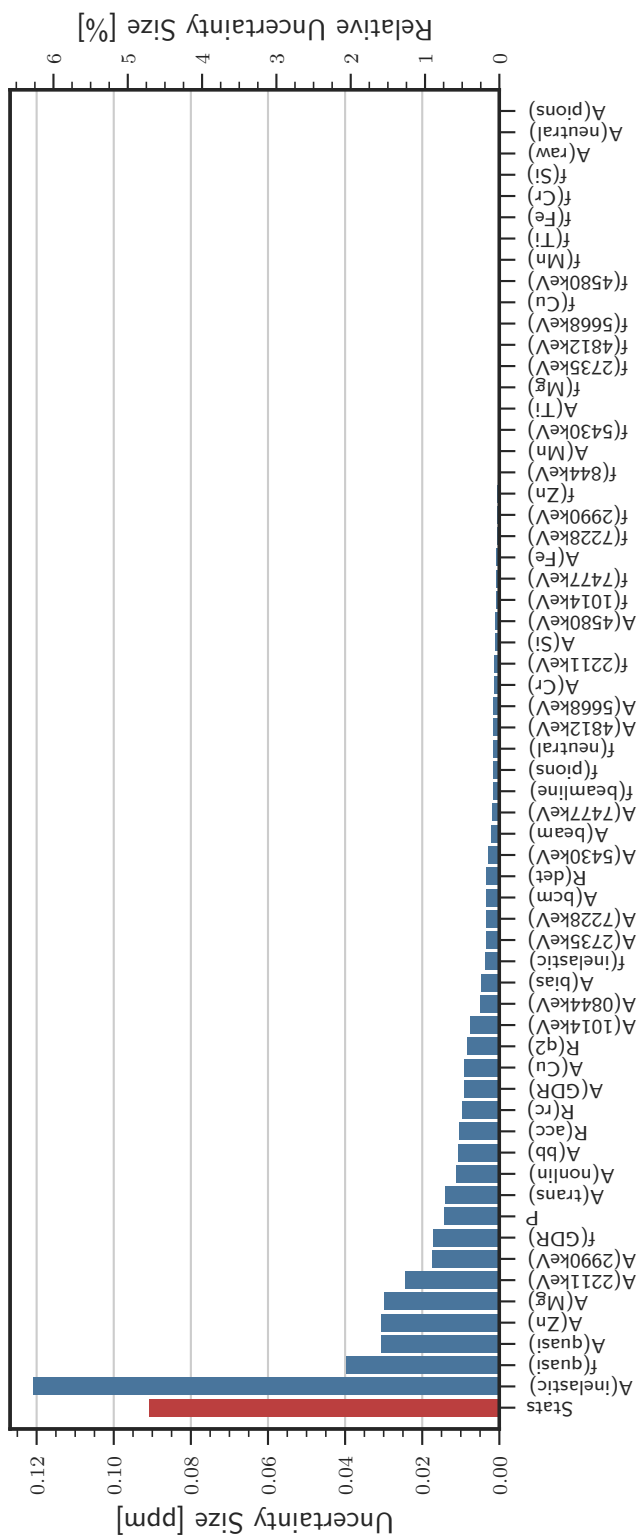
Figure 5.18: Uncertainty contributions on the final asymmetry extracted from the Monte Carlo technique, ordered by relative size. Statistical uncertainty given in red for comparison to the systematic contributions in blue.
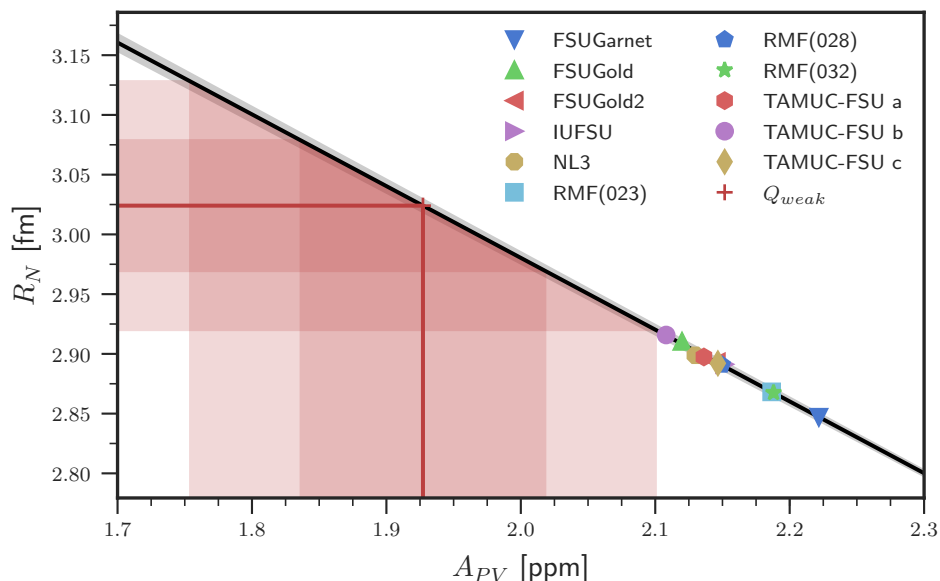
Figure 5.19: Determination of the ^{27}Al neutron distribution radius R_n from the measured A_{PV} as given by the red line via the many-model correlation technique. Correlation between R_n and A_{PV} given by black fit line. Outer red shaded region gives the total uncertainty on R_n from A_{PV}, where the inner region is just from the statistical uncertainty on the measured A_{PV}.
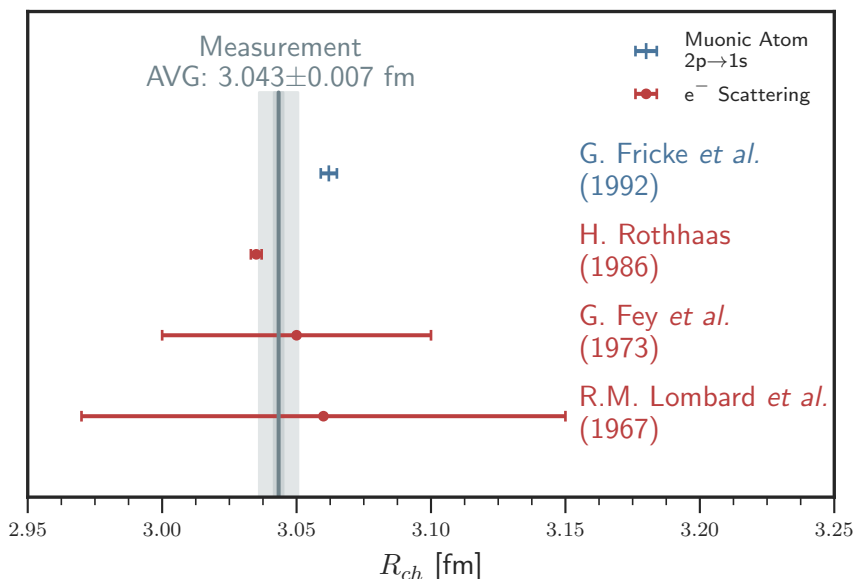
Figure 5.20: Historical comparison between the experimental determinations of the ^{27}Al charge radius. The gray line gives the error-weighted average of all of the experimental results. The gray error band on the average line represents the scaled uncertainty calculated used the techniques discussed in the PDG for averaging contentious results [9].

Table 5.14: Parity-Violating ^{27}Al asymmetry analysis correction summary.

Quantity	Asymmetry [ppm]	Section
A_{raw}	1.441 ± 0.068	5.2
A_{BCM}	0.0000 ± 0.0021	5.3.1
A_{reg}	0.0004 ± 0.0014	5.3.2
A_{BB}	-0.0047 ± 0.0066	5.3.3
A_L	-0.001 ± 0.007	5.3.4
A_T	-0.0034 ± 0.0088	5.3.5
A_{bias}	0.0054 ± 0.0030	5.3.6

Quantity	Background Fraction (f_i) [%]	Asymmetry (A_i) [ppm]	Section
0.844 MeV	0.27 ± 0.04	2.619 ± 1.310	
1.014 MeV	0.41 ± 0.10	2.563 ± 1.282	
2.211 MeV	1.35 ± 0.16	2.543 ± 1.271	
2.735 MeV	0.19 ± 0.02	2.590 ± 1.295	
2.990 MeV	0.93 ± 0.07	2.617 ± 1.308	
4.580 MeV	0.06 ± 0.01	2.783 ± 1.392	5.4.3
4.812 MeV	0.09 ± 0.02	2.379 ± 1.189	
5.430 MeV	0.17 ± 0.03	2.490 ± 1.249	
5.668 MeV	0.08 ± 0.02	2.542 ± 1.271	
7.228 MeV	0.18 ± 0.06	2.706 ± 1.353	
7.477 MeV	0.10 ± 0.07	2.753 ± 1.377	
Zn	2.375 ± 0.249	1.815 ± 0.908	
Mg	2.088 ± 0.219	2.013 ± 1.006	
Cu	0.683 ± 0.073	1.857 ± 0.929	
Cr	0.100 ± 0.011	1.920 ± 0.960	5.4.5
Si	0.080 ± 0.009	1.984 ± 0.992	
Fe	0.054 ± 0.006	1.883 ± 0.941	
Mn	0.018 ± 0.009	2.343 ± 1.172	
Ti	0.014 ± 0.007	2.148 ± 1.074	
Quasi-elastic	12.77 ± 1.22	-0.338 ± 0.169	5.4.1
Inelastic	7.39 ± 0.74	1.609 ± 1.149	5.4.2
GDR	0.58 ± 0.29	-2.217 ± 1.108	5.4.4
Pions	0.06 ± 0.06	0.000 ± 0.000	5.4.7
Neutrals	0.00 ± 0.45	1.7 ± 0.2	5.4.6
Beamline	0.69 ± 0.06	$-$	5.3.3

Quantity	Value	Section
P	0.8880 ± 0.0055	5.3.7
R_{det}	0.9913 ± 0.0017	5.5.2
R_{acc}	0.9960 ± 0.0054	5.5.1
R_{rc}	0.9981 ± 0.0050	5.5.3
R_{Q^2}	1.0000 ± 0.0043	5.5.4

Chapter 6

Elastic Beam-normal Single-spin ^{27}Al Asymmetry Analysis

During the ancillary physics studies performed by the collaborations, a series of measurements were made with transversely polarized beam on the ^{27}Al alloy target. These are the first measurements of the beam-normal single-spin asymmetry (BNSSA), also known as a transverse asymmetry, on the ^{27}Al nucleus. Previous experiments, such as HAPPEX and PREX [84] have already measured this observable for lighter nuclei and for ^{208}Pb, but they found that the ^{208}Pb measurement disagreed with its theoretically predicted value. As ^{27}Al is the highest atomic mass element to have its BNSSA measured, the analysis of this transverse aluminum data set stands to shine light on this disagreement.

This chapter discusses the analysis used to determine the transverse asymmetry from this aluminum data set. Many of the background scattering processes that contaminate this measured asymmetry have asymmetries that are not known. The final extracted BNSSA is reported as an "effective" asymmetry that includes effects from discrete excitations and collective motion excitations, such as the Giant Dipole Resonance. Corrections for other inelastic scattering backgrounds have been made and are discussed. Additional corrections for the other elements in the ^{27}Al alloy target have also been made using a simple scaling law. The resulting effective asymmetry is compared to theory along with the rest of the world data set of BNSSAs.

6.1   Data Selection and Quality Checks

Aluminum transverse asymmetries were measured both in Run 1 and Run 2. A selection of
these were performed at the QTOR currents of 8900 A, 7300 A, and 6700 A. Two separate
transverse polarization directions were used: vertical and horizontal.

During Run 1 a total of 13 runs, all in the vertical transverse polarization direction, were
recorded on February 9, 2011 with the ^{27}Al target. Almost a year later during Run 2, from
February 16–20, 2012, an additional 23 runs were recorded with the ^{27}Al target with both
polarization directions and at multiple QTOR currents. A completed list of runs included in
this transverse aluminum data and their experiment settings are tabulated in Table C.1.

The elastic ^{27}Al data set used in this analysis was extracted from both the Run 1 and
Run 2 data at the QTOR current of 8900 A. Only a small number of elastic runs exist over
this entire data set, thus quality cuts were only kept to the internal Q_{weak} analyzer cuts that
were applied when populating the analysis database.

6.2   Raw Asymmetry and Statistical Uncertainty

The BNSSA measured by the Q_{weak} apparatus is seen as an azimuthally varying asymmetry.
Extraction of this observable is done by fitting a generalized sinusoidal function to the
asymmetries measured by each detector in the main detector array. This function has the
form of

$$B_T(\phi) = B_H \sin\left(\frac{\pi}{4}\phi_H - \frac{\pi}{4} + \varphi_H\right) + B_V \cos\left(\frac{\pi}{4}\phi_V - \frac{\pi}{4} + \varphi_V\right) + C, \qquad (6.1)$$

where B_H (B_V) is the magnitude of the transverse asymmetry from the horizontal (vertical)
component, ϕ_H (ϕ_V) is the component of the azimuthal angle, φ_H (φ_V) is the component
of the phase offset, and C is a constant offset. The factors of $\frac{\pi}{4}$ are included in the phase
terms allow the fitting to be performed over the octant number for a given main detector,
with $\phi = 0$ set to beam left which corresponds to main detector 1. Corrections for shifts in
the azimuthal position from the nominal for each main detector are included later.

PMT-averaged asymmetries from each main detector, averaged over the entire period, for
a given polarization direction are fitted with the corresponding vertical or horizontal pieces

of that function. These fits are performed with a non-linear least squares routine from the

Python Scipy [154] package, where the best fit line was determined with a χ^2 minimization.

Fits are made on main detector asymmetries depending on the state of the IHWP, which

allows the extraction of the positive and negative amplitudes that depend on the helicity

state. A NULL hypothesis test was conducted by performing an unweighted average of the

IN and OUT state asymmetries for each main detector, which is written as

$$B^i_{NULL} = \frac{B^i_{IN} + B^i_{OUT}}{2}, \tag{6.2}$$

where the index i corresponds to detector number. An overall NULL was taken as the

error-weighted average over the eight main detectors. The raw physics asymmetry was

extracted as the amplitude of the sinusoidal fit performed on the sign-corrected PMT-averaged

asymmetries for a given polarization direction.

The results of these fits performed on unregressed, or raw, asymmetries for the Run 1

vertical, Run 2 horizontal, and Run 2 vertical data sets are tabulated in Table C.2, which is

located in the appendix. The extracted fit parameters from this analysis agree well with

ones determined from an earlier preliminary analysis [83].

The NULL asymmetries were all consistent with zero within their statistical uncertainties,

with the exception of the Run 2 vertical data subset. The mostly likely cause of this

inconsistent NULL value is the asymmetries associated with main detector 6, which are low

for both IHWP state. Plots of these positive, negative, NULL, and physics fits can be seen

for the Run 2 horizontal data subset in Fig. 6.1. Similar plots for the other two data subsets

are in Appendix C.

Physics asymmetries from those fits are summarized in Table 6.1. Their relative statistical

uncertainties are given in the last column. Combining all three aluminum data subsets yields

a $4.0\,\%$ statistical precision determination of the ^{27}Al BNSSA.
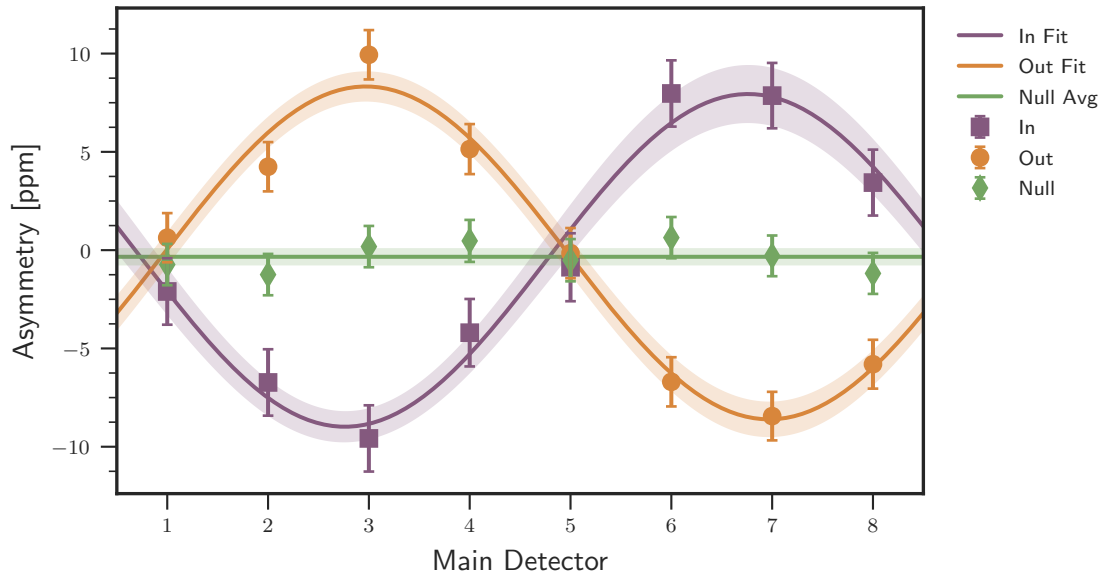
(a) IHWP plot
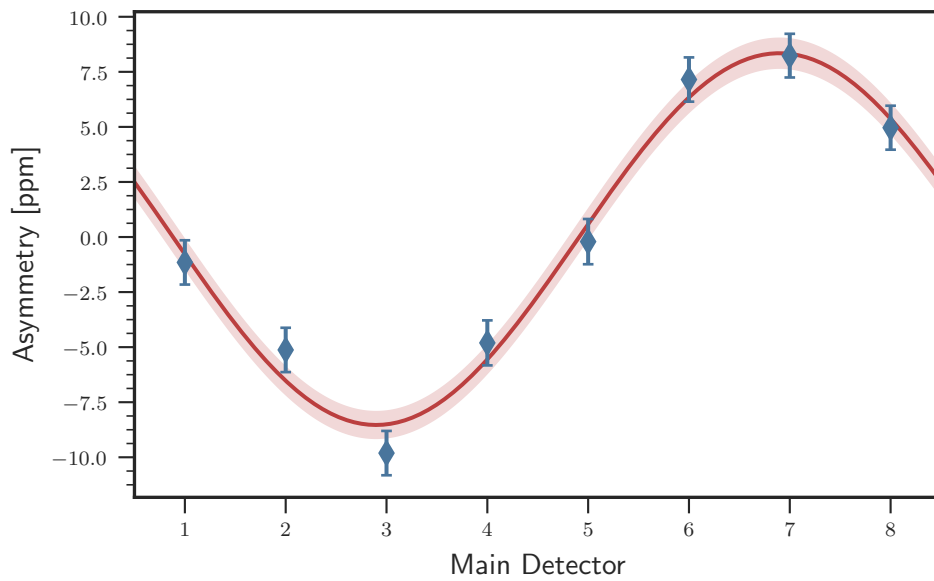
(b) Sign-corrected plot

Figure 6.1: Run 2 horizontal unregressed (raw) asymmetries. The physics asymmetry was
extracted as the amplitude of the sinusoidal variation in the lower plot. Labels "In" and
"Out" refer to the asymmetries that depend on the state of the IHWP. The "NULL" label
gives the non sign-corrected average of the "In" and "Out" asymmetries of the eight main
detectors.

Table 6.1: Unregressed physics asymmetries extracted from sinusoidal fits to transverse
aluminum data.

Data Subset	Asymmetry (B_{raw}) [ppm]	Relative Uncertainty [%]
Run 1 - Vertical	-9.214 ± 0.605	6.57
Run 2 - Horizontal	-8.440 ± 0.502	5.94
Run 2 - Vertical	-7.924 ± 0.736	9.29
Weighted Average	-8.576 ± 0.342	3.99

6.3 Measured Asymmetry Determination

Various systematic measurement-based corrections are applied to B_{raw} when determining
the measured asymmetry B_{msr}. These are corrections for azimuthal acceptance variations
(β_{acc}), helicity-correlated beam asymmetries (HCBA) (B_{reg}), choices of asymmetry fitting
function (B_{fit}), detector non-linearities (B_L), and a rescattering bias originating from the
lead preradiators on the main detectors (B_{bias}). B_{msr} is determined by applying these as
corrections with

$$B_{msr} = \frac{B_{raw}}{\beta_{acc}} + B_{reg} + B_{fit} + B_L + B_{bias}. \tag{6.3}$$

This section discusses each of these corrections. For corrections that have yet to be
determined, an outline of the steps needed to calculation them are provided.

6.3.1 Acceptance Correction

The Q_{weak} detector array only covers $49\,\%$ of the azimuthal angle, which causes an individual
detector to only see a 22° sector of the azimuthal angle. Average asymmetries measured by
a given detector need to be corrected to ones that represent a BNSSA measured over the
full azimuthal angle. This correction called β_{acc} is applied directly to B_{raw} and is given by

$$\beta_i = \frac{\langle \sin \phi \rangle_i}{\sin \phi_i}, \tag{6.4}$$

where $\langle \sin \phi \rangle_i$ is the average phi acceptance for detector i, and $\sin \phi_i$ is the calculated sector
of the azimuthal angle for a given detector i.

The correction for each detector can be easily determined by looking at the ϕ distributions

of accepted events in simulation. Presently these values have not been determined specifically
for this analysis, thus the value determined from the ^{12}C BNSSA analysis was adopted
here. That correction was taken as the weighted average of the eight individual corrections
calculated for all of the detectors. Its uncertainty was taken as the standard deviation of
those values. The correction adopted for this analysis was [88]

$$\beta_{acc} = 0.9862 \pm 0.0036. \tag{6.5}$$

6.3.2   Helicity-correlated Beam Corrections

False asymmetries originating from helicity-correlated beam motion were investigated using
the linear regression system built into the Q_{weak} analyzing software. Correlations between
the main detector and beam monitor asymmetries are used to remove these false asymmetries
as they can modify the asymmetries measured by a given detector, which effects the overall
amplitude of the azimuthal variation of the BNSSA.

Similar fits to those performed during the raw asymmetry extraction were also applied to
the regressed asymmetries. Regression set "on" was chosen for this analysis, in an effort to
stay consistent with the choice made for the parity-violating aluminum asymmetry analysis.
However, regressed asymmetries are available for regression sets: "on 5+1", "10", "11",
"12", and "13". Plots of these fitted regressed asymmetries, along with a tabulation of the
extracted fit parameters, are given in Appendix C.

The size of the correction was determined by taking the difference between the regressed
and the unregressed ("on" - "off") main detector asymmetries. The corrections for each main
detector in the three data subsets are plotted in Fig. 6.2. These corrections were as high as
700 ppb in main detectors 1 and 5 for the vertical polarization direction, which is about a
factor of two times larger that the regression corrections used in the H_2 BNSSA analysis [83].
Regression corrections for the horizontal polarization direction agree well with those found
in the H_2 BNSSA analysis [83] and the ^{12}C BNSSA analysis [88]. An investigation into the
sensitivities and beam monitor asymmetries used to make these corrections has not yet been
performed, but could help explain the large correction value associated with the vertical
polarization data subset.
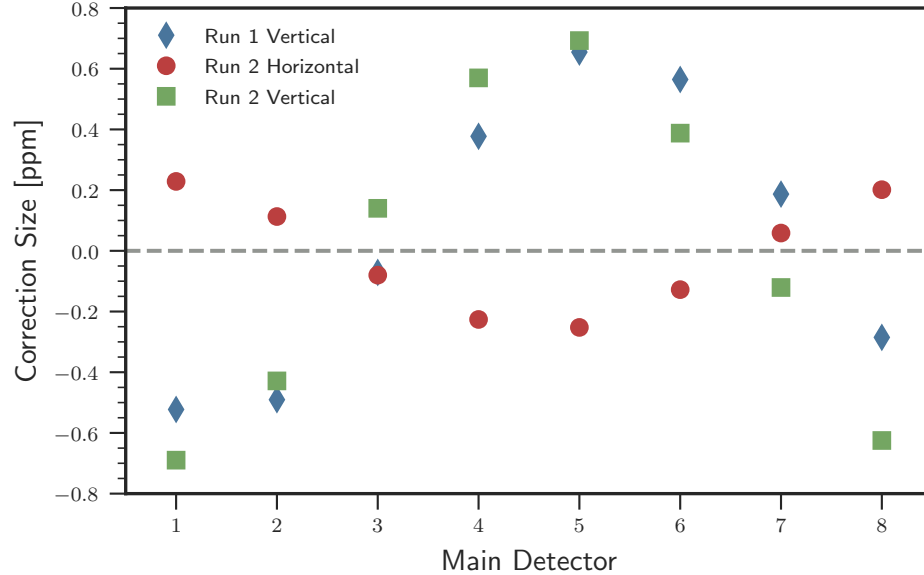
Figure 6.2: Regression corrections for each main detector over the three aluminum data subsets. The correction was determined as the difference between the "on" and "off" regression sets.

The systematic uncertainty on this correction primarily comes from the choice of regression set. Different sets, use different combination of beam monitors [128] and thus they have their own measured asymmetry characteristics. A systematic uncertainty can be easily determined by comparing the physics asymmetry amplitude extracted from each of the available regression sets. Table 6.2 shows the difference in the physics asymmetry amplitudes between the "on" set and the rest available for the aluminum data. In the Run 1 vertical data subset, sets 12 and 13 failed, the reason for this should be investigated in future efforts. The largest difference with respect to the "on" set was taken as the systematic uncertainties for each of the data subsets and these are tabulated in Table 6.3.

The final regression correction for each of the data subsets is taken as the difference between the "on" and "off" physics asymmetries given in Table C.3 and Table 6.1, respectively. These corrections are tabulated in Table 6.3. For the subsets that had vertical polarization direction, the corrections were on the order of the statistical uncertainty.

Table 6.2: Difference between regression set "on" and other available for the aluminum data subsets. Regression monitor sets 12 and 13 failed for the Run 1 vertical data subset, their entries in the table are left blank.

	Difference (w/ "on") [ppm]		
Scheme	Run 1 - V	Run 2 - H	Run 2 - V
on	0.0	0.0	0.0
on 5+1	−0.002	−0.003	−0.004
set10	−0.003	−0.003	−0.002
set11	0.0	0.0	0.0
set12	−	−0.020	0.0
set13	−	0.004	0.014

Table 6.3: Physics asymmetry regression correction for each of the aluminum data subsets. Determined as the difference between sets "on" and "off".

Data Subset	Correction (B_{reg}:"on" - "off") [ppm]
Run 1 - Vertical	−0.576 ± 0.003
Run 2 - Horizontal	−0.046 ± 0.020
Run 2 - Vertical	−0.695 ± 0.014

6.3.3   Fitting Scheme

An additional systematic effect comes from the choice of function used to extracted the azimuthally varying asymmetry. The generalized function used for fitting in this analysis, given in Eq. (6.1), could be replaced with several alternatives, as long as they include the amplitude and sinusoidal function pieces. Focusing only on the horizontal polarization direction, which uses the sine function component, alternative fit functions include:

$$B_T(\phi) = B \sin(\phi - \varphi), \tag{6.6}$$

$$B_T(\phi) = B \sin(\phi) + C, \tag{6.7}$$

$$B_T(\phi) = B \sin(\phi). \tag{6.8}$$

A similar set of functions are available for the vertical polarization direction with a change of sine to cosine. The uncertainty from this function choice is determined by taking the largest difference in amplitude extracted with each of those options.

This additional systematic effect has not been calculated for this aluminum analysis, but

a slightly inflated value of

$$B_{fit} = 0.000 \pm 0.050 \text{ ppm} \qquad (6.9)$$

was included based on the uncertainty determined in the ^{12}C BNSSA analysis [88].

6.3.4 Non-linearity

Non-linearity effects in the detectors and beam monitors are included in this analysis using
a similar method to the one applied for the parity-violating aluminum analysis, discussed in
Section 5.3.4. The non-linearity factor (f_L) was determined in a series of bench tests [131].
That value is used to determine the non-linearity correction and uncertainty in B_{msr} with

$$B_L \equiv -f_L B_{raw}, \quad \delta B_L \equiv \delta f_L |B_{raw}|. \qquad (6.10)$$

Applying this technique to the B_{raw} values in Table 6.1, yields non-linearity corrections
and uncertainties for each of the data subsets. These corrections are tabulated in Table 6.4.

Table 6.4: Non-linearity corrections and uncertainties for the aluminum data subsets.

Data Subset	Correction (B_L) [ppm]
Run 1 - Vertical	0.009 ± 0.046
Run 2 - Horizontal	0.008 ± 0.042
Run 2 - Vertical	0.008 ± 0.040
Weighted Average	0.008 ± 0.024

6.3.5 Rescattering Bias

An additional systematic effect arises from secondary scattering that occurs in the preradia-
tors in front of the main detectors during the transverse running. During the parity-violating
measurement, the presence of the preradiators introduced a false asymmetry that was
diagnosed by looking at the difference in the asymmetry measured by the two PMTs for a
given detector bar.

A similar investigation has been performed to identify any possible effects for the
transverse data sets, when the incoming beam polarization is maximally in the transverse
direction. Preliminary studies show that indeed the preradiators also introduce a false

asymmetry for the transverse data sets [203, 204]. However, the systematic effect cannot be
self diagnosed with same method as was used for the parity-violating measurements, see the
ELOG [203].

A correction for this effect comes straight from the simulation work performed by
the PMTDD subgroup, focused on this background contribution. Based on their initial
investigation with a selection of effective models, a correction of $\pm 85 \pm 15$ ppb is required for
transverse data sets [203]. However, the proper sign of the correction was unknown at the
time of making the correction. In a conservative effort, this analysis adopts a correction of

$$B_{bias} = 0.0 \pm 0.1 \text{ ppm}, \tag{6.11}$$

where the uncertainty is the sum of the recommended correction value and its uncertainty,
rounded up. This additional conservative correction is a factor of 5–7 times smaller than
the statistical uncertainty on any of the aluminum data subset asymmetries.

6.3.6   Beam Polarization

The magnitude of the transverse beam polarization was determined using the Møller po-
larimeter from periods of measured longitudinal polarization that straddle the series of
transverse asymmetry measurements. Since the polarimeter was designed to only mea-
sure longitudinally polarized beam, systematic studies were performed to ensure that the
polarizations before and after the transverse periods agreed. Polarization measurements
were conducted for both the Run 1 and Run 2 transverse polarization periods; these values
are tabulated in Table 6.5. Their error-weighted average is taken as the central value of
the polarization correction for this analysis and the largest uncertainty is adopted as the
uncertainty on that value.

6.4   Background Corrections

As mentioned in the introduction, many of the BNSSAs associated with non-elastic electron-^{27}Al
scattering are unknown theoretically, nor have they been measured before. A combination of

Table 6.5: Polarization values for the Run 1 and Run 2 transverse asymmetry measurements. References for each value are given in the last column. The final polarization is given as the error-weighted average of both runs.

Run	Beam Polarization [%]	Reference
1	88.95 ± 1.30	[83]
2	88.52 ± 0.68	[137]
Weighted Average	88.61	–

theoretical estimates and scaled measurements have been applied for the known backgrounds in this analysis when possible.

In particular, asymmetries for non-destructive excitations such as the discrete single particle excitations or the Giant Dipole Resonance are not known theoretically or experimentally, due to the lack of previous measurement. Given this lack of data, we chose not to include corrections for these backgrounds. Instead, the final asymmetry is reported as an "effective" measurement, which includes these contributions and a corresponding inflated uncertainty. In the future, if either theoretical models or measurements of these BNSSAs become available then the information in this document could be used to update this analysis with corrections for these effects.

Destructive excitations such as quasi-elastic and inelastic scattering, involving an $N \to \Delta$ excitation, are also theoretically not well understood. Corrections for these backgrounds are formed from other ancillary BNSSA measurements Q_{weak} performed with the liquid hydrogen target at different QTOR settings.

Corrections for the elements in the ^{27}Al alloy target are made with an order of magnitude estimate of the BNSSA taken from observations of previous measurements performed at similar beam energies to that of Q_{weak}.

The next sections discuss the corrections that have been made in this analysis and introduces approaches that can be applied in the future to determine corrections that have not been included.

6.4.1 Quasi-elastic Scattering

The background fraction piece is taken directly from earlier analysis work on the parity-violating ^{27}Al asymmetry using the Bosted-Mamyan quasi-elastic generator, see Section 5.4.1. That value also carries the same uncertainty as was previously assigned (Eq. (5.22)), it is

$$f_{quasi} = 12.77 \pm 1.22 \ \%. \tag{6.12}$$

No quasi-elastic BNSSA asymmetry has been specifically measured from the aluminum nucleus. Since electromagnetic quasi-elastic interactions typically prefer scattering from the proton, the BNSSA measured by Q_{weak} on the proton $B_n^p = -5.350 \pm 0.153 \, \mathrm{ppm}$ is adopted as the central value for this background asymmetry [83]. However, nuclear medium effects may be important for this correction, thus the uncertainty on the measured asymmetry is increased to match the correction used in the ^{12}C analysis [88]. The background asymmetry used in this analysis was

$$B_{quasi} = -5.4 \pm 1.0 \ \mathrm{ppm}. \tag{6.13}$$

6.4.2 Inelastic Scattering

Again, the background fraction piece for inelastic scattering was taken from the work done on the parity-violating ^{27}Al analysis (Section 5.4.2), which also included the same previously assigned uncertainty. The value adopted in that analysis was (Eq. (5.25))

$$f_{inel} = 7.39 \pm 0.74 \ \mathrm{ppm}. \tag{6.14}$$

The inelastic asymmetry correction for this analysis was taken from the $N \to \Delta$ measurement performed on the liquid hydrogen target at a QTOR current of 6700 A. The value and uncertainty adopted here was determined in the dissertation analysis by Nuruzzaman [205] and it is

$$B_{inel} = 43.0 \pm 16.0 \ \mathrm{ppm}. \tag{6.15}$$

The large uncertainty here primarily comes from model uncertainties associated with making a correction for the elastic radiative tail in the $N \to \Delta$ region. An additional uncertainty

for nuclear medium effects was not included since the uncertainty is already quite large.

In the future this inelastic correction could be revised by performing an analysis on a series of runs taken with the ^{27}Al target at a QTOR current of 6700 A. These runs and their experimental conditions are included in the run list tabulated in Appendix C. Additional simulation work could yield information about the size of corrections that would be needed for the radiative elastic tail and quasi-elastic contributions in the analysis of these data. Such an analysis could also determine an upper bound on the size of nuclear medium effects when compared to the $N \to \Delta$ measurement made on the liquid hydrogen target. This type of bound could then be used to confirm or possibly constrain the uncertainty applied to the quasi-elastic background asymmetry.

6.4.3   Non-Destructive Excitations

Effects from non-destructive excitations, like the discrete excited states and the Giant Dipole Resonance (GDR), can be bounded by comparing the results of the Q_{weak} [88] and PREX [84] ^{12}C BNSSA measurements. The Q_{weak} ^{12}C BNSSA measurements suffers from the same lack of theoretical understanding of these excitations, thus the final asymmetry is quoted an effective value. However the two results were shown to agree within uncertainties of Q_{weak} measurement, see Section 6.2 of the dissertation by M. J. McHugh III [88].

Based on this agreement, the ^{27}Al BNSSA analysis adopts the systematic uncertainty from the Q_{weak} ^{12}C BNSSA result as an additional uncertainty contribution, which is added in quadrature with the other uncertainties on B_n. The systematic uncertainty on the ^{12}C result was found to be $\delta B = 1.905\,\mathrm{ppm}$ [88].

6.4.4 ^{27}Al Alloy Elements

An estimate of the BNSSAs from the alloy elements in the ^{27}Al target was made using the simple first-order asymmetry approximation (Eq. (3.59)) introduced in Section 3.5 [206]. A momentum transfer value of $Q = 0.154\,\mathrm{GeV}$ and the same proportionality constant was used for all nuclei in that calculation. Uncertainties for each of the asymmetries were determined by taking the relative difference between predicted asymmetry values and an upper bound set by a line drawn between the central values of the PREX ^{12}C and ^{208}Pb

BNSSAs measurements [84, 206]. This approach is believed to be conservative, because
the model calculation that predicts this first order $\frac{A}{Z}$ relationship is known to be missing
corrections for Coulomb distortions [76, 84], which may be important for the higher-Z
elements in the alloy such as zinc, and copper.

The background fractions for these alloy element contributions, taken from the parity-
violating analysis, and their asymmetry estimates are tabulated in Table 6.6.

Table 6.6: Background fractions and asymmetry estimates for the alloy elements present
in the aluminum target material.

Element	Background Fraction (f_i) [%]	Asymmetry (B_i) [ppm]
Zn	2.375 ± 0.249	-11.72 ± 4.34
Mg	2.088 ± 0.219	-10.89 ± 1.24
Cu	0.683 ± 0.073	-11.79 ± 4.30
Cr	0.100 ± 0.011	-11.65 ± 3.53
Si	0.080 ± 0.009	-10.79 ± 1.34
Fe	0.054 ± 0.006	-11.55 ± 3.64
Mn	0.018 ± 0.009	-11.82 ± 3.86
Ti	0.014 ± 0.007	-11.70 ± 3.35

6.4.5 Beamline Background and Neutral Particles

Asymmetries that arise from the beamline background or neutrals particles are unknown for
this data set and should be investigated in the future. The ^{12}C analysis also had trouble
providing a definitive estimate of the asymmetries associated these backgrounds, but instead
provided large bounds [88].

However, since the background fractions determined from these processes are below 1%
conservative estimates of their asymmetries could easily be adopted without penalty. Thus,
zero valued corrections are adopted with large uncertainties of $\delta B = \pm 10\,\text{ppm}$.

6.5 Multiplicative Radiative and Acceptance Corrections

Three multiplicative factors were used to correct the background-corrected asymmetry
for effects from radiative corrections, light-weighting effect across the detectors, and the

uncertainty in the momentum transfer determination. The overall correction R_{tot} is given by

$$R_{tot} = R_{rc} R_{det} R_{Q^2}.$$ (6.16)

Radiative corrections have not been specifically investigated for this analysis. This remains an open task that should be addressed in the future when the radiative correction issue found during the parity-violating analysis has been resolved. However, a correction value of

$$R_{rc} = 1.00 \pm 0.01$$ (6.17)

has been adopted in this analysis, where the uncertainty is taken as twice the uncertainty assigned to the same correction used in the weak charge analysis [46].

Both R_{det} and R_{Q^2} require knowledge of the Q dependence of the BNSSA. As no theoretical calculations have been performed for the case of ^{27}Al that might indicate this dependence, Eq. (3.59) was used to calculate the slope factor needed to two determine these corrections. The slope was determined to be

$$\text{Slope} = \frac{\partial B_n}{\partial Q^2} \frac{Q^2}{B_n} \Rightarrow \frac{\partial B_n}{B_n} = \frac{\partial Q^2}{2Q^2}.$$ (6.18)

R_{Q^2} is calculated with a central value of 1 by definition and that slope factor is used to fold in the relative uncertainty on Q^2. Its 0.44 % relative uncertainty [170] translates to a B_n correction of

$$R_{Q^2} = 1.0000 \pm 0.0022.$$ (6.19)

The light-weighting correction R_{det} also uses this slope factor in its determination. Using the same procedure as the one described for the parity-violating ^{27}Al asymmetry analysis, the light-weighting correction was determined from tracking analysis extracted values [171, 172]. The major difference was the slope factor needed to convert the effect seen on the Q^2 measurements to one for the asymmetry B_n. Applying this slope correction, the light-weighting correction was determined to be

$$R_{det} = 0.9955 \pm 0.0017.$$ (6.20)

The uncertainty on this correction was not scaled by the slope as it was in other analyses.
Instead, it was kept in an effort to be conservative. Later theoretical input on the Q^2
dependence of this asymmetry could allow for a refinement of this value.

Combined, all three factors yield an R_{tot} value of

$$R_{tot} = 0.9955 \pm 0.0104. \tag{6.21}$$

6.6 ^{27}Al Asymmetry Extraction

Many of the corrections in this analysis were the same for the three data subsets. Thus, the
three B_{raw} values for each of the subsets were folded into a single value, by first applying
HCBA corrections (B_{reg}) individually, and were then combined by taking their error-weighted
average. For the subset-dependent measurement-based systematic corrections, such as B_{reg}
and B_L, the largest of their uncertainties was adopted as the uncertainty for that particular
correction in this combined analysis. This regression-corrected value was used as the input
into a Monte Carlo calculation method used to extract the final asymmetry.

The final BNSSA was determined using

$$B_n = R_{tot} \frac{\frac{B_{msr}}{P} - \sum_i^N f_i B_i}{1 - \sum_i^N f_i}, \tag{6.22}$$

where B_{msr} is the quantity discussed in Section 6.3, R_{tot} is the multiplicative factor discussed
in Section 6.5, and the $f_i B_i$ terms represent the background asymmetry corrections discussed
in Section 6.4.

The same Monte Carlo uncertainty propagation technique discussed in Section 5.7 was
adapted for this analysis, allowing the determination of a total systematic uncertainty. It
only included the corrections discussed in this chapter, but could be easily modified to
include updated corrections. Again, following the same analysis technique applied the the
parity-violating asymmetry, the combined statistical uncertainty was applied to the final
asymmetry as a relative value. Table 6.7 provides a summary of the values used in this
analysis.

Table 6.7: ^{27}Al BNSSA correction summary.

Quantity	Asymmetry [ppm]	Section
B_{raw}	-8.929 ± 0.340	6.2
β_{acc}	0.9862 ± 0.0036	6.3.1
B_{reg}	0.0000 ± 0.0197	6.3.2
B_{fit}	0.00 ± 0.05	6.3.3
B_L	0.0084 ± 0.0461	6.3.4
B_{bias}	0.0 ± 0.1	6.3.5

Quantity	Background Fraction (f_i) [%]	Asymmetry (A_i) [ppm]	Section
Zn	2.375 ± 0.249	-11.72 ± 4.34	
Mg	2.088 ± 0.219	-10.89 ± 1.24	
Cu	0.683 ± 0.073	-11.79 ± 4.30	
Cr	0.100 ± 0.011	-11.65 ± 3.53	
Si	0.080 ± 0.009	-10.79 ± 1.34	6.4.4
Fe	0.054 ± 0.006	-11.55 ± 3.64	
Mn	0.018 ± 0.009	-11.82 ± 3.86	
Ti	0.014 ± 0.007	-11.70 ± 3.35	
Quasi-elastic	12.77 ± 1.22	-5.4 ± 1.0	6.4.1
Inelastic	7.39 ± 0.74	43.0 ± 16.0	6.4.2
Neutrals	0.0000 ± 0.0045	0.0 ± 10.0	6.4.5
Beamline	0.0069 ± 0.0006	0.0 ± 10.0	6.4.5

Quantity	Value	Section
P	0.886 ± 0.013	6.3.6
R_{det}	0.9955 ± 0.0017	
R_{rc}	1.00 ± 0.01	6.5
R_{Q^2}	1.000 ± 0.022	

6.6.1   Elastic ^{27}Al Beam-normal Single-spin Asymmetry

The final effective elastic ^{27}Al beam-normal single-spin was determined to be

$$B_n = -16.322 \pm 0.620 \text{ (statistical)} \pm 1.779 \text{ (systematic)} \pm 1.905 \text{ (excitations) ppm}$$

$$(6.23)$$

$$B_n = -16.322 \pm 2.679 \text{(total) ppm.}$$

measured at $Q = 0.154\,\text{GeV}$. This is an $16\,\%$ precision determination of the asymmetry.
Corrections for non-destructive excitations, such as the GDR and discrete excited states,
have not been included in this analysis, but are bounded by the inclusion of an additional

systematic uncertainty introduced in Section 6.4.3. Aside from the large excitations uncer-
tainty, the result is dominated by the systematic uncertainty coming from the large inelastic
background correction of $f_{inel}B_{inel} = 3.2\,\text{ppm}$. Figure 6.3 provides a comparison between
the other uncertainty contributions.

Figure 6.4 compares this result to the previous HAPPEX and PREX BNSSA measure-
ments [84]. From that comparison it is easy to see that this measurement agrees with the
tend seen by the other lower atomic mass nuclei. The fact that this result agrees with the
trend only further supports the need for future BNSSA measurements of higher mass nuclei.
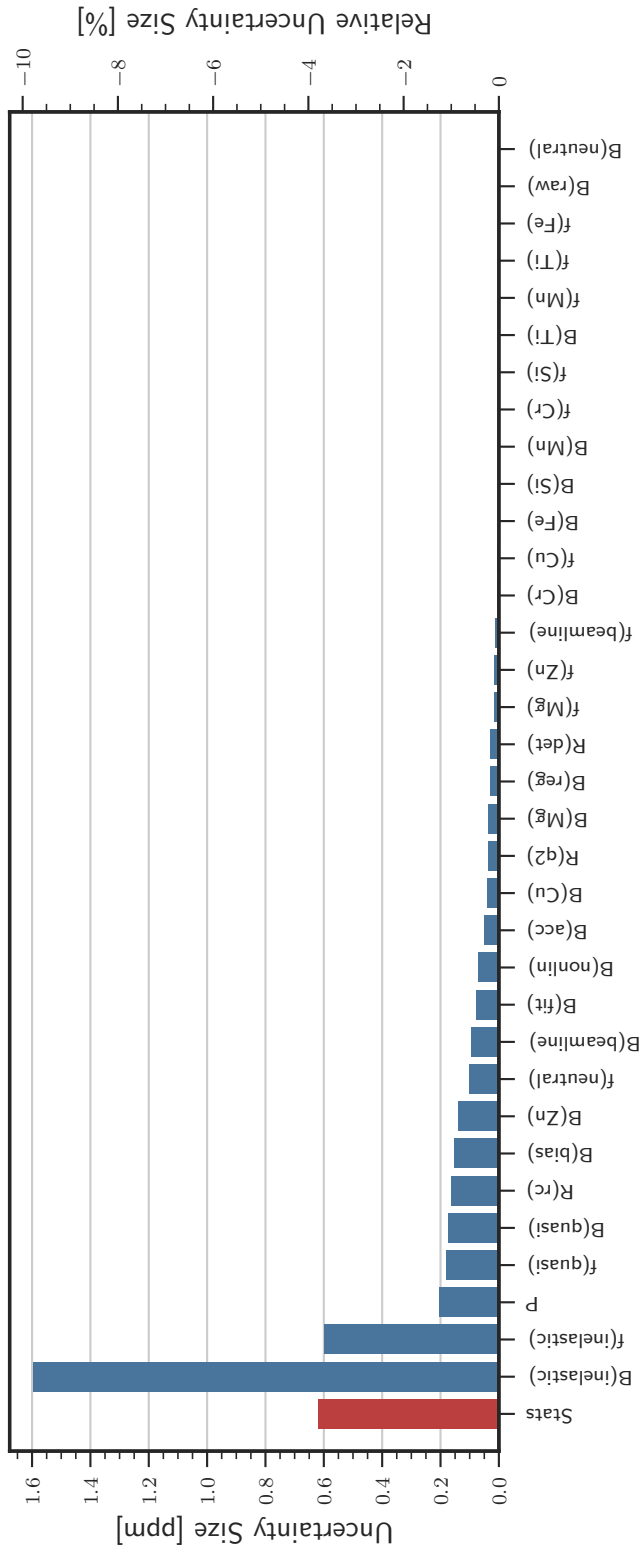
Figure 6.3:   Uncertainty contributions on the final ^{27}Al BNSSA extracted from the Monte Carlo technique, ordered by relative size. Statistical uncertainty given in red for comparison to the systematic contributions in blue.
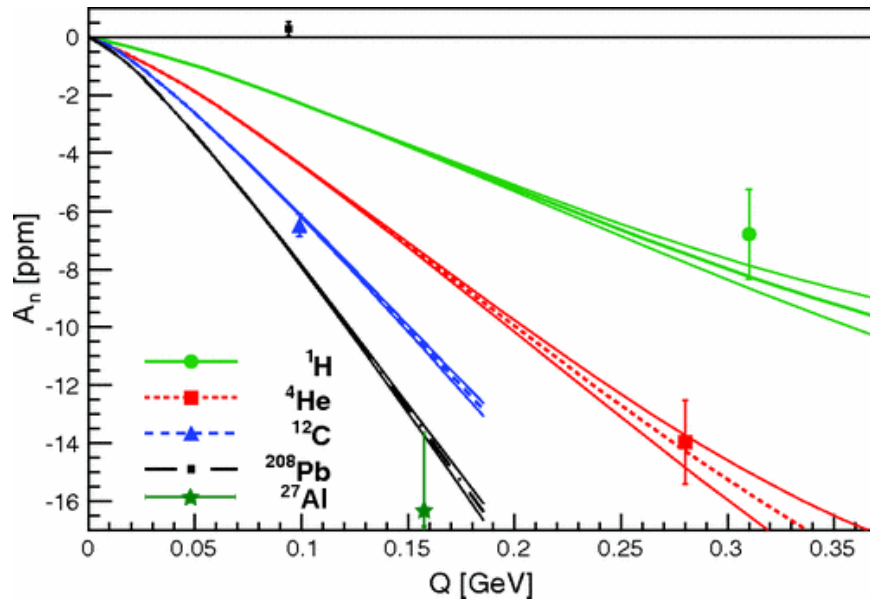
Figure 6.4: BNSSA measurements from the HAPPEX and PREX experiments compared
with theoretical calculation [76] and the Q_{weak} ^{27}Al BNSSA (given by the green star).
Figure taken from original publication [84]. The original publication uses A_n to denote a
BNSSA, which differs from the B_n notation used in this document.

Chapter 7

Q~weak~ Aluminum Target Background Analysis

During the initial planning stages of the weak charge experiment, it was known that one of the largest backgrounds requiring correction was the asymmetry contribution from the aluminum target windows [2]. Aluminum was predicted to have a parity-violating asymmetry an order of magnitude larger than that of the proton because of the higher number of neutrons that are preferred in neutral-current weak interactions. Despite efforts to reduce the background as much as possible, it still had to be explicitly measured in order to accurately account for it.

With this knowledge, the collaboration decided to commit beam time to performing an ancillary measurement of the aluminum parity-violating asymmetry from a thick auxiliary target constructed from the same material as the target windows. This chapter discusses the analysis efforts put into determining the background contributions from the target windows for the final Q~weak~ asymmetry analysis. It also discusses the effect this contribution had on the final asymmetry analysis in terms of uncertainty. In addition, the final results of the weak charge measurement are summarized.

7.1   Aluminum Target Windows

The aluminum target window correction for the weak charge measurement was treated as a known background asymmetry, given the label "1". During the analysis, background asymmetry contributions were subtracted from the polarization-corrected measured asymmetry (A_{msr}) with

$$A_{ep} = R_{tot} \frac{\frac{A_{msr}}{P} - \sum_{i=1,3,4} f_i A_i}{1 - \sum_{i=1}^{4} f_i}, \tag{7.1}$$

where A_{ep} is the final parity-violating elastic proton asymmetry, and the product of $f_1 A_1$ in the sum is the aluminum window correction. Two pieces form the aluminum target window correction: the background fraction (f_1) and the background asymmetry (A_1).

The background fraction piece was specifically determined for both Run 1 and Run 2 during low beam current data-taking; yield measurements were made with an evacuated liquid hydrogen target cell. QwGeant4 simulations were used to determine radiative corrections needed to account for the presence of the liquid hydrogen during normal operation. Details on this analysis are discussed at length in the dissertation of J. A. Magee [98]. The aluminum background fractions determined for both runs were [46]

$$f_1 = 2.471 \pm 0.056 \ \% \ \text{(Run 1)},$$
$$\tag{7.2}$$
$$f_1 = 2.516 \pm 0.059 \ \% \ \text{(Run 2)}.$$

The background asymmetry A_1 was determined using a combination of measured asymmetry data and simulation. Beam current restrictions prevented measurement of the parity-violating asymmetry directly from the target windows during evacuated running. Reducing the beam current to a safe level to avoid damaging the target window would have made a statistically relevant measurement of the asymmetry unfeasible in the time available. Instead, a separate thicker target, constructed from the same material as the target cell windows, was used to measure the background asymmetry at moderate beam currents. During post experiment analysis, simulation was used to convert this measured asymmetry to an effective target-window asymmetry after small kinematic and radiative corrections.

The target window asymmetry is assumed to be a combination of the individual upstream and downstream window asymmetries, with the total being expressed as the weighted average of the two contributions. This weighted average is written as

$$A_1 = \frac{Y_{US}A_{US} + Y_{DS}A_{DS}}{Y_{US} + Y_{DS}}, \tag{7.3}$$

where Y_{US} (Y_{DS}) is the averaged main detector signal yield and A_{US} (A_{DS}) is the averaged asymmetry measured from the upstream (downstream) target window, respectively. As individual measurements of either of these quantities were not possible, simulation was used to determine each of these components. In the case of the main detector signal yields, simulation was used to completely determine that contribution. However, upstream and downstream window asymmetries contributions were scaled from the measured aluminum asymmetry of the thicker target, using corrections from simulation.

In simulation a series of scattering generators were used to determine the rates[*] and asymmetries for each of the known processes that occur in electron-^{27}Al scattering. These considered processes include: elastic, quasi-elastic, inelastic ($N \rightarrow \Delta$), discrete single particle excited states, and collective excitations such as the Giant Dipole Resonance. With the exception of the elastic-^{27}Al scattering, many of these backgrounds have unknown asymmetries, thus effective models or educated guesses were used to approximate these asymmetries. Simulation of these processes were performed on three types of targets. These were isolated targets representing the upstream and downstream target windows and the thicker downstream auxiliary target (DS-4% X_0).

Each series of simulations allowed the determination of the total scattering rate and asymmetry for a given target. The total rate extracted from simulation for a particular target (T) is written as

$$R_{T,tot} = \sum_p R_{T,p}, \tag{7.4}$$

where the sum is over all the possible scattering processes (p) listed previously and $R_{T,p}$ is individual scattering process for a given target type, extracted from simulation using

---

[*]This early analysis made use of rates to calculate the signal contribution from each of the target windows. Corrections that turn these rates into detector yields are discussed later in this section.

the methods discussed in a technical report on the subject [138]. Relative asymmetry contributions from each of the scattering processes are determined with background fractions calculated using these rates. These background fractions are determined with

$$f_{T,p} = \frac{R_{T,p}}{R_{T,tot}},$$ (7.5)

for each process and then used to weight the sum of the asymmetries extracted from simulation. A total asymmetry for each target is then determined, using these background fraction weighting factors, with

$$A_{T,tot} = \sum_p f_{T,p} A_{T,p},$$ (7.6)

where the sum again is over all possible scattering processes and $A_{T,p}$ is the simulation extracted asymmetry for a given process from target type T.

Rates from the simulation were found to agree at the 5–10 % range with measured data, see Section 5.6 for more information. However, asymmetries extracted from simulation for these processes were not as well known. Instead of relying upon untrustworthy asymmetry models, the measured target asymmetry was compared and scaled with the simulation determined total asymmetries. Target window asymmetries were determined with

$$\begin{aligned} A_{US} &= A_{DS4\%}^{msr} \frac{A_{US}^{sim}}{A_{DS4\%}^{sim}}, \\ A_{DS} &= A_{DS4\%}^{msr} \frac{A_{DS}^{sim}}{A_{DS4\%}^{sim}}, \end{aligned}$$ (7.7)

where index T has been replaced with labels corresponding to the upstream (US), downstream (DS), and thicker aluminum target ($DS4\%$). The measured asymmetry from the thicker target was determined to be $A_{DS4\%}^{msr} = 1.6235 \pm 0.0795$ ppm [207]. The analysis of that measured asymmetry only included measurement-based systematic corrections, inelastic scattering backgrounds are left in as the true asymmetries from the target window include the effects from these other scattering processes. The individual corrections are summarized on the Q$_{\mathrm{weak}}$ wiki [208], but the reasons for making them are covered in more detail in

Chapter 5.

Applying this scaling shifted the measured asymmetry down by approximately $1.0\,\%$ for the downstream calculated window asymmetry and approximately $14\,\%$ for the upstream. The large shift in the upstream calculation is primarily due to the difference in Z-position of the upstream target versus the downstream position where the asymmetry measurement was conducted, which changes the momentum transfer Q^2 and thus the asymmetry. Additionally, only about half of the scattered electron profile from the upstream window sits on the face of the main detector array, which changes the relative ratio of processes that are determined in simulation.

Additional corrections were required to convert the simulation-determined rates into main detector yields, which are the actual observable measured by the main detector during the asymmetry measurement. A light-weighting correction factor was included to perform this conversion; its calculation is documented in the ELOG [209]. This correction was multiplicatively applied to the calculated total simulation rates before they were used to determine the effective window asymmetry.

The full calculation of the final effective window asymmetry, given by Eq. (7.3), was performed with a Monte Carlo uncertainty propagation technique [210]. The technique is a repetitive calculation of the effective window asymmetry. Each input is randomized with a pseudo random number generator based on a seed value. These randomized inputs were selected from a normal (Gaussian) distribution with a mean and width corresponding to the central value and uncertainty for a given input. The results from a given calculation were placed in a histogram and then repeated for a fixed number of trials.

This method allowed a complete calculation with all of the simulation-calculated rates and asymmetries for each of the processes, including correlations. Conservative uncertainties were applied to each rate and yield input into the calculation. The scattering-background corrections from common processes between target types are assumed to be correlated. The correlations imposed between these similar processes caused the overall uncertainty associated with this scaling technique to be on the order of the measurement-based systematic uncertainty on the measured asymmetry input [210].

Two separate calculations were performed, one for each running period. Both calculations

differed slightly, based on the simulation parameters used to determine Run 1 and Run 2 rates and asymmetries. For example, the beam energy and QTOR current in simulation differed between the two runs. The same Run 2 measured asymmetry was used as an input in both calculations. Additional aluminum asymmetry measurements were made during Run 1, but that data set was not analyzed at the time of this analysis. Any systematic effects from differences between the two running periods were accounted for during a separate series of simulations.

The resulting distributions from these two Monte Carlo calculations were slightly asymmetric, which was believed to be caused by the sum rule imposed on the background fraction calculation piece [210]. This rule made sure all randomized rate contributions totaled to 100 %. Figure 7.1 gives the resulting distribution of effective window asymmetries for both Run 1 and Run 2. As the final distributions were asymmetric, simply quoting the mean and width would not truly represent the central value and uncertainty of the calculated effective asymmetry. Instead, the median of the distribution was chosen to be the quoted value of the effective window asymmetry. The difference between the mean and median were below 1 %. Uncertainties were calculated by integrating a 1σ confidence interval about the median, following the general guidelines discussed in the statistical review of the PDG [9]. In the end, the collaboration made the decision to quote the largest bound of the confidence level as a 1σ symmetric uncertainty for use in the calculation of the parity-violating electron-proton asymmetry.

The final effective window asymmetries used in the final calculation of the elastic parity-violating electron-proton asymmetry were [46, 208, 210]

$$
\begin{aligned}
A_1 &= 1.514 \pm 0.071 \text{ (stat.)} \pm 0.021 \text{ (sys.)} \pm 0.020 \text{ (MC) ppm (Run 1)} \\
&= 1.514 \pm 0.077 \text{(total) ppm,} \\
A_1 &= 1.515 \pm 0.071 \text{ (stat.)} \pm 0.021 \text{ (sys.)} \pm 0.019 \text{ (MC) ppm (Run 2)} \\
&= 1.515 \pm 0.077 \text{(total) ppm.}
\end{aligned} \tag{7.8}
$$

These values were found to agree with ones determined from a separate implementation of the same calculation introduced in this section [210]. The major difference between
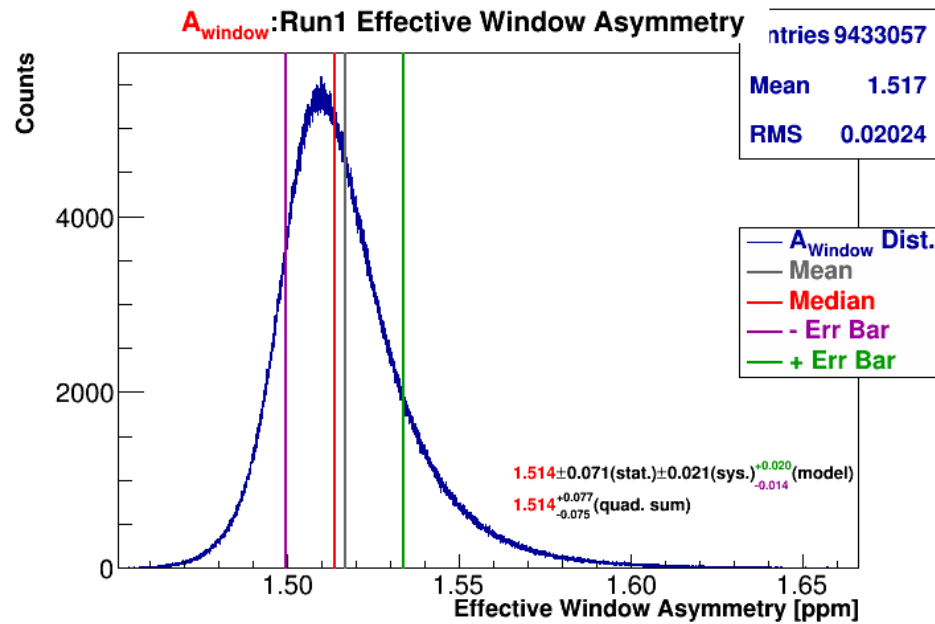
(a) Run 1
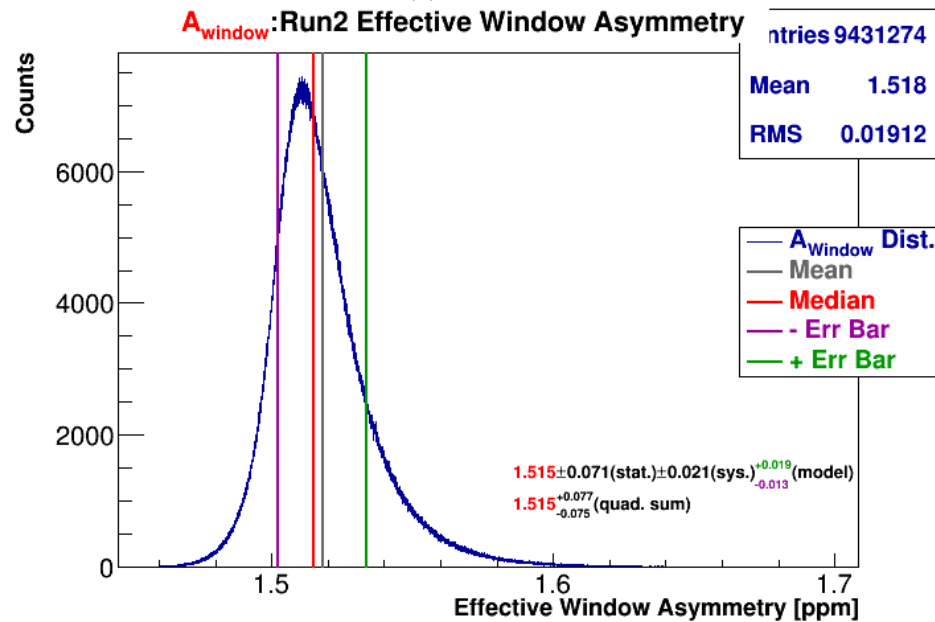
(b) Run 2

Figure 7.1: Distributions of calculated effective window asymmetries, for Run 1 and Run 2, from Monte Carlo calculation technique. Effective window asymmetry taken as the median of distribution (given by the red line). Upper and lower uncertainties are calculated by integrating a 1σ confidence level about the median (given by the purple and green lines). Figures taken from the ELOG [210].

the two calculations was the method used to propagate the uncertainties, the alternative

calculation employed a more traditional method. Combining the background fractions

discussed earlier in this section with these effective window asymmetries, the final aluminum window corrections to the Q_{weak} asymmetry analysis were $f_1 A_1 = 37 \pm 2$ ppb for Run 1 and $f_1 A_1 = 38 \pm 2$ ppb for Run 2.

Chapter 8

Results and Conclusions

The previous three chapters have discussed the analyses of the elastic parity-violating ^{27}Al asymmetry, the elastic beam-normal single-spin ^{27}Al asymmetry, and aluminum target window corrections for the main weak-charge analysis. This chapter provides a review of the results determined from each of the respective analyses, the impact these results have on the Q_{weak} experiment and future experiments, and advice on how future improvements could be made to each of the results.

8.1 Elastic Parity-Violating ^{27}Al Asymmetry

Chapter 5 discussed the rigorous analysis techniques used to determine the pure elastic parity-violating ^{27}Al asymmetry from the collaboration's ancillary measurement. This was the first time this asymmetry has been measured, and its value was used to determine the neutron distribution radius of ^{27}Al.

The raw asymmetry from this ancillary measurement, taken from the Run 2 aluminum data set, was found to be $A_{raw} = 1.441 \pm 0.068$ ppm, a 4.7% statistical precision measurement. Corrections for various measurement-based systematic effects were applied to this raw asymmetry, see Section 5.3. The majority of these corrections were found to have minor impact on the final systematic uncertainty. In addition, corrections for non-elastic scattering backgrounds from ^{27}Al and elastic scattering contributions from alloy elements were also applied. Each of these contributions are discussed in detail in the respective subsections

dedicated to them in Section 5.4.

Accounting for all of these effects, a final pure-elastic parity-violating ^{27}Al asymmetry was determined to be $A_{PV} = 1.927 \pm 0.173$ ppm (total), measured at $Q^2 = 0.0236 \pm 0.0001\,\mathrm{GeV}^2$. This result was dominated by the inelastic $(N \to \Delta)$ background determined from statistics-limited ancillary measurements. Figure 5.17 shows a comparison between this measured value and a theoretical calculation of the asymmetry.

As discussed in Section 5.4.2, any future effort dedicated to revisiting this analysis should focus on reducing the uncertainty due to this background contribution. One suggested method would be to seek theoretical help in performing a calculation of this inelastic asymmetry at Q_{weak} kinematics. Using a calculated result for this particular contribution would match with the methodology applied to the other background corrections considered in this analysis.

The analysis also has a few other areas that could benefit from improvement, namely, a full implementation of radiative corrections for most of the cross section generators used in simulation. Once implemented, a new series of simulations could be conducted in an effort to better benchmark the simulation with QTOR scan results, see Section 5.6. I considered this task to be an important next step, as the credibility of this analysis relies upon the accuracy of the simulation when determining the size of the background contribution diluting the measured asymmetry. However, it is important to mention that this analysis already includes an inflated uncertainty that covers the disagreement between data and simulation.

Working with theory results from C. J. Horowitz and collaborators at Indiana University, this first measurement of the asymmetry has been used to extract the neutron distribution of the ^{27}Al nucleus. The radius was determined to be $R_n = 3.024 \pm 0.104\,\mathrm{fm}$, which is a $3.4\,\%$ precision determination. Again the dominant uncertainty comes from the inelastic scattering background contribution on the asymmetry input. Aside from possible future improvements to the asymmetry's uncertainty, the theory calculations used to form the correlation between A_{PV} and R_n should be updated to account for the measurement's final momentum transfer value, which I believe would only yield a minor change. I believe the disagreement that was seen between the range of models and the Q_{weak} measurement placed on the correlation line is due to the choice of ^{27}Al charge radius used in those calculations.

Using an average charge radius with an inflated uncertainty from previous measurements might be a better option if the calculation is revisited.

As C. J. Horowitz states in his motivating publication [40], this determination is a useful check of the neutron distribution radius extraction procedure, which has been used before by the PREX collaboration on their measurement of ^{208}Pb [53, 122]. The same procedure will be used again in the future, when the PREX collaboration repeats their measurement in an effort to improve their uncertainty. Additionally, a new measurement will be conducted on ^{48}Ca directly after the repeated PREX measurement [89]. This new measurement will also make use of the neutron distribution radius extraction procedure.

Aside from comparing the extracted neutron distribution radius to those predicted by theory, additional confidence in the result is instilled by the agreement seen in the neutron skin thickness. The ^{27}Al skin thickness was determined to be $\Delta R_n = 0.092 \pm 0.104\,\text{fm}$, which is consistent with zero within its uncertainty. This confirms the naive expectation one would assume for ^{27}Al, as it has approximately an equal number of protons and neutrons. The fact that the result agrees with the naive expectation acts as an additional confirmation that this experimental procedure is valid.

8.2   Elastic Beam-Normal Single-Spin ^{27}Al Asymmetry

Chapter 6 covered the analysis of the elastic ^{27}Al beam-normal single-spin asymmetry. This difficult analysis yielded an effective value of the asymmetry. Due to the lack of theoretical understanding and previous measurements, many of the non-elastic scattering backgrounds were not well understood. This forced the adoption of many rough estimates for these backgrounds.

Corrections for the quasi-elastic and inelastic backgrounds were mainly based on previous Q_{weak} dissertation analyses. In particular, the inelastic background, which is the dominant uncertainty contribution on the final result, comes from a separate $N \to \Delta$ measurement performed with the liquid hydrogen target at lower QTOR current. Any future improvement to the uncertainty contributions on that analysis will directly improve the results of this analysis. Data from the ^{27}Al target at lower QTOR current are also available, which could

possibly help refine the uncertainty from this contribution.

Including all of the corrections discussed in Chapter 6, a final effective ^{27}Al beam-normal single-spin asymmetry was determined to be $B_n = -16.322 \pm 2.679$ ppm (total), measured at $Q = 0.154$ GeV. This is a 16 % precision determination of the asymmetry. Even though the asymmetry is reported as an effective quantity, its uncertainty has been conservatively inflated to account for any possible effects from missing excitation corrections.

The original motivation for performing this ancillary measurement was to help understand the observed disagreement between theory and the ^{208}Pb result from the HAPPEX and PREX measurements [84]. When compared to these previous measurements, this new result confirms the asymmetry trend seen by the lighter mass nuclei and thus only adds further motivation for future BNSSA measurements from nuclei with masses between ^{27}Al and ^{208}Pb.

Additionally, I hope this result will motivate a future theoretical prediction of the ^{27}Al BNSSA at these kinematics. Without an explicit theoretical calculation, an alternative method for comparing these measurements is to look at the atomic mass dependence of the BNSSAs at a common momentum transfer. Figure 8.1 shows all of the elastic beam-normal single-spin asymmetries from the HAPPEX, PREX, and Q$_{\text{weak}}$ experiments, scaled to at momentum transfer of $Q = 0.154$ GeV. That figure also includes a calculation of Eq. (3.59), over a range of stable isotopes up to ^{208}Pb, as a comparison to the measured BNSSAs. The calculation only includes the lowest order mass dependence of BNSSAs, as it was gleaned from the original asymmetry calculations performed for the HAPPEX and PREX results [76, 84]. A true comparison should be made with a more rigorous calculation once available.

8.3 ^{27}Al Target Background and Impact on Q$_{\text{weak}}$

Finally, an overview of the effective aluminum window asymmetry was given in Chapter 7. It was one of the largest background corrections to the Q$_{\text{weak}}$ parity-violating asymmetry analysis. A combination of measured background fractions and asymmetries were used to form this correction. Most of this analysis relied upon simulation to determine radiative corrections and scaling factors for both of these quantities.
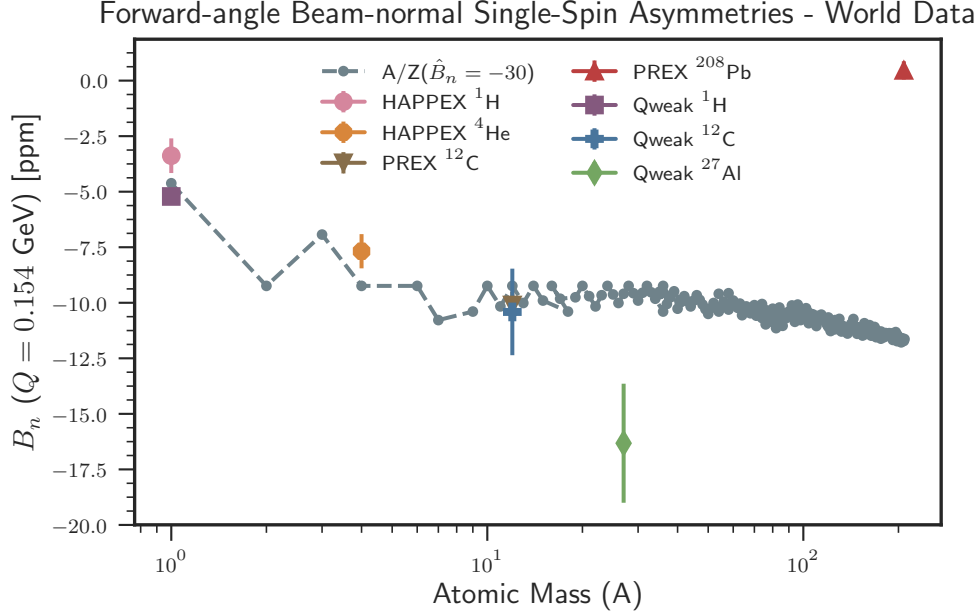
Figure 8.1: Comparison of all forward-angle BNSSA measurements with Eq. (3.59) cal-culated for stable isotopes at $Q = 0.154\,\text{GeV}$. HAPPEX and PREX results [84] are Q scaled to match the kinematics of Q_{weak}'s measurements. Q_{weak} dissertation analysis re-sults are used to quote the hydrogen [83] and carbon [88] points. Analysis of the aluminum measurement is discussed in Chapter 6.

In particular, the asymmetry extracted from the ancillary ^{27}Al target measurement during Run 2 was scaled to an effective asymmetry for each of the target windows. A final asymmetry from both the windows was taken as a rate weighted-average of their respective asymmetries. This final effective window asymmetry was calculated to be $A_1 = 1.514 \pm 0.077\,\text{ppm}$ (total) for Run 1 and $A_1 = 1.515 \pm 0.077\,\text{ppm}$ (total) for Run 2. Combined with the background fractions determined from evacuated target measurements [98], a total correction of $f_1 A_1 = 37 \pm 2\,\text{ppb}$ (Run 1) and $f_1 A_1 = 38 \pm 2\,\text{ppb}$ (Run 2) were used in the Q_{weak} asymmetry analysis.

The result of the final Q_{weak} analysis, which included this correction, determined the elastic parity-violating electron-proton asymmetry to be [46]

$$A_{ep} = -223.5 \pm 15.0 \text{ (statistical)} \pm 10.1 \text{ (systematic) ppb (Run 1)}$$

$$A_{ep} = -227.2 \pm 8.3 \text{ (statistical)} \pm 5.6 \text{ (systematic) ppb (Run 2)} \qquad (8.1)$$

$$A_{ep} = -226.5 \pm 7.3 \text{ (statistical)} \pm 5.8 \text{ (systematic) ppb (Combined)},$$

where the combined result accounts for correlations between the running periods. This was 4 % precision measurement and the final result agreed with the previously published Run 0 measurement performed at the beginning of the experiment [49]. From this asymmetry measurement the weak charge of the proton was determined to be $Q_W^p = 0.0719 \pm 0.0045$ [46], using the formalism discussed in Section 3.3.1. This weak charge value implies a general mass reach of $\Lambda_+/g = 7.4\,\text{TeV}$ and $\Lambda_-/g = 8.4\,\text{TeV}$ at the 95 % confidence level (see Section 3.4.2) [46]. Additional information about the impact of this asymmetry measurement, its weak charge determination, and its interpretation can be found in the publication of the final result [46].

8.4 Outlook

Future parity-violation experiments, such as MOLLER [107] at Jefferson Lab and P2 [108] at Mainz plan to measure asymmetries with even greater precision. Both plan to use liquid hydrogen targets and will require similar background corrections for their target windows. A number of lessons learned during this analysis could be applied to their future efforts.

First, target window material selection is extremely important, as different alloys have the possibility to contain numerous high-Z elements at varying concentrations. Section 4.5.2 introduced the idea of high-strength aluminum alloys containing lithium as a possible replacement for the Al 7075-T651 material used in Q_{weak}. In addition to material selection, all target components should have a precision assay of their elemental composition. This information provided to be extremely helpful in these studies.

Second, a full suite of ancillary measurements on a target made with the same material as the window is mandatory. For example, these would have to include systematic studies of changing spectrometer current and measurements on multiple targets of varying thickness. Again, all of this information was helpful in the simulation benchmarking process.

Lastly, at different kinematics than that of extreme forward angles, higher-order multipole terms become important in the theoretical models of these parity-violating asymmetries. Take Horowitz's ^{27}Al calculation [40]; he specifically states that one has to be careful of using his model outside of the assumption of forward angles. In particular, the model uncertainty

starts to increase dramatically in the diffractive minimum region of the asymmetry.

Interestingly, if both MOLLER and P2 measure asymmetries from an ^{27}Al auxiliary target, they would be determining the weak form factor of ^{27}Al at their specific kinematics. Combined with this Q_{weak} measurement, these measurements would effectively start to map the Q^2 dependence of ^{27}Al's weak form factor, only at the cost of analysis time and graduate student power. This type of study has been proposed before by C. J. Horowitz and Z. Lin, for heavier nuclei such as ^{48}Ca [211]. Multiple precision measurements on this light asymmetric nuclei could benefit theory in the future.

Other future experiments, such as PREXII and CREX, will make measurements of the parity-violating asymmetry from ^{208}Pb and ^{48}Ca, respectively. The PREXII motivation is ultimately to improve upon their previous measurement with a reduced statistical uncertainty. CREX is a completely new measurement that will directly follow PREXII. Both mostly likely will make ancillary measurements of the beam-normal single-spin asymmetry from these respective nuclei. A new ^{208}Pb measurement could either confirm or contradict their previous result. CREX will also make this measurement, which will be the first time this asymmetry will have been measured for ^{48}Ca. Unlike the ^{27}Al asymmetry, the CREX result will be at a much higher atomic mass. This enables a better experimental test of present theoretical models, which are known to be lacking Coulomb distortion effects.

Each of these future experiments should ultimately benefit from the analyses discussed in this dissertation. Of course as parity-violating experiments continue to improve their statistical power, the methods documented here will have to be improved upon, if they are going to meet their precision goals.

Appendix A

Aluminum Target Information Supplement

A.1 Alloy Radiation Length Calculation

This section documents the calculation of the radiation length for the aluminum alloy material used in this experiment. A radiation length of a material quantifies the amount of energy loss that highly-energetic electrons and photons deposit as they pass through a quantity of that material. In the case of electrons the radiation length quantifies the average distance the electron travels over which its energy is reduced by $1/e$ via the process of bremsstrahlung, known as braking radiation. The aluminum alloy target material includes a non-negligible fraction of heavier elements that modify the radiation length compared to that of a target made with pure aluminum, thus motivating this calculation.

The radiation length (X_0) of an element can be calculated using the following expression, taken from reference [9, 212],

$$\frac{1}{X_0} = 4\alpha r_e^2 \frac{N_A}{A} \big(Z^2[L_{rad}(Z) - f(Z)] + Z L'_{rad}(Z)\big) \tag{A.1}$$

where α is the fine-structure constant, r_e^2 is the classical electron radius, N_A is Avogadro's constant, A is the atomic mass of the element in units of $[\mathrm{g\,mol^{-1}}]$, and Z is the atomic

number. L_{rad} and L'_{rad} are functions of Z with the following forms:

$$L_{rad}(Z) = \ln\left(184.15Z^{-1/3}\right) \tag{A.2}$$

and

$$L'_{rad}(Z) = \ln\left(1194Z^{-2/3}\right). \tag{A.3}$$

These expressions are only valid for elements greater than $Z = 4$ (Beryllium). Values for those lighter elements are tabulated in [9].

The function $f(Z)$, a Coulomb correction term, is an infinite sum but can be accurately represented up to $Z = 92$ (Uranium) using this truncated expansion:

$$
\begin{aligned}
f(Z) &= \alpha^2 Z^2 \sum_{n=1}^{\infty} \frac{1}{n(n^2 + \alpha^2 Z^2)} \\
&\approx \alpha^2 Z^2 \left(\frac{1}{1 + \alpha^2 Z^2} + 0.202\,06 - 0.0369\alpha^2 Z^2 + 0.0083\alpha^4 Z^4 - 0.002\alpha^6 Z^6\right).
\end{aligned}
\tag{A.4}
$$

Using Eq. (A.1) in combination with Eqs. (A.2) to (A.4) the radiation length for the individual constituent elements of the aluminum alloy can be calculated. The resulting values are tabulated in Table A.1.

Table A.1: Atomic masses and calculated radiation lengths of the constituent elements that make up the aluminum alloy target material. Atomic masses are taken from IUPAC database [213] and the PDG [214].

Element	Atomic Mass $[\mathrm{g\,mol^{-1}}]$	Radiation Length $[\mathrm{g\,cm^{-2}}]$
Al	$26.981\,538\,5 \pm 0.000\,000\,7$	24.0109 ± 0.0005
Zn	65.38 ± 0.02	12.4287 ± 0.0005
Mg	24.305 ± 0.006	25.0312 ± 0.0005
Cu	63.546 ± 0.003	12.8627 ± 0.0005
Cr	51.9961 ± 0.0006	14.9443 ± 0.0005
Fe	55.845 ± 0.002	13.8383 ± 0.0005
Si	28.0855 ± 0.0003	21.8228 ± 0.0005
Mn	$54.938\,044 \pm 0.000\,003$	14.6397 ± 0.0005
Ti	47.867 ± 0.001	16.1632 ± 0.0005

Bragg's rule can be used to approximate the radiation length of a compound material using the radiation length of the compound's constituent elements [9, 215]. Applied to this

problem, Bragg's rule takes the form as noted in the following expression,

$$\frac{1}{X_0} = \sum_i^N \frac{w_i}{X_{0i}}$$ (A.5)

where X_0 is the radiation length of the compound, X_{0i} is the radiation length of a given element in the compound, and w_i is the fraction, by weight, of a given element in the compound.

The values from Table A.1, in conjunction with fractional weights from Tables 4.6 and 4.7, are used as inputs to Eq. (A.5). As three separate aluminum alloy materials were used depending on the target ladder location and run period (see Section 4.5.1 for further details), different radiation lengths can be calculated for each one. These calculated alloy radiation length values are tabulated in Table A.2. Comparing these calculated radiation lengths of the aluminum alloy with that of pure elemental aluminum, there is approximately a 7 % difference between the two. The presence of high Z transition metal elements such as Zinc, Copper, and Chromium have a sufficiently large fractional weight, which when combined with their low radiation lengths, reduce the overall radiation length of the aluminum alloy material.

Table A.2: Calculated radiation lengths for the aluminum alloy materials used in the upstream (US) and downstream (DS) targets during Run 1 and Run 2.

Run	Location	Radiation Length $[\text{g cm}^{-2}]$
1+2	US	22.4488
1	DS	22.4498
2	DS	22.4092

Appendix B

Parity-Violating ^{27}Al Asymmetry Analysis Supplement

B.1   Parity-violating Asymmetry Run List

Table B.1: List of runs and experimental parameters for the parity-violating aluminum data set taken during Run 2. The beam and QTOR currents are the maximum typical values for a given run; the beam current values are determined using BCM 6. The last three columns note the states of the slow-helicity reversal experimental controls.

Run	Slug	Wien	Beam Current [µA]	QTOR Current [A]	Precession State	Wien State	IHWP
14153	1028	6	56.0	8900.0	Reverse	Normal	OUT
14154	1028	6	56.0	8900.0	Reverse	Normal	OUT
14155	1028	6	57.0	8900.0	Reverse	Normal	OUT
14156	1028	6	58.0	8900.0	Reverse	Normal	OUT
14157	1028	6	57.0	8900.0	Reverse	Normal	OUT
14158	1028	6	56.0	8900.0	Reverse	Normal	OUT
14159	1029	6	56.0	8900.0	Reverse	Normal	IN
14160	1029	6	58.0	8900.0	Reverse	Normal	IN
14161	1029	6	57.0	8900.0	Reverse	Normal	IN
14162	1029	6	57.0	8900.0	Reverse	Normal	IN
14164	1029	6	58.0	8900.0	Reverse	Normal	IN
14165	1029	6	57.0	8900.0	Reverse	Normal	IN
14166	1030	6	57.0	8900.0	Reverse	Normal	OUT
14167	1030	6	57.0	8900.0	Reverse	Normal	OUT
14168	1030	6	57.0	8900.0	Reverse	Normal	OUT
14170	1030	6	57.0	8900.0	Reverse	Normal	OUT

Table B.1: List of runs and experimental parameters for the parity-violating aluminum
data set taken during Run 2. The beam and QTOR currents are the maximum typical
values for a given run; the beam current values are determined using BCM 6. The last
three columns note the states of the slow-helicity reversal experimental controls.

Run	Slug	Wien	Beam Current [μA]	QTOR Current [A]	Precession State	Wien State	IHWP
14171	1030	6	57.0	8900.0	Reverse	Normal	OUT
14172	1030	6	58.0	8900.0	Reverse	Normal	OUT
14173	1031	6	57.0	8900.0	Reverse	Normal	IN
14174	1031	6	58.0	8900.0	Reverse	Normal	IN
14175	1031	6	58.0	8900.0	Reverse	Normal	IN
14176	1031	6	58.0	8900.0	Reverse	Normal	IN
14177	1031	6	58.0	8900.0	Reverse	Normal	IN
14178	1032	6	58.0	8900.0	Reverse	Normal	OUT
14179	1032	6	57.0	8900.0	Reverse	Normal	OUT
14337	501 001	7	58.0	6698.0	Reverse	Reverse	IN
14338	501 002	7	58.0	6698.0	Reverse	Reverse	OUT
14364	501 001	7	58.0	6698.0	Reverse	Reverse	IN
14365	501 002	7	58.0	6698.0	Reverse	Reverse	OUT
15170	1033	8	58.0	8899.0	Normal	Reverse	IN
15171	1033	8	58.0	8899.0	Normal	Reverse	IN
15172	1033	8	59.0	8899.0	Normal	Reverse	IN
15173	1033	8	59.0	8899.0	Normal	Reverse	IN
15174	1033	8	59.0	8899.0	Normal	Reverse	IN
15175	1033	8	59.0	8899.0	Normal	Reverse	IN
15178	1033	8	58.0	8899.0	Normal	Reverse	IN
15179	1033	8	59.0	8899.0	Normal	Reverse	IN
15180	1034	8	58.0	8899.0	Normal	Reverse	OUT
15181	1034	8	58.0	8899.0	Normal	Reverse	OUT
15182	1034	8	58.0	8899.0	Normal	Reverse	OUT
15183	1034	8	58.0	8899.0	Normal	Reverse	OUT
15184	1034	8	58.0	8899.0	Normal	Reverse	OUT
15185	1034	8	58.0	8899.0	Normal	Reverse	OUT
15452	1035	8	49.0	8899.0	Normal	Reverse	OUT
15453	1035	8	50.0	8899.0	Normal	Reverse	OUT
15454	1035	8	49.0	8899.0	Normal	Reverse	OUT
15455	1035	8	49.0	8899.0	Normal	Reverse	OUT
15456	1035	8	50.0	8899.0	Normal	Reverse	OUT
15457	1035	8	50.0	8899.0	Normal	Reverse	OUT
15458	1035	8	49.0	8899.0	Normal	Reverse	OUT
15459	1035	8	50.0	8899.0	Normal	Reverse	OUT
15460	1035	8	50.0	8899.0	Normal	Reverse	OUT
15461	1035	8	50.0	8899.0	Normal	Reverse	OUT
15462	1035	8	50.0	8899.0	Normal	Reverse	OUT
15463	1035	8	51.0	8899.0	Normal	Reverse	OUT

Table B.1: List of runs and experimental parameters for the parity-violating aluminum
data set taken during Run 2. The beam and QTOR currents are the maximum typical
values for a given run; the beam current values are determined using BCM 6. The last
three columns note the states of the slow-helicity reversal experimental controls.

Run	Slug	Wien	Beam Current [μA]	QTOR Current [A]	Precession State	Wien State	IHWP
15464	1035	8	50.0	8899.0	Normal	Reverse	OUT
15465	1035	8	50.0	8899.0	Normal	Reverse	OUT
15466	1035	8	50.0	8899.0	Normal	Reverse	OUT
15467	1036	8	51.0	8899.0	Normal	Reverse	IN
15735	1036	8	61.0	8899.0	Normal	Reverse	IN
15736	1036	8	61.0	8899.0	Normal	Reverse	IN
15737	1036	8	61.0	8899.0	Normal	Reverse	IN
15738	1036	8	61.0	8899.0	Normal	Reverse	IN
15739	1036	8	61.0	8899.0	Normal	Reverse	IN
15740	1036	8	61.0	8899.0	Normal	Reverse	IN
15741	1037	8	61.0	8899.0	Normal	Reverse	OUT
15742	1037	8	61.0	8899.0	Normal	Reverse	OUT
15743	1037	8	61.0	8899.0	Normal	Reverse	OUT
15744	1037	8	61.0	8899.0	Normal	Reverse	OUT
15745	1037	8	61.0	8899.0	Normal	Reverse	OUT
15847	1038	8	61.0	8899.0	Normal	Reverse	IN
15848	1038	8	61.0	8899.0	Normal	Reverse	IN
15849	1038	8	62.0	8899.0	Normal	Reverse	IN
15850	1038	8	62.0	8899.0	Normal	Reverse	IN
15851	1038	8	61.0	8899.0	Normal	Reverse	IN
15852	1039	8	61.0	8899.0	Normal	Reverse	OUT
15853	1039	8	61.0	8899.0	Normal	Reverse	OUT
15854	1039	8	61.0	8899.0	Normal	Reverse	OUT
15855	1039	8	61.0	8899.0	Normal	Reverse	OUT
15856	1039	8	61.0	8899.0	Normal	Reverse	OUT
15857	1039	8	61.0	8899.0	Normal	Reverse	OUT
15858	1040	8	61.0	8899.0	Normal	Reverse	IN
15859	1040	8	61.0	8899.0	Normal	Reverse	IN
15860	1040	8	61.0	8899.0	Normal	Reverse	IN
15861	1040	8	61.0	8899.0	Normal	Reverse	IN
15862	1040	8	60.0	8899.0	Normal	Reverse	IN
15863	1041	8	60.0	8899.0	Normal	Reverse	OUT
15864	1041	8	61.0	8899.0	Normal	Reverse	OUT
15865	1041	8	61.0	8899.0	Normal	Reverse	OUT
15866	1041	8	61.0	8899.0	Normal	Reverse	OUT
15867	1041	8	60.0	8899.0	Normal	Reverse	OUT
15868	1042	8	60.0	8899.0	Normal	Reverse	IN
15869	1042	8	60.0	8899.0	Normal	Reverse	IN
15870	1042	8	60.0	8899.0	Normal	Reverse	IN
15871	1042	8	61.0	8899.0	Normal	Reverse	IN

Table B.1: List of runs and experimental parameters for the parity-violating aluminum data set taken during Run 2. The beam and QTOR currents are the maximum typical values for a given run; the beam current values are determined using BCM 6. The last three columns note the states of the slow-helicity reversal experimental controls.

Run	Slug	Wien	Beam Current [µA]	QTOR Current [A]	Precession State	Wien State	IHWP
15872	1042	8	60.0	8899.0	Normal	Reverse	IN
15873	1043	8	60.0	8899.0	Normal	Reverse	OUT
15874	1043	8	61.0	8899.0	Normal	Reverse	OUT
15875	1043	8	61.0	8899.0	Normal	Reverse	OUT
16483	1044	9	59.0	8898.0	Normal	Normal	IN
16484	1044	9	59.0	8898.0	Normal	Normal	IN
16485	1044	9	59.0	8898.0	Normal	Normal	IN
16486	1044	9	59.0	8898.0	Normal	Normal	IN
16487	1044	9	59.0	8898.0	Normal	Normal	IN
16488	1044	9	60.0	8898.0	Normal	Normal	IN
16489	1044	9	60.0	8898.0	Normal	Normal	IN
16490	1044	9	60.0	8898.0	Normal	Normal	IN
16491	1044	9	60.0	8898.0	Normal	Normal	IN
16492	1044	9	60.0	8898.0	Normal	Normal	IN
16493	1045	9	59.0	8898.0	Normal	Normal	OUT
16494	1045	9	59.0	8898.0	Normal	Normal	OUT
16495	1045	9	60.0	8898.0	Normal	Normal	OUT
16496	1045	9	59.0	8898.0	Normal	Normal	OUT
16497	1046	9	60.0	8898.0	Normal	Normal	IN
16500	1046	9	60.0	8898.0	Normal	Normal	IN
16501	1046	9	60.0	8898.0	Normal	Normal	IN
16502	1046	9	60.0	8898.0	Normal	Normal	IN
16503	1047	9	59.0	8898.0	Normal	Normal	OUT
16504	1047	9	60.0	8898.0	Normal	Normal	OUT
16506	1047	9	60.0	8898.0	Normal	Normal	OUT
16507	1047	9	60.0	8898.0	Normal	Normal	OUT
16508	1047	9	60.0	8898.0	Normal	Normal	OUT
16773	1048	9	60.0	8898.0	Normal	Normal	IN
16774	1048	9	60.0	8898.0	Normal	Normal	IN
16775	1048	9	60.0	8898.0	Normal	Normal	IN
16776	1048	9	60.0	8898.0	Normal	Normal	IN
16777	1049	9	60.0	8898.0	Normal	Normal	OUT
16778	1049	9	60.0	8898.0	Normal	Normal	OUT
16779	1049	9	60.0	8898.0	Normal	Normal	OUT
16780	1049	9	60.0	8898.0	Normal	Normal	OUT
16922	1050	9	60.0	8898.0	Normal	Normal	OUT
16923	1050	9	60.0	8898.0	Normal	Normal	OUT
16924	1050	9	60.0	8898.0	Normal	Normal	OUT
16925	1050	9	60.0	8898.0	Normal	Normal	OUT
16949	1051	9	60.0	8898.0	Normal	Normal	IN

Table B.1: List of runs and experimental parameters for the parity-violating aluminum data set taken during Run 2. The beam and QTOR currents are the maximum typical values for a given run; the beam current values are determined using BCM 6. The last three columns note the states of the slow-helicity reversal experimental controls.

Run	Slug	Wien	Beam Current [μA]	QTOR Current [A]	Precession State	Wien State	IHWP
16951	1051	9	60.0	8898.0	Normal	Normal	IN
16952	1051	9	60.0	8898.0	Normal	Normal	IN
16953	1051	9	60.0	8898.0	Normal	Normal	IN
16954	1052	9	60.0	8898.0	Normal	Normal	OUT
16962	1052	9	60.0	8898.0	Normal	Normal	OUT
16963	1052	9	60.0	8898.0	Normal	Normal	OUT
16964	1052	9	60.0	8898.0	Normal	Normal	OUT
16965	1052	9	60.0	8898.0	Normal	Normal	OUT
17370	1053	9	59.0	8898.0	Normal	Normal	OUT
17371	1053	9	59.0	8898.0	Normal	Normal	OUT
17372	1053	9	59.0	8898.0	Normal	Normal	OUT
17373	1053	9	59.0	8898.0	Normal	Normal	OUT
17376	1053	9	59.0	8898.0	Normal	Normal	OUT
17377	1053	9	59.0	8898.0	Normal	Normal	OUT
17378	1053	9	58.0	8898.0	Normal	Normal	OUT
17379	1054	9	59.0	8898.0	Normal	Normal	IN
17380	1054	9	59.0	8898.0	Normal	Normal	IN
17381	1054	9	59.0	8898.0	Normal	Normal	IN
17382	1054	9	59.0	8898.0	Normal	Normal	IN
17383	1055	9	59.0	8898.0	Normal	Normal	OUT
17384	1055	9	59.0	8898.0	Normal	Normal	OUT
17385	1055	9	58.0	8898.0	Normal	Normal	OUT
17386	1055	9	58.0	8898.0	Normal	Normal	OUT
17387	1056	9	58.0	8898.0	Normal	Normal	IN
17388	1056	9	59.0	8898.0	Normal	Normal	IN
17389	1056	9	58.0	8898.0	Normal	Normal	IN
17390	1056	9	59.0	8898.0	Normal	Normal	IN
17391	1057	9	57.0	8898.0	Normal	Normal	OUT
17392	1057	9	56.0	8898.0	Normal	Normal	OUT
17393	1057	9	57.0	8898.0	Normal	Normal	OUT
17394	1057	9	58.0	8898.0	Normal	Normal	OUT
17395	1058	9	58.0	8898.0	Normal	Normal	IN
17396	1058	9	58.0	8898.0	Normal	Normal	IN
17397	1058	9	58.0	8898.0	Normal	Normal	IN
17398	1058	9	58.0	8898.0	Normal	Normal	IN
17400	1058	9	58.0	8898.0	Normal	Normal	IN

B.2   Helicity-correlated Beam Corrections

- Regressed asymmetry plots: Fig. B.1

- Helicity-correlated beam parameters plots:

  - Target X differences: Fig. B.2

  - Target X' differences: Fig. B.3

  - Target Y differences: Fig. B.4

  - Target Y' differences: Fig. B.5

  - Target E differences: Fig. B.6

  - Target X sensitivities: Fig. B.7

  - Target X' sensitivities: Fig. B.8

  - Target Y sensitivities: Fig. B.9

  - Target Y' sensitivities: Fig. B.10

  - Target E sensitivities: Fig. B.11

B.3   Beamline Background

- Beamline background asymmetry plots: Fig. B.12

B.4   Transverse Leakage

- Transverse leakage plots:

  - Wien 6: Fig. B.13

  - Wien 9: Fig. B.14

B.5   Polarization

- Polarization-corrected asymmetry plots: Fig. B.15

B.6   Discrete Excited State Fits

- Discrete excited state fit plots:

  - 0.844 MeV fit: Fig. B.16

  - 0.844 MeV uncertainty: Fig. B.17

  - 1.014 MeV fit: Fig. B.18

  - 1.014 MeV uncertainty: Fig. B.19

  - 2.735 MeV fit: Fig. B.20

  - 2.735 MeV uncertainty: Fig. B.21

  - 2.990 MeV fit: Fig. B.22

  - 2.990 MeV uncertainty: Fig. B.23

  - 4.580 MeV fit: Fig. B.24

  - 4.580 MeV uncertainty: Fig. B.25

  - 4.812 MeV fit: Fig. B.26

  - 4.812 MeV uncertainty: Fig. B.27

  - 5.430 MeV fit: Fig. B.28

  - 5.430 MeV uncertainty: Fig. B.29

  - 5.668 MeV fits: Fig. B.30

  - 5.668 MeV uncertainty: Fig. B.31

  - 7.228 MeV fits: Fig. B.32

  - 7.228 MeV uncertainty: Fig. B.33

  - 7.477 MeV fits: Fig. B.34

  - 7.477 MeV uncertainty: Fig. B.35
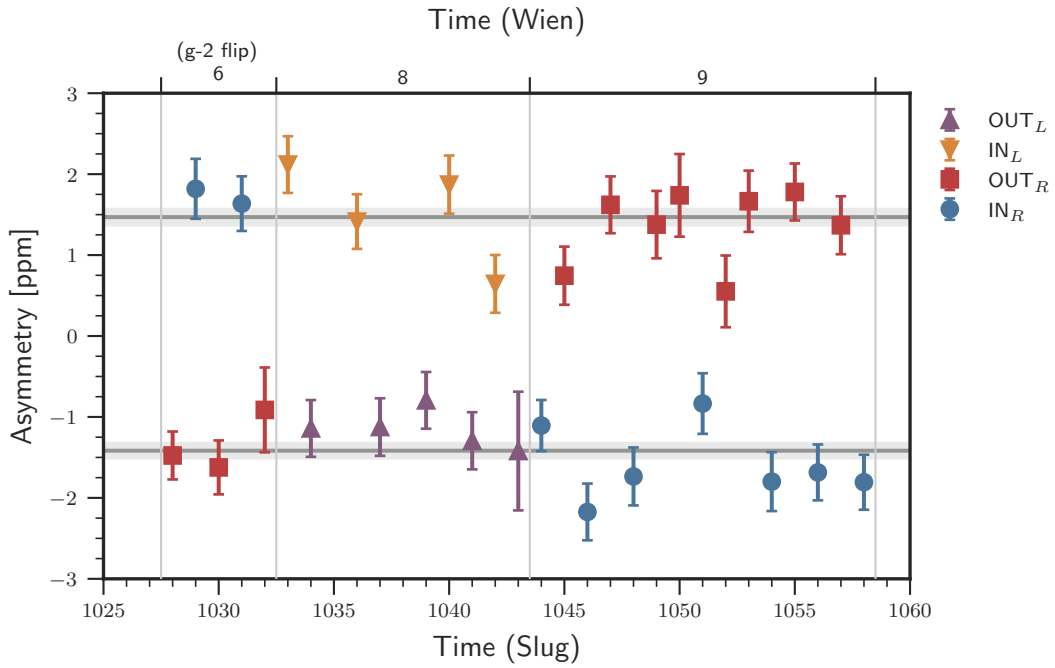
(a) Regressed asymmetry slug plot
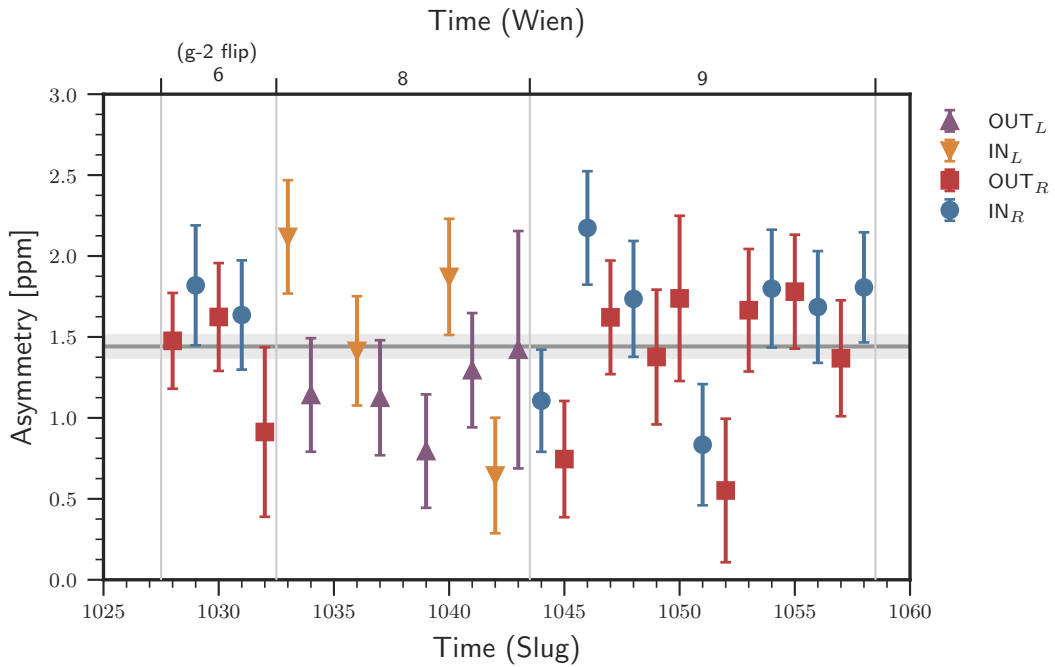
(b) Regressed sign-corrected asymmetry slug plot

Figure B.1: Regressed asymmetries from the Run 2 aluminum data set.
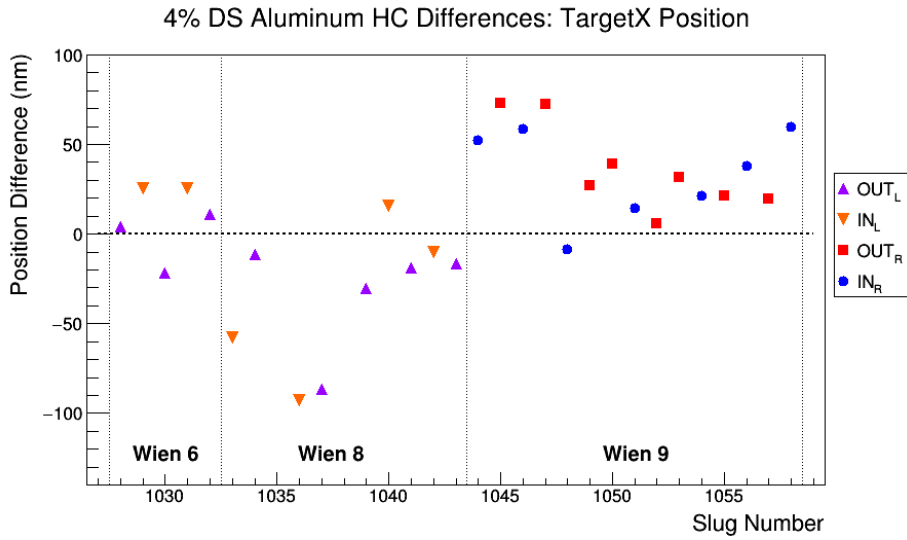
Figure B.2: Helicity-correlated differences in Target X for the Run 2 aluminum data set. Figure taken from the ELOG [127].
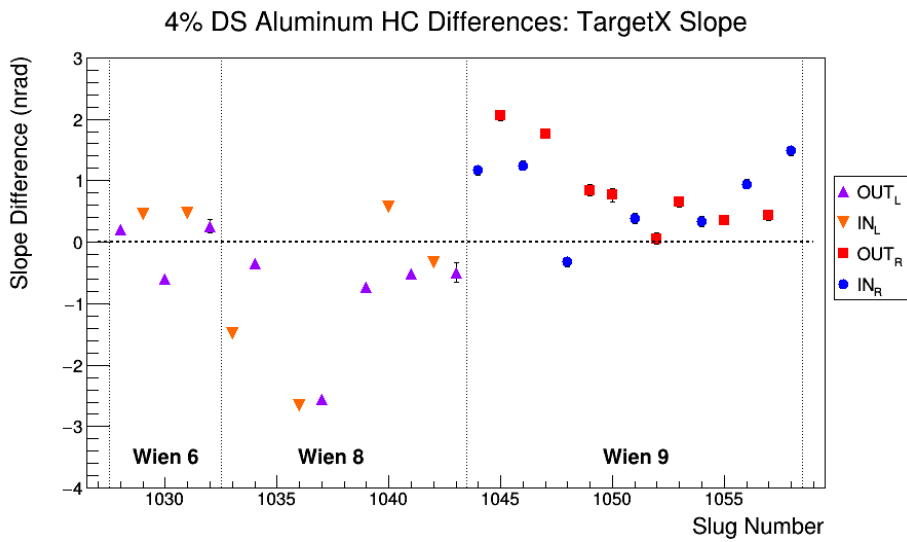
Figure B.3: Helicity-correlated differences in Target X slope for the Run 2 aluminum data set. Figure taken from the ELOG [127].
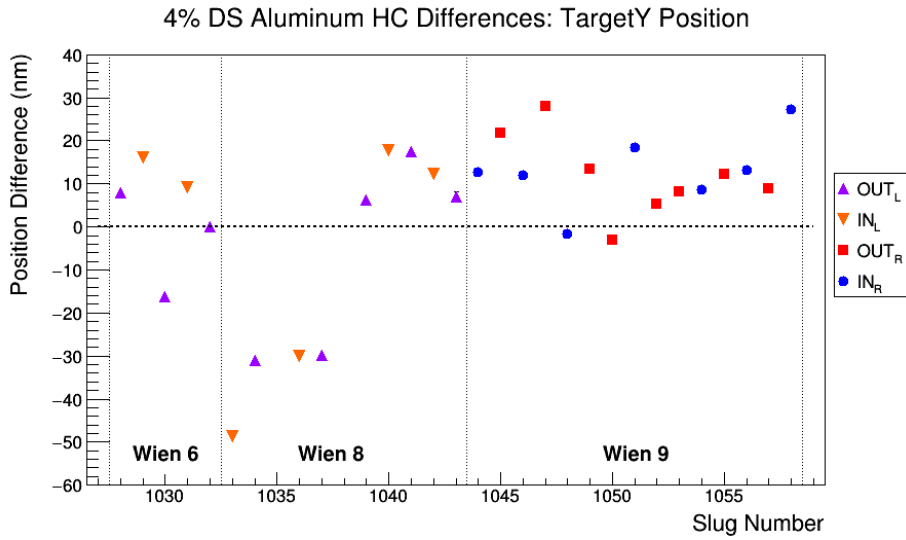
Figure B.4: Helicity-correlated differences in Target Y for the Run 2 aluminum data set. Figure taken from the ELOG [127].
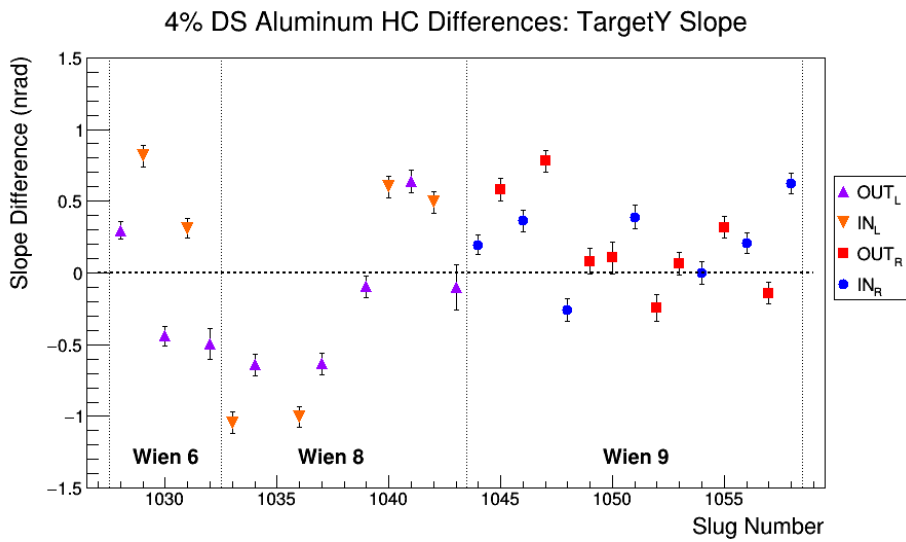
Figure B.5: Helicity-correlated differences in Target Y slope for the Run 2 aluminum data set. Figure taken from the ELOG [127].
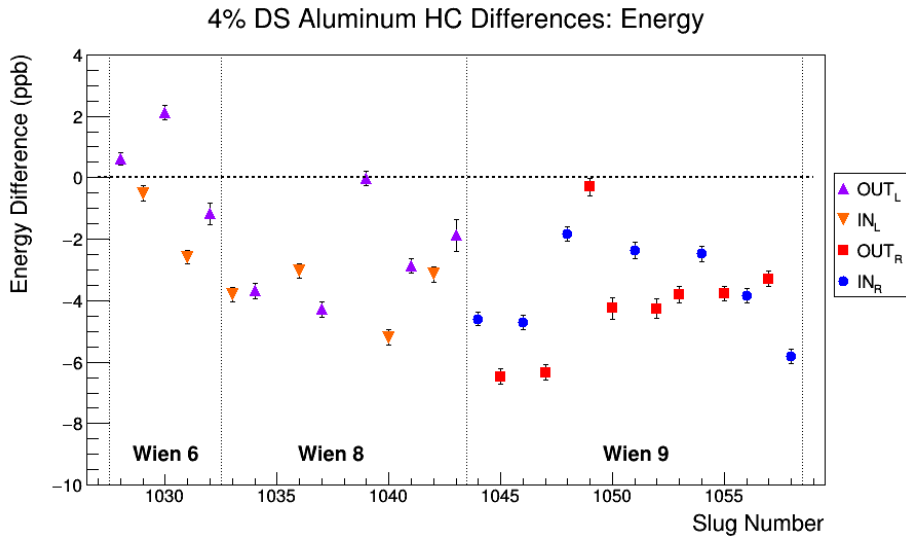
Figure B.6: Helicity-correlated differences in Energy for the Run 2 aluminum data set. Figure taken from the ELOG [127].
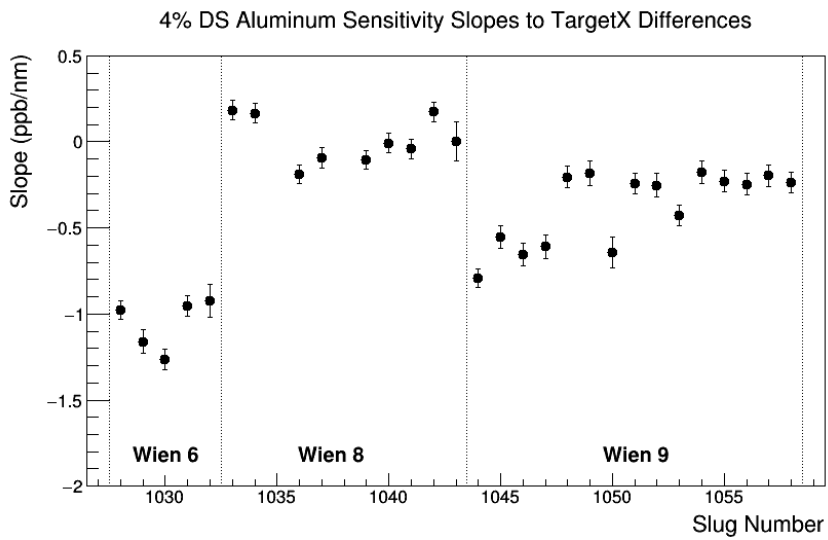
Figure B.7: Helicity-correlated sensitivities in Target X for the Run 2 aluminum data set. Figure taken from the ELOG [127].
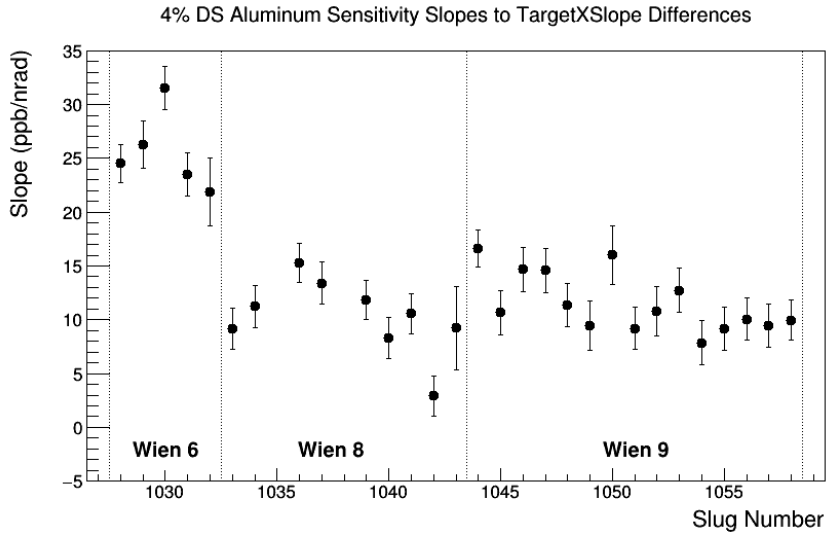
Figure B.8: Helicity-correlated sensitivities in Target X slope for the Run 2 aluminum data set. Figure taken from [127].
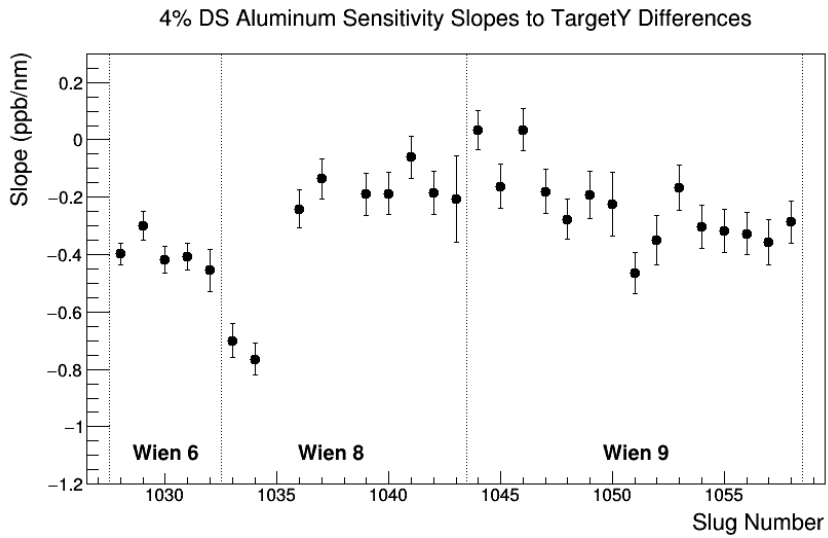
Figure B.9: Helicity-correlated sensitivities in Target Y for the Run 2 aluminum data set. Figure taken from ELOG [127].
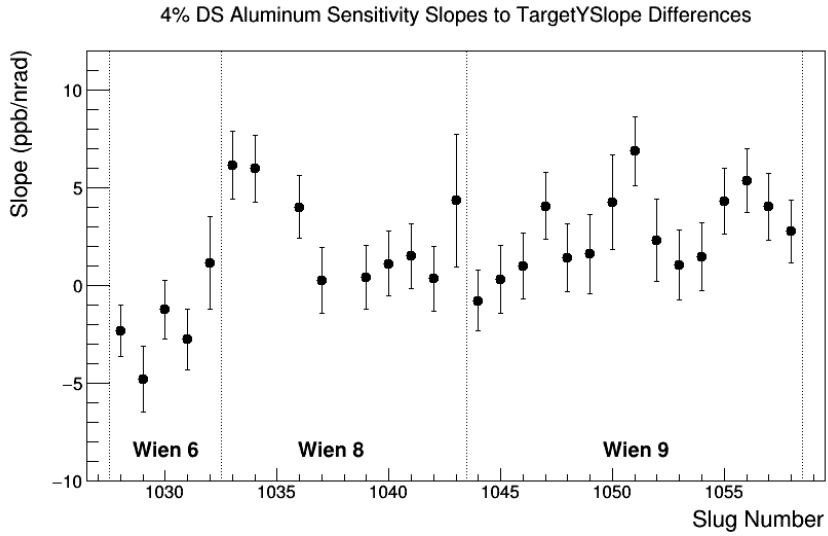
Figure B.10: Helicity-correlated sensitivities in Target Y slope for the Run 2 aluminum data set. Figure taken from ELOG [127].
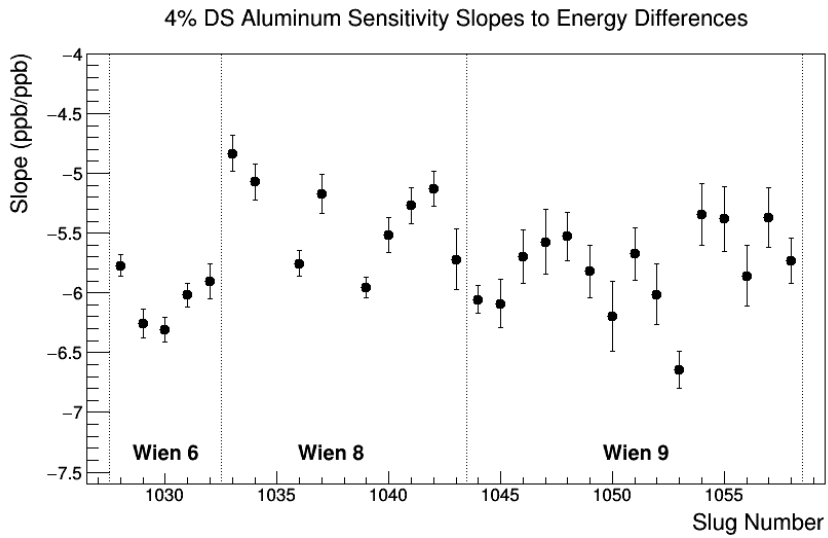
Figure B.11: Helicity-correlated sensitivities in Energy for the Run 2 aluminum data set. Figure taken from ELOG [127].
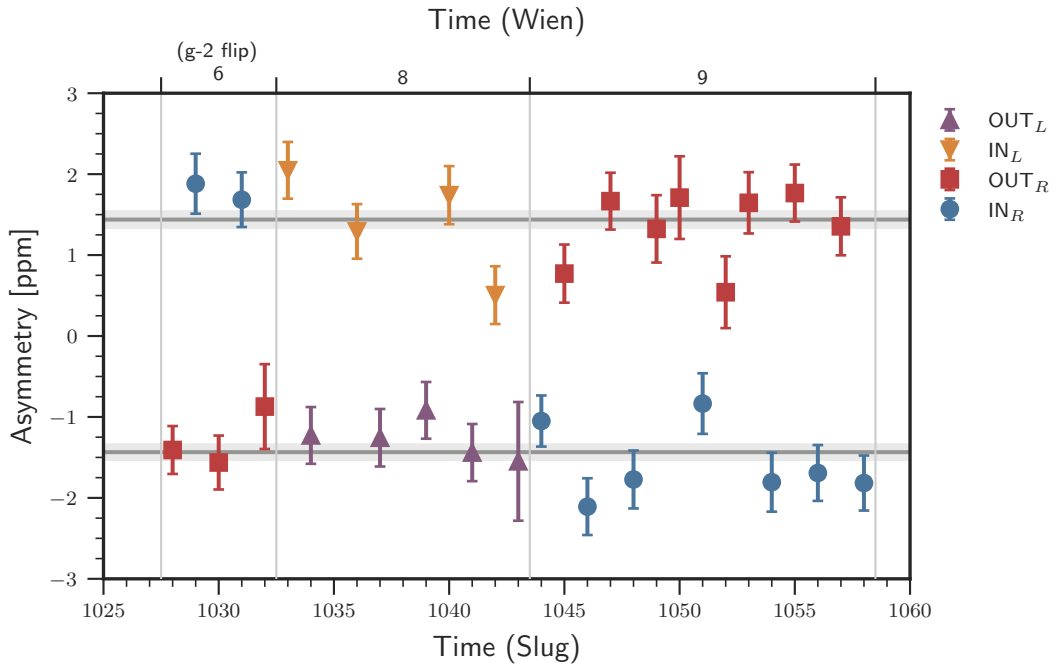
(a) Beamline background asymmetry slug plot
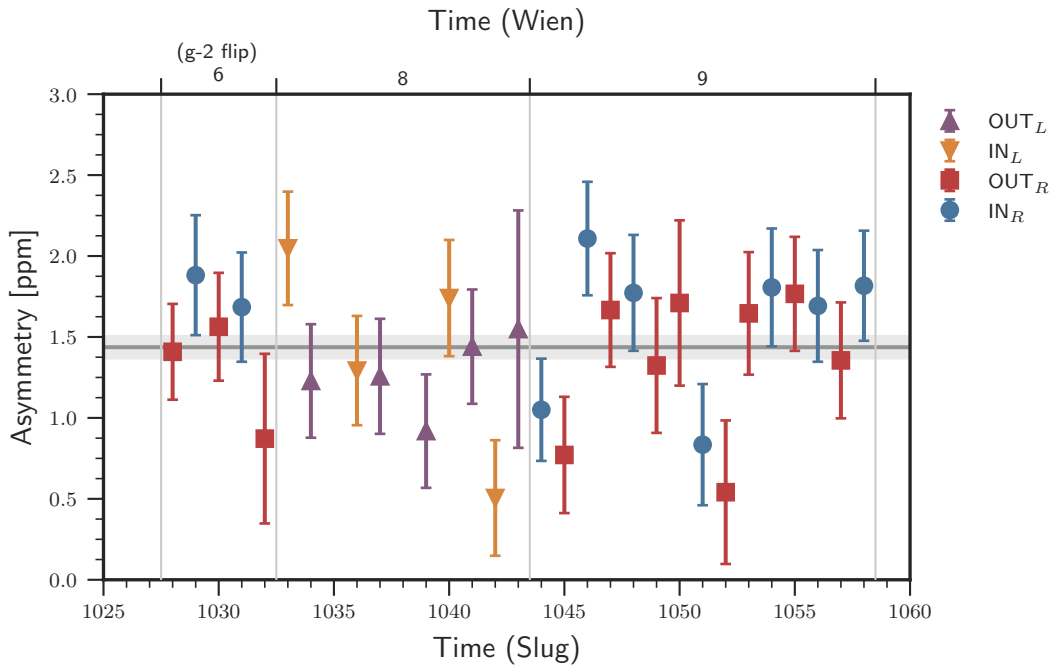
(b) Beamline background sign-corrected asymmetry slug plot

Figure B.12: Beamline background asymmetries from the Run 2 aluminum data set.
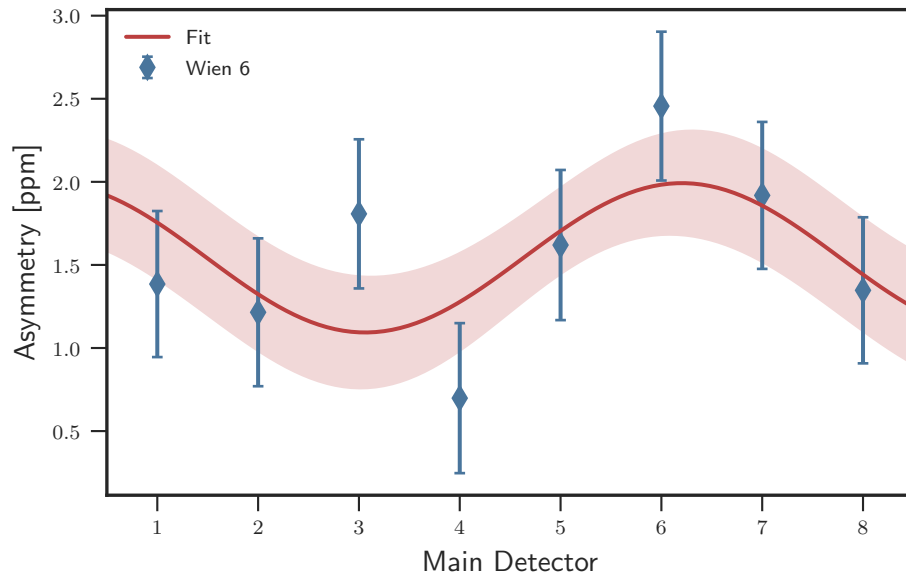
Figure B.13: Residual transverse polarization extraction using a sinusoidal fit to main detector regressed asymmetries in Wien 6. Uncertainties on blue data points are statistical only. The red band is a 1σ uncertainty associated with the fit.
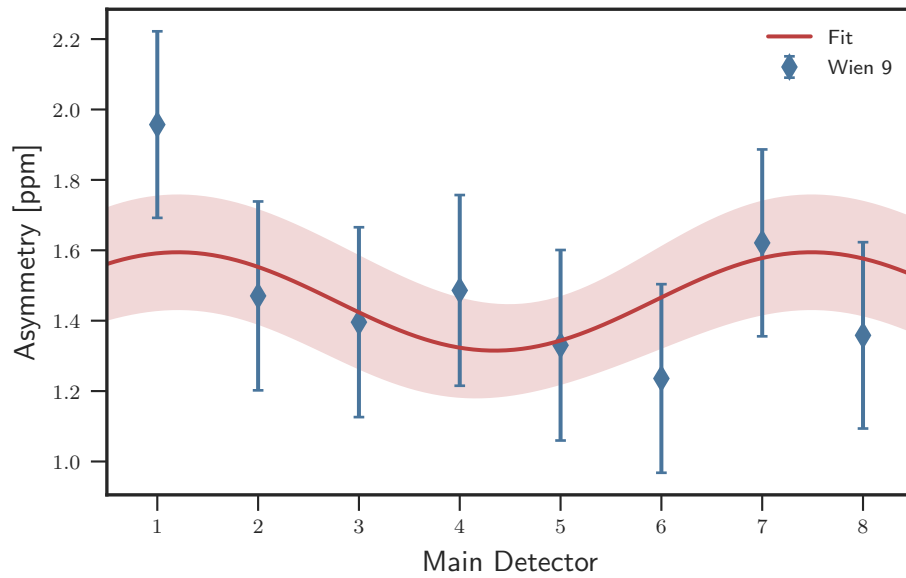
Figure B.14: Residual transverse polarization extraction using a sinusoidal fit to main detector regressed asymmetries in Wien 9. Uncertainties on blue data points are statistical only. The red band is a 1σ uncertainty associated with the fit.
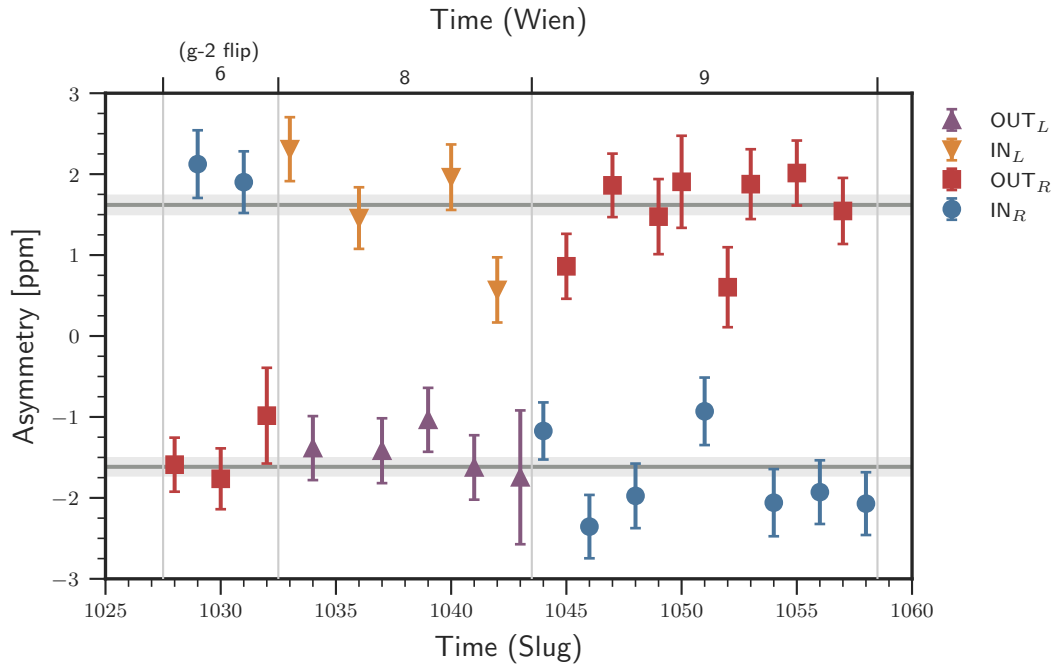
(a) Polarization-corrected asymmetry slug plot
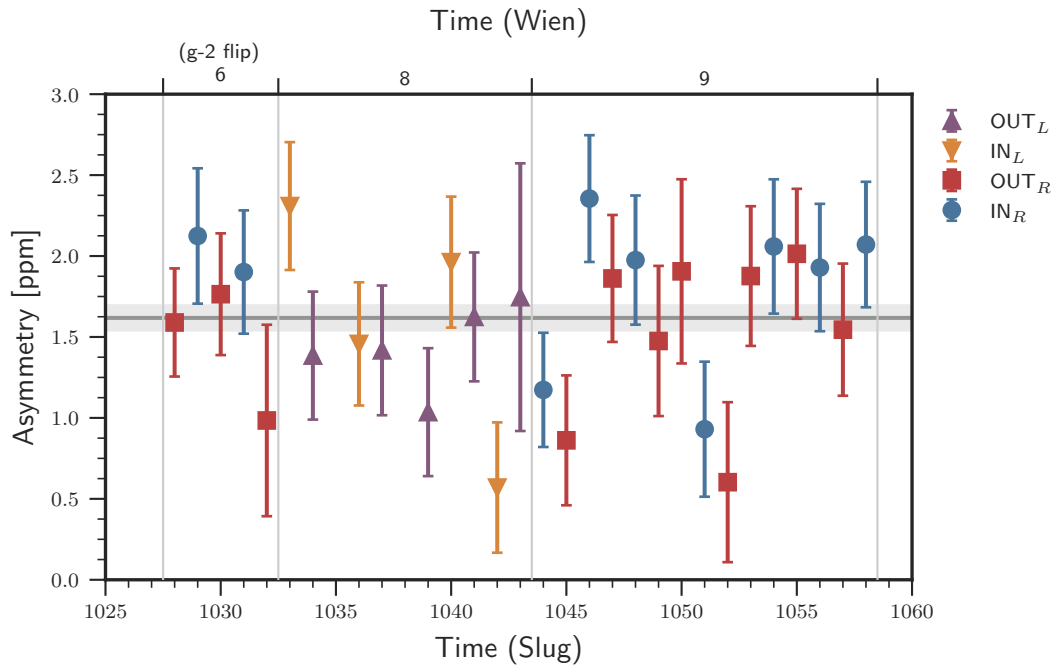
(b) Polarization sign-corrected asymmetry slug plot

Figure B.15: Polarization-corrected asymmetries from the Run 2 aluminum data set.
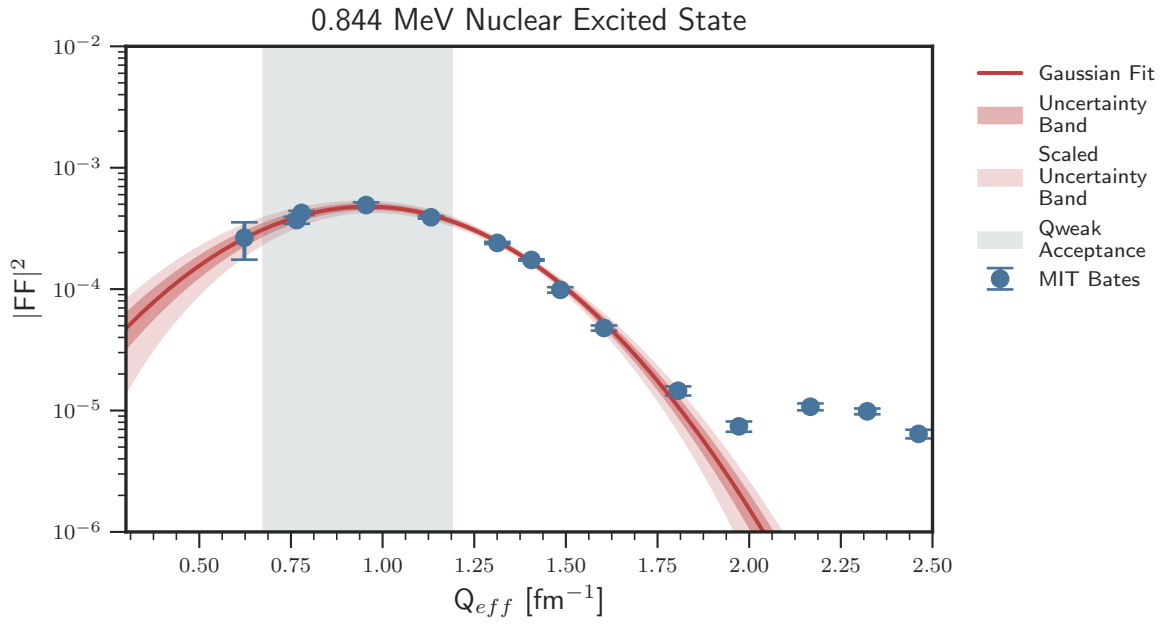
Figure B.16: Gaussian function fitted to ^{27}Al's 0.844 MeV excited state form factor data.
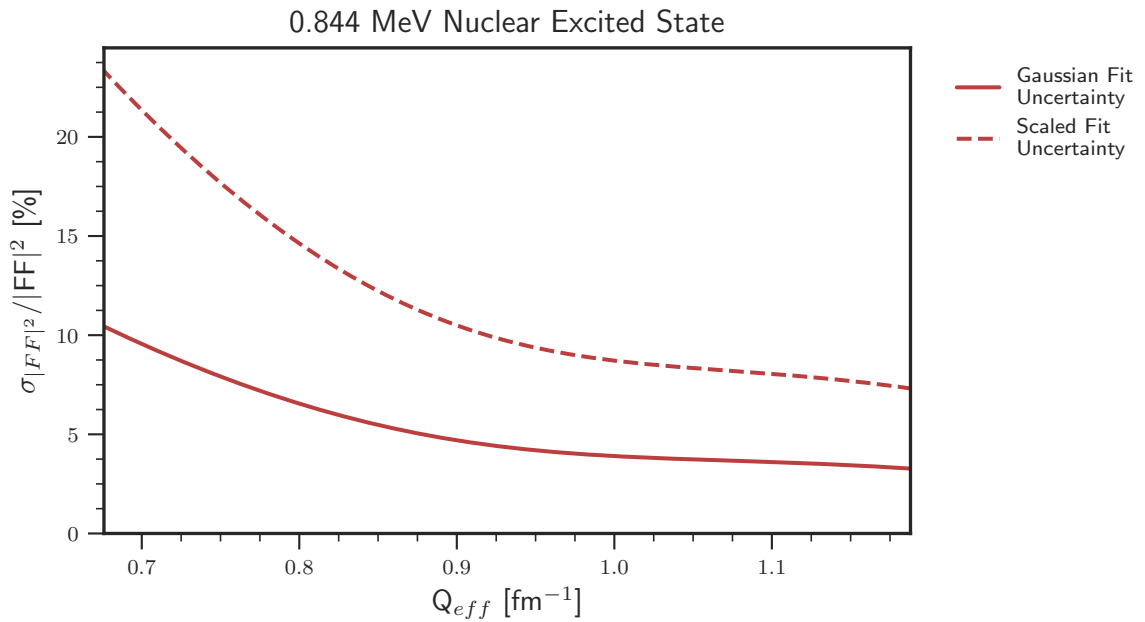
Figure B.17: Calculated fit uncertainty (relative) for 0.844 MeV excited state. Uncertainty assigned to simulation extracted yields taken from average Q value of the scaled uncertainty curve.
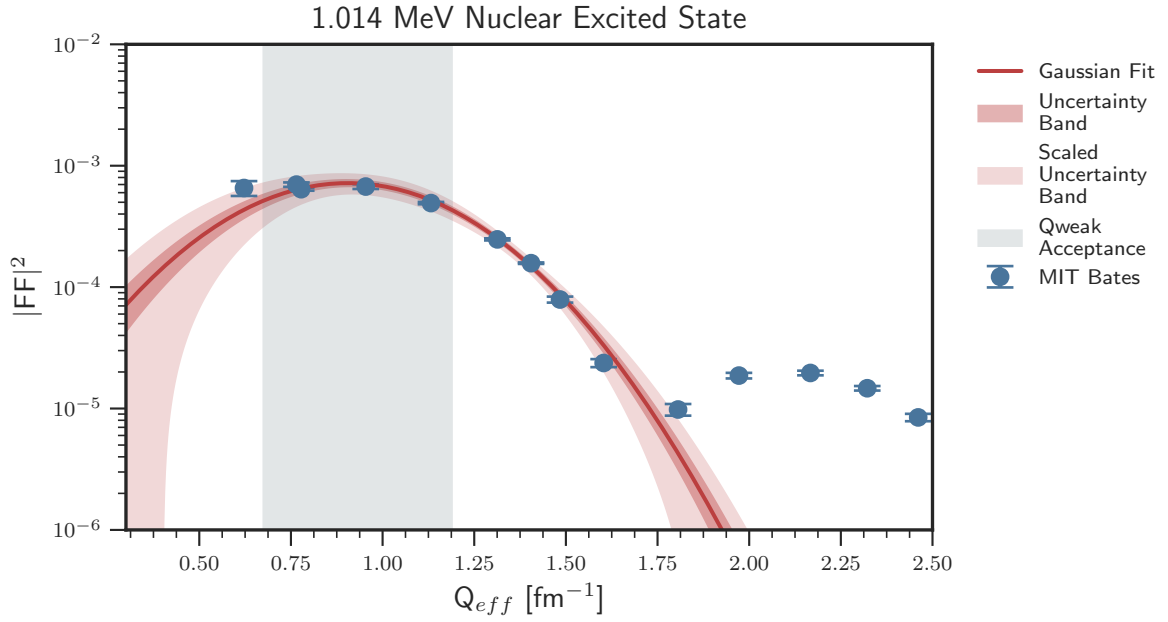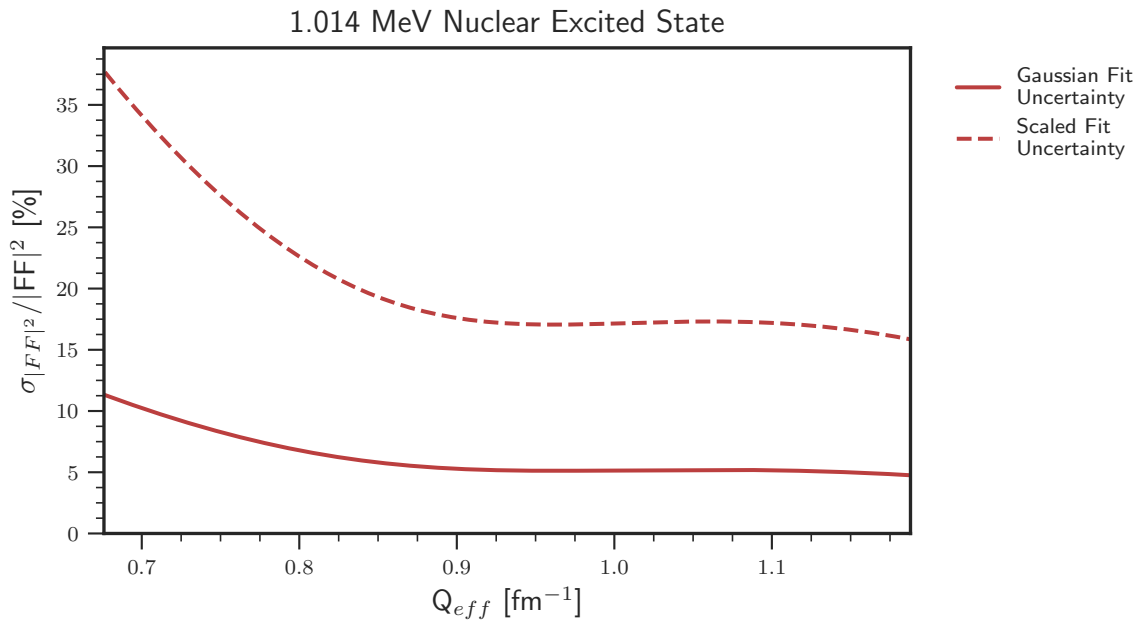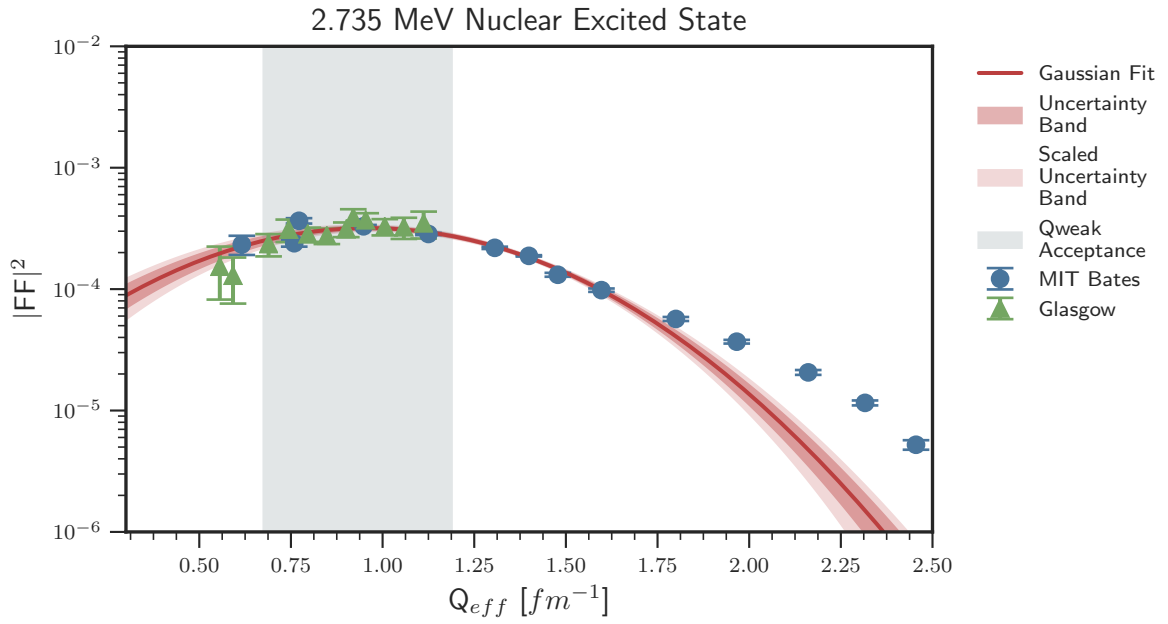
Figure B.18: Gaussian function fitted to ^{27}Al's 1.014 MeV excited state form factor data.
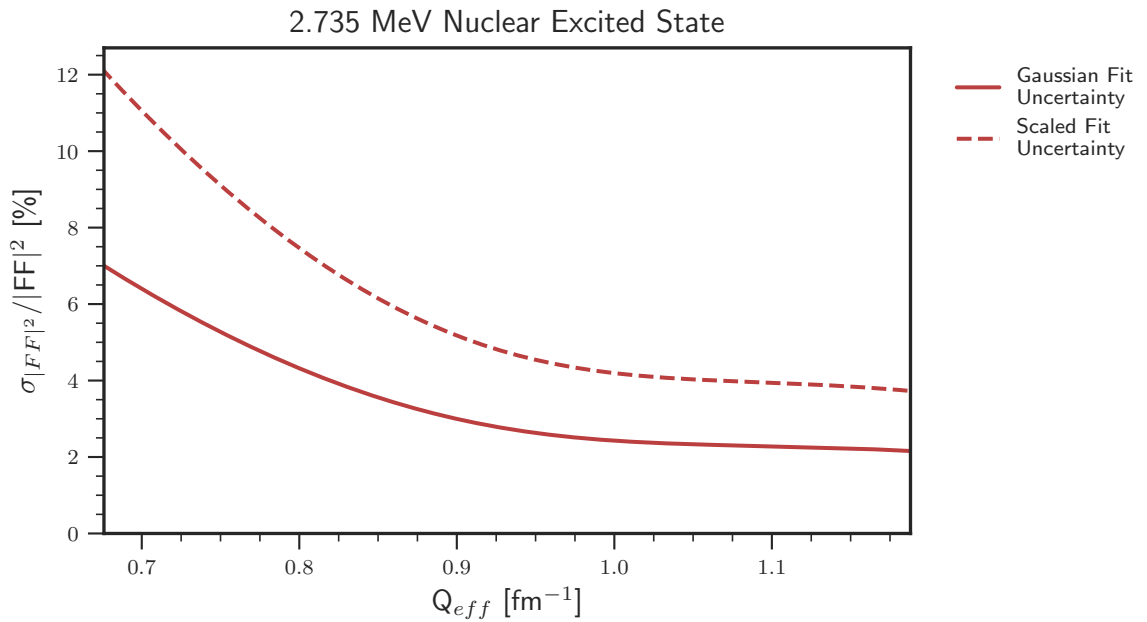

Figure B.19: Calculated fit uncertainty (relative) for 1.014 MeV excited state. Uncertainty assigned to simulation extracted yields taken from average Q value of the scaled uncertainty curve.

Figure B.20: Gaussian function fitted to ^{27}Al's 2.735 MeV excited state form factor data.

Figure B.21: Calculated fit uncertainty (relative) for 2.735 MeV excited state. Uncertainty assigned to simulation extracted yields taken from average Q value of the scaled uncertainty curve.
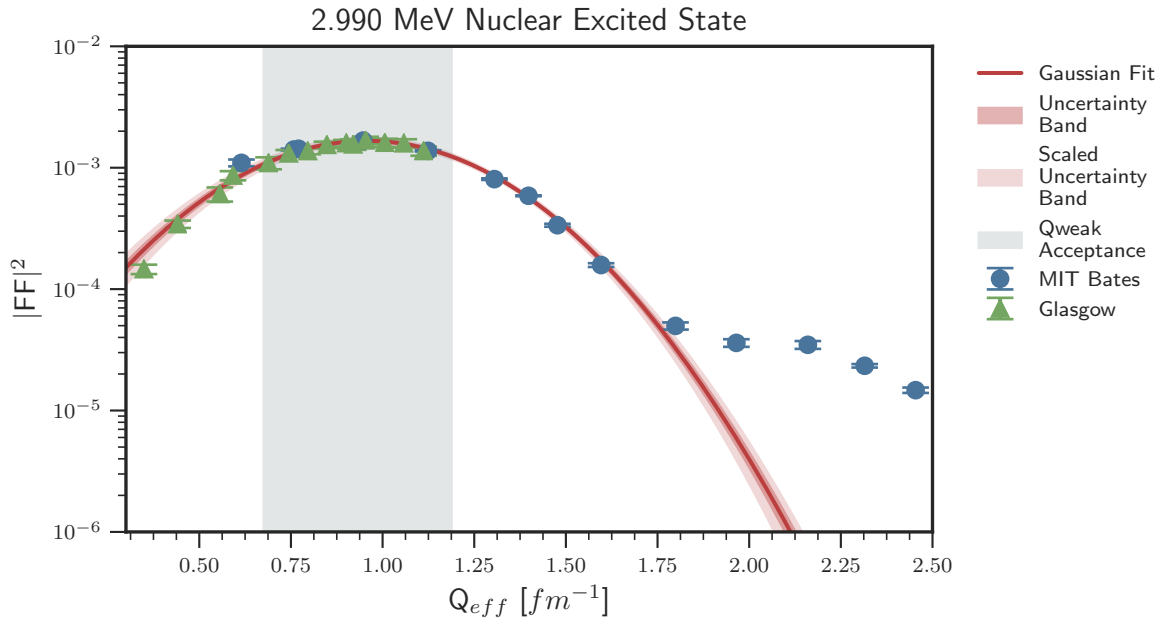
Figure B.22: Gaussian function fitted to ^{27}Al's 2.990 MeV excited state form factor data.
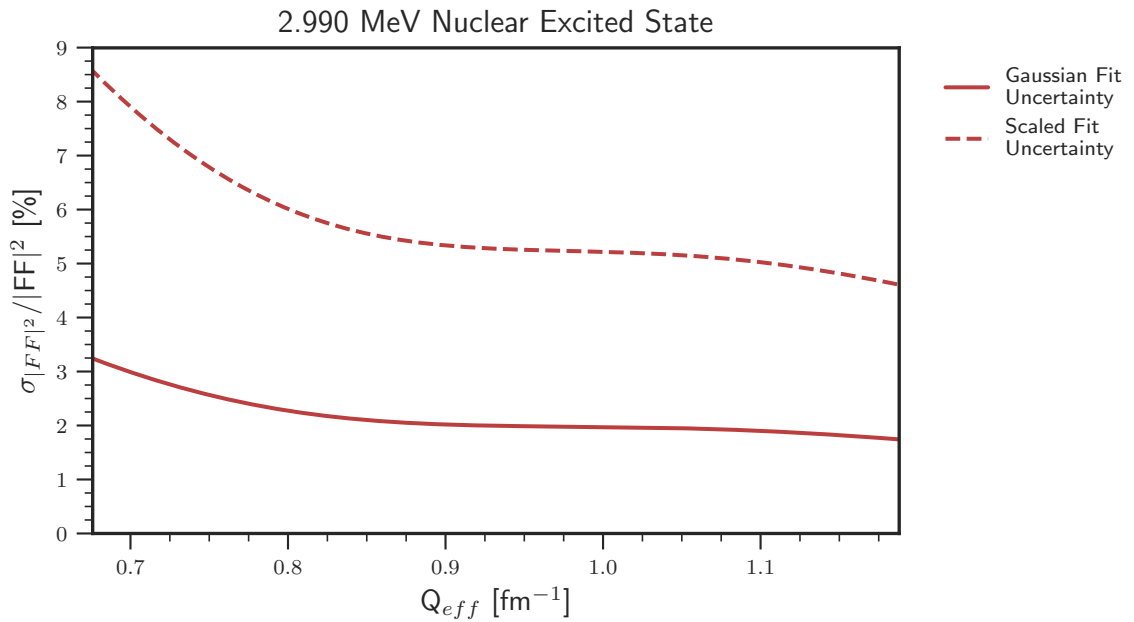

Figure B.23: Calculated fit uncertainty (relative) for 2.990 MeV excited state. Uncertainty assigned to simulation extracted yields taken from average Q value of the scaled uncertainty curve.
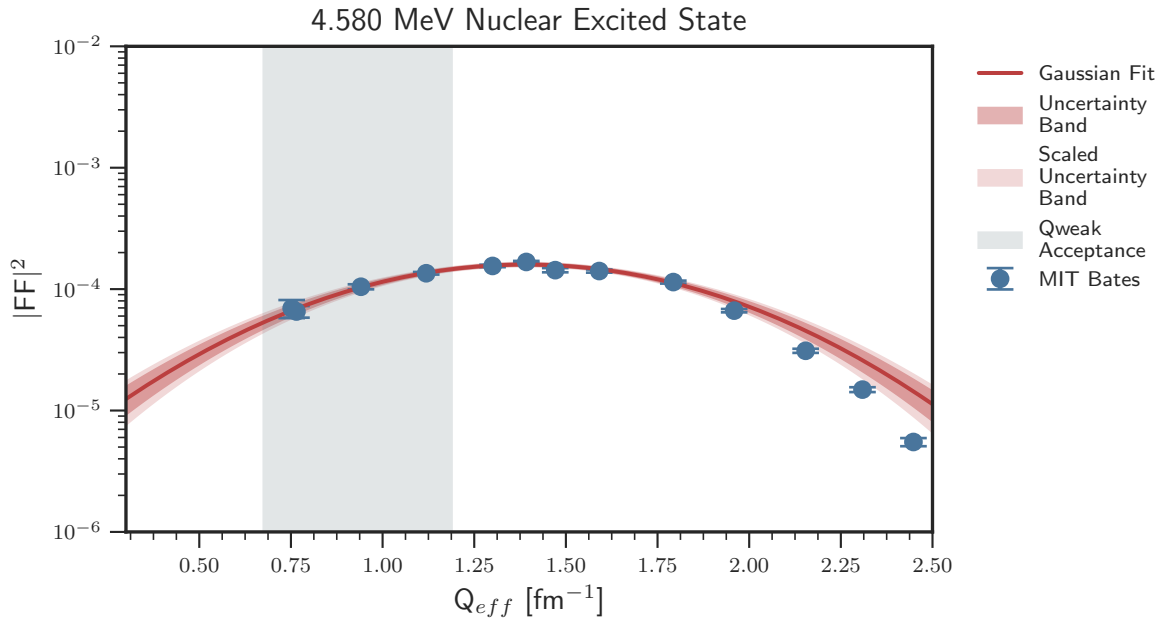
Figure B.24: Gaussian function fitted to ^{27}Al's 4.580 MeV excited state form factor data.

Figure B.25: Calculated fit uncertainty (relative) for 4.580 MeV excited state. Uncertainty
assigned to simulation extracted yields taken from average Q value of the scaled uncertainty
curve.

Figure B.26: Gaussian function fitted to ^{27}Al's 4.812 MeV excited state form factor data.
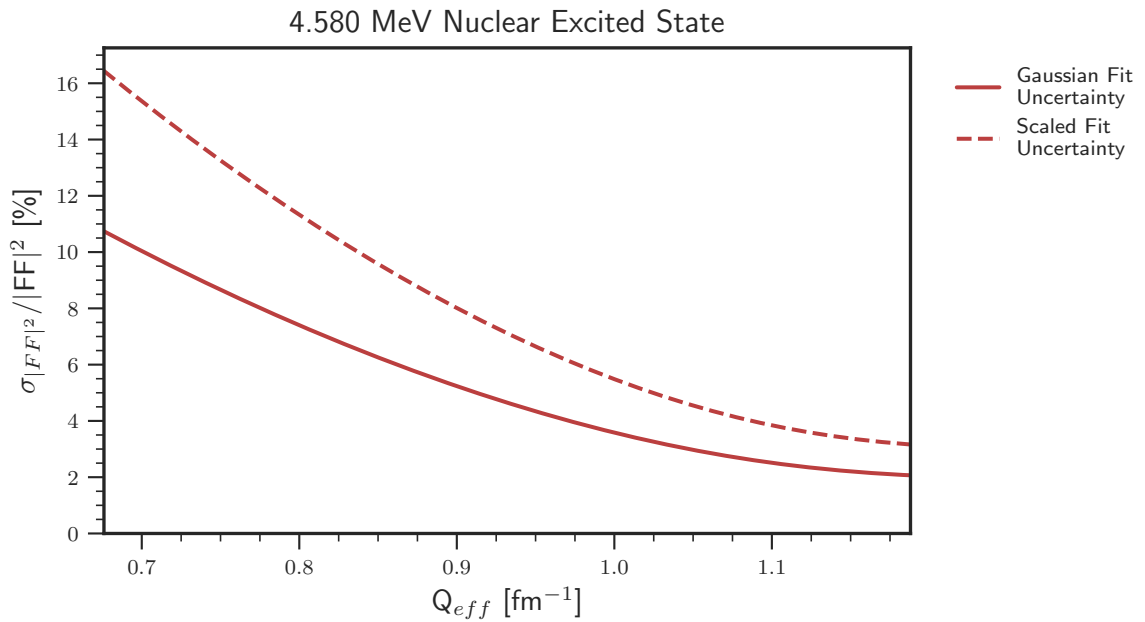

Figure B.27: Calculated fit uncertainty (relative) for 4.812 MeV excited state. Uncertainty assigned to simulation extracted yields taken from average Q value of the scaled uncertainty curve.

Figure B.28: Gaussian function fitted to ^{27}Al's 5.430 MeV excited state form factor data.

Figure B.29: Calculated fit uncertainty (relative) for 5.430 MeV excited state. Uncertainty assigned to simulation extracted yields taken from average Q value of the scaled uncertainty curve.
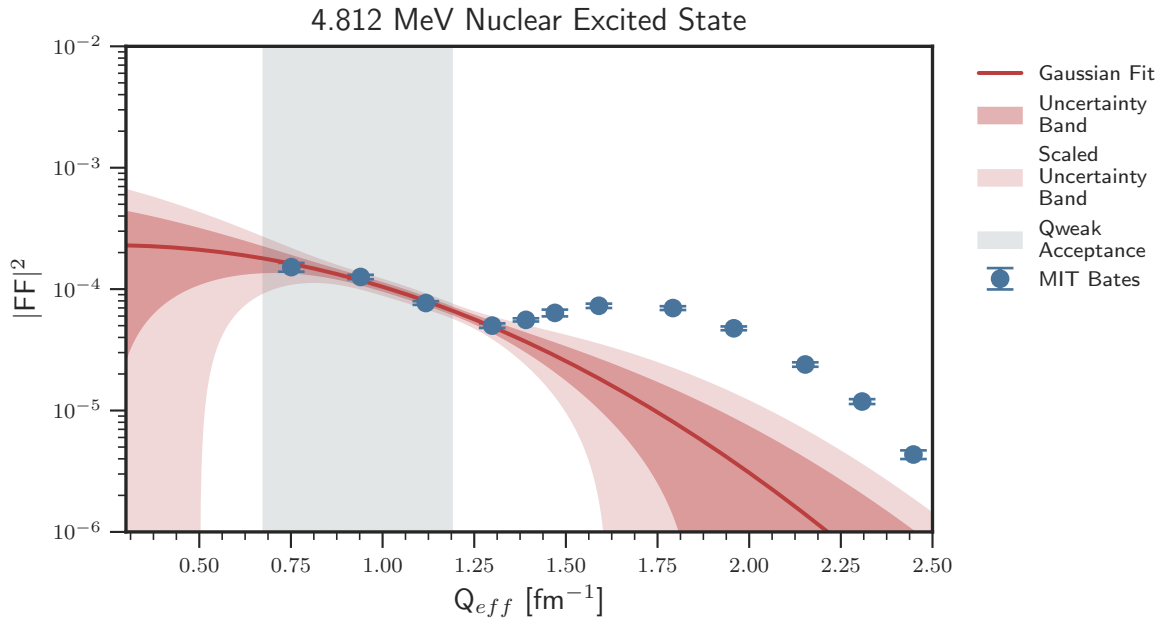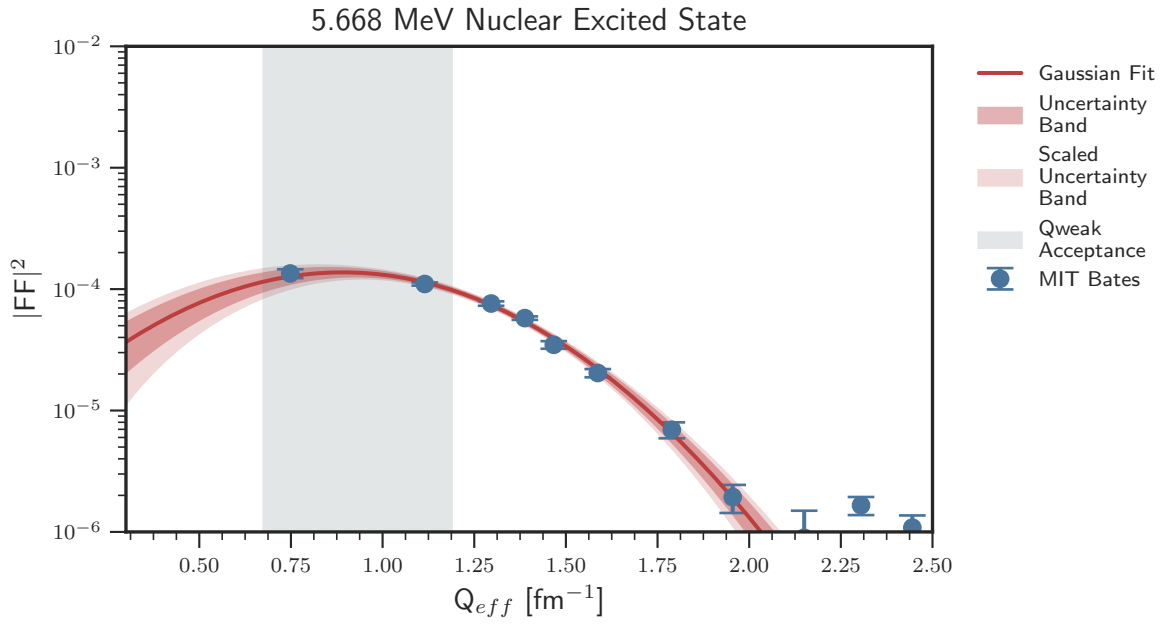
Figure B.30: Gaussian function fitted to ^{27}Al's 5.668 MeV excited state form factor data.
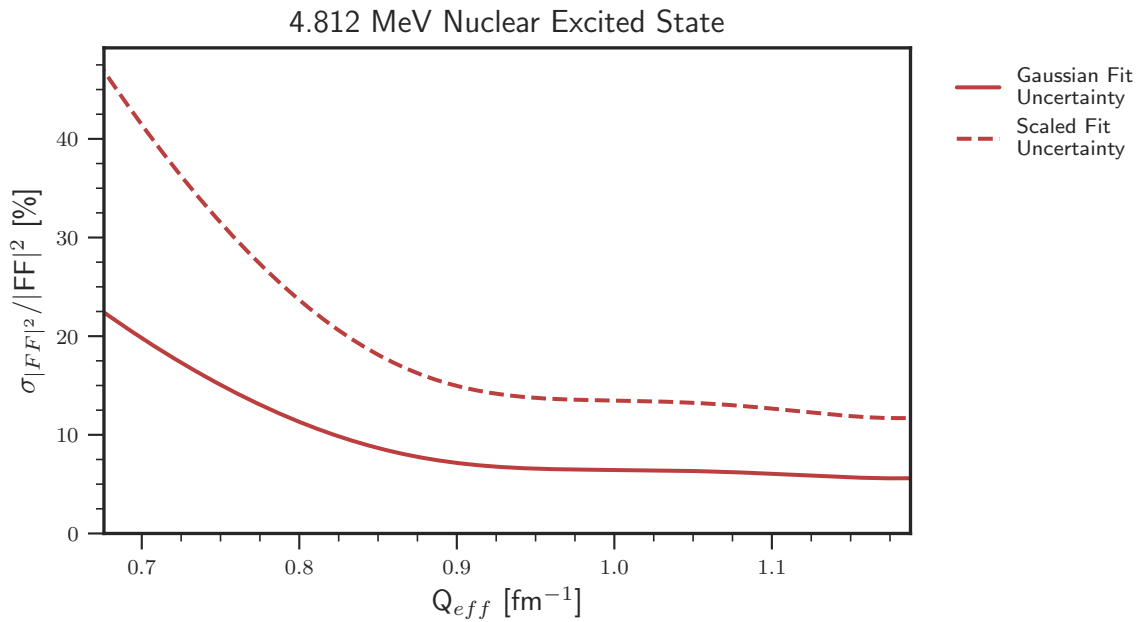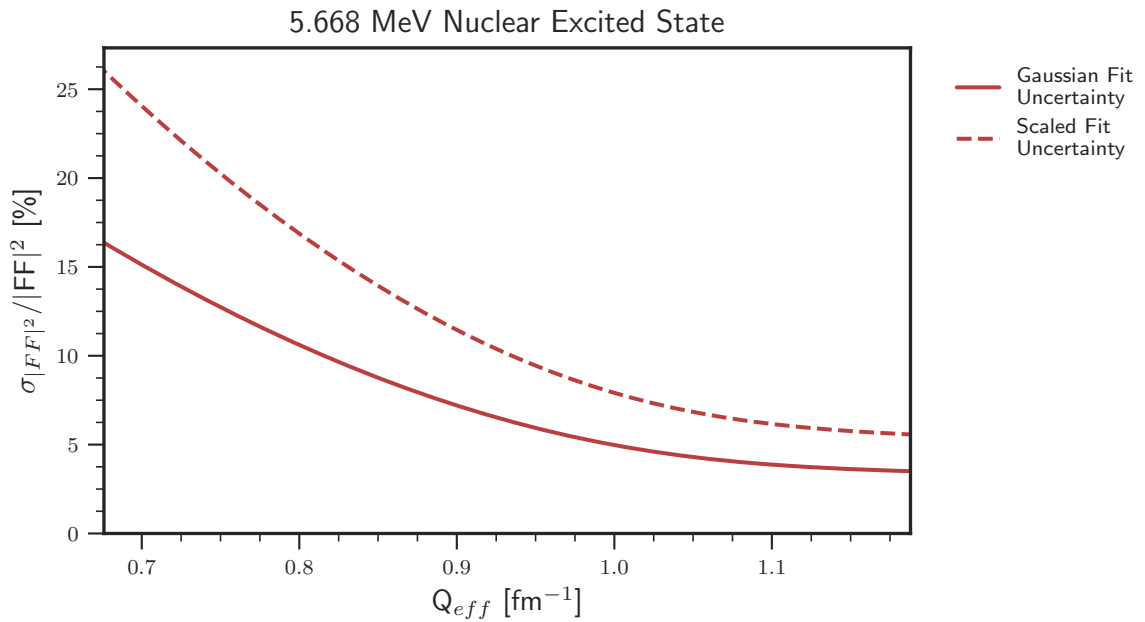

Figure B.31: Calculated fit uncertainty (relative) for 5.668 MeV excited state. Uncertainty assigned to simulation extracted yields taken from average Q value of the scaled uncertainty curve.
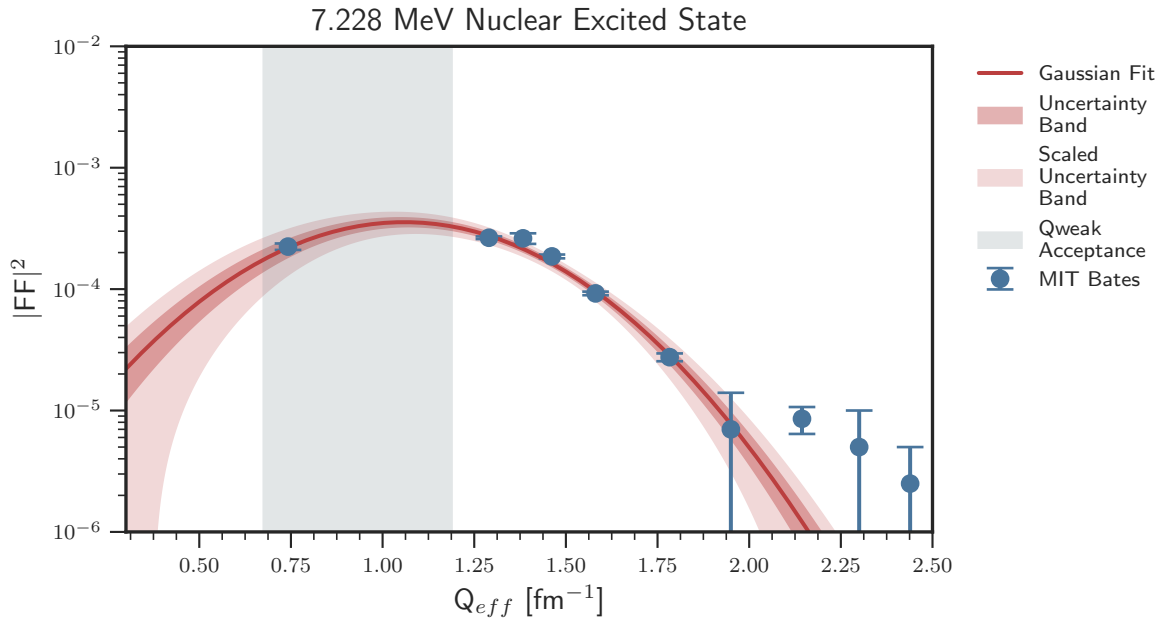
Figure B.32: Gaussian function fitted to ^{27}Al's 7.228 MeV excited state form factor data.

Figure B.33: Calculated fit uncertainty (relative) for 7.228 MeV excited state. Uncertainty assigned to simulation extracted yields taken from average Q value of the scaled uncertainty curve.
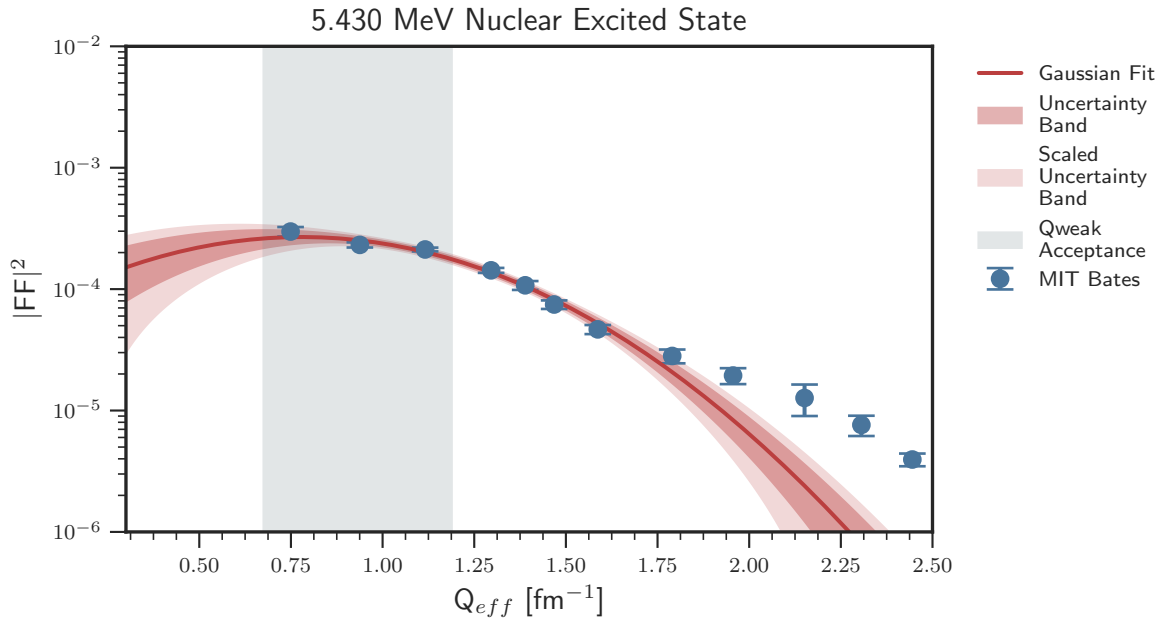
Figure B.34: Gaussian function fitted to ^{27}Al's 7.477 MeV excited state form factor data.
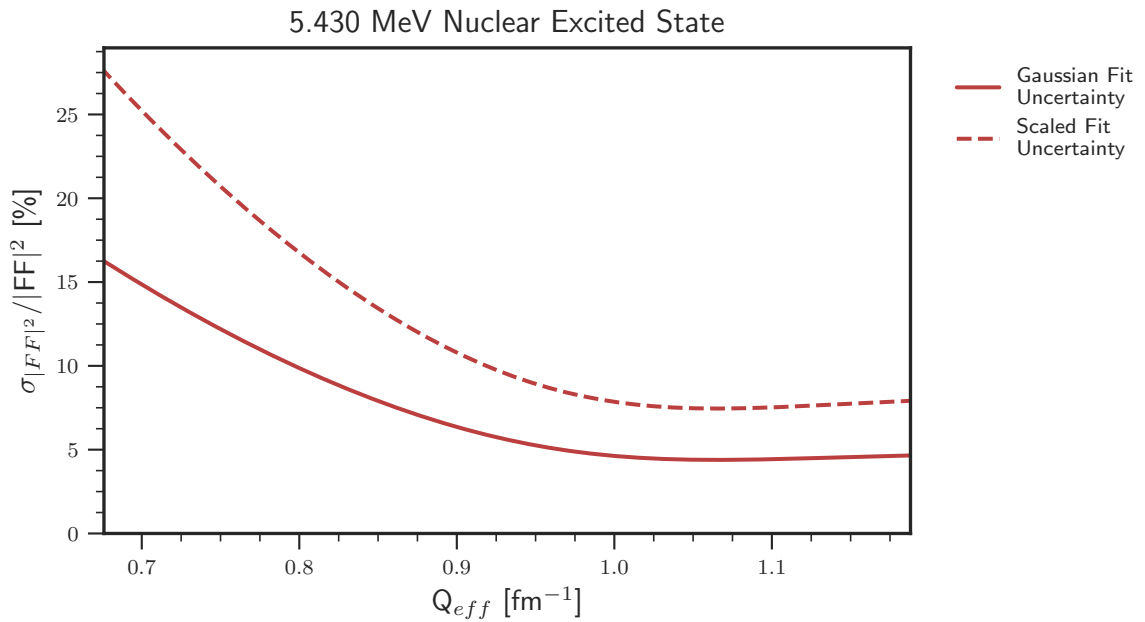

Figure B.35: Calculated fit uncertainty (relative) for 7.477 MeV excited state. Uncertainty assigned to simulation extracted yields taken from average Q value of the scaled uncertainty curve.
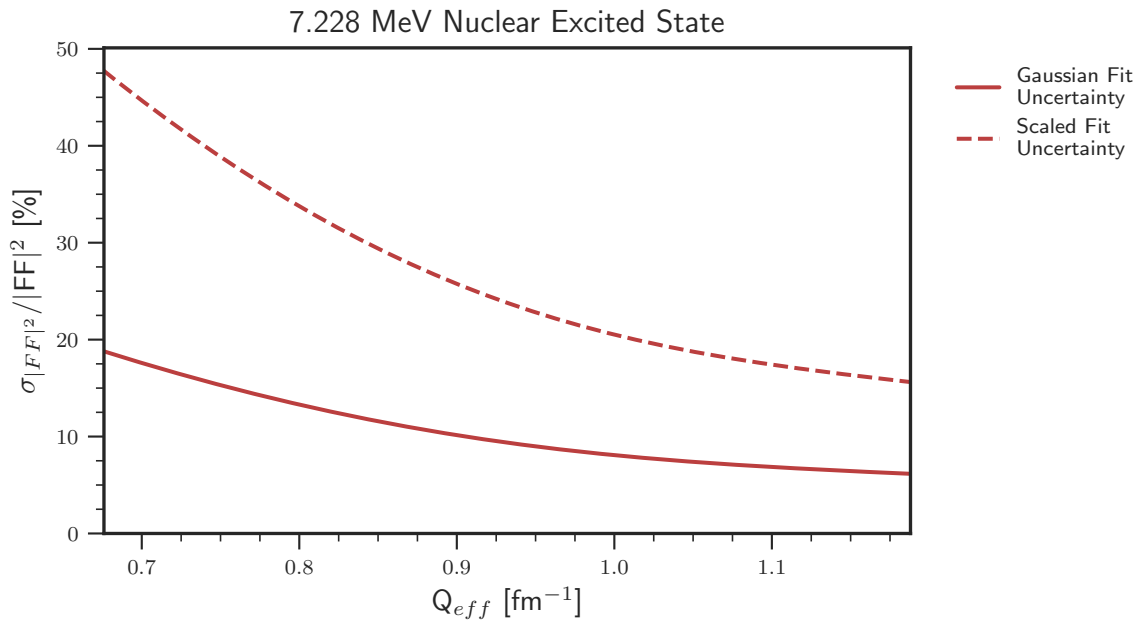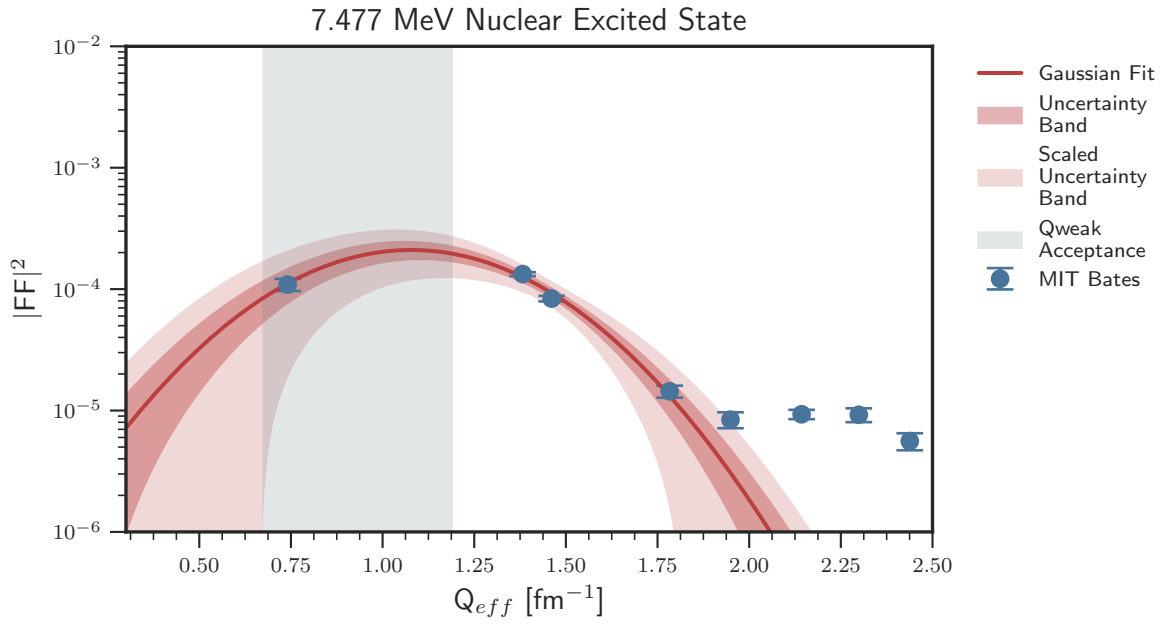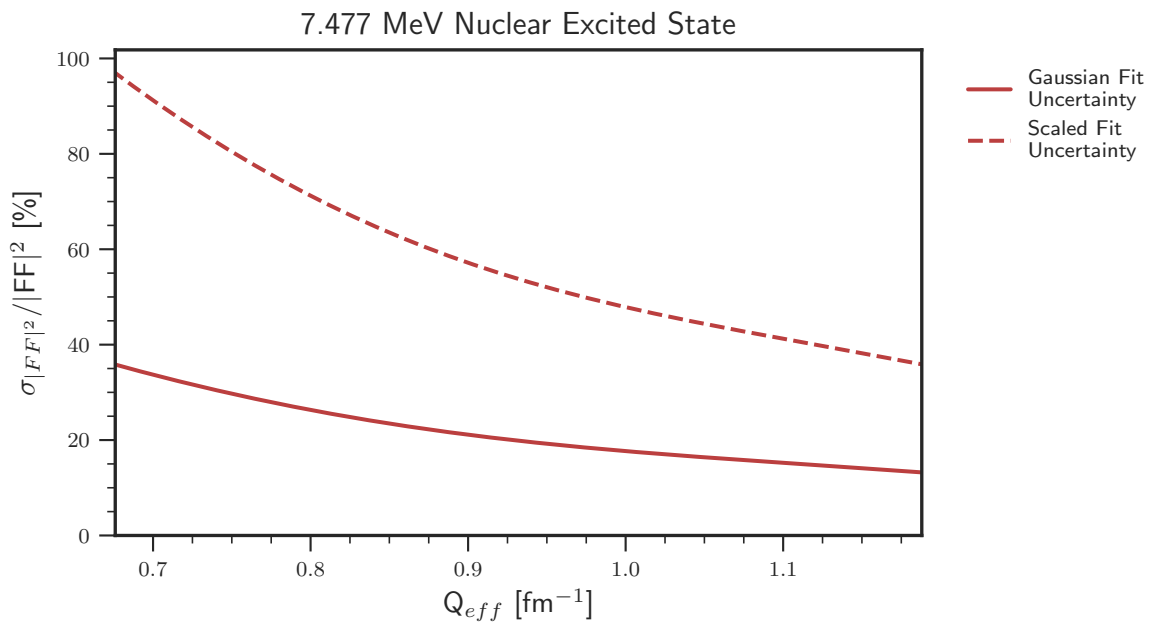
Appendix C

Beam-normal Single-spin ^{27}Al Asymmetry Analysis Supplement

C.1 Beam-normal Single-spin Asymmetry Run List

Table C.1: List of runs and experimental parameters for the beam-normal single-spin aluminum data set taken during Run 1 and Run 2. The beam and QTOR currents are the maximum typical values for a given run; the beam current values are determined using BCM 6. The last three columns note the states of the slow-helicity reversal experimental controls. In particular, the "Wien State" column indicates the direction of the transverse polarized beam.

Run	Slug	Beam Current [μA]	QTOR Current [A]	Precession State	Wien State	IHWP
Run 1				February 9, 2011		
9846	101 001	23.0	8920.0	Normal	Vertical	IN
9847	101 001	24.0	8920.0	Normal	Vertical	IN
9848	101 001	23.0	8920.0	Normal	Vertical	IN
9849	101 001	23.0	8920.0	Normal	Vertical	IN
9850	101 001	24.0	8920.0	Normal	Vertical	IN
9851	101 001	24.0	8920.0	Normal	Vertical	IN
9852	101 001	23.0	8920.0	Normal	Vertical	IN
9853	101 002	23.0	8920.0	Normal	Vertical	OUT
9854	101 002	23.0	8920.0	Normal	Vertical	OUT
9855	101 002	23.0	8920.0	Normal	Vertical	OUT
9856	101 002	23.0	8920.0	Normal	Vertical	OUT
9857	101 002	23.0	8920.0	Normal	Vertical	OUT
9858	101 002	23.0	8920.0	Normal	Vertical	OUT

Table C.1: List of runs and experimental parameters for the beam-normal single-spin aluminum data set taken during Run 1 and Run 2. The beam and QTOR currents are the maximum typical values for a given run; the beam current values are determined using BCM 6. The last three columns note the states of the slow-helicity reversal experimental controls. In particular, the "Wien State" column indicates the direction of the transverse polarized beam.

Run	Slug	Beam Current [µA]	QTOR Current [A]	Precession State	Wien State	IHWP
Run 2			February 16-20, 2012			
16067	601 001	61.0	6697.0	Normal	Vertical	IN
16068	601 002	62.0	6697.0	Normal	Vertical	OUT
16069	601 002	60.0	6697.0	Normal	Vertical	OUT
16070	101 003	60.0	8899.0	Normal	Vertical	OUT
16072	101 004	61.0	8899.0	Normal	Vertical	IN
16106	201 001	61.0	8899.0	Normal	Horizontal	OUT
16107	201 001	62.0	8899.0	Normal	Horizontal	OUT
16108	201 001	60.0	8899.0	Normal	Horizontal	OUT
16109	201 001	62.0	8899.0	Normal	Horizontal	OUT
16112	201 002	60.0	8899.0	Normal	Horizontal	IN
16113	201 002	61.0	8899.0	Normal	Horizontal	IN
16114	201 002	62.0	8899.0	Normal	Horizontal	IN
16115	701 001	61.0	6697.0	Normal	Horizontal	IN
16116	701 001	61.0	6697.0	Normal	Horizontal	IN
16118	701 002	61.0	6697.0	Normal	Horizontal	OUT
16119	701 002	61.0	6697.0	Normal	Horizontal	OUT
16120	701 003	61.0	7298.0	Normal	Horizontal	OUT
16121	701 003	61.0	7298.0	Normal	Horizontal	OUT
16122	701 004	61.0	7298.0	Normal	Horizontal	IN
16123	701 004	61.0	7298.0	Normal	Horizontal	IN
16124	701 004	61.0	7298.0	Normal	Horizontal	IN
16160	701 004	60.0	7298.0	Normal	Horizontal	IN
16161	701 005	61.0	7298.0	Normal	Horizontal	OUT

C.2   Raw Asymmetries

- Raw asymmetry plots:

  - Run 1 Vertical: Fig. C.1

  - Run 2 Vertical: Fig. C.2

- Raw asymmetry fit parameters: Table C.2

C.3   Helicity-correlated Beam Corrections

- Regressed asymmetry plots:

    - Run 1 Vertical: Fig. C.3

    - Run 2 Horizontal: Fig. C.4

    - Run 2 Vertical: Fig. C.5

- Regressed asymmetry fit parameters: Table C.3
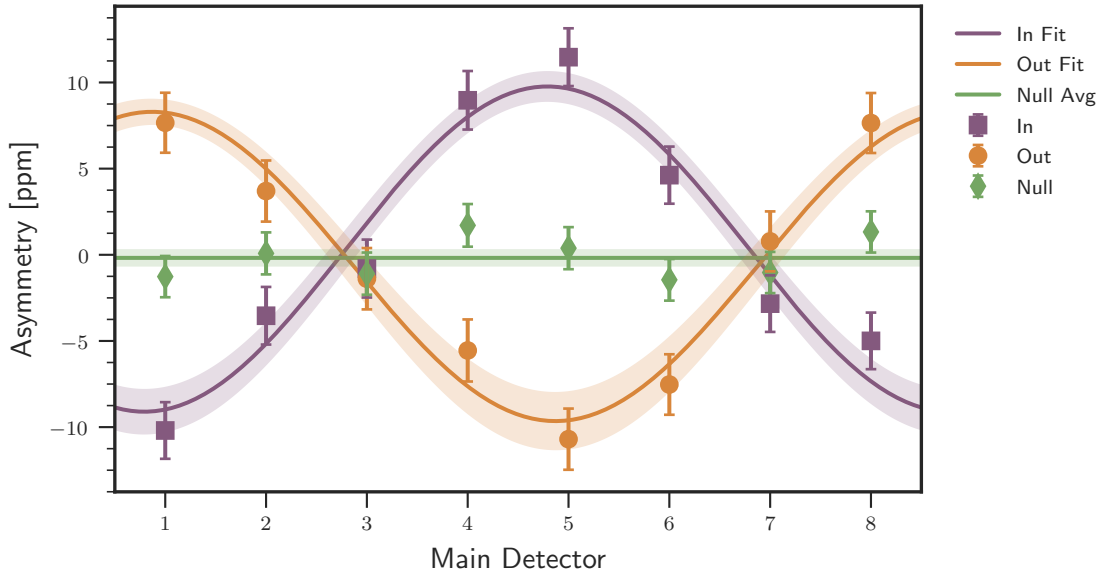
(a) IHWP plot
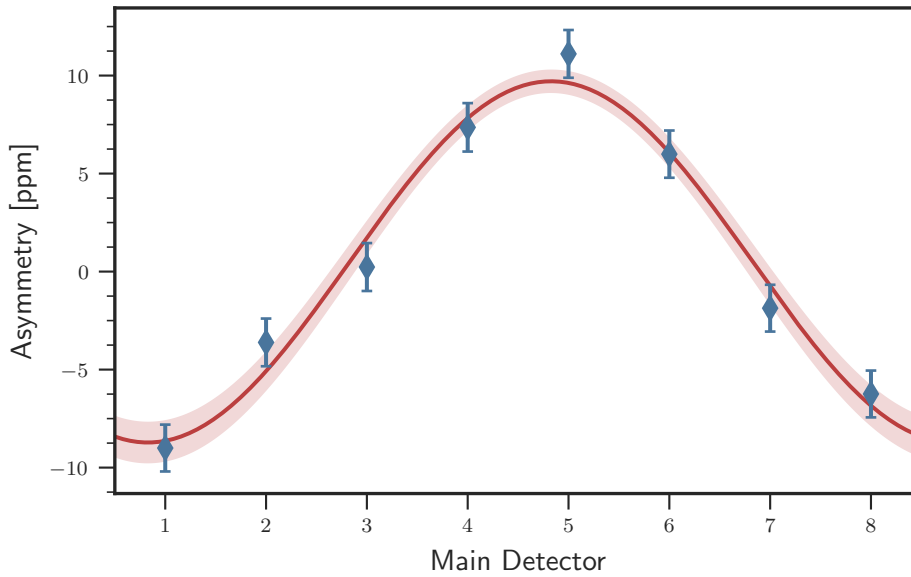
(b) Sign-corrected plot

Figure C.1: Run 1 vertical unregressed (raw) asymmetries. The physics asymmetry is
extracted as the amplitude of the sinusoidal variation in the lower plot.

(a) IHWP plot

(b) Sign-corrected plot

Figure C.2: Run 2 vertical unregressed (raw) asymmetries. The physics asymmetry is
extracted as the amplitude of the sinusoidal variation in the lower plot.

Table C.2: Fit parameters and statistics from the unregressed transverse aluminum data set. Uncertainties provided are statistical only.

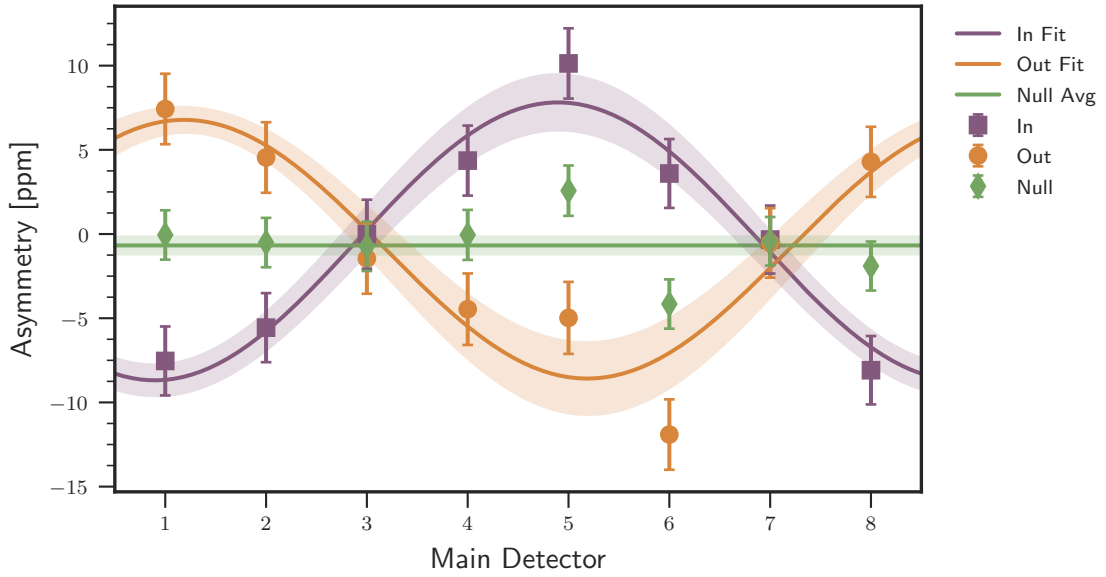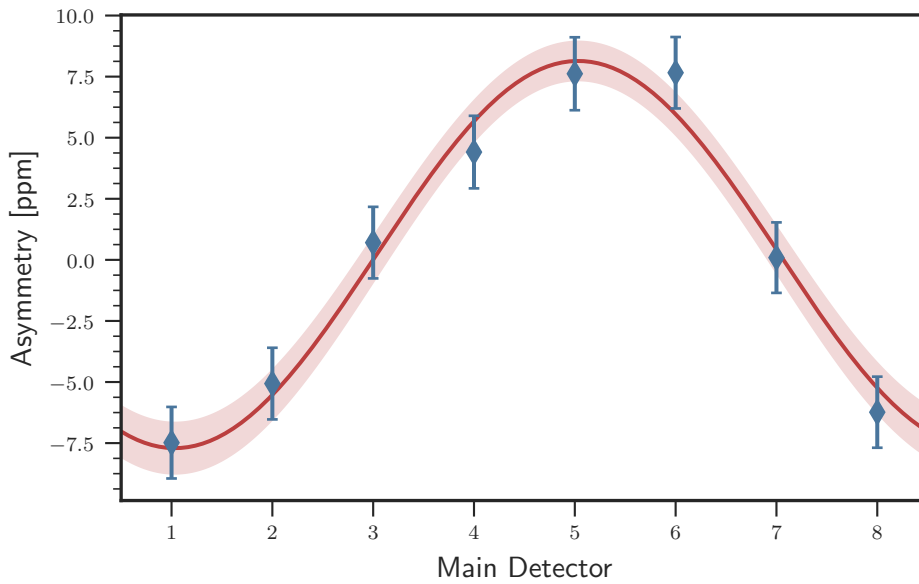| Quantity	Amplitude (B) [ppm]	Phase (φ) [rad]	Constant (C) [ppm]	χ^2/DOF	χ^2 Prob.
		Run 1 - Vertical			
IN	-9.4369 ± 0.8318	0.1639 ± 0.0881	0.3314 ± 0.5883	1.8154	0.106
OUT	8.9736 ± 0.8815	0.1018 ± 0.0982	-0.6765 ± 0.6234	0.7088	0.6167
NULL	–	–	-0.1788 ± 0.4285	1.0234	0.412
PHYS	-9.2144 ± 0.6050	0.1355 ± 0.0657	0.4939 ± 0.4279	1.1649	0.3237
		Run 2 - Horizontal			
IN	-8.4628 ± 0.8413	0.1873 ± 0.1005	-0.5206 ± 0.5981	0.6148	0.6886
OUT	8.4669 ± 0.6249	0.0232 ± 0.0744	-0.1405 ± 0.4436	0.8351	0.5244
NULL	–	–	-0.3375 ± 0.3723	0.4635	0.8615
PHYS	-8.4397 ± 0.5016	0.0813 ± 0.0600	-0.0941 ± 0.3563	1.1447	0.3341
		Run 2 - Vertical			
IN	-8.2527 ± 1.0298	0.0810 ± 0.1237	-0.4350 ± 0.7252	0.6221	0.683
OUT	7.6828 ± 1.0529	-0.1457 ± 0.1360	-0.9008 ± 0.7417	1.9569	0.0816
NULL	–	–	-0.6771 ± 0.5186	1.6439	0.118
PHYS	-7.9236 ± 0.7363	-0.0257 ± 0.0922	0.2175 ± 0.5185	0.6115	0.6911
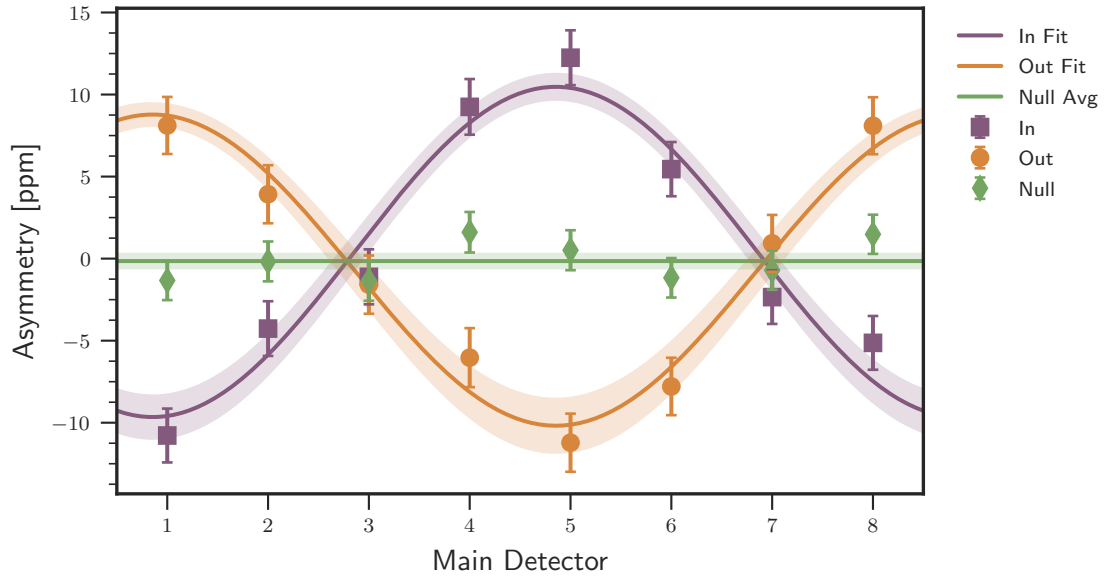
(a) IHWP plot

(b) Sign-corrected plot

Figure C.3: Run 1 vertical regressed (set "on") asymmetries. The physics asymmetry is
extracted as the amplitude of the sinusoidal variation in the lower plot.
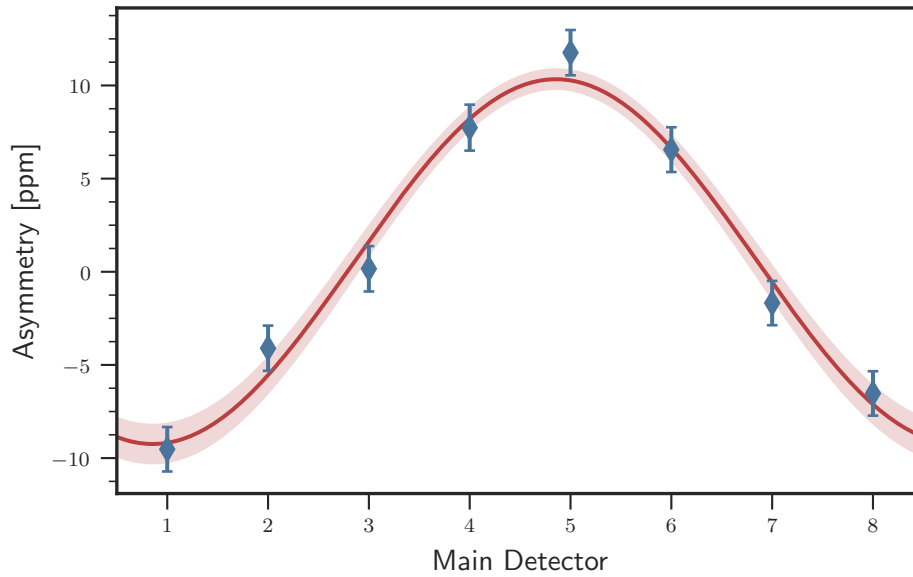
(a) IHWP plot

(b) Sign-corrected plot

Figure C.4: Run 2 horizontal regressed (set "on") asymmetries. The physics asymmetry is
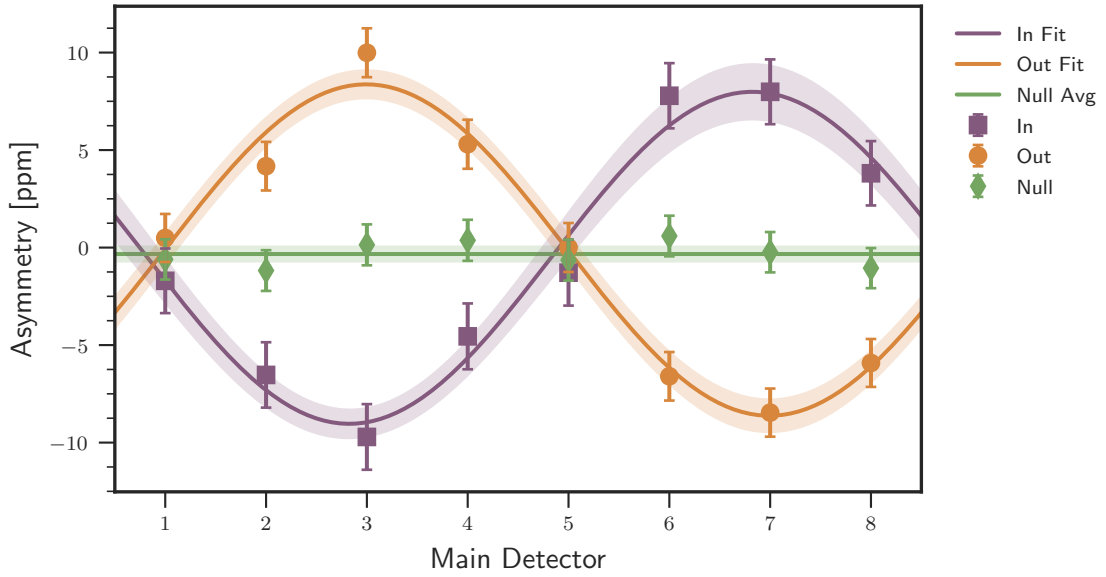extracted as the amplitude of the sinusoidal variation in the lower plot.
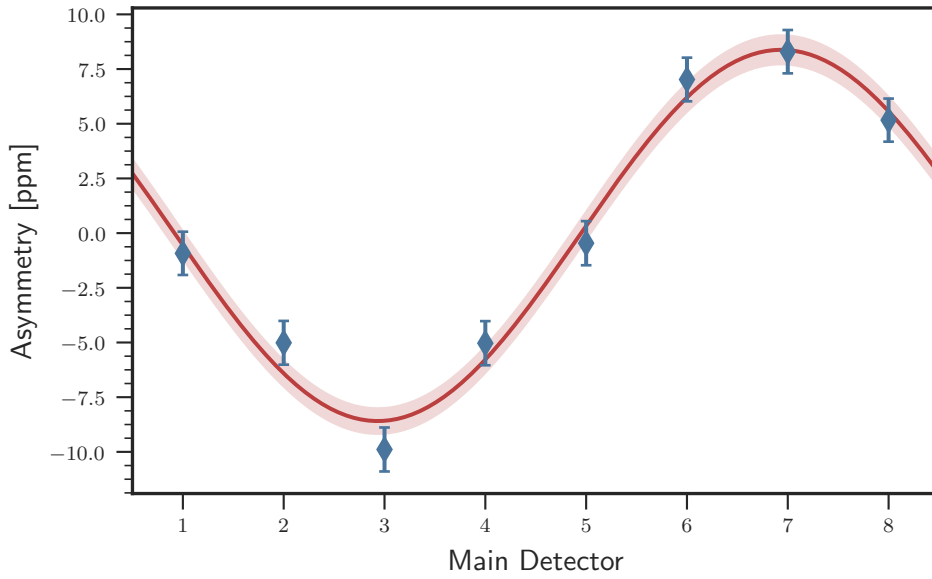
(a) IHWP plot
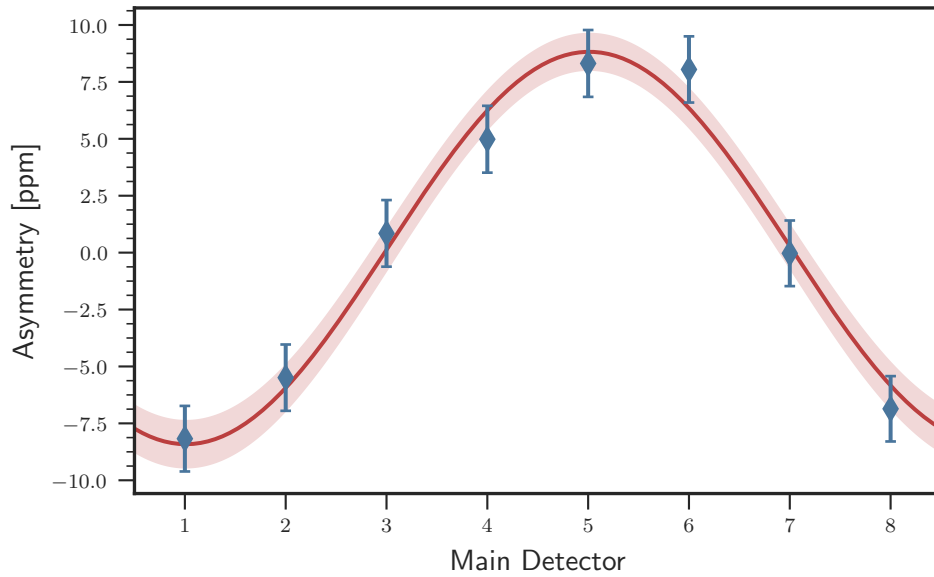
(b) Sign-corrected plot

Figure C.5: Run 2 vertical regressed (set "on") asymmetries. The physics asymmetry is
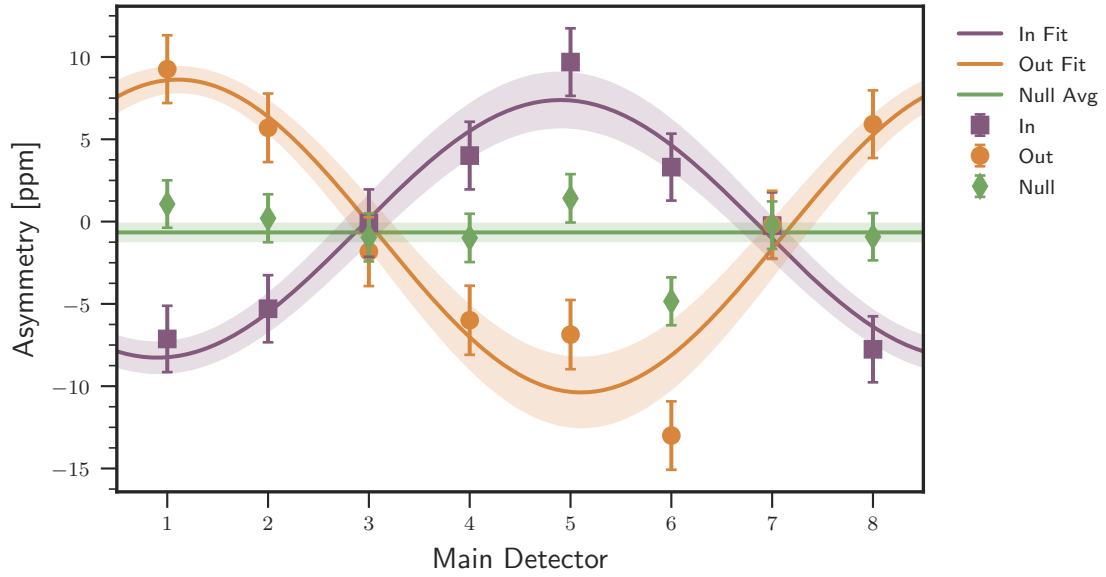extracted as the amplitude of the sinusoidal variation in the lower plot.

Table C.3: Fit parameters and statistics from the regressed transverse aluminum data set, using regression set "on". Uncertainties provided are statistical only.

Quantity	Amplitude (B) [ppm]	Phase (φ) [rad]	Constant (C) [ppm]	χ^2/DOF	χ^2 Prob.
Run 1 - Vertical					
IN	-10.0640 ± 0.8299	0.1136 ± 0.0824	0.4072 ± 0.5867	1.8064	0.1078
OUT	9.4836 ± 0.8797	0.1140 ± 0.0927	-0.7009 ± 0.6219	0.7161	0.6113
NULL	–	–	-0.1502 ± 0.4274	1.0093	0.4222
PHYS	-9.7907 ± 0.6037	0.1138 ± 0.0616	0.5454 ± 0.4268	1.1555	0.3285
Run 2 - Horizontal					
IN	-8.5127 ± 0.8361	0.1375 ± 0.0982	-0.5249 ± 0.5911	0.6451	0.6652
OUT	8.4968 ± 0.6221	0.0056 ± 0.0732	-0.1264 ± 0.4400	0.8408	0.5204
NULL	–	–	-0.3306 ± 0.3684	0.3933	0.9069
PHYS	-8.4856 ± 0.4991	0.0527 ± 0.0588	-0.1057 ± 0.3530	1.1669	0.3226
Run 2 - Vertical					
IN	-7.8265 ± 1.0168	0.0776 ± 0.1299	-0.4407 ± 0.7189	0.642	0.6677
OUT	9.5031 ± 1.0397	-0.0827 ± 0.1093	-0.8770 ± 0.7349	1.995	0.0759
NULL	–	–	-0.6570 ± 0.5139	1.7535	0.0919
PHYS	-8.6186 ± 0.7270	-0.0085 ± 0.0843	0.2033 ± 0.5139	0.6281	0.6783

References

Citations that reference either the Q_{weak} electronic logbook (Q_{weak} ELOG) or Q_{weak} document database (Q_{weak} docDB) presently require credentials to access. For assistance accessing documents of this type please contact the author directly at the following address, kdbartlett@email.wm.edu.

[1] D. Armstrong et al. (Q_{weak} Collaboration), *The Q_{weak} Experiment: "A Search for New Physics at the TeV Scale via a Measurement of the Proton's Weak Charge"*, Jefferson Laboratory, (2001) `https://www.jlab.org/exp_prog/proposals/02/PR02-020.pdf`.

[2] D. Armstrong et al. (Q_{weak} Collaboration), *The Q_{weak} Experiment: "A Search for New Physics at the TeV Scale via a Measurement of the Proton's Weak Charge"*, Jefferson Laboratory, (2004) `https://www.jlab.org/exp_prog/proposals/05/PR05-008.pdf`.

[3] D. Armstrong et al. (Q_{weak} Collaboration), *The Q_{weak} Experiment: "A Search for New Physics at the TeV Scale via a Measurement of the Proton's Weak Charge"*, Jefferson Laboratory, (2007) `https://www.jlab.org/exp_prog/proposals/08/PR-08-016.pdf`.

[4] C. Burgard, *Standard Model of Physics*, TeXample.net, (2016) `http://www.texample.net/tikz/examples/model-physics/`.

[5] D. Galbraith, *UX: Standard Model of the Standard Model*, CERN Webfest 2012, (2017) `http://davidgalbraith.org/portfolio/ux-standard-model-of-the-standard-model/`.

[6] E. Noether, Gott. Nachr. **1918**, 235 (1918).

[7] C. S. Wu, E. Ambler, R. W. Hayward, D. D. Hoppes, and R. P. Hudson, Physical Review **105**, 1413 (1957).

[8] T. D. Lee and C. N. Yang, Physical Review **104**, 254 (1956).

[9] C. Patrignani et al. (Particle Data Group), Chinese Physics **C40**, 100001 (2016).

[10] T. Donnelly, J. Formaggio, B. Holstein, R. Milner, and B. Surrow, *Foundations of Nuclear and Particle Physics*, 1st ed. (Cambridge University Press, Cambridge, 2017).

[11] S. L. Glashow, Nuclear Physics **22**, 579 (1961).

[12] S. Glashow, J. Iliopoulos, and L. Maiani, Physical Review D **2**, 1285 (1970).

[13] S. Weinberg, Physical Review Letters **19**, 1264 (1967).

[14] A. Salam, in Elementary particle theory, Proceedings of the Eighth Nobel Symposium, edited by N. Svartholm (1968), pp. 367–377.

[15] A. Salam and J. Ward, Physics Letters **13**, 168 (1964).

[16] *The Nobel Prize in Physics 1979*, Nobel Media AB, (2014) `https://www.nobelprize.org/nobel_prizes/physics/laureates/1979/`.

[17] P. W. Higgs, Physical Review Letters **13**, 508 (1964).

[18] F. Englert and R. Brout, Physical Review Letters **13**, 321 (1964).

[19] P. Langacker, *The Standard Model and Beyond*, 1st ed. (CRC Press, Boca Raton, 2010).

[20] *How to draw Mexican Hat potential?*, Tex StackExchange, (2015) `https://tex.stackexchange.com/questions/229178/how-to-draw-this-particular-mexican-hat-potential/229217#229217`.

[21] B. Povh, K. Rith, C. Scholz, and F. Zetsche, *Particles and Nuclei: An Introduction to the Physical Concepts*, 3rd ed. (Springer, Berlin, 1999).

[22] B. Foris and C. N. Papanicolas, Annual Review of Nuclear and Particle Science **37**, 133 (1987).

[23] K. S. Krane, *Introductory Nuclear Physics*, 1st ed. (John Wiley & Sons, Inc., Hoboken, 1988).

[24] V. M. Gray, "Determination of the Kinematics of the Q_{weak} Experiment and Investigation of the Atomic Hydrogen Mller Polarimeter", PhD thesis (College of William & Mary, 2018).

[25] F. J. Ernst, R. G. Sachs, and K. C. Wali, Physical Review **119**, 1105 (1960).

[26] M. N. Rosenbluth, Physical Review **79**, 615 (1950).

[27] M. Kohl, Nuclear Physics A **805**, INPC 2007, 361c (2008).

[28] C. Crawford et al., Physical Review C **82**, 045211 (2010).

[29] C. Perdrisat, V. Punjabi, and M. Vanderhaeghen, Progress in Particle and Nuclear Physics **59**, 694 (2007).

[30] S. Galster, H. Klein, J. Moritz, K. Schmidt, D. Wegener, and J. Bleckwenn, Nuclear Physics B **32**, 221 (1971).

[31] Z. Ye, J. Arrington, R. J. Hill, and G. Lee, Physics Letters B **777**, 8 (2018).

[32] D. W. Higinbotham, A. A. Kabir, V. Lin, D. Meekins, B. Norum, and B. Sawatzky, Physical Review C **93**, 055207 (2016).

[33] M. Musolf, T. Donnelly, J. Dubach, S. Pollock, S. Kowalski, and E. Beise, Physics Reports **239**, 1 (1994).

[34] F. Maas and K. Paschke, Progress in Particle and Nuclear Physics **95**, 209 (2017).

[35] J. Green, S. Meinel, M. Engelhardt, S. Krieg, J. Laeuchli, J. Negele, K. Orginos, A. Pochinsky, and S. Syritsyn, Physical Review D **92**, 031501 (2015).

[36] R. S. Sufian, Y.-B. Yang, A. Alexandru, T. Draper, J. Liang, and K.-F. Liu (χQCD Collaboration), Physical Review Letters **118**, 042001 (2017).

[37] D. Armstrong and R. McKeown, Annual Review of Nuclear and Particle Science **62**, 337 (2012).

[38] R. B. Firestone, *Table of Isotopes*, edited by V. S. Shirley, C. M. Baglin, S. F. Chu, and J. Zipkin, 8th ed. (John Wiley & Son, Inc., New York, 1996), pp. 65–69.

[39] T. Stovall, D. Vinciguerra, and M. Bernheim, Nuclear Physics A **91**, 513 (1967).

[40] C. J. Horowitz, Physical Review C **89**, 045503 (2014).

[41] G. C. Li, M. R. Yearian, and I. Sick, Physical Review C **9**, 1861 (1974).

[42] P. P. Singhal, A. Watt, and R. R. Whitehead, Journal of Physics G: Nuclear Physics **8**, 1059 (1982).

[43] T. W. Donnelly and I. Sick, Review of Modern Physics **56**, 461 (1984).

[44] C. J. Horowitz, Private Communication, June 22, 2017.

[45] R. D. Young, J. Roche, R. D. Carlini, and A. W. Thomas, Physical Review Letters **97**, 102002 (2006).

[46] D. Androi et al. (Q_{weak} Collaboration), Nature **557**, 207 (2018).

[47] J. Erler, A. Kurylov, and M. J. Ramsey-Musolf, Physical Review D **68**, 016006 (2003).

[48] R. D. Young, R. D. Carlini, A. W. Thomas, and J. Roche, Physical Review Letters **99**, 122003 (2007).

[49] D. Androic et al. (Q_{weak} Collaboration), Physical Review Letters **111**, 141803 (2013).

[50] J. Liu, C. Xu, S. Wang, and Z. Ren, Physical Review C **96**, 034314 (2017).

[51] T. Donnelly, J. Dubach, and I. Sick, Nuclear Physics A **503**, 589 (1989).

[52] C. J. Horowitz, S. J. Pollock, P. A. Souder, and R. Michaels, Physical Review C **63**, 025501 (2001).

[53] C. J. Horowitz et al., Physical Review C **85**, 032501 (2012).

[54] A. Ong, J. C. Berengut, and V. V. Flambaum, Physical Review C **82**, 014320 (2010).

[55] F. J. Fattoyev, J. Piekarewicz, and C. J. Horowitz, Physical Review Letters **120**, 172702 (2018).

[56] L. W. Mo and Y. S. Tsai, Review of Modern Physics **41**, 205 (1969).

[57] Y. S. Tsai, *Radiative Corrections to Electron Scatterings*, (1971) `http://www-public.slac.stanford.edu/sciDoc/docMeta.aspx?slacPubNumber=SLAC-PUB-0848`.

[58] M. E. Peskin and D. V. Schroeder, *An Introduction to Quantum Field Theory*, 1st ed. (Westview Press, 1995).

[59] J. Erler and M. J. Ramsey-Musolf, Physical Review D **72**, 073003 (2005).

[60] A. Ferroglia, G. Ossola, and A. Sirlin, The European Physical Journal C - Particles and Fields **34**, 165 (2004).

[61] A. Czarnecki and W. J. Marciano, International Journal Modern Physics **A15**, 2365 (2000).

[62] J. Dowd, "Probe of Electroweak Interference Effects in Non-Resonant Inelastic Electron-Proton Scattering", PhD thesis (College of William & Mary, 2018).

[63] C. S. Wood, S. C. Bennett, D. Cho, B. P. Masterson, J. L. Roberts, C. E. Tanner, and C. E. Wieman, Science **275**, 1759 (1997).

[64] V. A. Dzuba, J. C. Berengut, V. V. Flambaum, and B. Roberts, Physical Review Letters **109**, 203003 (2012).

[65] N. H. Edwards, S. J. Phipp, P. E. G. Baird, and S. Nakayama, Physical Review Letters **74**, 2654 (1995).

[66] P. A. Vetter, D. M. Meekhof, P. K. Majumder, S. K. Lamoreaux, and E. N. Fortson, Physical Review Letters **74**, 2658 (1995).

[67] D. M. Meekhof, P. Vetter, P. K. Majumder, S. K. Lamoreaux, and E. N. Fortson, Physical Review Letters **71**, 3442 (1993).

[68] M. J. D. Macpherson, K. P. Zetie, R. B. Warrington, D. N. Stacey, and J. P. Hoare, Physical Review Letters **67**, 2784 (1991).

[69] J. Guna, M. Lintz, and M. A. Bouchiat, Physical Review A **71**, 042108 (2005).

[70] K. Kumar, S. Mantry, W. Marciano, and P. Souder, Annual Review of Nuclear and Particle Science **63**, 237 (2013).

[71] M. Ramsey-Musolf and S. Su, Physics Reports **456**, 1 (2008).

[72] P. Langacker, Review of Modern Physics **81**, 1199 (2009).

[73] H. Davoudiasl, H.-S. Lee, and W. J. Marciano, Physical Review D **92**, 055005 (2015).

[74] K. Cheung, Physics Letters B **517**, 167 (2001).

[75] L. Diaconescu and M. J. Ramsey-Musolf, Physical Review C **70**, 054003 (2004).

[76] M. Gorchtein and C. J. Horowitz, Physical Review C **77**, 044606 (2008).

[77] B. Pasquini and M. Vanderhaeghen, Physical Review C **70**, 045206 (2004).

[78] A. V. Afanasev and N. Merenkov, Physics Letters B **599**, 48 (2004).

[79] D. Borisyuk and A. Kobushkin, Physical Review C **75**, 038202 (2007).

[80] M. Gorchtein, Physical Review C **73**, 055201 (2006).

[81] M. Gorchtein, P. Guichon, and M. Vanderhaeghen, Nuclear Physics A **741**, 234 (2004).

[82] E. D. Cooper and C. J. Horowitz, Physical Review C **72**, 034602 (2005).

[83] D. B. P. Waidyawansa, "A 3% Measurement of the Beam Normal Single Spin Asymmetry in Forward Angle Elastic Electron-Proton Scattering using the Q_{weak} Setup", PhD thesis (Ohio University, 2013).

[84] S. Abrahamyan et al. (HAPPEx and PREx Collaborations), Physical Review Letters **109**, 192501 (2012).

[85] D. S. Armstrong et al. (G0 Collaboration), Physical Review Letters **99**, 092301 (2007).

[86] S. P. Wells et al., Physical Review C **63**, 064001 (2001).

[87] D. B. Ros et al., Physical Review Letters **119**, 012501 (2017).

[88] M. J. McHugh III, "A Measurement of the Transverse Asymmetry in Forward-Angle Electron-Carbon Scattering Using the Q_{weak} Apparatus ", PhD thesis (George Washington University, 2017).

[89] J. Mammei, D. McNulty, R. Michaels, K. Paschke, S. Riordan, P. Souder, et al. (CREX), *CREX:Parity-Violating Measurement of the Weak Charge Distribution of ^{48}Ca to 0.02 fm Accuracy*, (2012) `http://hallaweb.jlab.org/parity/prex/c-rex2013_v7.pdf`.

[90] T. Allison et al. (Q_{weak} Collaboration), Nuclear Instruments and Methods in Physics Research Section A: Accelerators, Spectrometers, Detectors and Associated Equipment **781**, 105 (2015).

[91] D. Jones, "Measuring the Weak Charge of the Proton via Elastic Electron-Proton Scattering", PhD thesis (University of Virginia, 2015).

[92] E. Kargiantoulakis, "A Precision Test of the Standard Model via Parity-Violating Electron Scattering in the Q_{weak} Experiment", PhD thesis (University of Virginia, 2015).

[93] J. Bergoz and Bergoz, Nuclear Physics A **525**, 595 (1991).

[94] K. E. Myers, "The First Determination of the Proton's Weak Charge Through Parity-Violating Asymmetry Measurements in Elastic e + p and e + Al Scattering", PhD thesis (The George Washington University, 2012).

[95] J. C. Cornejo, "Compton Scattering Polarimetry for the Determination of the Proton's Weak Charge Through Measurements of the Parity-Violating Asymmetry of 1H(e,e')p", PhD thesis (College of William & Mary, 2016).

[96] A. Narayan et al., Physical Review X **6**, 011013 (2016).

[97] A. Narayan, "Determination of electron beam polarization using electron detector in Compton polarimeter with less than 1% statistical and systematic uncertainty", PhD thesis (Mississippi State University, 2015).

[98] J. A. Magee, "A Measurement of the Parity-Violating Asymmetry in Aluminum and its Contribution to a Measurement of the Proton's Weak Charge", PhD thesis (College of William & Mary, 2016).

[99] J. Magee et al., Physics Letters B **766**, 339 (2017).

[100] A. Subedi, "Determination of the weak charge of the proton through parity violating asymmetry measurements in the elastic e+p scattering", PhD thesis (Mississippi State University, 2014).

[101] G. Smith, *Q_{weak} ELOG: Solid Target Thickness Measurements*, (July 3, 2013) `https://qweak.jlab.org/elog/Target/21`.

[102] K. Bartlett, *Q_{weak} ELOG: Updated Al Target Thickness: Comparison Data to Simulation All Octants (Run1)*, (Dec. 17, 2015) `https://qweak.jlab.org/elog/Analysis+%26+Simulation/1583`.

[103] G. Smith, *Q_{weak} ELOG: Chemical Composition of Our Cell Windows & Dummy Targets*, (July 3, 2013) `https://qweak.jlab.org/elog/Target/22`.

[104] G. Smith, *Q_{weak} ELOG: Elemental Composition of the Run 2 Dummy Target*, (July 13, 2017) `https://qweak.jlab.org/elog/Target/30`.

[105] S. Joshi, W. G. Fahrenholtz, and M. J. O'Keefe, Applied Surface Science **257**, 1859 (2011).

[106] J. Evertsson et al., Applied Surface Science **349**, 826 (2015).

[107] J. Benesch et al. (MOLLER), *The MOLLER Experiment: An Ultra-Precise Measurement of the Weak Mixing Angle Using Mller Scattering*, 2014.

[108] D. Becker et al. (Mainz P2), *The P2 Experiment - A Future High-Precision Measurement of the Electroweak Mixing Angle at Low Momentum Transfer*, 2018.

[109] *International Alloy Designations and Chemical Composition Limits for Wrought Aluminum and Wrought Aluminum Alloys*, The Aluminum Association, (2015) `http://www.aluminum.org/sites/default/files/TEAL_1_OL_2015_FinalPrinted_0.pdf`.

[110] *MatWeb Material Property Data*, (2018) `http://matweb.com/index.aspx`.

[111] H. D. Vries, C. D. Jager, and C. D. Vries, Atomic Data and Nuclear Data Tables **36**, 495 (1987).

[112] G. Fricke, C. Bernhardt, K. Heilig, L. Schaller, L. Schellenberg, E. Shera, and C. Dejager, Atomic Data and Nuclear Data Tables **60**, 177 (1995).

[113] S. Agostinelli et al. (Geant4 Collaboration), Nuclear Instruments and Methods in Physics Research Section A: Accelerators, Spectrometers, Detectors and Associated Equipment **506**, 250 (2003).

[114] J. Allison et al. (Geant4 Collaboration), IEEE Transactions on Nuclear Science **53**, 270 (2006).

[115] J. Allison et al. (Geant4 Collaboration), Nuclear Instruments and Methods in Physics Research Section A: Accelerators, Spectrometers, Detectors and Associated Equipment **835**, 186 (2016).

[116] *QwGeant4 SVN Repository*, (2018) `https://qweaksvn.jlab.org/repos/Simulation/trunk/QWGEANT4/`.

[117] K. Bartlett, Q_{weak} *ELOG: 4% DS Aluminum Target Simulation Acceptance Function*, (July 13, 2017) `https://qweak.jlab.org/elog/Analysis+%26+Simulation/1673`.

[118] P. Wang, "A Measurement of the Proton's Weak Charge Using an Integration Cerenkov Detector System", PhD thesis (University of Manitoba (Canada), 2011).

[119] S. Yang, "A Precision Measurement of the Weak Charge of the Proton at Low Q^2: Kinematics and Tracking", PhD thesis (College of William & Mary, 2016).

[120] J. Pan, "Towards a Precision Measurement of Parity-Violating e-p Elastic Scattering at Low Momentum Transfer", PhD thesis (University of Manitoba (Canada), 2012).

[121] R. S. Beminiwattha, "A Measurement of the Weak Charge of the Proton through Parity Violating Electron Scattering using the Q_{weak} Apparatus: A 21% Result", PhD thesis (Ohio University, 2013).

[122] S. Abrahamyan et al. (PREx Collaboration), Physical Review Letters **108**, 112502 (2012).

[123] K. Mesick, Q_{weak} *ELOG: Run2 pass5b Aluminum: good_for_gui changes 1/29/2015*, (Jan. 30, 2015) `https://qweak.jlab.org/elog/Analysis+%26+Simulation/1365`.

[124] J. Magee, Q_{weak} *ELOG: Run 2 4%-DS Aluminum Data Quality + Cuts*, (July 25, 2013) `https://qweak.jlab.org/elog/Analysis+%26+Simulation/957`.

[125] K. Mesick, Q_{weak} *ELOG: Asymmetry for 4% DS Aluminum - Updated w/o Wien 10*, (Feb. 1, 2016) `https://qweak.jlab.org/elog/Analysis+%26+Simulation/1593`.

[126] P. Zang (Q$_{weak}$ Collaboration), *Q$_{weak}$ dobDB: BCM Renormalization (Pass5c+)*, (Feb. 17, 2017) `https://qweak.jlab.org/DocDB/0023/002344/010/BCM_Normalization_in_RUN1_and_RUN2_Pass5c%2B_new_mdMrn_norm.pdf`.

[127] K. Mesick, *Q$_{weak}$ ELOG: Regression Scheme Dependence for 4% DS Aluminum*, (July 31, 2015) `https://qweak.jlab.org/elog/Analysis+%26+Simulation/1517`.

[128] Nuruzzaman, *Q$_{weak}$ ELOG: Q-weak Regression Schemes*, (Apr. 16, 2012) `https://qweak.jlab.org/elog/Management/5`.

[129] K. Mesick, *Q$_{weak}$ ELOG: Beamline Background Study for Run 2 Aluminum*, (July 7, 2015) `https://qweak.jlab.org/elog/Analysis+%26+Simulation/1501`.

[130] K. Mesick, *Q$_{weak}$ ELOG: Beamline Background Dilution for Aluminum Run 2*, (Apr. 2, 2015) `https://qweak.jlab.org/elog/Analysis+%26+Simulation/1439`.

[131] W. Duvall, "Precision Measurement of the Protons Weak Charge using Parity-Violating Electron Scattering", PhD thesis (Virginia Polytechnic Institute and State University, 2017).

[132] K. Bartlett, *Q$_{weak}$ ELOG: Aluminum Transverse Leakage*, (Aug. 18, 2017) `https://qweak.jlab.org/elog/Analysis+%26+Simulation/1675`.

[133] C. Gal, D. Armstrong, W. Duvall, M. Gericke, P. King, J. Pan, K. Paschke, and V. Owen (Q$_{weak}$ Collaboration), *Q$_{weak}$ DD studies*, (May 7, 2018) `https://qweak.jlab.org/doc-private/ShowDocument?docid=2455`.

[134] G. Smith, *Q$_{weak}$ ELOG: A$_{bias}$ for Aluminum*, (Sept. 14, 2016) `https://qweak.jlab.org/elog/Analysis+%26+Simulation/1646`.

[135] K. Mesick, *Q$_{weak}$ ELOG: Systematic Corrections and Uncertainties for 4% DS Aluminum*, (July 31, 2015) `https://qweak.jlab.org/elog/Analysis+&+Simulation/1518`.

[136] V. Owen, *Q$_{weak}$ ELOG: Al DS 4% PMTDD and Abias*, (Mar. 12, 2018) `https://qweak.jlab.org/elog/Analysis+%26+Simulation/1687`.

[137] D. Gaskell, *Q$_{weak}$ ELOG: Run 2 Final Polarizations - Updated Proposal*, (May 6, 2015) `https://qweak.jlab.org/elog/DAQ+%26+Analysis/334`.

[138] J. Dowd, *Q$_{weak}$ ELOG: Rate and Yield Variables in QwGeant4*, (Apr. 14, 2014) `https://qweak.jlab.org/elog/Analysis+%26+Simulation/1128`.

[139] A. Bohr and B. R. Mottelson, *Nuclear Structure*, 2nd ed., 2 vols. (World Scientific Publishing Co. Pte. Ltd., Singapore, 1998).

[140] P. E. Bosted and V. Mamyan, *Empirical Fit to Electron-Nucleus Scattering*, 2012.

[141] P. Bosted, *Peter Bosted's Fits*, (2009) `https://userweb.jlab.org/~bosted/fits.html`.

[142] V. Tvaskis, J. Steinman, and R. Bradford, Nuclear Physics B - Proceedings Supplements **159**, 163 (2006).

[143] K. Bartlett, *Q$_{weak}$ ELOG: Updated Aluminum Bosted Model Uncertainty for QwGeant4*, (Aug. 30, 2017) `https://qweak.jlab.org/elog/Analysis+%26+Simulation/1677`.

[144] C. J. Horowitz and J. Piekarewicz, Physical Review C **47**, 2924 (1993).

[145] C. J. Horowitz and Z. Lin, Private Communication, Aug. 30, 2017.

[146] Z. Lin and C. Horowitz, Q_{weak} *ELOG: Quasi-elasic Scattering of Al27*, (Aug. 30, 2017) `https://qweak.jlab.org/elog/Analysis+%26+Simulation/1679`.

[147] R. Gonzlez-Jimnez, J. A. Caballero, and T. W. Donnelly, Phyical Review C **91**, 045502 (2015).

[148] K. Bartlett, Q_{weak} *ELOG: Aluminum N to Delta Asymmetry Extraction*, (Nov. 20, 2017) `https://qweak.jlab.org/elog/Analysis+&+Simulation/1683`.

[149] P. Amore, R. Cenni, T. Donnelly, and A. Molinari, Nuclear Physics A **690**, 509 (2001).

[150] R. Singhal, A. Johnston, W. Gillespie, and E. Lees, Nuclear Physics A **279**, 29 (1977).

[151] R. S. Hicks, A. Hotta, J. B. Flanz, and H. deVries, Physical Review C **21**, 2177 (1980).

[152] P. J. Ryan, R. S. Hicks, A. Hotta, J. Dubach, G. A. Peterson, and D. V. Webb, Physical Review C **27**, 2515 (1983).

[153] P. J. Ryan, R. S. Hicks, A. Hotta, J. Dubach, G. A. Peterson, and D. V. Webb, *AIP document # PRVCA-27-2515-18*, (1983) `http://ftp.aip.org/epaps/phys_rev_c/E-PRVCA-27-2515-18/PRVCA-27-2515-19.PDF`.

[154] E. Jones, T. Oliphant, P. Peterson, et al., *SciPy: open source scientific tools for Python*, (2018) `http://www.scipy.org/`.

[155] P. R. Bevington and D. K. Robison, *Data Reduction and Error Analysis for the Physical Sciences*, 3rd ed. (McGraw Hill, Boston, 2003).

[156] K. Bartlett, Q_{weak} *ELOG: Aluminum Nuclear Excited States QwGeant4 Generator Revisited: Final Fits and Uncertainties*, (May 11, 2017) `https://qweak.jlab.org/elog/Analysis+%26+Simulation/1671`.

[157] P. Endt, Nuclear Physics A **521**, 1 (1990).

[158] P. Endt, Nuclear Physics A **633**, 1 (1998).

[159] K. Bartlett, Q_{weak} *ELOG: Aluminum Nuclear Excited States QwGeant4 Generator Revisited: Asymmetry*, (May 5, 2017) `https://qweak.jlab.org/elog/Analysis+%26+Simulation/1670`.

[160] J. Goldemberg, Y. Torizuka, W. C. Barber, and J. D. Walecka, Nuclear Physics, 242 (1963).

[161] A. Varlamov, V. Varlamov, D. Rudenko, and M. Stepanov, *Atlas of Giant Dipole Resonances*, (Jan. 1999) `https://www.iaea.org/inis/collection/nclcollectionstore/_public/30/003/30003843.pdf`.

[162] J. Ahrens et al., Nuclear Physics A **251**, 479 (1975).

[163] R. Silwal and R. Michaels, Q_{weak} *docDB: Asymmetry Estimates for Inelastic States and Isotope Contamination*, (Jan. 10, 2014) `https://qweak.jlab.org/doc-private/ShowDocument?docid=2285`.

[164] C. J. Horowitz and Z. Lin, Private Communication, July 5, 2017.

[165] K. Bartlett, Q_{weak} *ELOG: Horowitz Distorted Wave Cross-section and Parity-violating Asymmetry Calculations*, (July 7, 2017) `https://qweak.jlab.org/elog/Analysis+%26+Simulation/1672`.

[166] K. Mesick, *Q_{weak} ELOG: Models for Aluminum Alloy Cross Sections*, (Nov. 12, 2014) `https://qweak.jlab.org/elog/Analysis+%26+Simulation/1309`.

[167] M. McHugh, *Q_{weak} docDB: Measurement of the QTor Transport Channel Neutral Background*, (May 31, 2016) `https://qweak.jlab.org/doc-private/ShowDocument?docid=2337`.

[168] D. E. Wiser, "Inclusive Photoproduction of Protons, Kaons, and Pions at SLAC Energies", PhD thesis (University of Wisconsin-Madison, 1977).

[169] S. Riordan, N. Ton, Z. Zhao, and X. Zheng, *Comparison between Wiser π^- Rates Calculation and Data from Transversity and PVDIS Experiments*, (Dec. 23, 2014) `http://hallaweb.jlab.org/experiment/E05-007/SoLID/EC/meetings/wiser_calc/memo46-wiser.pdf`.

[170] D. Armstrong, *W&M ELOG: Q^2 for Run 2 4% DS Aluminum target*, (Mar. 7, 2018) `https://dilbert.physics.wm.edu/Physics/225`.

[171] K. Bartlett, *Q_{weak} ELOG: Aluminum Asymmetry R_{det}*, (Oct. 6, 2017) `https://qweak.jlab.org/elog/Analysis+%26+Simulation/1682`.

[172] D. Armstrong, *Q_{weak} ELOG:Q^2 Light-Weighting for Al Windows: Summary*, (June 3, 2016) `https://qweak.jlab.org/elog/Tracking/241`.

[173] D. Armstrong, *Q_{weak} ELOG: R_{det} (Light-Weighting Correction) for Hydrogen*, (June 2, 2016) `https://qweak.jlab.org/elog/Tracking/239`.

[174] D. T. Spayde, "Measurement of the Strange Magnetic Form Factor of the Proton Using Elastic Electron Scattering", PhD thesis (University of Maryland, 2001).

[175] C. Ellis, "Measurement of the Strange Quark Contribution to Nucleon Structure Through Parity-Violating Electron Scattering", PhD thesis (University of Maryland, 2010).

[176] H. berall, *Electron Scattering from Complex Nuclei*, 1st ed., 2 vols. (Academic Press, Inc., New York, 1971).

[177] V. Gray, *W&M ELOG: Al Radiative Correction*, (Mar. 16, 2018) `https://dilbert.physics.wm.edu/Physics/230`.

[178] D. Armstrong, *W&M ELOG: R_{Q^2} and dR_{Q^2} for Aluminum PV Measurement*, (Oct. 5, 2017) `https://dilbert.physics.wm.edu/Physics/214`.

[179] V. Gray, *W&M ELOG: Al Q^2 Studies - Full Stats*, (Feb. 12, 2018) `https://dilbert.physics.wm.edu/Physics/221`.

[180] D. Armstrong, *W&M ELOG: Raster size dependence of Q^2 - Updated*, (Mar. 3, 2015) `https://dilbert.physics.wm.edu/Physics/126`.

[181] V. Gray, *W&M ELOG: Al Q^2 Studies - Thickness*, (Jan. 16, 2018) `https://dilbert.physics.wm.edu/Physics/219`.

[182] V. Gray, *W&M ELOG: Al Q^2 Studies - QTor Scan*, (Feb. 13, 2018) `https://dilbert.physics.wm.edu/Physics/223`.

[183] V. Gray, *W&M ELOG: Al Q^2 Studies - QTor Scan*, (Feb. 13, 2018) `https://dilbert.physics.wm.edu/Physics/229`.

[184] V. Gray, *W&M ELOG: Al Q^2 Studies - Position*, (Jan. 15, 2018) `https://dilbert.physics.wm.edu/Physics/218`.

[185] V. Gray, *W&M ELOG: Al Q^2 Studies - QTor Field Rotations*, (Mar. 1, 2018) `https://dilbert.physics.wm.edu/Physics/224`.

[186] V. Gray, *W&M ELOG: Al Q^2 Studies - MD Locations*, (Feb. 12, 2018) `https://dilbert.physics.wm.edu/Physics/222`.

[187] V. Gray, *W&M ELOG: Al Q^2 Studies - Primary Collimator Location*, (Jan. 16, 2018) `https://dilbert.physics.wm.edu/Physics/220`.

[188] D. Armstrong, *W&M ELOG: Al: Collimator Imperfections Contribution to Q^2 Uncertainty*, (Dec. 14, 2017) `https://dilbert.physics.wm.edu/Physics/215`.

[189] K. Bartlett, *Q_{weak} ELOG: Aluminum Asymmetry Slope Calculation for R_{Q^2}*, (Oct. 6, 2017) `https://qweak.jlab.org/elog/Analysis+%26+Simulation/1681`.

[190] K. Bartlett, *Q_{weak} ELOG: 4% DS Aluminum Simulation QTorscan Revisited*, (Sept. 14, 2017) `https://qweak.jlab.org/elog/Analysis+&+Simulation/1680`.

[191] V. Gray, *W&M ELOG: Al Schwinger Correction - DeltaE Variable*, (Mar. 26, 2018) `https://dilbert.physics.wm.edu/Physics/231`.

[192] B. G. Todd-Rutel and J. Piekarewicz, Physical Review Letters **95**, 122501 (2005).

[193] W.-C. Chen and J. Piekarewicz, Physics Letters B **748**, 284 (2015).

[194] W.-C. Chen and J. Piekarewicz, Physical Review C **90**, 044305 (2014).

[195] F. J. Fattoyev, C. J. Horowitz, J. Piekarewicz, and G. Shen, Physical Review C **82**, 055803 (2010).

[196] G. A. Lalazissis, J. Knig, and P. Ring, Physical Review C **55**, 540 (1997).

[197] G. Lalazissis, S. Raman, and P. Ring, Atomic Data and Nuclear Data Tables **71**, 1 (1999).

[198] F. J. Fattoyev and J. Piekarewicz, Physical Review Letters **111**, 162501 (2013).

[199] C. J. Horowitz, F. Fattoyev, and Z. Lin, Private Communication, Dec. 12, 2017.

[200] R. Lombard and G. Bishop, Nuclear Physics A **101**, 601 (1967).

[201] G. Fey, H. Frank, W. Schtz, and H. Theissen, Zeitschrift fr Physik **265**, 401 (1973).

[202] G. Fricke, J. Herberz, T. Hennemann, G. Mallot, L. A. Schaller, L. Schellenberg, C. Piller, and R. Jacot-Guillarmod, Physical Review C **45**, 80 (1992).

[203] D. Armstrong, *Q_{weak} ELOG: New source of A_{bias} for Transverse Data*, (May 21, 2018) `https://qweak.jlab.org/elog/Detector/221`.

[204] D. Armstrong, *Q_{weak} ELOG: More on A_{bias} for Transverse Data*, (May 29, 2018) `https://qweak.jlab.org/elog/Detector/223`.

[205] Nuruzzaman, "Beam normal single spin asymmetry in forward angle inelastic electron-proton scattering using the Q_{weak} apparatus", PhD thesis (Hampton University, 2015).

[206] K. Bartlett, *Q_{weak} ELOG: Estimate of Beam-Normal Single-Spin Asymmetry from Al Alloy Elements*, (Mar. 23, 2016) `https://qweak.jlab.org/elog/Ancillary/246`.

[207] K. Bartlett, *Q_{weak} ELOG: Check of the Measured 4% DS Aluminum Asymmetry Extraction*, (Nov. 11, 2016) `https://qweak.jlab.org/elog/Analysis+%26+Simulation/1650`.

[208] K. Mesick, K. Bartlett, and J. Magee, *Qweak Wiki:Aluminum Background*, `https://qweak.jlab.org/wiki/index.php/Aluminum_Background#Measured_Asymmetry_Analysis_Summary`.

[209] D. Armstrong, Q_{weak} *ELOG: Effective Aluminum Window Asymmetry: Light-Weighting and Window Thickness Uncertainties*, (May 27, 2016) `https://qweak.jlab.org/elog/Analysis+%26+Simulation/1624`.

[210] K. Bartlett and K. Mesick, Q_{weak} *ELOG: Final Determination of the Effective Aluminum Window Asymmetry($A_{b1} \pm dA_{b1}$) using Monte Carlo Method*, (Nov. 12, 2016) `https://qweak.jlab.org/elog/Analysis+&+Simulation/1651`.

[211] Z. Lin and C. J. Horowitz, Physical Review C **92**, 014313 (2015).

[212] Y. S. Tsai, Review Modern Physics **46**, [Erratum: Rev. Mod. Phys.49,521(1977)], 815 (1974).

[213] *Standard Atomic Weights*, CIAAW IUPAC, (2015) `http://www.ciaaw.org/atomic-weights.htm`.

[214] *Atomic and Nuclear Properties of Materials*, Particle Data Group, (2016) `http://pdg.lbl.gov/2017/AtomicNuclearProperties/`.

[215] W. Leo, *Techniques for Nuclear and Particle Physics Experiments*, 2nd ed. (Springer-Verlag, Berlin, 1994).